Optimizing the Processability of Selenium Nanowires and Their Chemical Transformation into Polymer Coated Semiconductor Materials

by

Michael Chih-Pin Wang

B.Sc., Simon Fraser University, 2007

Thesis Submitted In Partial Fulfillment of the
Requirements for the Degree of
Doctor of Philosophy

in the
Department of Chemistry
Faculty of Science

SIMON FRASER UNIVERSITY

Spring 2014

Approval

Name: **Michael Chih-Pin Wang**

Degree: **Doctor of Philosophy (Chemistry)**

Title of Thesis: ***Optimizing the Processability of Selenium Nanowires and Their Chemical Transformation into Polymer Coated Semiconductor Materials***

Examining Committee: **Chair:** David J. Vocadlo
Professor

Dr. Byron D. Gates
Senior Supervisor
Associate Professor

Dr. Zuo-Guang Ye
Supervisor
Professor

Dr. Daniel B. Leznoff
Supervisor
Professor

Dr. Hua-Zhong Yu
Internal Examiner
Professor
Department of Chemistry

Dr. Daniel R. Gamelin
External Examiner
Professor, Department of Chemistry
University of Washington

Date Defended/Approved: April 07, 2014

Partial Copyright Licence

Abstract

This thesis seeks out to optimize the sonochemically-induced synthesis and the ease of handling high-aspect-ratio selenium nanowires. Understanding the selenium nanowire's surface chemistry is crucial to controlling their dimensions during growth and to facilitate the manipulation of these materials. The surface chemistry of the nanowires was analyzed with a variety of surface sensitive techniques and electron microscopy. This knowledge of the surface chemistry of selenium nanowires was utilized to increase their colloidal stability. A stable dispersion of selenium nanowires improves the ease of handling and processing these materials for subsequent assembly or use in templated reactions. For example, surfactant stabilized nanowires enhanced their colloidal stability in media that are otherwise poor at stabilizing the nanowires and improved the uniformity of products from templated reactions on the nanowire surfaces. We also discovered that dispersions of selenium nanowires in a low dielectric constant solution could be organized by electrokinetic techniques into fibers that oriented along the electric field. We developed a general method for the assembly of the selenium nanowires into either macroscopic fibers or an array of fibers of various lengths over large areas. Isolated fibers of selenium nanowires could reversibly bend in response to electrostatic charges. These flexible selenium fibers also exhibited a photoconductive response when illuminated with white light. These properties of selenium nanowires can degrade over time as these nanowires are susceptible to oxidative damage, but we were able to demonstrate the first passivation of selenium nanowires with a thin layer of polystyrene. The thin layer of polystyrene was grafted onto the selenium surfaces by a surface-initiated atom transfer radical polymerization reaction. These encapsulated nanostructures demonstrate an enhanced resistance towards oxidative damage, such as corrosion. We were also able to synthesize polystyrene encapsulated copper selenide nanowires by a similar route in a template-engaged reaction in conjunction with a surface-initiated atom transfer radical polymerization reaction.

Keywords: one-dimensional selenium nanostructures; sonochemically-induced synthesis; polymer coated semiconductor nanowire; electrokinetic assembly; template-engaged transformation; surface-initiated atom transfer radical polymerization

Dedication

To my beloved family.

Acknowledgements

First, I want to express my appreciation to my Senior Supervisor, Professor Byron D. Gates, for his unrelenting support over the course of my graduate career, for giving me freedom to design and shape my projects, also for providing me with opportunities to collaborate with other researchers.

I would like to thank Professor Nabyl Merbouh and Professor Hogan H.-Z. Yu for their mentoring, while I was an undergraduate student.

I wish to thank Nathanael Sieb and Bryan Wood who have helped me getting up to speed when I was a new graduate student and his invaluable advice.

I would like to express my gratitude to Dr. Xin Zhang, Elham Majidi, Penny Wu, and Clara Fabre for their help with experiments, also Kevin Nedelec for his help with COMSOL FEM simulation of electric field.

I would like to thank Professor Karen Kavanagh, Dr. Li Yang, Bryan Wood, and Dr. Xin Zhang for training me on the scanning and transmission electron microscopes.

I would like to thank Peter Farr and Dr. Chris Moffitt from Kratos Analytical Ltd. for their training and assistance on the Kratos Axis Ultra DLD spectrophotometer.

I thank Jeff Rudd from the Physics Department at Simon Fraser University for providing the high voltage power supply for the electrokinetic assembly of semiconductor and metallic nanowires' project.

I was fortunate to learn atomic force microscopy from Hanifa Jalali, as well as Keith Jones of Asylum Research.

I am grateful for my fellow group members and graduate students in the chemistry department who have made my graduate student career colorful and enjoyable.

Table of Contents

List of Tables

List of Figures

List of Acronyms

A.L.	Acceptor Level
APTES	3-Aminopropyltriethoxysilane
a-Se	Amorphous Selenium
1-ButOH	1-Butanol
C.B.	Conduction Band
CCD	Charge Coupled Device
cDNA	Complementary Deoxyribonucleic Acid
CMOS	Complementary Metal-Oxide-Semiconductor
CTAB	Cetyl Trimethylammonium Bromide
CuSe-Cu_2Se	Cuprous and Cupric Selenide
CuSe-Cu_2Se@PS	Cuprous and Cupric Selenide Encapsulated in Polystyrene
DNA	Deoxyribonucleic Acid
D.L.	Donor Level
ε'	Dielectric Constant
ED	Electron Diffraction
EDS	Energy Dispersive X-ray Spectroscopy
EELS	Electron Energy Loss Spectroscopy
E_F	Fermi Energy
EG	Ethylene Glycol
e^--h pair	Electron-Hole Pair
ESCA	Electron Spectroscopy for Chemical Analysis
EtOH	Ethanol
FCC	Face-Centered Cubic
FEM	Finite Element Method
FFT	Fast Fourier Transform
FWHM	Full Width at Half Maximum
HAADF	High-Angle Annular Dark Field
HCP	Hexagonally Close Packed
HUT	11-Hydroxylundecane-1-thiol
ICP-MS	Inductively Coupled Plasma Mass Spectrometry
IMFP	Inelastic Mean Free Path

*i*PA	Isopropanol
LB	Langmuir Blodgett
LED	Light-Emitting Diodes
μ-CP	Microcontact Printing
MAUD	Materials Analysis Using Diffraction
MeOH	Methanol
MONO Al	Monochromatic Aluminum X-ray
MOSFET	Metal-Oxide-Semiconductor Field Effect Transistors
MV/m	Megavolt per Meter
NWs	Nanowires
1-OctOH	1-Octanol
OTS	Octadecyltrichlorosilane
P’	Solvent Polarity
PDMS	Polydimethylsiloxane
PEG	Polyethylene Glycol
PS	Polystyrene
PVA	Polyvinyl Alcohol
PVP	Poly(vinylpyrrolidone)
RT	Room Temperature
SAED	Selected Area Electron Diffraction
SDS	Sodium Dodecyl Sulfate
SEM	Scanning Electron Microscopy
SI-ATRP	Surface-Initiated Atom Transfer Radical Polymerization
SIMS	Secondary Ion Mass Spectrometry
S/m	Siemens per Meter
ssDNA	Single-Stranded Deoxyribonucleic Acid
STEM	Scanning Transmission Electron Microscopy
TEM	Transmission Electron Microscopy
t-Se	Trigonal Selenium
t-Se NWs	Trigonal Selenium Nanowires
t-Se@PS	Trigonal Selenium Encapsulated in Polystyrene
t-Se@Pt-NPs	Trigonal Selenium Nanowires Decorated with Platinum Nanoparticles
UV-Vis	Ultraviolet-Visible Spectrophotometer

V.B.	Valence Band
VLS	Vapour-Liquid-Solid
XPS	X-ray Photoelectron Spectroscopy
XRD	X-ray Diffraction

Glossary

Amorphous Material	Material that lacks long range order at the atomic level.
Auger Electron	An Auger electron is produced when an atom's core orbital electron is removed with an external stimulus (i.e. photon or electron irradiation), leaving a hole in the core level. This hole in the core level is, subsequently, filled by an electron from the outer orbital. In the process of filling the hole in the core level, the outer orbital electron loses an amount of energy that is equivalent to the difference in orbital energies (i.e. outer orbital energy – core orbital energy). Then the lost energy is absorbed by an outer orbital electron that leads to its ionization.
Band-gap	Energy separation between the highest electronic state of the valence band and the lowest electronic state of the conduction band.
Bend Contour	Bend contours occur when a single crystalline sample of uniform thickness is bent slightly, such that a particular set of diffracting planes are not parallel throughout the sample.
Bragg's Law	Scattered waves are only in-phase (i.e. constructively interfere) if the additional distance travelled by the other waves are equal to a multiple of the wavelength (i.e. nλ). When the crystal orientation with respect to incident electromagnetic radiations produces scattered waves that are in-phase, they are said to be under Bragg condition.
Cavitation	A process that involves the formation and implosion of bubbles in a liquid medium. Shockwaves generated by the imploding bubbles have sufficient energy to cause localized chemical and/or physical damage.
Chain Propagation	The progress that leads to the lengthening of polymer chains in a polymerization reaction. In the chain propagation stage of polymerization, the reactive intermediate is continually regenerated after the reactive end-groups of a polymer chain have reacted with a new monomer. The newly attached monomer then becomes the subsequent reactive end-group with which a new monomer will react with.
Chain Termination	A step in polymerization that stops the regeneration of reactive intermediates in a chain propagation process.
Colloidal Dispersion	Colloids having dimensions between 1 μm and 1 nm are dispersed in a continuous phase of a different composition or state.
Colloidal Stability	The ability of a colloidal dispersion to resist flocculation, aggregation, coagulation, sedimentation and phase separation.

Conduction Band	The range of allowable electronic states an electron can occupy that allows the electron to dissociate from a particular atom and become a free charge carrier in the material.
Corrosion	Gradual degradation of materials due to oxidation.
Dielectric Constant	A measure of a substance's ability to insulate either electrostatic or electronic charge.
Crystalline Material	A structure of material that consists of regular, repeating planes of atoms that form a crystal lattice.
d-spacing	In X-ray diffraction analysis, d-spacing refers to the distance between crystalline planes of repeating structure with the same atomic arrangement.
Electrokinetic Assembly	Dipoles of polarized dispersants are aligned along the path of electric field when the sample is exposed to an electric potential difference across the dispersion medium.
Electron Diffraction	Atoms within a solid act as diffraction gratings to scatter the incident electrons in a periodic fashion. Information such as crystallinity of the material, crystal phases, d-spacing, texture of specimen, and crystal orientation can be deduced from electron diffraction pattern.
Electron Energy Loss Spectroscopy	See Transmission Electron Microscopy – Electron Energy Loss Spectroscopy.
Electrostatic Stabilization	Particles in a colloidal dispersion have similar surface charges and, therefore, these particles do not agglomerate because of a mutual repulsion of like electrical charges.
Electron Spectroscopy for Chemical Analysis	See X-ray Photoelectron Spectroscopy.
Face-Centered Cubic Packing	An atomic arrangement of equal size atoms that has an A-B-C-A-B-C…stacking pattern. Interstitial sites in the first layer of close packed structure are occupied by atoms of equal size. Then the interstitial sites of the second layer atoms are filled with atoms without repeating the x and y coordinates of the first layer of close-packed atoms.
Fast Fourier Transform	Fast Fourier transform is an algorithm that converts a set of data consisting of time/spatial domain into frequency domain. For example, a lattice-fringe image of a crystalline specimen obtained on an electron microscopy can be transformed into its corresponding frequency domain image by FFT to provide the inverse d-spacing (i.e. 1/d-spacing) of the periodic atomic arrangement.
Ferromagnetic Material	Large domains of magnetic dipoles are aligned in the same direction, giving the material a net magnetic dipole greater than zero.

Full Width at Half Maximum	Width at half of the maximum intensity of a waveform.
Grafting Polymers	Addition of polymer chains onto the surfaces of a substrate through chemical reaction(s).
Hexagonal Close-Packing	An atomic arrangement of equal size atoms that has an A-B-A-B-…stacking pattern. The second layer atoms are positioned at the interstitial sites on the layer below, which is also arranged in a close-pack fashion. Then the third layer of atoms is positioned in the same x and y coordinates as the first layer of atoms.
Inelastic Mean Free Path	The distance an electron can travel through a medium before losing energy due to scattering.
Langmuir-Blodgett Trough	An apparatus that is used to compress monolayers of materials at the air-liquid or liquid-liquid interphase into close-packing or multilayered structures.
Langmuir-Blodgett Deposition	Transfer of materials at the air-liquid or liquid-liquid interphase in a Langmuir-Blodgett trough onto a solid substrate. For example, a substrate submerged perpendicularly with respect to the meniscus of the subphase is slowly elevated above the liquid phase after the material deposited at the interphase is compacted to a certain surface pressure by the trough's barriers. Surfaces of the substrate are coated with the materials when the substrate is removed from the liquid phase.
Lattice-Fringe	Lattice-fringe patterns are caused by the constructive and destructive interferences of the diffracted incident electrons as they travel through a crystalline specimen. The lattice fringes provide information on the lattice spacing and angles between intersecting lattice planes of a crystalline sample.
Light Induced Charge Separation	Absorption of a photon by a ground state electron promoting the electron to a higher energy level of an atom/molecule, subsequently the excited electron leaves the atom/molecule traveling to a nearby electron acceptor.
Soft Lithography	A group of techniques that are used to fabricate and replicate structures on a receiving substrate, using elastomeric stamps, molds and masks.
Lyophilization	Removal of a frozen solution/solvent by sublimation under vacuum.
Microcontact Printing	A soft lithography technique that uses a patterned/non-patterned elastomeric stamp to transfer molecule/particle of interest onto a receiving substrate.
Moiré Fringe	A type of interference pattern that is observed under electron microscopy, which resulted from overlaying two crystal lattices at an offset angle, or when two crystals of different d-spacing that have parallel lattices to each other are superimposed.

Monochromatic Energy	A beam of energy of a narrow band of wavelengths.
Optoelectronic	An area of electronics that is concerned with electronic devices for modulating, transmitting, emitting, and sensing of visible electromagnetic radiation.
Ostwald Ripening	Dissolution of small crystals or sol particles, these dissolved crystals and particles are subsequently redeposited on the surfaces of a larger crystal or sol particles. The smaller particles have a higher surface energy than larger particles and, therefore, they also have a higher solubility.
Oxidation	A process that describes the loss of electrons or an increase in oxidation state of a molecule, atom, or ion.
Photoconductivity	A phenomenon that describes the increase in electrical conductivity of a material due to absorption of photons.
Photoelectric Effect	Electrons are emitted from an object (solid, liquids, or gases) when irradiated with photons of a sufficient energy.
Photovoltaics	A device that is capable of converting photons into electrical energy, using appropriate semiconductor materials.
Plasma	Charged gas molecules or atoms that are created through ionization of their corresponding neutrals under elevated temperature or electromagnetic radiation.
Polycrystalline	Solids that are composed of multiple crystals of varying size and crystal orientation.
Polymerization	A chemical reaction that links monomers together to produce a polymer chain or three dimensional polymer networks.
Reduction	A process that describes the gain of electrons or a decrease in oxidation state of a molecule, atom, or ion.
Relative Permittivity	A substance’s ability to store electrical charge with respect to vacuum of the same dimensions.
Rietveld Refinement	A technique capable of extracting structural information, phase composition, and texturing of a specimen by deconvoluting its corresponding diffraction data.
Scanning Electron Microscopy	A type of electron microscopy that can provide topographical and elemental composition information of a specimen by scanning the sample with a focused beam of electrons.
Secondary Ion Mass Spectrometry	A surface sensitive analysis technique that is capable of analyzing the composition of solid surfaces and thin films. The surface of interest is bombarded with a focused primary ion beam producing secondary elemental, isotopic, or molecular ions that are then analyzed by a mass spectrometer.
Semiconductor	A material that possesses both characteristics of a conductor and an insulator. Typically, the material has a less than 3 eV and

	greater than 0 eV separation between the filled valence band and the empty conduction band. Semiconductors will behave like a conductor when energy (e.g., electromagnetic radiation, heating) is imparted on it, promoting the valence band electrons into the conduction band.
Single Crystalline	A solid that only has one crystal lattice present and has no crystallographic defects such as grain boundaries.
Solvothermal Synthesis	A reaction that is performed at an elevated temperature and pressure inside an autoclave. The precursors dissolve in appropriate solvents before they decompose and otherwise react at the elevated pressures and temperatures.
Sonochemically-Induced Synthesis	The use of sonic waves to initiate a chemical reaction. Sonic waves are capable of rapidly increasing the local temperature and pressure within a reaction vessel through a phenomenon called acoustic cavitation.
Steric Stabilization	Colloids in a dispersion are passivated with polymers or surfactants to prevent them from getting too close to each other by steric repulsion, decreasing the possibilities of colloid flocculation.
Superparamagnetic Material	Superparamagnetism is found in ferrimagnetic or ferromagnetic nanoparticles that have a single magnetic domain. In the absence of a magnetic field and at room temperature, for example, the net magnetic moment of the system is zero, because these nanoparticles' magnetic moments are randomly aligned due to Brownian motion of the nanoparticles as well as changes in the magnetic moment of each nanoparticle at random.
Surface-Initiated Atom Transfer Radical Polymerization	Surface-initiated atom transfer radical polymerization is a type of controlled living polymerization that has been adopted to modify the chemistry and properties of surfaces. Surfaces of a material are modified to have the appropriate functional groups, which become radical initiators in the polymerization.
Surfactant Assisted Dispersion	See Electrostatic Stabilization and Steric Stabilization.
Texture	The tendency of crystallites in a polycrystalline specimen to orient in a certain direction.
Transmission Electron Microscopy	A transmission electron microscope (TEM) passes collimated electrons to through a thin specimen (<100 nm thick). Contrast of the image arises from a variation in density and thickness of the specimen. For example, thick and dense areas of the sample strongly scatter or absorb the incident electrons these areas appear as dark features, while thin or less electron dense regions of the specimen that are almost electron transparent appear as bright features in the image. The transmitted electrons are projected onto a phosphorescent screen, negative film, or CCD

	camera for viewing and recording. TEM is capable of resolving atomic lattices of crystalline materials due to the small de Broglie wavelength of electrons under an applied accelerating potential (e.g. 200 kV). In addition, the technique is capable of providing information on the chemical composition, chemical state, crystal orientation, and electronic structure of specimens.
Transmission Electron Microscopy – Bright Field Image	When a TEM image is formed from only the incident electron beam (000), while the diffracted electrons are excluded by an objective aperture.
Transmission Electron Microscopy – Dark Field Image	When a TEM image is formed from reflections other than the incident electron beam. The diffracted electrons are selected by an objective aperture.
Transmission Electron Microscopy – Electron Energy Loss Spectroscopy	Electron energy loss spectroscopy (EELS) is a complementary technique to energy dispersive X-ray spectroscopy and X-ray photoelectron spectroscopy. This technique is capable of providing information on both the elemental composition and chemical states of the specimen. It works by passing a monochromatic energy beam of electrons through a thin specimen in a TEM. The transmitted electrons are analyzed by an electron spectrometer, which measures the amount of energy lost by the electrons due to specimen-electron interactions (i.e. inelastic scattering). The amount of energy lost by the electrons can be correlated to the elements that exist in the specimen.
Scanning Transmission Electron Microscopy	Similar to a scanning electron microscope, the scanning transmission electron microscope (STEM) scans the specimen with a focused electron beam, but instead of detecting the backscattered electrons, transmitted (forwardly scattered) electrons are detected with an annular detector located below the specimen. Contrast of a STEM image comes not only from the sample thickness and electron density, but also is directly related to the atomic number of the elements present within the specimen.
Scherrer Equation	An equation used to approximate the size of crystallites in a sample from their X-ray diffraction pattern based on the full width at half maximum value of a diffraction peak.
Selected Area Electron Diffraction	See Electron Diffraction.
Valence Band	The range of allowable electronic states that are the highest energies a bound electron can occupy and still be associated with a particular atom within a solid.
X-ray Diffraction	An analytical technique used for the determination of crystal structures of single crystalline solid materials and crystalline liquid samples. In contrast, information such as crystal phases, texture, and d-spacing are obtainable from a polycrystalline sample. In a crystalline material, atoms are arranged in a

	repeating sequence in various planes of a crystal lattice. When a collimated beam of X-rays interacts with the specimen, the X-ray beams can be diffracted by the atoms of the sample. If the orientation of the crystal with respect to the incident X-ray beam satisfies the Bragg condition, the X-ray beams are scattered in-phase with respect to each other.
X-ray Photoelectron Spectroscopy	A surface sensitive analysis technique that is capable of providing information on a sample that includes quantitative composition, chemical state, and electronic state of the elements present within the first 1 to 10-nm of the specimen. Photoelectrons are generated from specimens by irradiating them with a high energy electromagnetic radiation (e.g. Al Kα = 1486.6 eV), in a phenomenon called the photoelectric effect (see Photoelectric Effect).
Z-Contrast Image	See Scanning Transmission Electron Microscopy.
Zeta Potential	Zeta potential is the potential difference between the dispersion medium and the electrical double layer that surrounds a charged particle. Zeta potential is used to assess the colloidal stability of colloidal dispersions. A high absolute value of zeta potential means that the dispersion is stable and the colloids within the suspension will resist flocculation.

1. Motivations to Study Selenium, Polymer Coated Selenium and Polymer Coated Metal Selenide Nanostructures

1.1. Semiconducting Materials

The world we live in is made of materials. They are essential to our lives and when used correctly they can improve our quality of life. Materials can be categorized into three groups based on their conductivity (S/m), a quantifiable property that represents the ability of the material to conduct electric current. These categories are: conductors, semiconductors, and insulators. At room temperature, metals have a conductivity between 10^2 and 10^9 S/m, while materials having conductivity less than 10^{-9} S/m are considered as insulators. Materials with conductivities in between 10^{-9} and 10^2 Sm are semiconductors. Another difference between metals, insulators, and semiconductors is how their conductivity change as a function of temperature (Figure 1.1 – blue).[1] The conductivity (σ; Eqn. 1.1) of metals decreases as the temperature increases,

$$\sigma = ne\mu \qquad \text{(Eqn. 1.1)}$$

where n is the number of charge-carriers, e is the corresponding charge of the carriers, and μ is their mobility.[1] Decreased conductivity at elevated temperatures is attributed to a decrease in electrons' mobility (μ) due to increased probability of electron-phonon collisions. In contrast, conductivity of insulators and intrinsic semiconductors increases with increasing temperature (Figure 1.1 – black and red). At elevated temperatures the valence band electrons are promoted into the conduction band, increasing the number of charge-carriers (n), thus increasing the conductivity, in both materials in comparison to the conductivity at room temperature. Population of charge-carriers (Eqn. 1.2), n, in a semiconductor/insulator at certain temperature can be estimate by

$$n = n_0 exp(-E/kT) \quad \text{(Eqn. 1.2)}$$

where n_0 is the total number of electrons, E is the activation energy, k is the Boltzmann's constant, and T is temperature. Although the mobility of the charge-carriers decreases with increasing temperature, a drastic increase in the charge-carrier population exhibits a greater impact on the overall conductivity of these materials. This phenomenon is exhibited up to the melting or degradation temperature of the intrinsic semiconductors and insulators.[1] Majority of the charge-carriers in extrinsic semiconductors came from dopants. Furthermore, the total population of charge-carriers is much greater than the thermally generate concentration of intrinsic semiconductors. The conductivity of extrinsic semiconductors as a function of temperature displays similar trend to that of metals (Figure 1.1 – orange; top – high dopant concentration and bottom – low dopant concentration), because the charge-carrier concentration of both materials are independent of temperature.[1] The conductivity of extrinsic semiconductors decreases as temperature increases, because the number of electron-phonon interaction increases at high temperature which leads to a decrease in charge-carrier mobility (μ ; Eqn. 1.1).

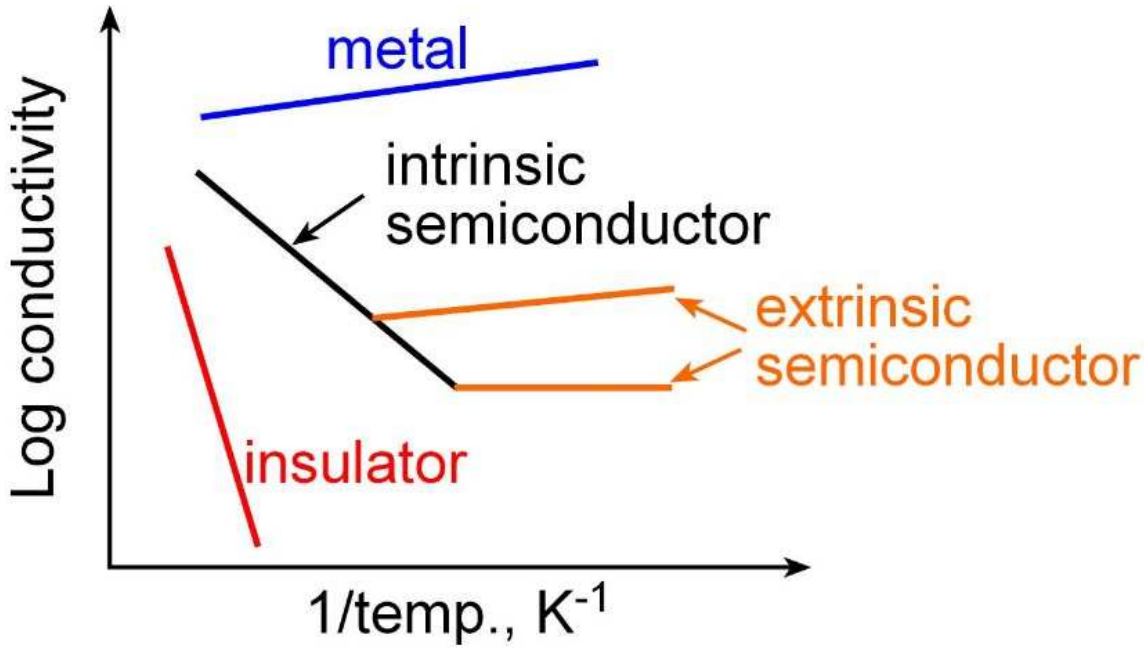

Figure 1.1 The conductivity of metals, semiconductors, and insulators as a function of the inverse of temperature. (Modified from Ref. 1.)

Semiconductors are further categorized into two classes: intrinsic and extrinsic semiconductors. Intrinsic semiconductors are pure materials, at room temperature they do not have large number of charge-carriers and hence their conductivities are much lower in comparison to the extrinsic semiconductors. Extrinsic semiconductors are produced by introducing impurities into intrinsic semiconductors (e.g., Ge, Si, Se, Te) to improve and control their properties, such as conductivity. The process used to incorporate impurities into the pure semiconductor materials is called *doping*. An *n*-type semiconductor is produced when an electron rich element, relative to the electronic structure of the intrinsic semiconductor, is incorporated into an intrinsic semiconductor. For example, *n*-type silicon substrates are doped with elements such as phosphorus or arsenic. These partially filled energy levels of the P or As do not mix with either the valence band (V.B.) or the conduction band (C.B.) of the silicon. These dopants occupy discrete level, known as donor level (D.L.), ~0.1 eV below the conduction band (Figure 1.2a). At room temperature, the electrons in the D.L. have sufficient energy to move into the conduction band of silicon, increasing both the charge-carrier concentrations (*n*) and thus the conductivity (σ, Eqn. 1.1). Doping an intrinsic semiconductor with an element that is electron deficient in comparison to the pure material will result in the formation of a *p*-type semiconductor (i.e., silicon doped with boron; Figure 1.2b). Electron deficient dopants contribute to discrete levels that reside ~0.1 eV above the valence band of the silicon. These discrete levels, also known as the acceptor levels (A.L.), are capable of accepting electrons of sufficient thermal energy from the valence band. Electrons promoted to the A.L. leads to the formation positive charge-carriers (i.e., holes) within the valence band. This increase in the positive charge-carrier population (*n*) results in the increased conductivity of the material (Eqn. 1.1). Extrinsic semiconductors are used as key components in many electronic devices such as field-effect transistors, photovoltaic devices, and light-emitting diodes.[2]

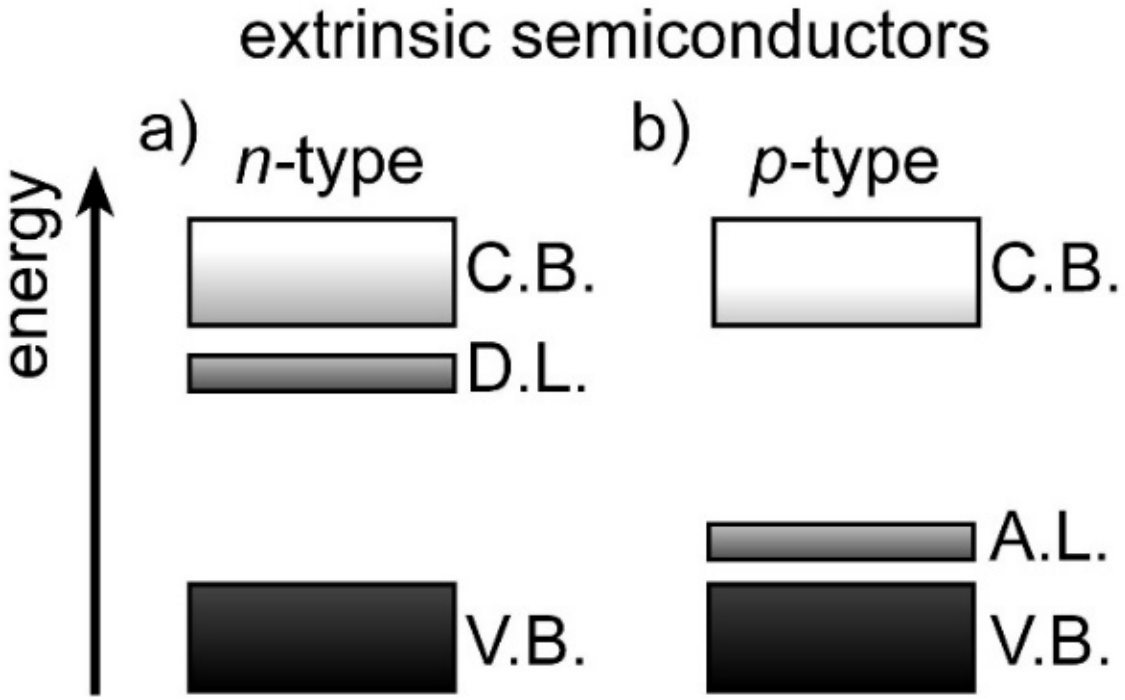

Figure 1.2 Electronic band structures of (a) n-type (e.g., silicon doped with phosphorus) contain partially filled donor levels (D.L.) that come from the electron rich and (b) p-type (e.g., boron doped silicon) semiconductors. C.B., V.B., D.L., and A.L. are conduction band, valence band, donor level, and acceptor level, respectively.

1.1.1. Applications of Semiconducting Materials

In the 20th and 21st centuries, the word semiconductor has become synonymous with advanced electronics,[3-4] optoelectronics,[3, 5] and alternative energy harvesting technologies.[6-8] Most of these devices use p-n junctions as the elementary building blocks. The interface between *p*-type and *n*-type semiconductors inside a single crystal semiconductor or an epitaxially grown crystal forms a p-n junction. Charge carriers (i.e., electrons and holes) are depleted at the interface of p-n junction due to diffusion of both electrons and holes in the opposite directions in an attempt to re-establish an equilibrium for electron concentrations in the *p*- and *n*-type semiconductors, creating a permanent electric field within the crystal. This area within the p-n junction is called the *depletion region*. This phenomenon rendered all constructs of p-n junctions non-conductive in the absence of an applied electric field. In addition, current can only flow from *n*- to *p*-type semiconductors, but not in reverse. Since its discovery, p-n junctions have been used widely in semiconductor electronic devices.

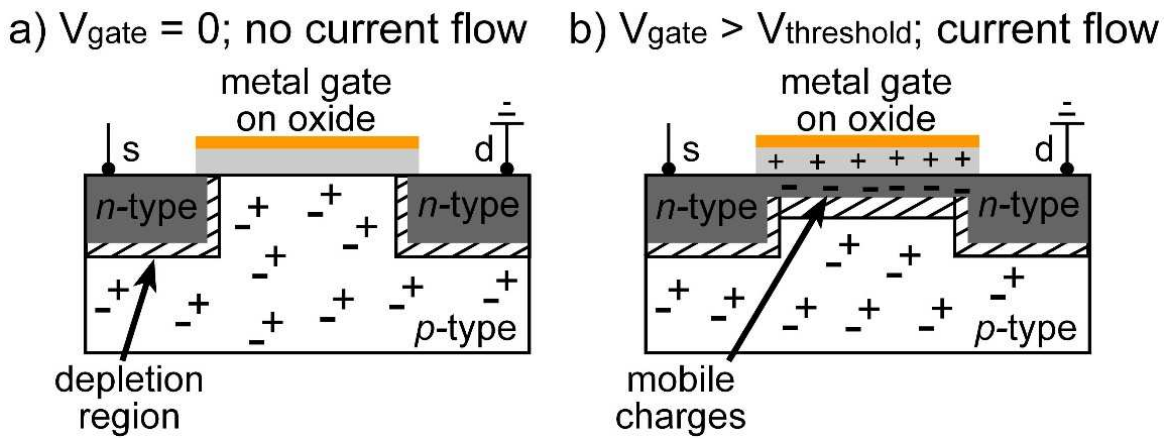

Figure 1.3 A cross-sectional view of a metal-oxide-semiconductor field effect transistor (MOSFET) in the (a) off and (b) on states.

Semiconducting materials, most notably doped silicon, have been used as key components in integrated circuits found in microprocessors that control the electronic appliances we use everyday.[9] For example, metal-oxide-semiconductor field effect transistors (MOSFET) perform as on-off switches in electronic devices to regulate the flow of electrons and signal transductions via an applied gate voltage.[2, 10-11] In the presence of an applied potential between the source (s) and drain (d) electrodes, but in the absence of an applied potential on the gate electrode (V_{gate}), electrons cannot flow from the transistor's source to drain electrode (Figure 1.3a).[10] When a voltage greater than the threshold voltage of the material is applied to the gate electrode, the oxide layer becomes positively charged. At the same time, positive charge carriers in the *p*-type semiconductor at and near the metal-oxide-semiconductor interface are repelled, leaving behind a conducting channel between the transistor's source and drain. This conducting channel permits the transport of electrons between the source and drain terminals if there is a potential difference between them (Figure 1.3b).[10]

Semiconductors also have been used as emitter materials in lasers[5] and light-emitting diodes (LEDs).[12-13] Light-emitting diodes are widely used in display, illumination, and communication technologies. They are attractive because of their high energy efficiency, robustness, small size, long lifetime, and fast switching properties. In addition, the wavelength of the emitted electromagnetic radiation can be varied by using semiconductors of desired band-gaps.[14] In the presence of an applied potential, the electrons in the *n*-type semiconductor and the holes in the *p*-type semiconductor would

recombine at the p-n junction by radiative transitions, producing photons whose energy correspond to the band-gap of the material (Figure 1.4).

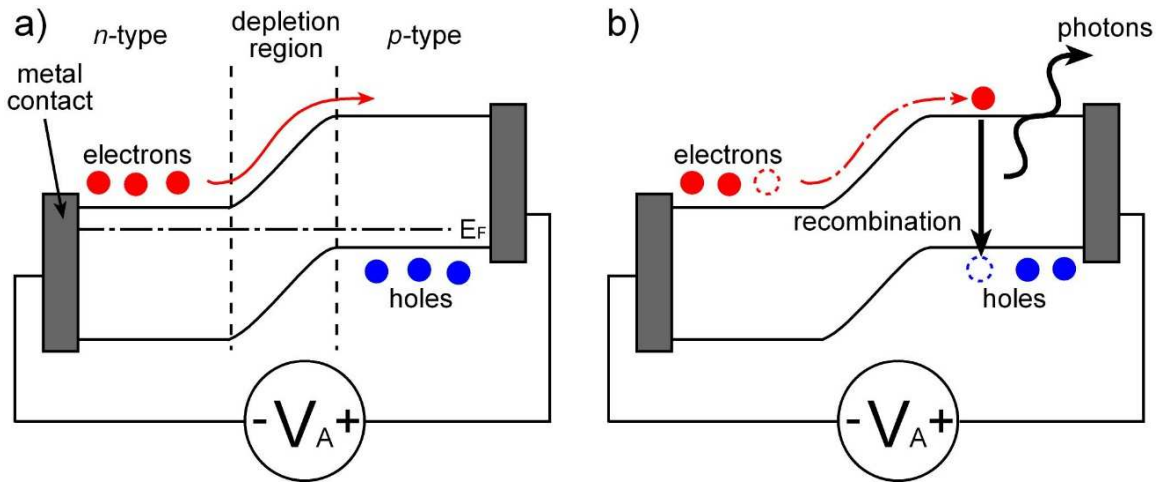

Figure 1.4 (a) Migration of charges carriers toward the p-n junction under applied potential (forward bias) in a light-emitting diode (LED). (b) Recombination of opposite charged carriers leads to the emission of photons.

Some of the semiconductor materials that have been used to generate emitted radiations of a specific wavelength under applied potential can also be used to convert electromagnetic radiation into electrical energy.[15] These devices are known as p-n junction photovoltaic cells. The p-n junction photovoltaic cell consists of a thin layer of *n*-type semiconductor on top of a thicker layer of *p*-type semiconductor (Figure 1.5a).[15] There are metal contacts on both types of semiconductors, connecting them through an external circuit. An electrical current is produced when the device is exposed to electromagnetic radiation that has an energy greater than the band-gap of the semiconductor material. Photons are absorbed by the *p*-type semiconductor, creating electron-hole pairs through the photoelectric effect. The resulting photoelectrons are driven in the direction of the *n*-type semiconductor by the permanent electric field within the p-n junction. These photoelectrons are subsequently collected by the metal contacts, transporting them through an external circuit and generating electrical energy (Figure 1.5b). The hole carriers recombine with the photoelectrons at the electrical contacts located on the *p*-type semiconductor.[15]

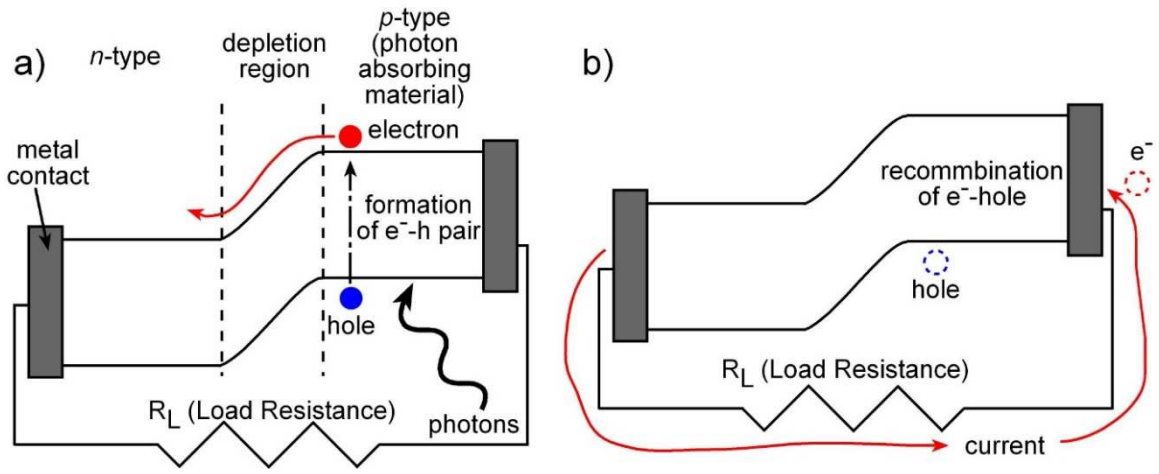

Figure 1.5 (a) Electron-hole pairs (e^--h pair) are generated after absorption of photons of appropriate energies in a p-n junction based photovoltaic device. (b) These electrons traveling through an external electrical can be used to perform work or stored.

Charge separation generated within p-n junctions by the photoelectric effect is also used for the detection of electromagnetic radiation. Such a device is be able to detect photons with energies overlapping with the band-gap of the semiconductor, as well as the intensity of the incident electromagnetic radiation based on the number of charge carriers generated. In addition, digital images and videos can be captured from a 2-dimensional array of these semiconductor based detectors, such as charge-coupled devices (CCD), and complementary metal-oxide-semiconductor (CMOS) sensors.[10, 16]

Semiconductor based integrated circuits and semiconductor based architectures are fabricated through lithographic techniques that are expensive to implement and are limited in the choice of materials, structures, and dimensions. In addition, the relentless miniaturization of the integrated circuits, a natural progression of the semiconductor industry, is driven by demands of faster clock rates, and lower power consumption of electronic devices.[17] The task of shrinking the size of integrated circuits below 100-nm while maintaining the device's architecture through the use of conventional scaling methods (e.g., top-down lithography) have become increasingly challenging. A principle architecture within these nanoscale devices are the one-dimensional semiconductor nanostructures that serve as interconnects. Semiconductor nanowires with diameters between 1 and 100-nm and lengths up to several kilometers, on the other hand, can be prepared through solution-phase,[18] vapour-liquid-solid (VLS),[19] thermal

evaporation/vapour deposition,[17] and thermal-drawing[20] processes with controlled dimensions and uniformity. These processes can also produce nanowires with a distinct chemical composition that is otherwise difficult or impossible to obtain through top-down lithography techniques. For example, memory architectures based on phase changing nanomaterials is only accessible through synthetic techniques because lithographic techniques tend to damage these materials.[19] These synthetic techniques have been used to produce building blocks for semiconductor nanowire devices. These building blocks could subsequently be manipulated either through self-assembly or directed assembly processes.[17, 21-22] Nanowires synthesized by solution-phase processes are less complex and are inexpensive to use in comparison to other synthetic and lithography techniques. While not applicable to all materials some semiconductor nanowires, such as selenium nanowires, could be produced in large-scale using simple solution-phase synthesis techniques.

1.2. Why Are We Interested in Selenium Nanowires?

Selenium is found in copper and lead rich soles, in the mineral forms of *crookesite* ($Cu_7(Tl,Ag)Se_4$) and *clausthalite* ($Pb_{0.72}Se_{0.28}$).[23] Majority of the selenium in the world is produced from copper and lead refineries as a by-product. Selenium exists in several allotropic forms. These allotropes of selenium share the same elemental composition and differ only in their atomic arrangement of the selenium atoms. All selenium allotropes are crystalline, except one. These allotropes of selenium are rhombohedral (Se_6), trigonal (*t*-Se), *α*-, *β*-, and *γ*-monoclinic (*α,β,γ*-Se_8) in crystal forms.[24-25] Amorphous selenium (*a*-Se) is the only non-crystalline form of selenium and is composed of a mixture of randomly arranged fragments of Se_6, *t*-Se, and *α,β,γ*-Se_8.[25]

Trigonal selenium is the most thermodynamically stable allotrope. It is composed of covalently bonded selenium atoms arranged in a helical fashion along the length of the *c*-axis (Figure 1.6a). These selenium atoms within a single helical chain have bond distance of 2.373(5) Å[26] and bond angle of 104°.[27] Joannopoulos, *et al.* reported a tight-binding model, suggesting that the intrachain selenium-selenium bond arose from the interaction of a mixture of *s*, *p*, and *d* orbitals. The Se-Se bonds are predominately composed of *p* orbital contributions, although they also consist of ~5-10% and ~1-5% of

s and *d* orbital characteristics, respectively.[27] The lower energy of these *p* characteristic hybrid orbitals is exclusively involved in relatively weak intrachain bonding. While the higher energy *p*-like bonding states contribute to interchain bonding. The interchain bond distance of selenium atoms on the adjacent chains is ~3.436 Å.[26] In a trigonal selenium single crystal, these helical chains of selenium atoms are held together by these weaker interchain covalent bonds in a hexagonal lattice that spans in all directions.[27] Selenium intrachain grow preferentially along the *c*-axis or from the {001} facets (Figure 1.6b) because it is more thermodynamically favorable to form covalent bonds between selenium atoms within individual chains than to form only selenium interchain interactions via extended covalent forces. The unique arrangement of atoms within selenium nanowires also influence their physical properties, such as thermoconductivity, piezoelectric response, photoconductivity, and photovoltaic response.[28]

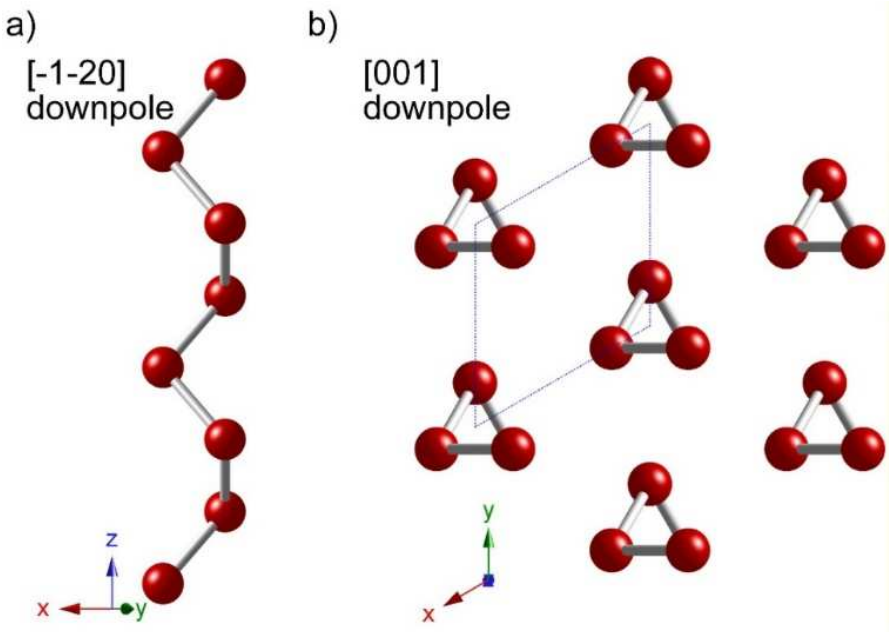

Figure 1.6 (a) Selenium atoms arranged in a helix, viewed from [-1-20] direction, propagating along the c-axis/<001> directions. (b) Several of these helices, viewed from [001] direction, are packed hexagonally in a trigonal selenium (t-Se) single crystal. The extended covalent bonds between the helical chains of selenium are omitted for simplicity. The unit cell of t-Se is highlighted by the diamond. Crystal structures were drawn using CrystalMaker©.

Pure selenium is an intrinsic *p*-type semiconductor with a band-gap of ~1.8 eV. As a one-dimensional (1D) nanostructure its band-gap is tunable due to quantum

confinement when its diameter is appropriately narrow.[2] These quantized effects are only observed in nanostructured materials, and not in bulk selenium.[28] Selenium nanowires can be produced in large quantities using relatively simple synthetic methods. These techniques include hydrothermal,[29] solvothermal,[30] sonochemical,[31] and thermal drawing processes.[32] Another versatility of selenium nanowires is the ability of selenium to act as a template to form chalcogenide nanowires (e.g., lead, tin, zinc, silver, cadmium, lead, copper selenides).[33] Chalcogenide nanowires, such as silver selenide, have a comparable quantum hall mobility and field effect mobility to silicon selenide.[34] For example, quantum hall mobility of silver selenide (2000 $cm^2V^{-1}s^{-1}$)[35] is greater than that of polycrystalline silicon (1560 $cm^2V^{-1}s^{-1}$).[36] Single crystalline chalcogenide nanowires are hard to directly synthesize because they have a tendency to form zero dimensional structures (i.e., nanoparticles).[18, 37] In some cases, the synthesis of anisotropic structures requires a combination of catalysts and exotic seed crystals for which it can be challenging to select the right combinations of materials.

Our ability to synthesize selenium nanowires with controlled dimensions requires in-depth knowledge of selenium's surface chemistry. Selenium nanowires synthesized by sonochemically-induced transformation of amorphous selenium colloid is simple and the procedure can be scaled-up for mass production. There are, however, no detailed reports examining the parameters that influence the dimensions of the selenium nanowires synthesized in the absence of surfactants. Since the selenium nanowires are produced in the absence of surfactants, an improved understanding of selenium's surfaces is also required to uniformly disperse the nanowires for ease of processing and handling. Another challenge that remains is a selection of appropriate techniques to assemble and otherwise process these nanowires, which have lacked in the development despite the many benefits of selenium and chalcogenide nanowires. This deficiency must be addressed prior to incorporating these nanowires as functional and reliable components into electronic and optoelectronic devices. As the scale of these material decreases, the surface-area-to-volume ratio increases. It is, therefore, important to improve our understanding of selenium's surface chemistry and to prevent chemical degradation of the material that could lead to a significant loss of properties or functions during and after processing of these nanostructures.

1.3. Key Challenges of Working with Selenium Nanowires

There are several key challenges that impede the adoption of solution-phase synthesized selenium nanowires in electronic devices. One of the challenges is the lack of monodispersity in the length as well as the diameter of the selenium nanowires produced by the sonochemically-induced synthesis. In addition, selenium nanowires are synthesized in the absence of surfactant, making the nanowires difficult to disperse and to keep suspended in solution for long periods of time. It is essential to develop techniques to improve the dispersion and colloidal stability of selenium nanowires, in order to make handling and processing of the material less challenging. An improved dispersion would also facilitate the uniform transformation of selenium nanowires into other metal selenides, metal decorated, or polymer coated selenium nanowires. Another challenge is the lack of techniques to assemble selenium nanowires either en mass or individually. The ability to manipulate and control the density and orientation of assembled nanowires is key to the wide use of selenium- and metal selenide-based nanowire interconnects in electronic devices. These selenium and metal selenide nanowire based architectures can be used only if they are stable against corrosion. Corrosion is a form of degradation that causes the loss of material. The loss of material from a nanomaterial due to corrosion would be detrimental to their properties and function.[38] It is, therefore, essential to develop techniques to protect selenium based anisotropic nanostructures from corrosion.

These key challenges are distilled down into four questions: 1) how can we synthesize selenium nanowires with controlled diameter and length?; 2) how can we alter the surfaces of the selenium nanowires to facilitate colloidal stability and dispersion of the nanowires for easier processing and to facilitate a more uniform chemical reaction on these templates?; 3) how do we manipulate selenium nanowires en mass as well as individually?; and 4) how do we prevent the chemical degradation of selenium? These challenges are tied together by the selenium nanowires' surface chemistry, which contribute to difficulties in growing high-aspect-ratio nanowires, creating stable dispersions, manipulating the nanowires en mass or individually, and minimizing their chemical degradation. Addressing these challenges requires an increased understanding of the surface chemistry of selenium nanowires.

This thesis addresses these key challenges by first gaining knowledge about the surfaces of selenium nanowires. For example, the favorable interaction between solubilized selenium atoms with specific crystal facet(s) of the trigonal selenium crystal is examined by introducing a competitive inhibitor to the reaction mixture during nanowire growth. Successful competitive inhibition would not only provide information on the nature of surfaces with respect to the crystal facets of the selenium nanowires, but also provide insight on the mechanism of growth. This information could be used to fine-tune the synthetic procedures to prepare selenium nanowires and to potentially enable control of the nanowire's dimensions, such as diameter and length. In addition, the surface chemistry of the selenium nanowires is investigated by surface sensitive techniques, such as water contact angle measurements, X-ray photoelectron spectroscopy and secondary ion mass spectrometry. The knowledge from these studies is used to improve the colloidal stability of the selenium nanowires in different media in order to facilitate the handling and manipulation of these anisotropic nanostructures. Colloidally stable dispersions of selenium nanowires is sought either by dispersing the nanowires in an appropriate medium, or adding surfactants/polymers to solution.

A second focus of this thesis is to develop techniques to direct the assembly of selenium nanowires and facilitate their incorporation into devices. Our goal is to develop methods of assembly that are capable of manipulating nanowires en mass over long distances, as well as assembling individual nanowires with micrometer precision. Chemical degradation of selenium nanowires would have to be avoided when these nanostructures are used as key components in electronic devices. Corrosion of selenium will occur when exposed to oxidative environments and moisture. A method to minimize corrosion of selenium nanowires could be to coat their surfaces with a moisture barrier, which will resist nanowire corrosion in an oxidizing environment. We aim to develop the first example of polymer encapsulation of selenium nanowires. Lastly, the thesis demonstrates the feasibility to synthesize polymer encapsulated metal selenide core-shell nanowires from a one-pot synthesis using selenium nanowire templates with techniques developed in the prior thesis chapters.

1.4. Objectives of the Thesis

In the 21st century, semiconductor based electronic devices have become an integral part of our daily lives. Most of these devices are fabricated by lithography techniques that are expensive to implement and are limited in the choice of materials, their structure, and their size. In addition, it has become more challenging to shrink the size of integrated circuits below 100-nm while maintaining the device's basic structures using conventional scaling methods. One-dimensional nanostructures produced by solution-phase syntheses are an alternative means of creating sub 100-nm semiconductor features to be used as building blocks in electronic and optoelectronic devices. There are several challenges that will have to be overcome before solution-phase synthesized nanowires can be adopted as building blocks for these devices. Most of these challenges can be resolved through an improved understanding of a material's surface chemistry. Herein, the following chapters provide different in-sights into selenium nanowires' surfaces and their chemical states that will allow: 1) control over the dimension of the synthesized nanowires; 2) an ability to create uniform dispersions; 3) a means to assemble the nanowires en mass over long distances; and 4) methods to increase the corrosion resistance of selenium nanowires. Lastly, we demonstrated that selenium nanowires can be used as templates to synthesize copper selenide nanowires coated with a polymer using knowledge gained about selenium nanowires' surface chemistry and techniques developed in previous chapters.

Challenges highlighted at the beginning of this chapter, such as 1) how to synthesize selenium nanowires with controlled diameter and length?; 2) how to improve the colloidal stability and dispersion of the nanowires for easier processing and to facilitate a more uniform chemical reaction on these templates?; 3) how to manipulate selenium nanowires en mass as well as individually?; and 4) how to prevent the chemical degradation of selenium?, will be addressed in the following chapters. We will start with a study to optimize the sonochemically-induced synthesis of high-aspect-ratio selenium nanowires. The colloidal stability of selenium nanowire dispersions was subsequently evaluated by time-resolved photograph and spectroscopy techniques, and different methods were investigated to improve the colloidal stability of these dispersions. The knowledge from these studies was used to assemble selenium

nanowires into centimeter long fibers in the presence of an applied electric field. The surface chemistry of the selenium nanowires was also analyzed by an array of surface sensitive techniques. Using this knowledge, a novel technique was demonstrated to alter the surface chemistry of selenium nanowires and to improve their resistance toward corrosion.

2. Synthesis of High-Aspect-Ratio Selenium Nanowires

2.1. Introduction to Different Synthetic Approaches to form Selenium Nanowires

A nanowire is a one-dimensional (1D) nanostructure that has a diameter below 100-nm and an unconstrained length. A nanowire with a high-aspect-ratio, or a large length-to-diameter ratio, is a flexible material. These materials are capable of achieving a high degree of curvature without fragmenting into separate pieces, whereas lower aspect-ratio 1D nanostructures are more rigid. These shorter materials are referred to as nanorods. Nanorods under the same degree of material deformation will lead to structural failure (i.e. fracturing, or fragmentation).

Trigonal selenium (*t*-Se) nanowires can be grown in solution by techniques include hydrothermal,[29, 39] solvothermal,[28, 30] sonochemical methods,[31, 40-41] and template-assisted methods.[42-43] Each of these techniques can produce single crystalline selenium nanowires. There are, however, other differences either in the final dimensions of the nanowire or the time required for each synthesis. Hydrothermally synthesized selenium nanostructures are typically greater than 500 nm in diameter, which is much larger than our target of 30 nm and narrower.[29] Solvothermal synthesis can produce selenium nanowires with diameters from 10 to 30 nm.[28, 30] The solvothermal procedure is, however, not suitable for our research because it requires 10 to 20 days to transform amorphous selenium (*a*-Se) into *t*-Se nanowires. On the other hand, sonochemical techniques produce selenium nanowires with diameters between 30 to 90 nm in less than 24 h.[31] Therefore, this synthetic approach is selected as our preferred method of synthesizing selenium nanowires.

The detailed mechanism at which *a*-Se colloids transform into 1D selenium nanostructures is still poorly understood. The transformation from *a*-Se to *t*-Se

nanowires could have proceeded either by Ostwald ripening[1, 4, 18-19] or oriented attachment processes.[44-46] Ostwald ripening process involves transport of mobile species from the smaller particles, which have higher surface free energy (i.e., higher solubility in comparison to particles of a larger size), to the larger particles in order to reduce the overall surface free energy of the system. As a result, the larger particles grow at the expense of smaller particles (Figure 2.1a). In contrast, growth by oriented attachment involves the spontaneous self-organization of crystalline nanoparticles. These nanoparticles self-arrange into a particular orientation such that each nanocrystal shares a similar crystallographic orientation with the adjacent nanoparticle. These nanoparticles would then coalesce at the particle-to-particle interface, forming anisotropic structures (Figure 2.1b). In an oriented attachment growth mechanism, large quantities of *t*-Se nanocrystals should be observable by electron microscopy during early stages of nanowire formation. In addition, selenium nanowires form by oriented attachment of *t*-Se nanocrystals of different sizes should produce anisotropic nanostructures of varying diameter along the growth axis. In this chapter, the mechanism of selenium nanowire growth is examined using time dependent electron microscopy analysis.

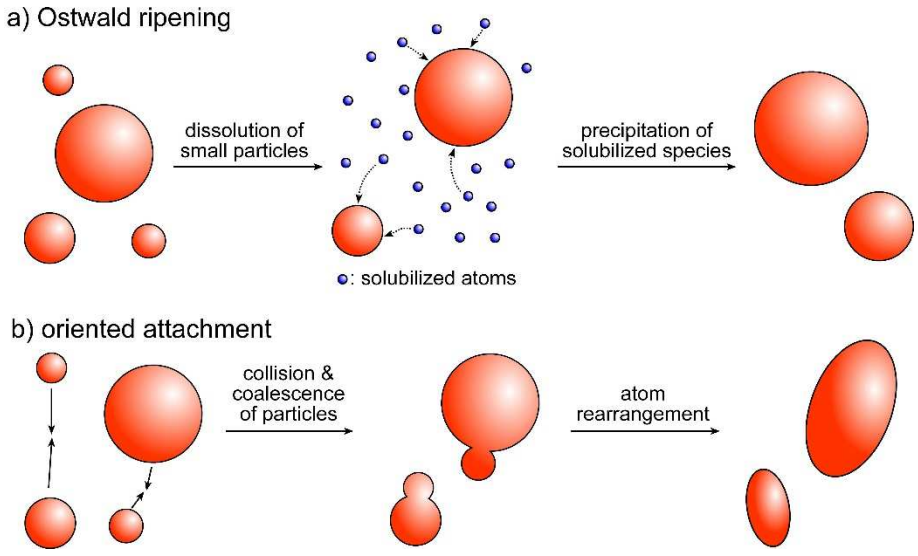

Figure 2.1 Schematic representation of crystal growth by a) Ostwald ripening and b) oriented attachment processes.

Another key factor to develop a high yield synthesis of selenium nanowires is the interaction of organic material with the surfaces of the *t*-Se seed. For example, the work

of Ko, *et al.* demonstrated the correlation between surface energy of the substrate on which selenium nanowires were grown and the resulting morphology of these nanostructures.[35] They determined that selenium nanostructures grown in the presence of hydrophilic substrates (e.g., cleaned, oxidized silicon wafers) produced nanowires. In contrast, those nanostructures grown in the presence of hydrophobic substrates (e.g., octadecyltrichlorosilane modified silicon surfaces) resulted in porcupine-like arrays of selenium nanorods. We have determined that this correlation of morphology and surface chemistry extends to the choice of reaction vessel used for the growth of selenium nanowires. We synthesized all of our selenium nanowires in cleaned hydrophilic glass vials. In addition, an article published by Mayers, *et al*. determined three ideal solvents (i.e., methanol, ethanol, and isopropanol) for synthesizing single crystalline *t*-Se nanowires by the sonochemical method.[40] Some organic solvents were found to impede the growth of the *c*-termini/{001} facets (Figure 2.2) of the selenium nanowires, yielding tapered nanowires or nanorods. We refined the synthesis of Mayers, *et al*. through an iterative process of synthesis and characterization using scanning electron microscopy (SEM) and transmission electron microscopy (TEM). The result suggests that 95% ethanol is the best solvent for consistently synthesizing long selenium nanowires with a narrow diameter with uniform consistency.[47] Other variables, such as growth temperature and concentration of the *a*-Se are examined in this chapter to determine the optimal conditions for synthesizing high-aspect-ratio selenium nanowires.

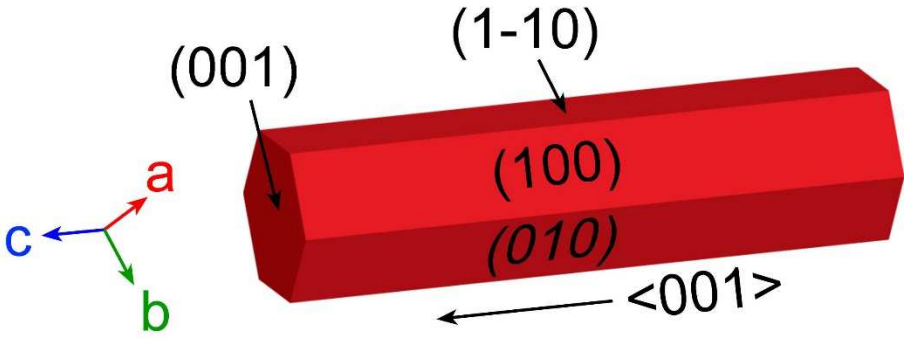

Figure 2.2 A 3-dimensional model of a trigonal selenium nanowire that elongates along the <001> directions. Each facet is label with the corresponding Miller index.

The dimensions of the synthesized selenium nanowires are influenced by their rate of growth and the solubility of *a*-Se in the growth solvent. For example, although the

solvothermal based synthesis of selenium nanowires takes longer than the sonochemical route, the former method consistently produces nanowires with diameters narrower or equal to 30 nm. Selenium nanowires are produced ~70 times and ~35 times faster via the sonochemical method in ethanol (EtOH) and isopropanol (*i*PA), respectively. Faster conversion of *a*-Se particles to selenium nanowires is accompanied with an increased diameter of the resulting nanowires (up to 90 nm). Increased rate of growth is likely a result of an increased dissolution of selenium in alcohols. The larger diameter of these nanowires is most likely the result of an increased availability of dissolved selenium in solution during nanowire growth. When dissolved selenium exists in high concentration, they can attach non-preferentially to lower energy {100} and {110} facets[43] of the selenium nanowires (Figure 2.2), thus, increasing the diameter of the nanowires (Figure 2.3 – concentration range **III**). We believe that high-aspect-ratio selenium nanowires can be synthesized by controlling the amount of dissolved selenium in solution. At low concentrations of dissolved selenium, the surface area of available {001} facets on the selenium nanowires is greater than the local concentration of solubilized selenium atoms. The majority of the solubilized selenium would, therefore, attach preferentially to the highest energy {001} facets of the selenium nanowire (Figure 2.3 – concentration range **II**). We hypothesized that there might be a concentration range where the axial rate of growth (i.e., lengthening) of selenium nanowires would be significantly greater than the radial rate of growth (i.e., increase in nanowire diameter by addition of selenium atoms to both {100} and {110} facets). The *a*-Se colloids would not transform into selenium nanowires, when selenium is not soluble in the growth medium (Figure 2.3 – concentration range **I**). We hypothesized that the rate of nanowire growth depends on both temperature of the reaction and concentration of dissolved selenium. The concentration of dissolved selenium could be controlled by adjusting the temperature, selecting a solvent of different solubility for *a*-Se, or addition of a “poor” solvent for selenium into the growth medium. Therefore, we focused our studies on fine tuning these conditions to assist in synthesizing high-aspect-ratio selenium nanowires with narrow diameters. Selenium nanowires, for example, were grown at different temperatures with the same *a*-Se/*i*PA (*w/v*) ratio, at different *a*-Se/EtOH (*w/v*) ratios at a constant temperature, and with a different amount of water (a non-solvent for selenium) added to the absolute EtOH growth medium. The resulting selenium nanostructures were analyzed by optical, scanning electron, and transmission electron microscopies.

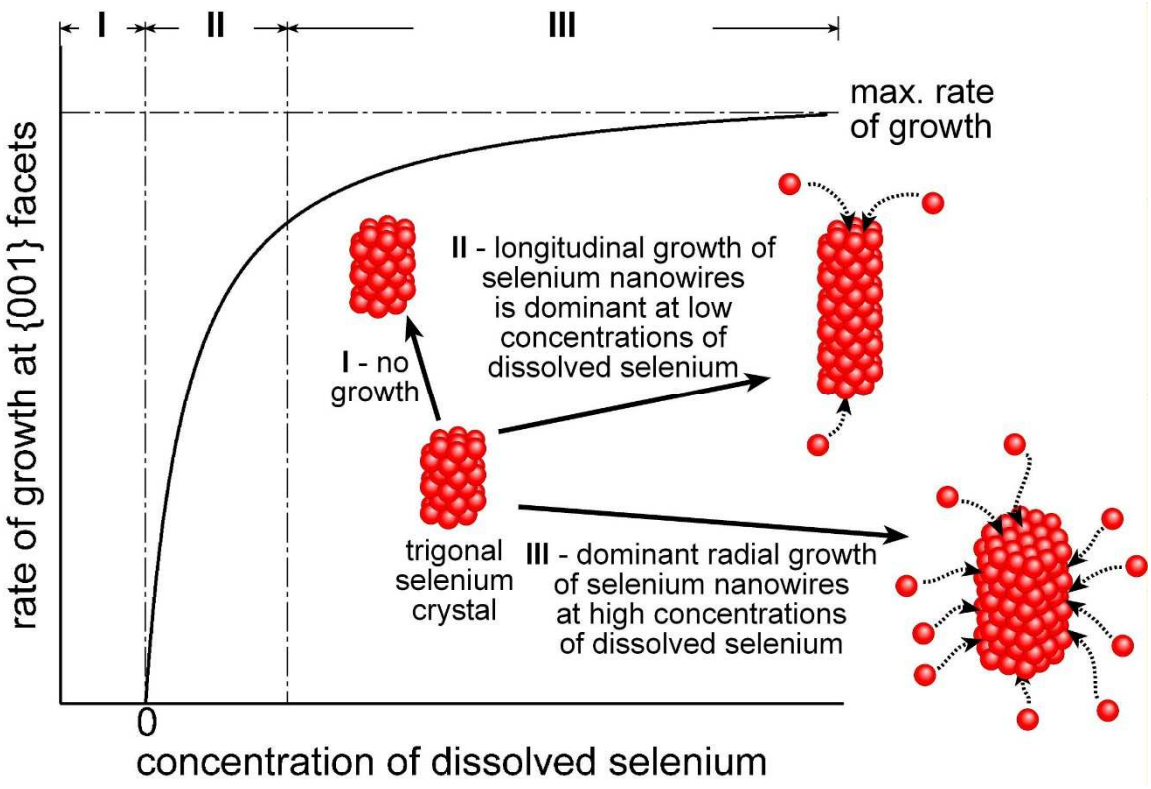

Figure 2.3 A hypothetical plot showing the dependence of axial rate of growth of trigonal selenium nanowires (i.e., addition of selenium atoms to the {001} facets of the hexagonal close-packed structure of trigonal selenium) on the concentration of dissolved selenium (red spheres).

One of the ways to verify that solubilized selenium atoms, at low concentrations, bind preferentially to the {001} facets of the *t*-Se nanowires could be through selectively inhibiting the high energy facets to prevent lengthening of the nanowires. The {001} facets of the selenium nanowires could be selectively passivated during nanowire formation by introducing an organic molecule, which would bind competitively to the high surface energy facets (i.e., {001} facets). If the solubilized selenium atoms could not bind to the high energy facets due to competitive inhibition, they would bind to facets of lower surface energies instead. The result is an increase to the diameter of the anisotropic nanostructure (i.e., producing rod-like nanostructures). Molecules such as alkanethiols (R-SH) have demonstrated selective binding to high energy facets on 1D noble metal nanocrystals.[48] To validate that selenium atoms would bind to {100} or {110} facets of the *t*-Se in the presence of an inhibitor, a solution containing 11-hydroxylundecane-1-thiol (HUT) was introduced to dispersions of *a*-Se in EtOH after selenium nanowire growth was initiated for a specified time (Figure 2.4). The diameter and length of the

synthesized 1D selenium nanostructures were analyzed by scanning electron, and transmission electron microscopies. Herein, we demonstrate the ability to control the length as well as the diameter of the selenium nanowires by further control of the growth conditions, such as solution temperature, concentration of *a*-Se colloid, and choice of solvent.

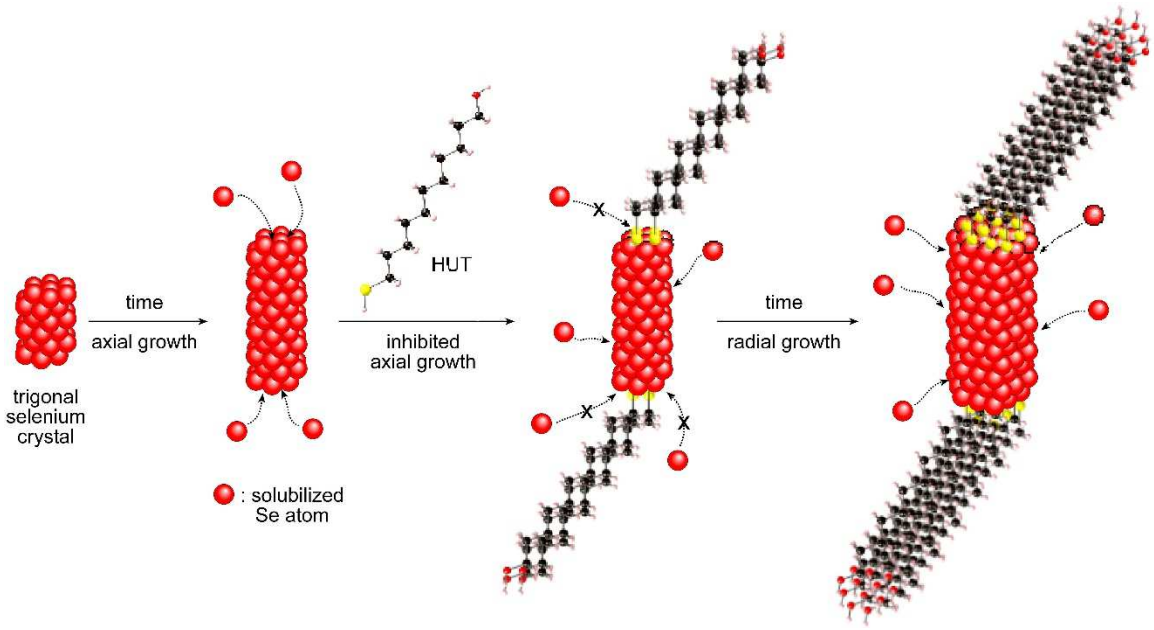

Figure 2.4 A schematic showing the axial growth of selenium nanowires at low concentrations of solubilized selenium. Elongation of selenium nanowires is suppressed by introducing an inhibitor molecule, such as 11-hydroxylundecane-1-thiol (HUT) to the reaction vessel. The selenium nanostructure would grow radially under competitive inhibition from HUT.

Preventing the *a*-Se colloids from coalescing into large clusters is another key parameter to optimize in order to achieve a high yield of high-aspect-ratio selenium nanowires per synthesis. Unlike other recrystallizations of organic and inorganic crystals that require total dissolution of the material in a solvent at elevated temperatures, sonochemically initiated transformation of *a*-Se to *t*-Se does not require complete dissolution of *a*-Se. The growth of selenium nanowires proceeds through an Ostwald ripening process that is driven by the dissolution of small amorphous colloids (Figure 2.5a). Although cavitation created during sonication is used to break up the *a*-Se colloidal flocculates, it also causes coalescence of *a*-Se colloids due to localized heating to temperatures beyond its glass transition temperature (T_g).[49] The resulting larger

particles are less soluble than smaller *a*-Se colloids, because the later has a higher Gibbs free energy than the former.[50] The formation of a high quantity of large, coalesced particles can prevent the complete consumption of the precursor, and is detrimental to the nanowire formation process. Sufficiently large particles of *a*-Se are not able to dissolve at the necessary rate to sustain the growth of selenium nanowires before they settle to the bottom of the vial. Once the *a*-Se colloids have settled to the bottom of the vial they form into a densely packed layer of selenium, resulting in a further decrease in the solubility of the material (Figure 2.5b). In addition, a high water content in the growth medium would lead to agglomeration of *a*-Se colloids because selenium is hydrophobic (see Chapter 3). These agglomerates are difficult to disperse by the brief sonication and can lead to an incomplete consumption of the precursor. The size of the fused particle can be controlled by adjusting the concentration of *a*-Se colloids in the growth solvent, as well as using a solvent containing very little water.

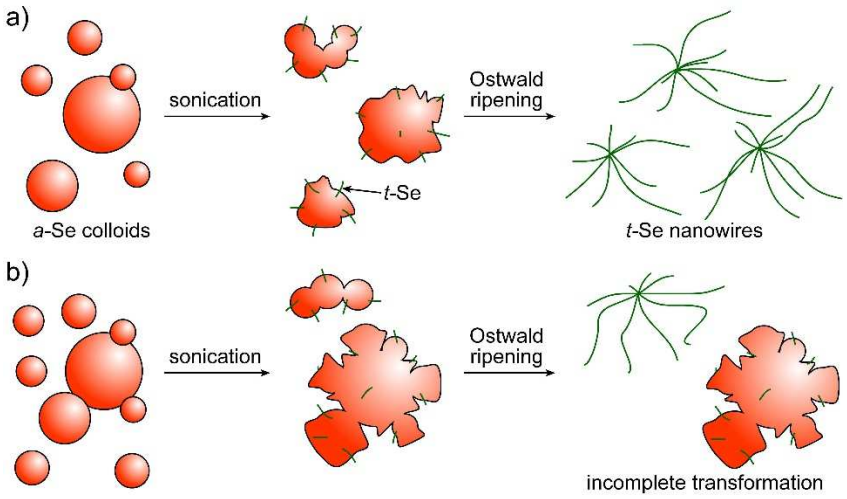

Figure 2.5 Schematic showing the (a) complete transformation of a-Se colloids into t-Se nanowires, and (b) incomplete transformation due to the formation large a-Se aggregates.

Optimizing the conditions to produce high-aspect-ratio selenium nanowires is essential to increase the success rate of positioning metal contacts the ends of selenium nanowires. Long nanowires are much easier work with in comparison to short nanowires using photolithographic techniques developed in our laboratory.[51]

2.2. Experimental Section

2.2.1. Synthesis of Amorphous Selenium Colloids – A Precursor to Selenium Nanowires

To synthesize amorphous selenium, 2.73 g (21.1 mmol) of selenious acid (H_2SeO_3, 98%; Sigma-Aldrich) was dissolved in 100 mL of 18.0 MΩ·cm water (purified using a Barnstead NANOpure DIamond Life Science water filtration system) in a 250 mL round bottom flask. The H_2SeO_3 solution was cooled to ice-water temperatures in an ice-water bath before the H_2SeO_3 was reduced with 3 mL (61.1 mmol) of hydrazine (N_2H_4, 50-60% in water; Sigma-Aldrich). The N_2H_4 was introduced over a 2 min period through a drop-by-drop addition into the reaction mixture under magnetic stirring (1,000 rpm). The reduction of selenious acid to amorphous selenium can be monitored by a change of the solution from colorless to a light orange color and finally a change to a brick-red, color indicating the presence of selenium colloids.

We determined that the selenium precipitate should be filtered 15 min after initiation of the reaction to maximize both the yield and quality of the *a*-Se. The chilled hydrazine solution was introduced slowly to avoid drastic temperature increases in the reaction vessel. Temperature was controlled in order to prevent the rapid formation of undesirable black *t*-Se nanoparticles. After a total reaction time of 15 min, the red precipitate was collected by vacuum filtration onto a PVDF membrane (catalogue number: VVLP04700; Millipore). If the reaction was continued beyond 15 min, the isolated product will contain a high yield of *a*-Se, but will also contain larger crystals of *t*-Se. A sample of *a*-Se containing large crystals of *t*-Se would produce large, *t*-Se nanorods instead of nanowires. The filtrate was rinsed with 200 mL of ice-cold high purity water to remove residual N_2H_4. The resulting wet solid was stored in a desiccator to remove the moisture in darkness at 22℃ (RT) for 3 days. *Note: Unused a-Se colloids should be stored in a desiccator and in darkness. The quality of amorphous selenium degrades over time, probably due to a change in the ratios between the trigonal, rhombohedral and monoclinic phases.*

2.2.2. Monitoring Growth of Selenium Nanowires by Electron Microscopy

Selenium nanowires were produced by sonicating (Branson Model 1510) for 20 s a dispersion of 2 mg of amorphous selenium (*a*-Se) powder in 1 mL of isopropanol (*i*PA, 99.5%; ACS Reagent Grade, Caledon Lab Ltd.) within a sealed 1-dram glass vial. The nanowires grow over a period of 12 h while this sonicated solution was stored in darkness at RT. After a specified time to allow the *a*-Se colloids to transform into *t*-Se nanowires, a ~10 µL aliquot was removed from the 1-dram vial for electron microscopy analysis.

2.2.3. Sonochemically-Induced Synthesis of Selenium Nanowires at Different Temperatures

Selenium nanowires were produced by sonicating for 20 s a dispersion of 2 mg of amorphous selenium powder in 1 mL of *i*PA within a sealed 1-dram glass vial. The nanowires grow over a period of 12 h while this sonicated solution was stored in darkness at the specified temperatures of -20, 4, 22 (RT), 50, 60 or 80°C. To synthesize selenium nanowires at temperatures below RT, the sonicated solution was stored in a freezer or a refrigerator maintained -20 and 4°C, respectively. To synthesize selenium nanowires at elevated temperatures, the glass vials were heated in an oil bath maintained at the specified temperatures. Also, these vials were wrapped in aluminum foil to keep out the light during nanowire growth.

2.2.4. Inhibiting the Preferential Growth of Selenium Nanowires by Addition of 11-hydroxylundencane-1-thiol (HUT)

Selenium nanowires were produced by sonicating for 20 s a dispersion of 2 mg of amorphous selenium powder in 1 mL of 95% EtOH (EtOH, 95%; Commercial Alcohols) within a sealed 1-dram glass vial. The nanowires grow over a period of 12 h while this sonicated solution was stored in darkness at RT for specified durations before addition of 10 µL of 0.11 M 11-hydroxylundecane-1-thiol (HUT, 97%; Aldrich). The HUT solution was prepared by dissolving the white powder in 95% EtOH. After the HUT solution was added to the growing nanowires, the samples were further incubated at RT in the absence of light for another 24 h.

2.2.5. Sonochemically-Induced Synthesis of Selenium Nanowires at Different Ratios of Amorphous Selenium to Ethanol

Selenium nanowires were synthesized from different amounts of amorphous selenium powder dispersed in EtOH. Concentrations of 5, 4, 3, 2, 1.5, 1, 0.5, and 0.25 (mg *a*-Se/mL EtOH) were analyzed for the success of transformation into *t*-Se nanowires. Selenium nanowire syntheses were carried out in 1-dram glass vials. All samples were aged for 12 h in the absence of light after receiving an initial 20 s of sonication at RT.

2.2.6. Materials Characterization Techniques

Scanning electron microscopy (SEM) images and energy-dispersive X-ray spectroscopy (EDS) data were acquired with Strata DB235 FESEM operating at 5 kV. Samples for SEM analysis were prepared by either drop-casting a solution of nanowires or otherwise positioning the sample of interest onto a 1 cm^2 piece of silicon wafer. Bright field transmission electron microscopy (TEM) images were obtained with a Tecnai G^2 STEM operating at 200 kV. These TEM samples were prepared by drop-casting or dip-coating solutions of nanowires onto a 300 mesh copper grid coated with formvar/carbon (catalogue number: FCF300_CU_50; Cedarlane Laboratories Limited). Average dimensions of the nanowires were calculated from more than 100 measurements obtained on different nanowires.

X-ray diffraction (XRD) patterns were acquired with a Rigaku diffractometer using Cu Kα radiation (λ = 0.15418 nm). Copper X-rays were generated from a copper target by electron bombardment at 42 kV and 40 mA. A 0.8-mm collimator was placed between the X-ray source and the sample. Samples for X-ray analysis were prepared by casting a suspension of nanowires from EtOH or *i*PA onto a glass slide and drying the sample under vacuum.

2.3. Results and Discussion

Essential to achieving a high yield of selenium nanowires is the use of freshly synthesized *a*-Se colloids. At room temperature (RT), the thermodynamically unstable *a*-Se slowly converts to *t*-Se, which is the most thermodynamically stable selenium allotrope.[52] At RT, these large crystals of *t*-Se are not as soluble as the other allotropes of selenium. The successful transformation of *t*-Se colloids to *t*-Se nanowires is only observed at elevated temperatures and pressures, where the *t*-Se colloids are readily soluble.[53] Therefore, it is important to synthesize high quality a-Se colloids with a low content of *t*-Se. Sonochemical synthesis of selenium nanowires used high quality *a*-Se colloids synthesized by reducing selenious acid with hydrazine at ice-water temperatures over a reaction time of 15 min (Eqn. 2.1). Analysis by X-ray diffraction (XRD), suggested there was no detectable crystalline material in the *a*-Se colloid that was synthesized in 15 min (Figure 2.6a). These *a*-Se colloids had an approximate diameter of 400-nm (Figure 2.6a, inset). A longer reaction time or reducing the selenious acid at RT would lead to the formation of large *t*-Se crystals. A reaction time of 72 h produced a mixture of *a*-Se and *t*-Se. X-ray diffraction pattern of this mixture consists of distinct diffraction peaks, which corresponds to *t*-Se, on top of an amorphous background (Figure 2.6b and inset). Since the *a*-Se colloids have a relatively low glass transition temperature (T_g) of 32°C,[49] it was important to use freshly synthesized *a*-Se precursors for the nanowire synthesis. Storing these precursors at RT under darkness for more than 6 months would lead to the coalescence of these colloids, as well as formation of microscopic sized rods observed in SEM analysis (Figure 2.6c). The fused *a*-Se have a lower surface free energy in comparison to individual colloids. Thus, the *a*-Se clusters have a decreased solubility. A decrease in the solubility of the precursors could prevent the complete transformation of the *a*-Se colloids into *t*-Se nanowires. A mixture of selenium nanowires, nanorods, and *t*-Se microstructures were produced by sonochemically initiated transformation using a 6 month old sample of *a*-Se (Figure 2.6d). Reaction shorter than 15 min would result in a significantly lower yield of *a*-Se colloids. In summary, a reaction time of 15 min produced high quality *a*-Se colloids without sacrificing yield of the precursor synthesis.

$$H_2SeO_3\ (aq) + N_2H_4\ (aq) \rightarrow a\text{-}Se\ (s) + N_2\ (g) + 3H_2O\ (l) \qquad \text{(Eqn. 2.1)}$$

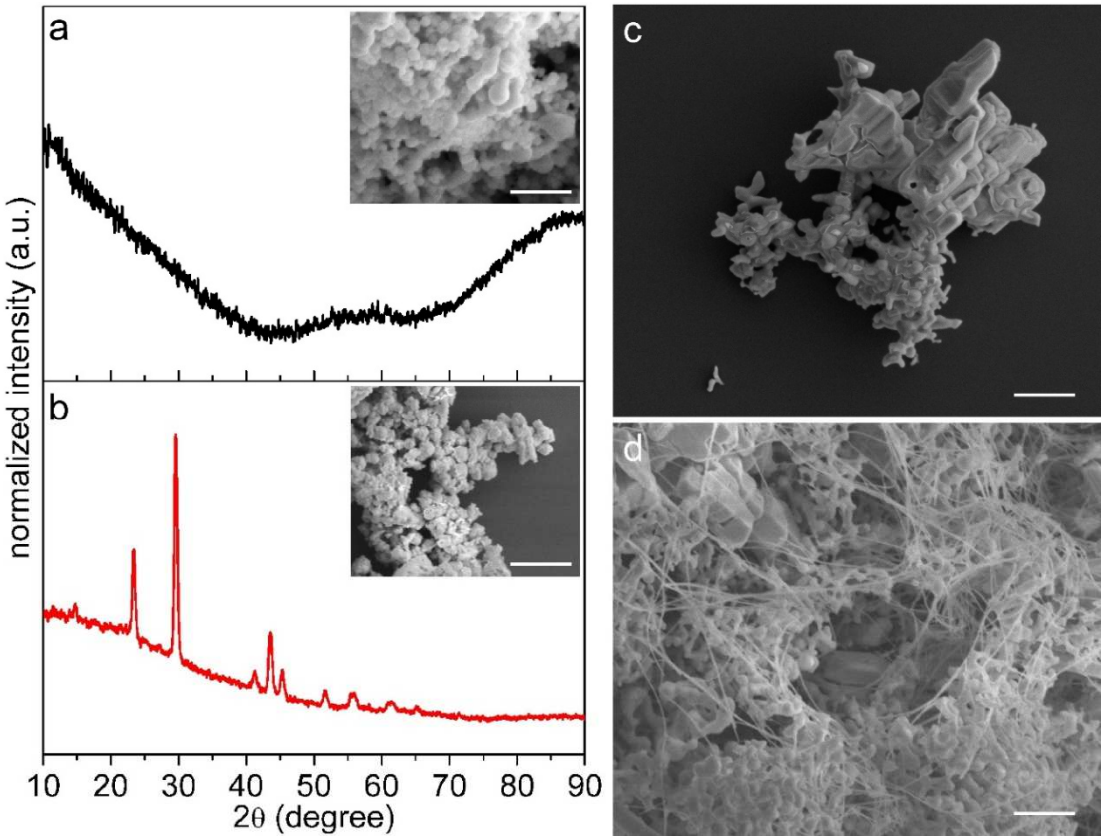

Figure 2.6 X-ray diffraction patterns of selenium colloids synthesized by reducing selenious acid with hydrazine at a reaction time of (a) 15 min and (b) 72 h. Inset in (a,b) are the SEM images of the corresponding samples. Scanning electron micrographs of (c) 6 month old sample of a-Se colloids, and (d) selenium nanostructures produced from a 6 month old sample of a-Se colloids via the sonochemical process. Scale bars are 2 µm.

The progress of transformation from *a*-Se colloids to *t*-Se nanowires was monitored by SEM. The as-synthesized spherical *a*-Se colloids were dispersed in alcohol (i.e., 95% EtOH or 99.5% *i*PA) before the sample was exposed to sonication to initiate the transformation process. Sonication induced heating[54] elevated the local temperature within the dispersant above the T_g of *a*-Se, leading to coalescence of the *a*-Se colloids (Figure 2.7a). After 0.5 h of incubation in darkness at RT, short and narrow diameter anisotropic nanostructures were observed on the surfaces of the deformed and coalesced *a*-Se (Figure 2.7b – inset red arrows). Each *a*-Se cluster or colloid was capable of supporting the growth of multiple nanowires (Figure 2.7c-e – insets). Scanning electron microscopy analysis also indicated that the majority of the selenium nanowire growth occurred at the surfaces of *a*-Se clusters/colloids. We did not observe

selenium nanowires growing from *t*-Se seed crystals that are not adhered to the surfaces of *a*-Se cluster/colloid. These anisotropic nanostructures grew in length while they remain tethered to the surfaces of *a*-Se colloids with increasing incubation time (Figure 2.7b-i). The diameter of these selenium nanowires were wider at the base, where they are tethered to the *a*-Se cluster/colloid. The diameter of the nanowires taper as they are further away from the surfaces of *a*-Se (Figure 2.7e,f – insets). The tapered diameter of the selenium nanowires disappeared after a growth period of 5 h (Figure 2.7g). Analysis by SEM suggested that the middle segment of the selenium nanowires have consistent diameters along the growth axis after a period of at least 5 h (Figure 2.7g-i). It took approximately 12 h for the *a*-Se precursors to completely transform into *t*-Se nanowires (Figure 2.7i). The growing end of selenium nanowires remained tapered while the base of the nanowires was still wider than the rest of the anisotropic nanostructures. Since several selenium nanowires could be growing from a single cluster of *a*-Se colloids, the final structure is similar in appearance to a sea urchin after the precursors had been consumed. Electron diffraction analysis of selenium colloids produced diffuse diffraction rings, suggesting that these colloids were amorphous (Figure 2.7j). Atoms in an amorphous material exhibited short-range order, but lack the long-range order that was observed in crystalline solids, which interacted with electromagnetic radiation (below a wavelength of 0.2-nm) to produce distinct interference patterns. The distance from the transmitted electron beam (i.e., 000 spot) to a diffraction spot corresponded to the inverse of a specific interplanar spacing (d-spacing) within the crystal that electromagnetic waves scattered from to produce a constructive interference. An electron diffraction pattern acquired from a cluster of randomly oriented selenium nanowires produced distinct diffraction rings of different diameters (Figure 2.7k). These diffraction rings correspond to {010}, {011}, {110}, {012}, and {111} planes of the *t*-Se crystal. Selected area electron diffraction (SAED) from an individual selenium nanowires yielded a set of periodic diffraction spots, signifying that the nanowire is single crystalline. The diffraction pattern is associated to the [120] zone axis of a hexagonal closed-packed crystal (Figure 2.7l). Electron microscopy analysis suggested that selenium nanowires did not grow by oriented attachment of *t*-Se nanocrystals. In an oriented attachment growth process, we would expect to observe large quantities of *t*-Se nanocrystal at the earlier stages of nanowire growth.

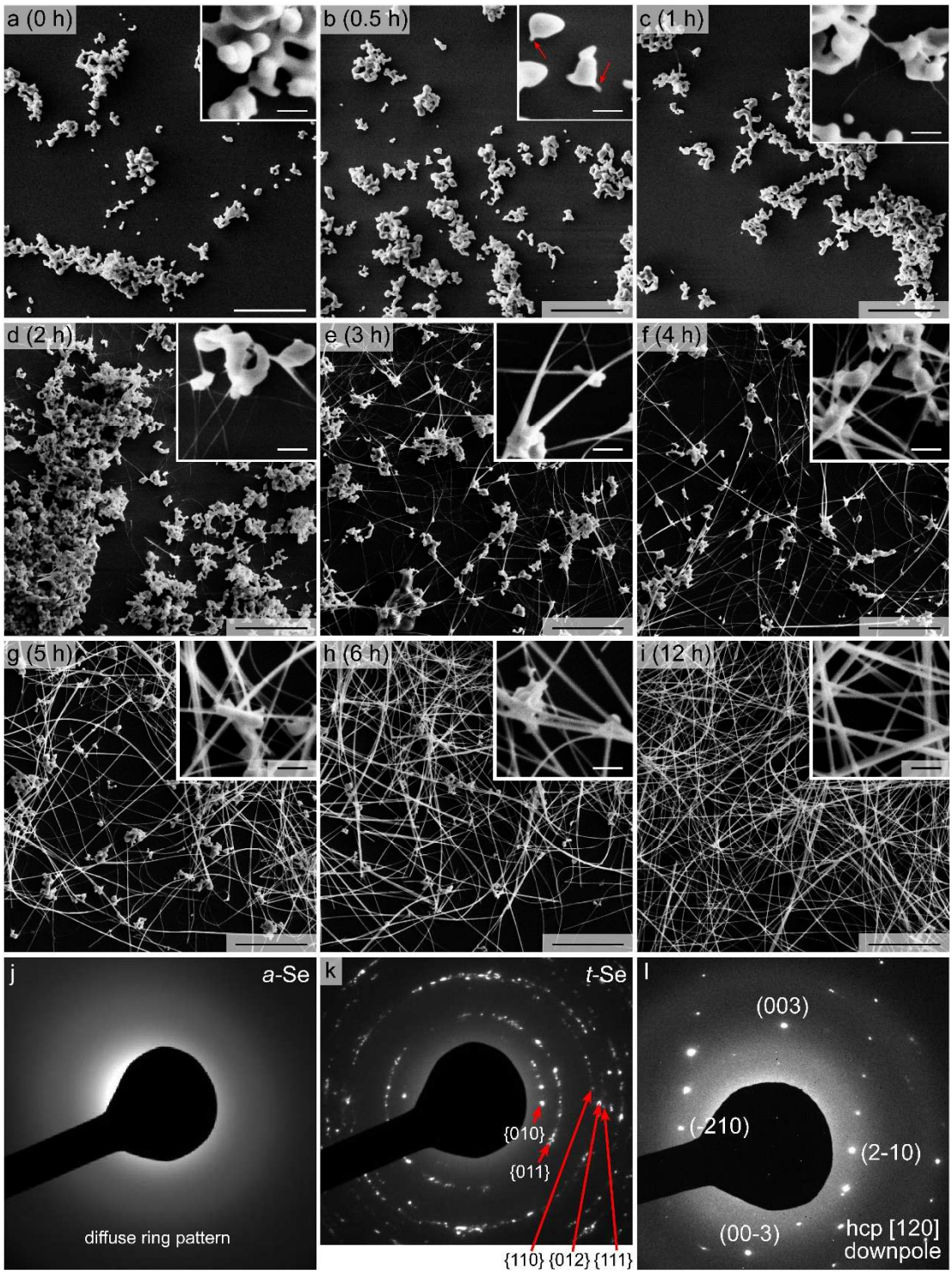

Figure 2.7 (a-i) SEM images showing the progressive transformation of a-Se colloids to t-Se nanowires. Diffraction pattern of a cluster of randomly oriented (j) a-Se and (k) t-Se, respectively. (l) Selected area electron diffraction pattern of an individual selenium nanowire. Scale bars are 5 µm and inset scale bars are 0.5 µm.

The absence of large quantity of *t*-Se nanocrystals and the formation of tapered nanowires as intermediates suggested that the selenium nanowires grew by Ostwald ripening process rather than oriented attachment. We believed the *a*-Se colloids were transformed into *t*-Se nanowires of uniform diameters along the axis of growth proceeded by a sequence of processes that involved dissolution-nucleation-recrystallization. In brief, selenium nanowires synthesized by the sonochemical method started with *a*-Se dispersed in an alcohol. The acoustic cavitation during sonication generated localized hot spots[54] that facilitated the dissolution of *a*-Se colloids as well as to initiate the nucleation of *t*-Se seeds. During nucleation, *t*-Se crystalline seeds were formed in solution and grow larger in size by the Ostwald ripening process. These seeds spontaneously collect at the surface of the *a*-Se colloids, probably because they had similar surface energies in comparison to the solvent. These trigonal seeds served as nucleation sites for further recrystallization until sources of solubilized selenium had been exhausted. The solubilized selenium atoms deposited preferentially onto the high energy {001} facets of the *t*-Se seeds, which grew into single crystalline 1D nanostructures. As the selenium nanowires grow axially, the solution in proximity to the {001} facets became depleted of precursors for sustained growth because it took longer for solubilized selenium atoms to diffuse from the *a*-Se colloids to these high energy facets. The base of the selenium nanowires that was attached to an *a*-Se colloid did, however, still had access to abundant amount of solubilized selenium atoms, allowing the base to grow radially. As a result, selenium nanowires synthesized in EtOH and *i*PA through the sonochemical method were tapered towards the end that protruded from the surfaces of the *a*-Se colloid (Figure 2.8).

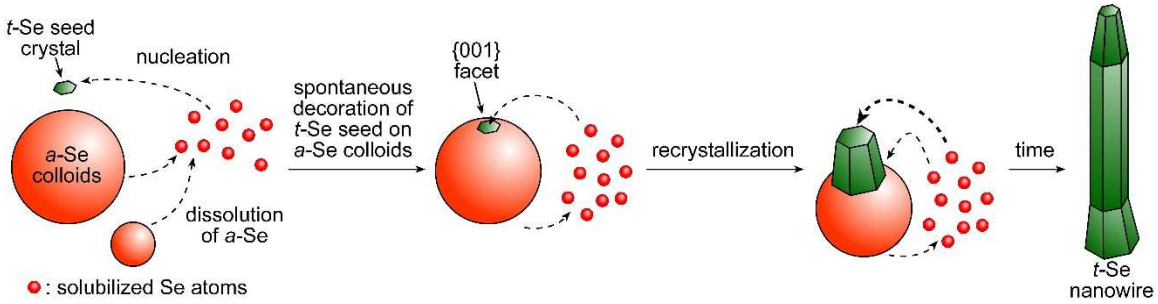

Figure 2.8 A schematic representation of the Ostwald ripening process following sonication of a-Se colloids dispersed in alcohol.

To verify that at low concentrations of solubilized selenium the selenium atoms bind preferentially to the {001} facets of the *t*-Se nanowires, 11-hydroxylundecane-1-thiol (HUT) was added during the elongation phase of the nanowires to inhibit preferential growth in the <001> directions. Selenium nanowires grown in the absence of HUT have narrow diameters and were long (Figure 2.9a) in comparison to the samples that had HUT introduced at early stages of the nanowire growth. Inhibition of nanowire growth in the preferential axial direction forced the anisotropic nanostructures to grow radially instead (Figure 2.9b-f). The observed 1D nanostructures were shorter in length and wider in diameter than the nanowires grown in the absence of HUT. When HUT was added to the growth medium at a later stage the *t*-Se nanostructures were narrower, but they were not as narrow as the control sample (Figure 2.10). The average diameters were 214 ± 72, 217 ± 52, 136 ± 42, 97 ± 39, and 75 ± 29 nm, respectively, for HUT added after an increasingly longer period of nanowire growth. Selenium nanowires synthesized in the absence of HUT for this experiment had an average diameter of 57 ± 18 nm.

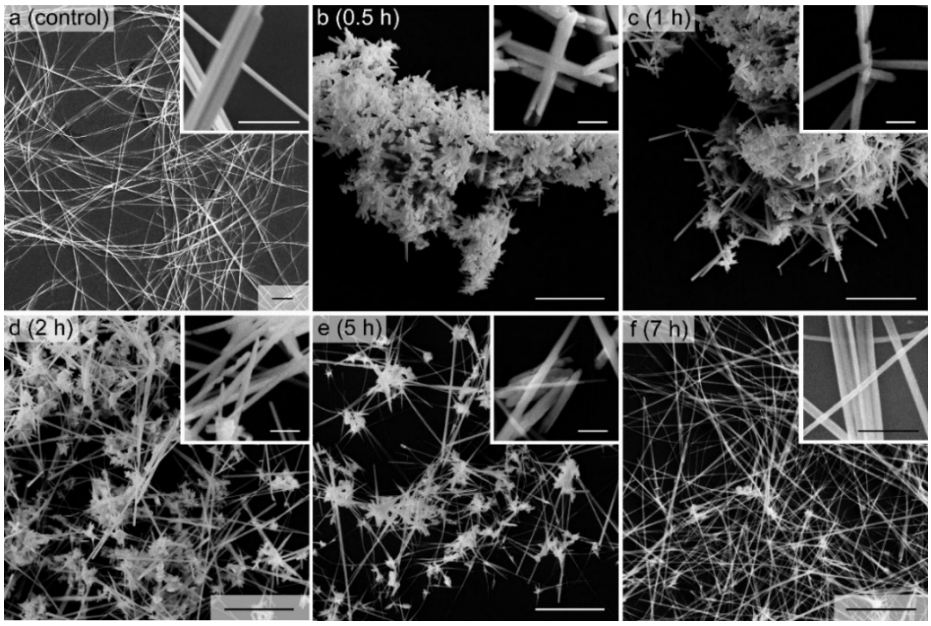

Figure 2.9 SEM images of (a) selenium nanowires grown in the absence of 11-hydroxylundecane-1-thiol (HUT), and following the addition of HUT at (b) 0.5, (c) 1, (d) 2, (e) 5, and (f) 7 h after the initiation of selenium nanowires growth. Scale bars are 5 µm and inset scale bars are 500 nm.

Addition of the nanowire growth inhibitor at 0.5 h yielded dendritic nanostructures of ~2 µm in length, while inhibitor introduced at a later stage resulted in progressively longer features. The corresponding length of these features at 1, 2, 5, and 7 h are ~4, ~7, ~10, and >10 µm, respectively. Furthermore, the morphology of these selenium nanostructures evolved from sisal- (Figure 2.9b-d, inset) to urchin-like structures (Figure 2.9e,f, inset). We did not have spectroscopic evidence to support that HUT molecules were chemisorbed on the {001} facets of the selenium nanowires. The concentration of inhibitor at these facets were below the detection limit of energy dispersive X-ray spectroscopy techniques by scanning transmission electron microscopy. This study provided indirect evidence of HUT molecules binding to the higher energy {001} facets of *t*-Se to inhibit further addition of selenium atoms.

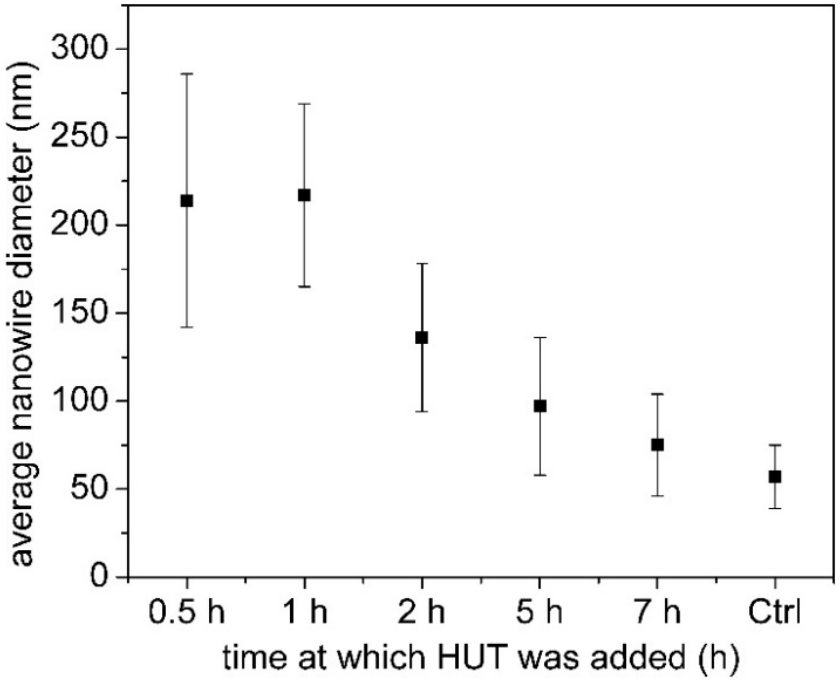

Figure 2.10 Average diameter of anisotropic selenium nanostructures synthesized in the presence and absence of 11-hydroxyundecan-1-thiol (HUT). The HUT inhibitor was added at the specified times (see Figure 2.9), and Ctrl refers to selenium nanowires synthesized in the absence of HUT.

Dissolution of *a*-Se colloids in the growth medium is one of the main driving forces in transforming the *a*-Se colloids into *t*-Se nanowires. A decrease in temperature of the solution should be accompanied by a decrease in the solubility of amorphous

selenium in the solvent, thus slowing down the Ostwald ripening process. In contrast, higher solvent temperatures should increase nanowire growth rates due to an increased dissolution of selenium fragments in the solvent. A series of temperatures were evaluated for the selenium nanowire growth to provide insight into the control over nanowire growth that can be achieved by tuning the solubility of *a*-Se colloids and the rate of Ostwald ripening. Each sample contains 2 mg of *a*-Se dispersed in 2 mL of *i*PA in a 1 dram glass vial. The *a*-Se colloids were dispersed by 20 s of sonication in a 22°C (RT) water bath. These samples were subsequently aged under darkness for 12 h. Selenium nanowires are grown in the absence of light because electromagnetic radiation from the visible and near IR spectra have sufficient energy to convert *a*-Se into large *t*-Se nanocrystals.[55] These larger *t*-Se crystals are not very soluble in *i*PA under ambient conditions, resulting in the formation of micron sized by-products. During the aging process the vials were maintained at -20, 4, 22, 50, 60, and 80°C, respectively. Analysis by SEM revealed that the *a*-Se colloids did not transform into selenium nanowires at -20°C (Figure 2.11a). The morphology of the fused cluster of *a*-Se colloids, produced by sonication of the dispersed *a*-Se colloids, are preserved after 12 h of aging. These results suggest that the system had insufficient energy to dissolve the *a*-Se and to initiate Ostwald ripening. Since little to no dissolution of *a*-Se occurred at -20°C, nucleation of *t*-Se seed crystal and recrystallization processes could not occur. Therefore, no selenium nanowires were formed at this temperature. The conditions describing the lack of nanowire formation correlates to Figure 2.3 – region **I**. The sample maintained at 4°C produced a few short and narrow nanowires of selenium (Figure 2.11b). At 4°C, there is sufficient energy within the system to dissolve a small amount of *a*-Se. These solubilized precursors were able to nucleate into seed crystals that led to the formation of selenium nanowires during the recrystallization processes. A longer aging period was, however, required at 4°C to completely transform the *a*-Se to *t*-Se nanowires. The rate of nanowire growth reflected the condition described by a lower concentration of solubilized selenium in region **II** of Figure 2.3. At a temperature of 22°C, 100% of *a*-Se were transformed into *t*-Se nanowires after 12 h (Figure 2.11c and inset). The synthesized selenium nanowires were longer and wider in comparison to those grown at 4°C. The majority of the selenium nanowires produced at 22°C for this experiment were narrower than 100-nm. The diameter of the selenium nanowires

increases as the growth temperature also increases (Figure 2.11d-f). The diameters of nanowires synthesized above 22°C were approximately 1.5 to 3 times wider, in comparison to selenium nanowires synthesized at 22°C. The larger diameter selenium nanowires produced at elevated temperatures could be attributed to higher concentrations of solubilized selenium. At high temperatures there was more solubilized selenium than the total surface area available on the {001} facets. Hence, there was an excess of solubilized selenium even though the {001} facet was growing at or very close to the maximum rate (Figure 2.3 – region **III**). The excess solubilized selenium started to add to the lower energy surfaces (i.e., {010} and {110} facets of Figure 2.2), causing the selenium nanowires to grow in a radical direction. Aspect-ratio of the selenium nanowires synthesized by the sonochemical method can be tuned by controlling the temperature at which nanowires are grown.

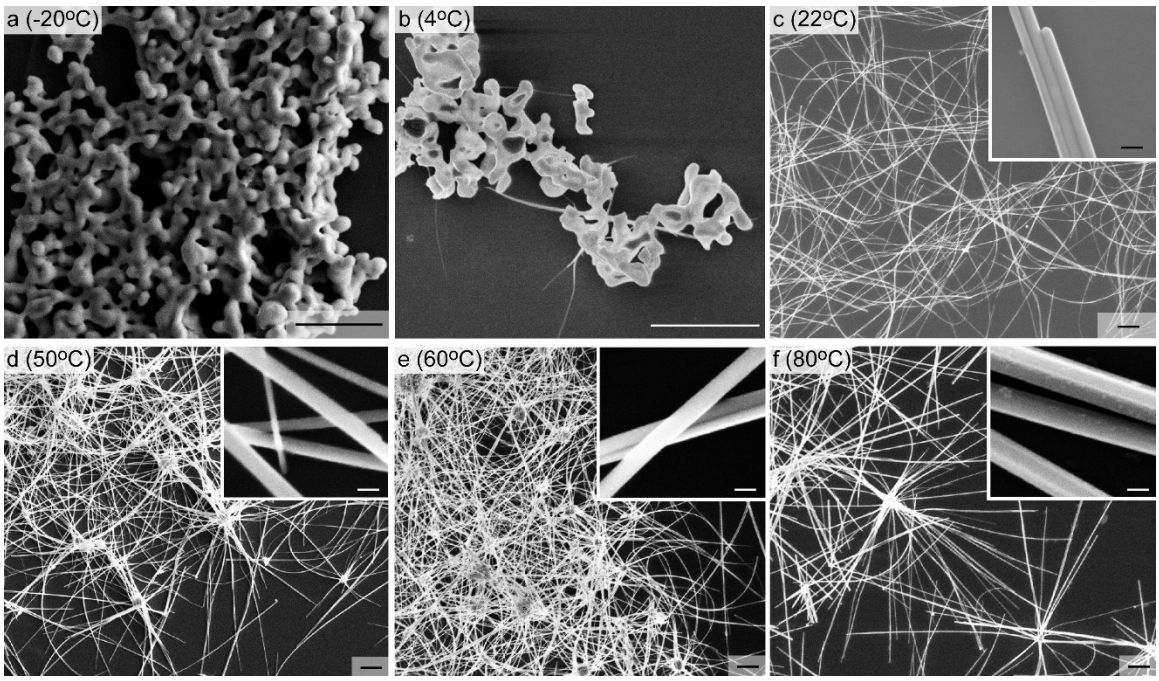

Figure 2.11 The transformation of a-Se into t-Se at various temperatures as examined by SEM. All samples were analyzed 12 h after the initial sonication (for 20 s) in isopropanol (iPA). Temperature for growth was: (a) -20, (b) 4, (c) 22, (d) 50, (e) 60, and (f) 80 ℃. Scale bars are 2 µm and inset scale bars are 100 nm.

Minimizing the formation of large *a*-Se aggregates is crucial to obtain a high nanowire yield, as well as to increase the success of the sonochemically initiated

transformations. One of the ways to minimize aggregation of *a*-Se is to increase the inter-particle distance by lowering the concentration of selenium precursor. In order to further improve on the current sonochemical synthesis technique, we investigated the effect of decreasing selenium precursor concentration on the rate of successful transformation and the quality of resulting selenium nanowires. The precursor concentrations are expressed as the ratio of *a*-Se (mg) to EtOH (mL). Scanning electron microscopy analysis revealed the presence of large aggregates greater than 1 µm in diameter in samples containing higher concentrations of *a*-Se precursor, such as 5 to 3 mg/mL (Figure 2.12a,b). The coalesced colloids, which have a much lower solubility relative to small *a*-Se colloids, could not dissolve at a rate that was sufficient to support the growth of selenium nanowires. As a result, few or no 1D nanostructures were observed by SEM analysis of these samples (Figure 2.12a,b – inset). In contrast, samples with concentrations of *a*-Se between 2 to 0.25 mg/mL generated anisotropic *t*-Se nanostructures with ~100% successful conversion into nanowires (Figure 2.12c,d). Selenium nanowires synthesized from concentrations of *a*-Se ≤ 2 mg/mL also have similar diameters. The average diameters measured from at least 100 selenium nanowires in the order of samples of decreasing *a*-Se concentrations were 33 ± 7, 30 ± 7, 32 ± 8, 31 ± 7, and 29 ± 9, respectively (Figure 2.12e). The quantity of *a*-Se colloids available was crucial in determining the complete transformation of the precursor material into selenium nanowires, but it did not have a significant role in fine tuning nanowires' diameters.

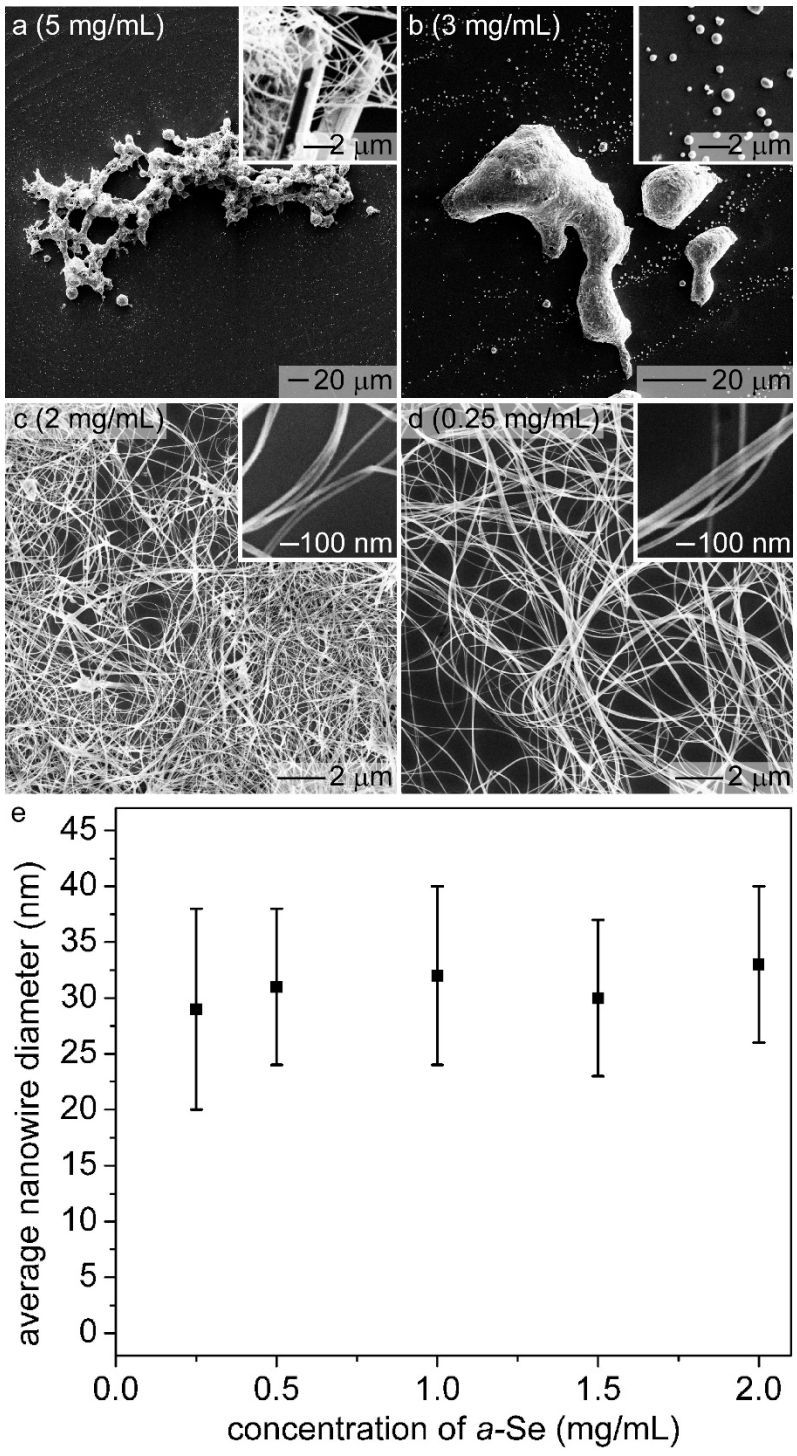

Figure 2.12 (a-d) SEM images of the nanostructures produced from various concentrations of a-Se (mg/mL) after 12 h, in 95% ethanol. (e) Average diameter of selenium nanowires synthesized from different concentrations of a-Se.

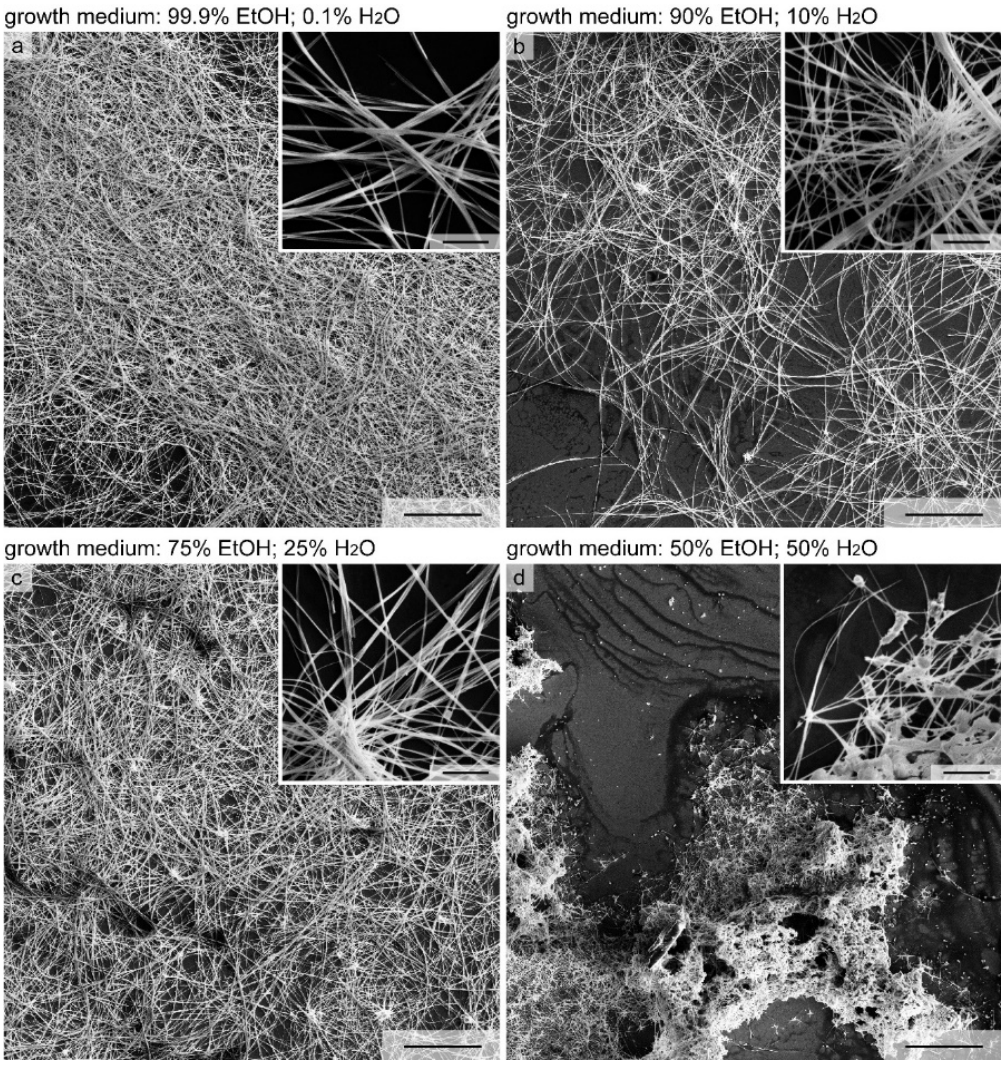

Figure 2.13 SEM images of selenium nanowires synthesized from ethanol (EtOH) containing different concentrations of H_2O. Each synthesis has 2 mg of a-Se per mL of growth medium. Scale bars are 20 µm and inset scale bars are 2 µm.

We, also, investigated the effect of water content in a growth medium on the success of the transformation of *a*-Se colloids into *t*-Se nanowires. Synthesis of *a*-Se precursor in water in the absence of a polymer surfactant would lead to the agglomeration of the selenium colloids, suggesting that the colloids are hydrophobic. We observed that using a growth medium with a high water content would facilitate aggregation of the precursor material and lead to an unsuccessful sonochemical transformation (Figure 2.13). Selenium nanowires were synthesized from ethanol containing ~0.1, 10, 25, and 50% water by volume, respectively. Selenium nanowires

were synthesized at RT with an *a*-Se concentration of 2 mg/mL using absolute EtOH, which has a ~0.1% water content. Deionized water was used to dilute the EtOH to obtain the specified compositions. Scanning electron microscopy analysis indicated selenium nanowire synthesis was reproducible even when the solvent composition contains up to 25% of water (Figure 2.13a-c). Urchin-like nanostructures were observed at a higher frequency with increasing water content in the growth medium (Figure 2.13b,c – insets). A solvent containing ≥50% water led to an incomplete conversion of *a*-Se into *t*-Se nanowires (Figure 2.13d and inset). The incomplete conversion to *t*-Se nanowires was attributed to a decreased solubility of the *a*-Se aggregates.

2.4. Conclusions

In conclusion, selenium nanowires grow by the Ostwald ripening process. Sonication generated cavitation was used to facilitate the dissolution and dispersion of *a*-Se. The solubilized selenium atoms nucleated into *t*-Se seed crystals, from which subsequent recrystallization took place. The recrystallization occurred preferentially on the high energy {001} facets of *t*-Se, leading to the formation of anisotropic nanostructures. Sonochemically synthesized selenium nanowires are single crystalline and grew preferentially along the <001> directions. Diameter of the synthesized selenium nanowires was tailored by adjusting the temperature at which nanowires were grown. Temperature was used to control the availability of solubilized selenium and the rate of nanowire growth. Dissolution of *a*-Se colloids is required to initiate and maintain the growth of selenium nanowires. High aspect-ratios selenium nanowires are produced at low concentrations of solubilized selenium, while an overabundance of the solubilized selenium led to the formation of low aspect-ratio selenium nanowires (i.e., nanorods). In addition, we have shown evidence that further suggested that solubilized selenium attached preferentially to the higher surface energy facets. Selectively inhibiting their axial growth was achieved by controlled passivation of the highest surface energy facets. Addition of 11-hydroxyundecane-1-thiol selectively inhibited the {001} facets from further recrystallization, forcing the anisotropic nanostructures to subsequently grow radially. We have also determined that the concentration of *a*-Se colloids and water content of the growth medium have a direct impact on the success of the sonochemically initiated transformation. Both high concentration of *a*-Se and water content can lead to

aggregation of the *a*-Se colloids, decreasing the solubility of *a*-Se. In these instances, the *a*-Se could not dissolve fast enough to support the growth of selenium nanowires. The combination of these factors lowered the chance of a successful sonochemically initiated transformation. Using the optimized parameters developed in this study, we were able to consistently produce selenium nanowires with average diameters of 29 ± 9 nm.

2.5. Future Directions in Synthesizing High-Aspect-Ratio Selenium Nanowires

Aspect-ratio of the selenium nanowires resulting from a sonochemically-induced synthesis depend primarily on the factors explored in this chapter. These factors are reaction temperature, solvent, water content within the solvent, and the mass-to-volume ratio between *a*-Se and solvent. We have examined some of these variables in-depth to determine the optimal conditions to synthesize high-aspect-ratio selenium nanowires with different diameters. Another parameter that we would like to study in relation to the transformation to *t*-Se nanowires is the effect of varying the allotrope compositions in *a*-Se colloids and its impact on the aspect-ratio of the selenium nanowires. Raman spectroscopic analysis of *a*-Se colloids has indicated that the amorphous colloids consist of a mixture of trigonal, rhombohedral (Se_6), and monoclinic (Se_8) phases of selenium.[25] We hypothesize that synthesizing the *a*-Se at different temperatures (i.e., 0, 10, and 22^{o}C) would result in different allotrope compositions, which would be determined by Raman spectroscopy analysis. Amorphous selenium colloids of varying allotrope compositions could also be produced by aging the as-synthesized colloids in the absence of light and moisture at RT. Since the amorphous selenium is thermodynamically unstable, at RT it is transformed into the more thermodynamically stable allotropes, such as trigonal, rhombohedral, and monoclinic phases. These *a*-Se colloids of different allotrope compositions would be used to synthesize selenium nanowires by the sonochemical method. The success of transformation and aspect-ratio of the resulting selenium nanowires as observed by SEM analysis would be subsequently correlated to the allotrope composition of these *a*-Se colloids. The outcome of these studies could be a further refinement of and understanding in the sonochemically-induced transformation of *a*-Se colloids to *t*-Se nanowires.

3. Creating a Stable Dispersion of Selenium Nanowires*

3.1. Motivations to Increase the Colloidal Stability of Selenium Nanowires

Single crystalline selenium nanowires are readily produced by solution-phase synthetic techniques.[28, 31, 39-40, 56-57] These anisotropic selenium nanostructures are attractive materials for their tunable electrical properties[28] and they are used in template-engaged syntheses to produce various anisotropic selenides,[33, 58-59] core-shell materials,[60] and polymer coated semiconductor materials.[47, 61] These metal selenides have demonstrated promising applications in the areas of bio-labeling,[33, 59, 62-63] phase-change memory,[64] and energy harvesting.[65-66] Selenium has also been used in electromagnetic radiation sensors,[57, 67-70] xerography,[55] templates for catalysis,[71] biomedicine,[72-73] antimicrobial agents,[74] and remediation of heavy metals.[75-76] Selenium based nanowires are, however, not easily processed or otherwise manipulated en mass. Most manipulations require dispersions of these nanowires with colloidal stability. Our goal is to produce stable suspensions of selenium nanowires to facilitate processing, handling, assembling, and incorporation of these nanowires into advanced materials and devices. We aim to create techniques to stabilize these dispersions in order to make selenium nanowires more accessible for a range of applications.

Solution-phase synthesized selenium nanowires can have relatively high-aspect-ratios (ratio of the length and diameter of nanowire). These ratios are typically between 500 and 10,000. These high-aspect-ratio nanowires are flexible and easily entangle into

* All experiments were carried out by Michael C. P. Wang. “Stabilizing dispersions of large quantities of selenium nanowires” manuscript was co-written by Michael C. P. Wang and Professor Byron D. Gates. The contents of this publication were reproduced with the permission of Cambridge publication, and co-authors.[88]

a form that is reminiscent of cooked spaghetti (Figure 3.1a). One of the challenges of working with these high-aspect-ratios nanowires, which are synthesized in the absence of surfactants, is to uniformly disperse the entangled nanowires and to create stable dispersions for subsequent processing. Surfactants are, however, generally used to passivate the surfaces of nanostructures in order to promote a preferred orientation of growth and to facilitate their dispersion in the growth medium. Due to the absence of surfactants, the selenium nanowires tend to minimize their overall surface energy by forming bundles (Figure 3.1a – inset). These bundles or flocculates of selenium nanowires are held together by van der Waals forces. Although van der Waals forces are relatively weak, the sum of the interactions between nanowires make it difficult to separate the nanowires. Shielding the van der Waals interactions between the nanowires will be key to creating a well-dispersed and stable colloidal suspension of the selenium nanowires.

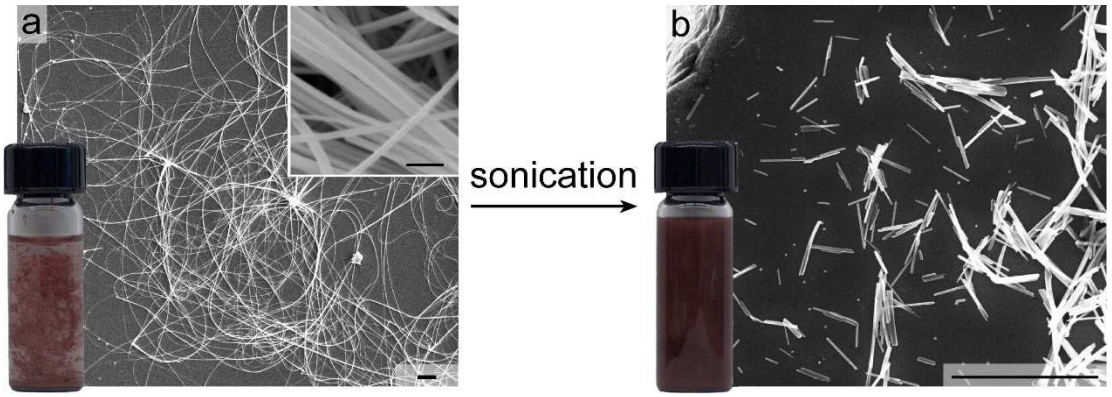

Figure 3.1 (a) Digital photograph of a vial containing as-synthesized selenium nanowires suspended in ethanol (EtOH) dispersed by manual shaking and the corresponding scanning electron microscopy (SEM) analysis of these nanowires. (a, inset) Bundling of selenium nanowires due to van der Waals interactions. (b) Through sonication selenium nanowires can be uniformly dispersed in EtOH. These selenium nanowires, however, became shorter in length, indicating that they are structurally damaged. Scale bars are 2 µm and the inset scale bar is 200 nm.

A flocculated sample of selenium nanowires can be dispersed through serial dilution, however, this process is impractical on a larger scale. Mechanical agitation such as stirring, shaking, or sonication can also be used to disperse the flocculated selenium nanowires. Stirring and shaking can disperse some material, although the process is

inefficient for dispersing most of the flocculated materials. On the other hand, sonication is more efficient because it uses high frequency acoustic waves to create cavitation processes that break up flocculates.[77-80] Sonication is efficient at peptizing flocculated nanostructures, but it can also induce undesirable changes to the surface chemistry of these materials and inflict structural damage to nanostructures. Literature has reported that prolonged sonication would result in oxidation of the surfaces of nanostructures[78-79, 81] and shortening of the anisotropic nanostructures by cavitation induced scission.[82-84] Cavitation induced scission might not be as prevalent in a more robust material (*e.g.*, carbon nanotube), but high-aspect-ratio selenium nanowires are susceptible to fracture and fragmentation during sonication (Figure 3.1b). Therefore, gentler methods were sought to disperse the high-aspect-ratio selenium nanowires.

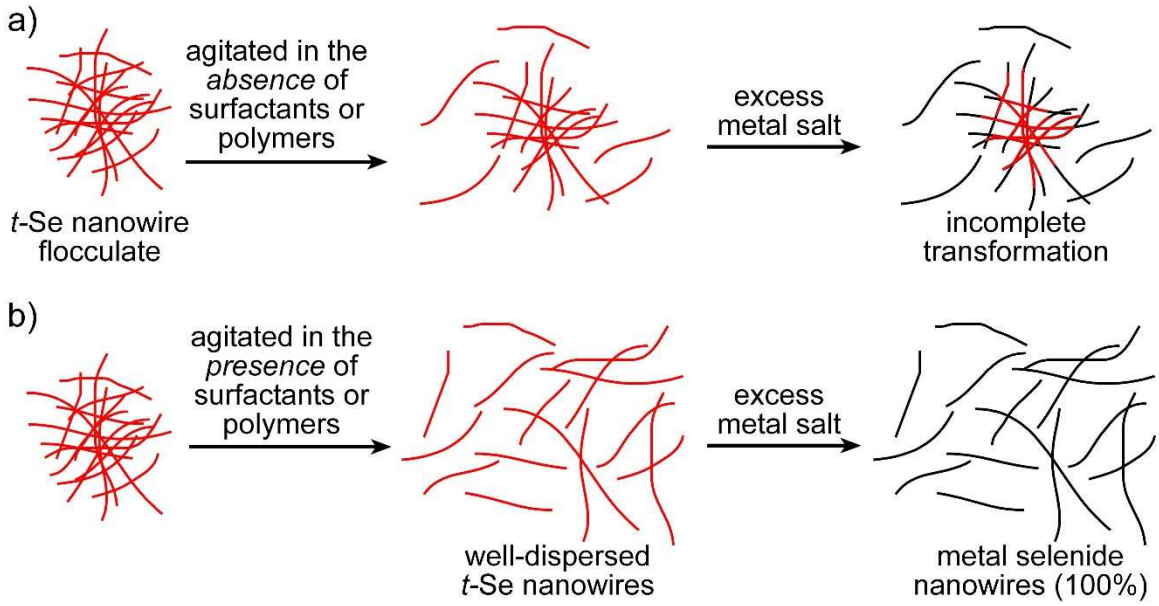

Figure 3.2 Template-engaged transformation of (a) flocculated and (b) dispersed selenium nanowires into metal selenide nanowires. (a) Flocculation of selenium nanowires prevented the uniform transformation to the corresponding metal selenides. (b) Additives, such as surfactants or polymers, were used to facilitate the dispersion of the flocculated selenium nanowires.

Well-dispersed colloidal solutions of one-dimensional (1D) nanostructures are commonly achieved with the addition of surfactants to minimize the van der Waals interactions between nanowires.[77, 85] Having stable dispersions of selenium nanowires are of particular importance for the synthesis of other chalcogenide based nanowires

when using the selenium as a template. Selenium nanowires have been used as template in the synthesis of metal decorated selenium nanowires,[71, 86] as well as Ag_2Se, CdSe, ZnSe, BiSe, and CuSe nanowires.[33-34, 58-59] Scaling up these reactions and extending the preparation to other materials will require uniform dispersion of the selenium nanowire templates to ensure complete and uniform conversion to the desired product (Figure 3.2). Flocculation of the selenium nanowires or their product would significantly decrease the yield of large-scale transformations into chalcogenides and other functional materials. In order to develop stable suspensions of selenium nanowires, we need to investigate the interactions between nanowires dispersed in various solvents and with the addition of surfactants. Preventing the selenium nanowires from settling too fast is also essential for their subsequent assembly into well-defined patterns (Figure 3.3). Organizing these materials through an assembly process is essential for taking advantage of their unique optoelectronic properties.[57] In addition, overcoming the tendency of selenium nanowires to settle from solution is also important for the subsequent assembly of these materials into well-defined patterns.

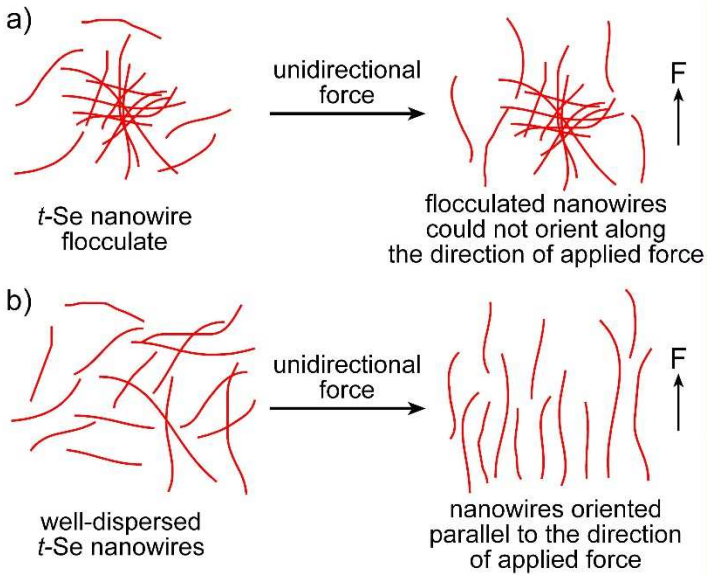

Figure 3.3 Responses of (a) flocculated and (b) well-dispersed selenium nanowires to a unidirectional force.

Herein, we provide a systematic study to create stable suspensions of selenium nanowires in a variety of media. We demonstrate the formation of stable dispersions of hydrophobic selenium nanowires in both polar organic and aqueous solutions with the

addition of appropriate surfactants. We have investigated the interaction of a number of solvents and surfactants to build an understanding of how to stabilize suspensions of selenium nanowires. In this study, we demonstrate the capability of dispersing and stabilizing selenium nanowires as suspensions in various solvents. We analyze the results using both qualitative and quantitative measurements based on time-resolved photography and time-resolved absorption spectroscopy.

3.2. Experimental Section

3.2.1. Materials

All chemicals were used as received without further purification. Poly(vinylpyrrolidone) ($PVP_{10.3k}$, M_w = 10,300; PVP_{55k}, M_w = 55,000; and PVP_{360k}, M_w = 360,000), poly(vinyl alcohol) (PVA, M_w = 6,000 – 15,000, 87-89% hydrolyzed), poly(vinyl alcohol), TWEEN 20 (M_n = 1228), Triton X-100 (contains <3% PEG), Zonyl FSN (40% solid in (1:1) water and *i*PA), hydrazine hydrate (N_2H_4•nH_2O, 50-60%) and selenious acid (H_2SeO_3, 98%), were obtained from Sigma-Aldrich. 1-butanol (1-BuOH, ≥99.4%), methanol (MeOH, ≥99.8%), acetone (≥99.5%), and chloroform (>99%) were acquired from Caledon. 2-propanol (*i*PA, ≥99.5%) and dichloromethane (DCM, ≥99.5%) were bought from Anachemia. 1-octanol (1-OctOH, 99%), absolute ethanol (abs. EtOH, 99.9%) and ethyl acetate (EtOAc, ≥99.5%) were procured from Alfa Aesar, Commerical Alcohols Inc., and Fisher Scientific, respectively.

3.2.2. Synthesis of Selenium Nanowires

In a modified procedure, amorphous selenium was prepared by dissolving 2.73 g (21.1 mmol) of selenious acid in 100 mL of 18.2 MΩ·cm water (purified using a Barnstead NANOpure DIamond Life Science water filtration system) in a 250 mL round bottom glass flask containing an egg-shaped Teflon coated magnetic stir bar rotated at 500 rpm. This solution was then cooled from room temperature to ice-water temperatures in an ice-water bath before introducing the reducing agent, hydrazine. An ice-water chilled solution of hydrazine, 3 mL (61.1 mmol), was introduced drop-by-drop into the reaction solution under constant magnetic stirring (500 rpm) over a period of 1

min. After 15 min of continuous stirring at 500 rpm, the brick red precipitate was collected by vacuum filtration onto a PVDF membrane with an average pore size of 0.1 µm (catalogue #: VVLP04700; Millipore). The filtrate was rinsed with 200 mL of 18.2 MΩ·cm water to remove residual N_2H_4. The resulting red solid was stored in a plastic petri-dish wrapped in aluminum foil and dried in a desiccator filled with drierite (catalogue #: 22891-040; VWR) at room temperature for 2 days. Electron microscopy and X-ray diffraction analysis indicate these sub-micron spherical colloids of selenium are amorphous (Figure 2.6).

A solvochemical route was used to convert the synthesized amorphous selenium colloids into selenium nanowires. In brief, a dispersion containing 9 mg of amorphous selenium powder in 18 mL of isopropanol (*i*PA, ≥99.5%; Anachemia) dispersed in a 20 mL liquid scintillation vial (catalogue #: 03-341-25T; Fisher Scientific) was sonicated for 20 s. The vial was covered with an aluminum sleeve and placed in a dark cabinet maintained at 22℃ for a period of ~12 h. The resul ting product is a red-brown colored sponge (Figure 3.1a) that consisted of millions of entangled crystalline selenium nanowires as identified by X-ray diffraction and electron microscopy analyses (Figure 2.6 and Figure 2.7h). These selenium nanowires had an approximate diameter of 70 nm and a polydisperse length that ranged from 30 to 60 µm. The sponge-like product was transferred into another vial and diluted 40 times with *i*PA. The product was agitated manually to redisperse the selenium nanowires. To disperse the selenium nanowires in other solvents or aqueous solutions, 1.5 mL aliquots of the dispersed nanowires were separated from *i*PA by centrifugation at 1000 rpm for 30 min (IEC Microlite RF Microcentrifuge; ThermoFisher Scientific). The supernatant was decanted and replaced with another solvent of interest. This solvent exchange procedure was repeated a total of 3 times to remove residual *i*PA. Upon each solvent exchange process, the solution of nanowires was manually shaken for ~30 s to redisperse the nanowires.

3.2.3. Synthesis of Platinum Decorated Selenium Nanowires

Selenium nanowires, synthesized from EtOH at a ratio of 1 mg of *a*-Se to 1 mL of 95% EtOH, were used as sacrificial templates to synthesize platinum decorated selenium nanowires. In brief, 25 mg of PVP_{55k} (M_w = 55,000) was added to a 25 mL round-bottom flask containing 5 mg of selenium nanowires dispersed in 5 mL of EtOH.

While under magnetic stirring, 13 mg of hexachloroplatinic acid (H_2PtCl_6; 99.9% trace metals basis; Aldrich) dissolved in 5 mL of EtOH was added to the reaction mixture. The reaction mixture was refluxed for 12 h before workup. In the workup, platinum decorated selenium nanowires were concentrated by centrifugation at 3,000 rpm for 10 min. The unreacted H_2PtCl_6 solution was decanted, and subsequently replaced with 10 mL of 95% EtOH. This process was repeated a total of 3 times to ensure complete removal of residual H_2PtCl_6.

3.2.4. Materials Characterization Techniques.

Scanning electron microscopy (SEM) images were acquired with an FEI Strata DB235 FESEM operating at 10 kV. Samples for SEM analysis were prepared by drop-casting a solution of nanowires onto a piece of approximately 1 cm^2 polished silicon wafer. Transmission electron microscopy (TEM) images were obtained with an FEI Tecnai G^2 F20 scanning TEM (STEM) with a Schottky field emission source operating at 200 kV. For TEM analysis, samples were prepared by drop-casting or dip-coating solutions of nanowires onto a 300 mesh copper grid coated with formvar/carbon (catalogue number: FCF300_CU_50; Cedarlane Laboratories Ltd.)

3.2.5. Time-Resolved Spectroscopy and Photography to Monitor Dispersions of Selenium Nanowires

Time-resolved photography was conducted on 2 mL of nanowire suspensions in 2.5 mL screw capped glass vials. These images were acquired with a HP Photosmart 945 or with a Nikon D700 digital camera that was setup to acquire time-resolved photographs at 5 min intervals. Dispersions of selenium nanowires were monitored by time-resolved optical spectroscopy measurements using a Varian Cary 300 Bio spectrophotometer operating a Scanning Kinetics program. The program was setup to acquire a spectrum every 10 min. Absorbance data from wavelengths of 300 to 900 nm were acquired at a scan rate of 600 nm/min at an integration of 100 ms at a step size of 1 nm. Samples of nanowires were suspended in 3 mL of the solvent of interest within a 1 cm path length quartz cell (catalogue number: 100-10-40, Type 100-QS, Hellma Analytics).

3.2.6. Water Contact Angle Measurement

Water contact angle was measured on a dried sheet of selenium nanowires using a digital AST Optima contact angle system. The system is equipped with a horizontal light beam to illuminate the sample. Deionized water, ~1 µL, was delivered to the surface of the sheet of selenium nanowires using a micropipette. The contact angle between the water droplet and the surface of the sheet of selenium nanowires was calculated through the manufacture software. The reported water contact angle was an average of 2 individual measurements and the error reflected ± 1 standard deviation.

3.3. Results and Discussion

Throughout this chapter, we will be studying the colloidal stability of selenium nanowires synthesized in *i*PA. These nanowires have lower aspect-ratios in comparison to nanowires synthesized in EtOH and do not produce as many urchin-like dendritic structures, which form when there are multiple nucleation sites on a single *a*-Se colloid/cluster. These dendritic structures are very challenging to disperse due to their ability to interact with several other nanowires at once, they have a tendency to agglomerate and quickly settle out of the dispersant (Figure 3.1a). The presence of these dendritic nanostructures can influence both the qualitative and quantitative assessments of a solvent's effectiveness to form uniform dispersions of selenium nanowires. Selenium nanowires synthesized from *i*PA, on the other hand, are shorter in length (30-60 μm) and wider in diameter (~70 nm). Upon manual agitation these nanowires can be dispersed uniformly in solution, providing a better frame of reference to indicate whether the solvent is capable of interacting favorably with the surfaces of selenium nanowires.

We obtained both qualitative and quantitative data on the colloidal stability of selenium nanowires. As a qualitative analysis, digital images of the samples taken at various time intervals, provide information on how the selenium nanowires settled out of solution (e.g., settling out of solution individually or as an ensemble). Measurements made with a UV-visible spectrometer provided a quantitative analysis. The spectrometer was programmed to obtain a spectrum every 10 min over a period of 4 or 24 h. We assessed the rate at which the nanowires settled out of solution by monitoring the time dependent changes in maximum absorbance intensity at 400 nm. This spectral position corresponds to one of the absorbance edges of the selenium nanowires (Figure 3.4). This absorbance band is less sensitive to interchain electronic transitions, which can vary with nanowire diameter, for trigonal selenium and possibly nanowire to nanowire contacts present in flocculating suspensions. The spectroscopic analysis of nanowire suspensions is not sufficient to understand the dynamics taking place in solution. For example, flocculates of nanowires in solution could scatter some of the incident light. Hence, time-resolved photography was carried in conjunction with the spectroscopic analysis to monitor for the presence of flocculates that may also influence the

absorbance intensity. A study was conducted on suspensions of selenium nanowires dispersed in different solvents to provide indirect knowledge about the surface chemistry of selenium nanowires, and the chemical and physical characteristics of the solvent required to keep the selenium nanowires well-dispersed and to remain in suspension without settling. A decrease in the absorbance intensity at 400 nm over time indicated the selenium nanowires were settling out of the solution. Through a correlation with results from the time-resolved photography analysis, we were able to determine that the selenium nanowires were settling out of some solutions as flocculates (Figure 3.4 – t = 60 min).

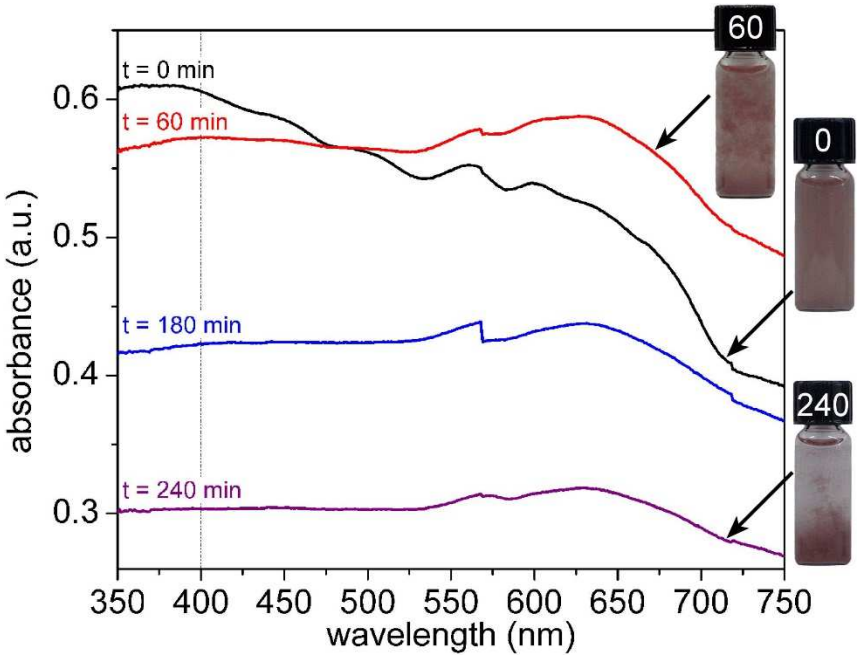

Figure 3.4. UV-visible absorption spectra of selenium nanowires suspended in a liquid medium at t = 0 (black), 60 (red), 180 (blue), and 240 min (purple), respectively. The images correspond to time-resolved photographs acquired at specified times in min, which are labelled on the cap of each vial. The dashed vertical line indicates the absorbance intensities at 400 nm that were used to create time-resolved plots of the settling process.

The hydrophobicity of the selenium nanowires was analyzed to determine an appropriate selection of solvents and surfactants for dispersion of the selenium nanowires. Surface chemistry of the selenium nanowires was first indirectly evaluated by monitoring dispersions of nanowires in ethanol solutions containing different amounts of water (Figure 3.5). The homogeneous red coloration of the pure ethanol solutions

suggested a uniform dispersion of the selenium nanowires. As the concentration of water increased in the ethanol, the selenium nanowires formed flocculates. These flocculates increased in size with increasing water content. The solutions eventually became colorless as the ethanol concentration decreased and the selenium nanowires collect at the bottom of the vials as a red sediment. Selenium nanowires also form flocculates in a solution of high ionic strength (Figure 3.5 – sat. brine) suggesting that the surfaces of selenium nanowires are non-ionic and are hydrophobic. In addition, a sample of as-synthesized selenium nanowires deposited on an Si/SiOx substrate has an average water contact angle of 116 ± 2°. These results suggest that the surfaces of the selenium nanowires are hydrophobic.

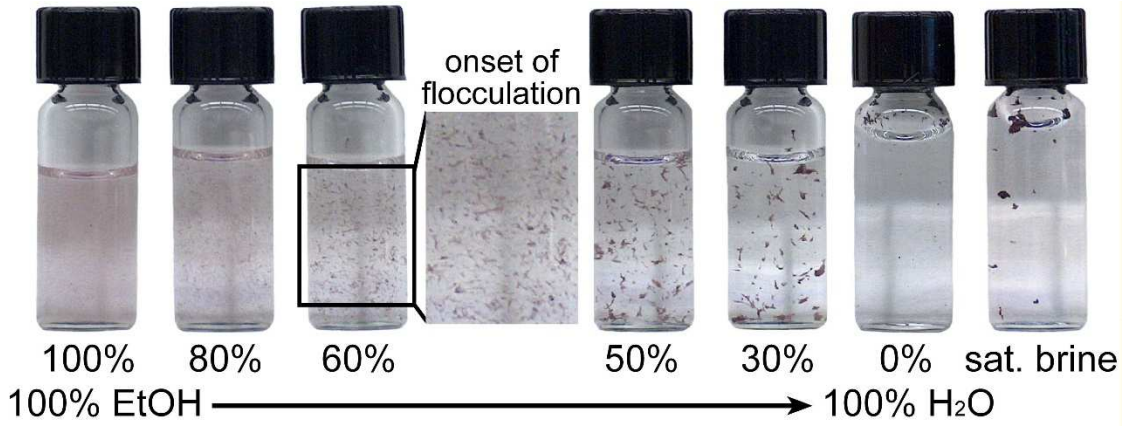

Figure 3.5 Photographs of selenium nanowires dispersed in ethanol solutions of increasing water content and in saturated brine (NaCl) solution. "Reprinted with permission from Cambridge publication."[87]

Further studies were performed to quantify the concentration of selenium nanowires in solution. Studies were conducted using between 40 and 70 µg of selenium nanowires per mL of solvent. The absorbance intensity at 400 nm for different concentrations of the selenium nanowires were monitored and these values used to approximate the suspended concentrations using the Beer-Lambert Law. Selenium nanowires were fragmented by sonication for a period of 10 min to create a more uniform dispersion of 1D selenium nanostructure for spectroscopy measurements. This sonication process fragmented the nanowires, increasing the accuracy of determining the concentration of selenium by the Beer-Lambert Law. Selenium nanowires synthesized from 2 mg of *a*-Se in 1 mL of *i*PA were further diluted with 1 mL *i*PA to make a stock solution that contains 1 mg of selenium nanowires per mL of *i*PA. The stock

solution was serially diluted to make 4, 10, 20, 30, 40, and 200 times more dilute. In comparison to high-aspect-ratio selenium nanowires, the fragmented selenium nanowires are uniformly dispersed in the solution. It is easier to partition aliquots of this dispersed sample that contain the same concentrations of 1D selenium nanostructures. Samples that were diluted more than 10 times and up to 200 times exhibited a linear relationship between the sample concentration and the sample absorption intensity at 400 nm (Figure 3.6). These results suggest that a linear correlation can be established between the absorbance and the concentration of dispersed nanowires, as long as these nanostructures are stabilized in solution.

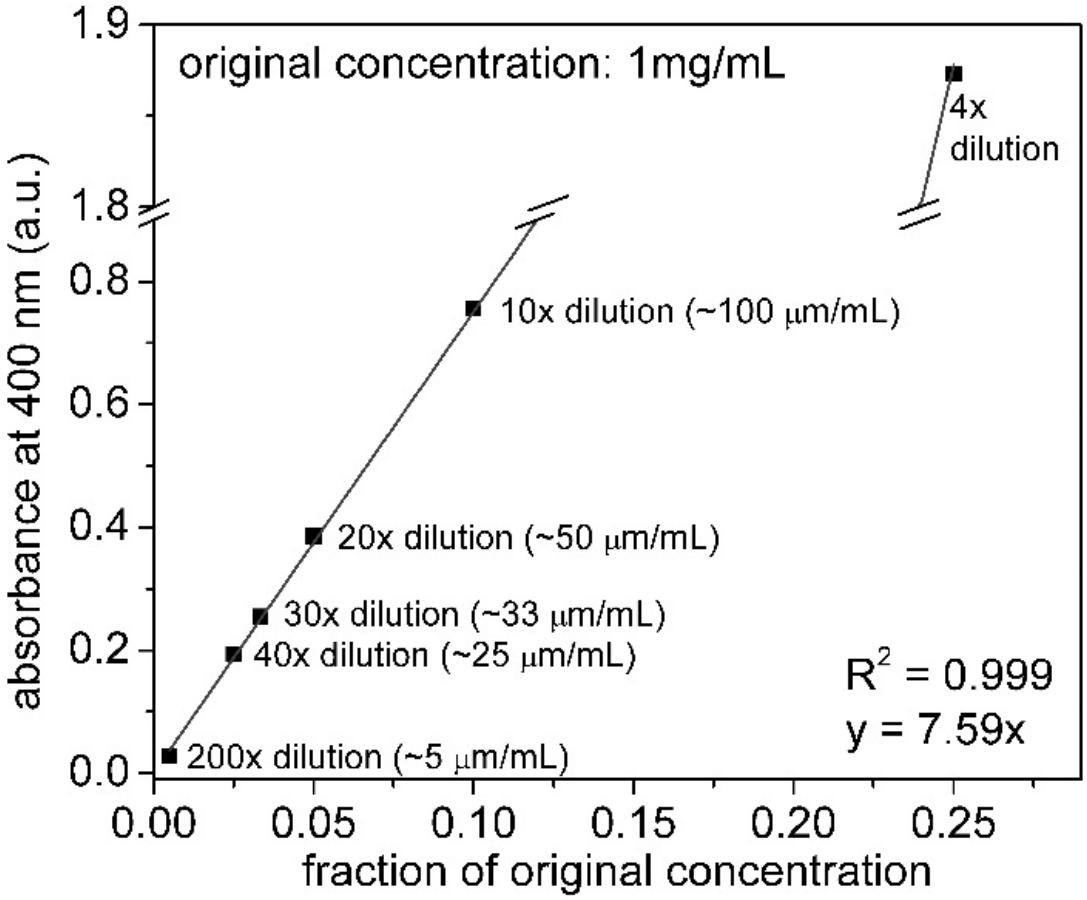

Figure 3.6 Beer-Lambert plot of fragmented selenium nanowires of different concentrations. These samples were made by serial dilution from a 1 mg/mL sample of selenium nanowires that had been sonicated for 10 min.

The ease of dispersing selenium nanowires in an absolute ethanol solution suggest that stable suspensions of nanowires can be formed in organic solvents. To

further evaluate the potential utility of organic solvents as dispersing media, these nanostructures were dispersed into a variety of organic solvents. We evaluated both polar protic and polar aprotic solvents. Low dielectric constant organic solvents are not analyzed in comparative study because dispersions of selenium nanowires in these solvents can readily assemble into macroscopic fibers in the presence of electrostatic fields.[88]

3.3.1. Monitoring the Colloidal Stability of Different Lengths of Selenium Nanowires

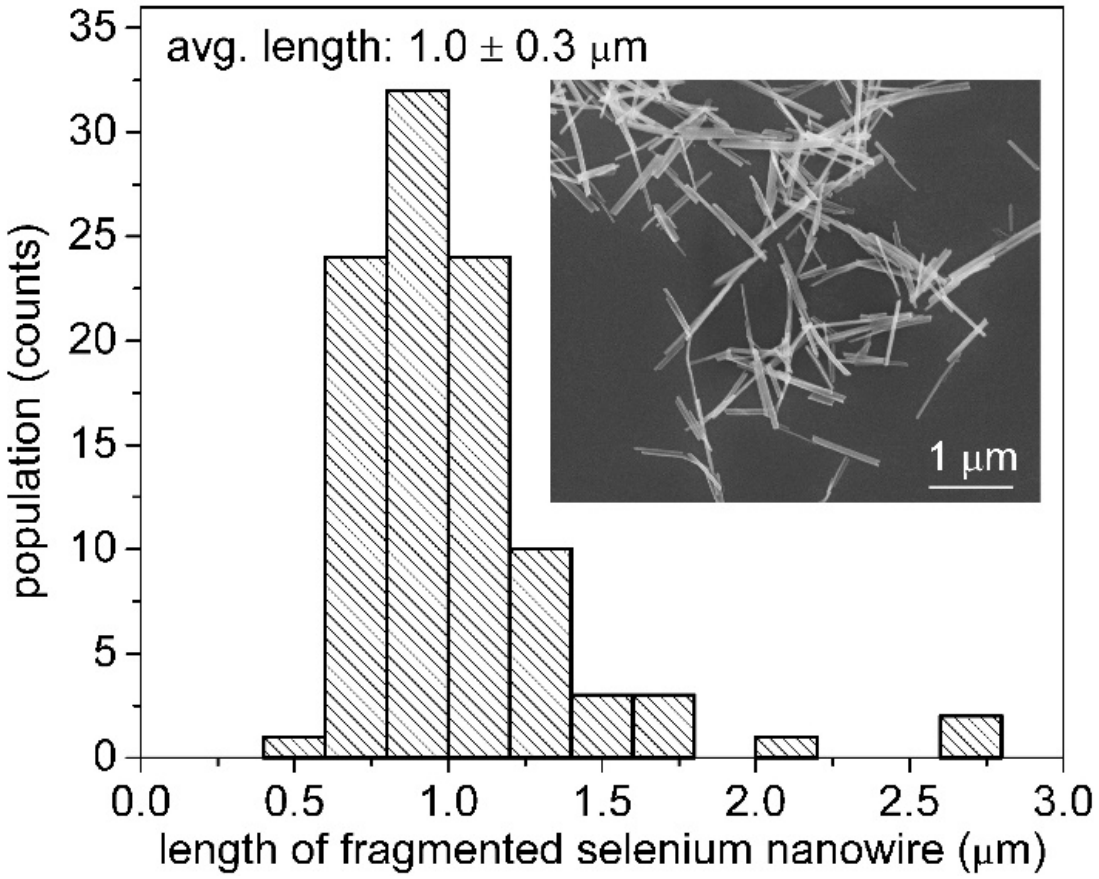

Figure 3.7 The length distribution of fragmented selenium nanowires that were produced by exposing the as-synthesized nanowires to sonication. Inset is a scanning electron micrograph of the fragmented selenium nanowires (i.e., nanorods).

As a control experiment, time-resolved spectroscopy was performed on different aspect-ratios of selenium nanowires. These nanowires were fragmented by exposing an

as-synthesized sample of selenium nanowires to 10 min of continuous sonication. This process reduced the length of nanowires to 1.0 ± 0.3 µm from an original length of 30 to 60 µm (Figure 3.7). We demonstrated that selenium nanowires with smaller aspect-ratios (i.e., nanorods) take longer to settle out of solution in comparison to those with higher aspect-ratios (Figure 3.8). The colloidal stability of selenium nanorods is ~9 times higher than the as-synthesized nanowires. Since there could be a significant variation in aspect-ratio of the selenium nanowires between different synthetic batches. It would be challenging to compare data acquired from selenium nanowires synthesized from different reactions. Hence, the colloidal stability studies performed herein are for selenium nanowires prepared from the same synthetic batch. These solutions of selenium nanowires were manually agitated to achieve uniform dispersions, and data collected subsequent to this period of gentle agitation were monitored for their stability over time (e.g., a non-agitated sample). As a visual reference, time-resolved photography was used to initially visualize the progression of selenium nanowires settling out of solution.

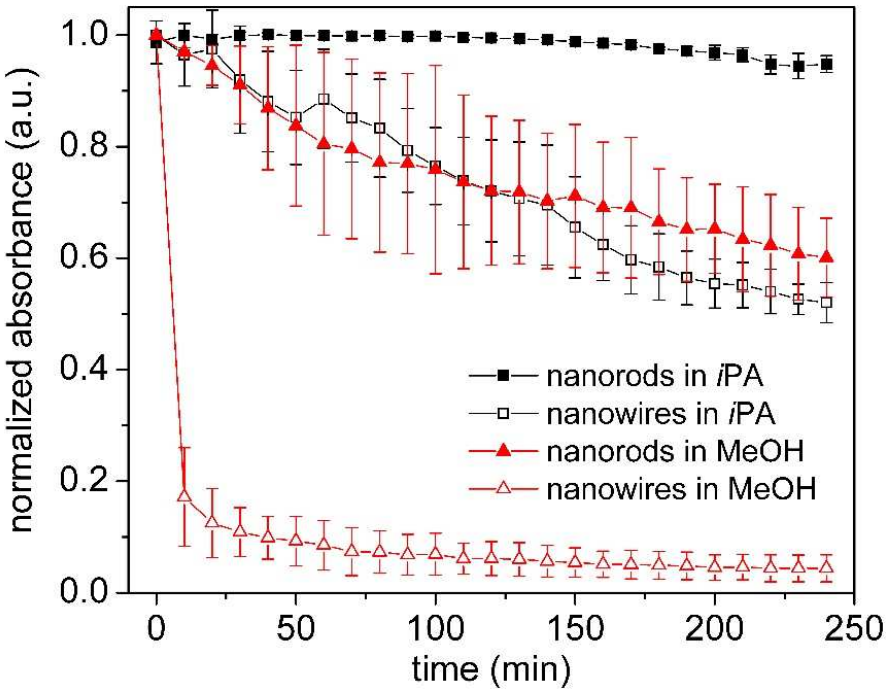

Figure 3.8 A settling study comparing selenium nanowires and selenium nanorods dispersed in isopropanol (iPA) and methanol (MeOH) over a period of 240 min.

3.3.2. Monitoring the Colloidal Stability of Selenium Nanowire Dispersions in Alcohols

Time-resolved photography of selenium nanowires revealed a time dependent evolution of settling and flocculation within the samples. The presence of flocculates were identified in methanol (MeOH) at t = 0 min, indicating that MeOH was unable to stabilize the selenium nanowires (Figure 3.9). These flocculates in MeOH quickly settled to the bottom of the vial in less than 10 min as observed by the clearing of the red coloration in the MeOH medium. There could be residual selenium nanowires suspended in solution, but the concentration of these nanowires was too low to be observable by the naked eye. In contrast, ethanol (EtOH), 2-propanol (*i*PA), 1-butanol (1-ButOH), and 1-octanol (1-OctOH) were able to uniformly disperse the selenium nanowires. Selenium nanowires dispersed in EtOH start to form flocculates at a later time (Figure 3.9 – ethanol; 20 min) in comparison to methanol. These destabilized flocculates settled to the bottom of the vial in a similar manner to the observed in MeOH, but over a longer duration of time. In addition, photographic evidence of increasing red intensity at the bottom of the vials prior to the formation of observable flocculates suggested that the selenium nanowires were settling out of the *i*PA, 1-ButOH, and 1-OctOH (Figure 3.9). We observed that flocculates formed in these three solutions after an initial delay during the settling process. The observed onset of flocculation at later times was correlated to the increasing chain length of the aliphatic alcohol. Flocculation was observed at 0 min for MeOH, 20 min for EtOH, 50 min for *i*PA, and 80 min for 1-ButOH, respectively, while selenium nanowires dispersed in 1-OctOH remained well-dispersed and were colloidally stable throughout the duration of the analysis (e.g., up to 240 min).

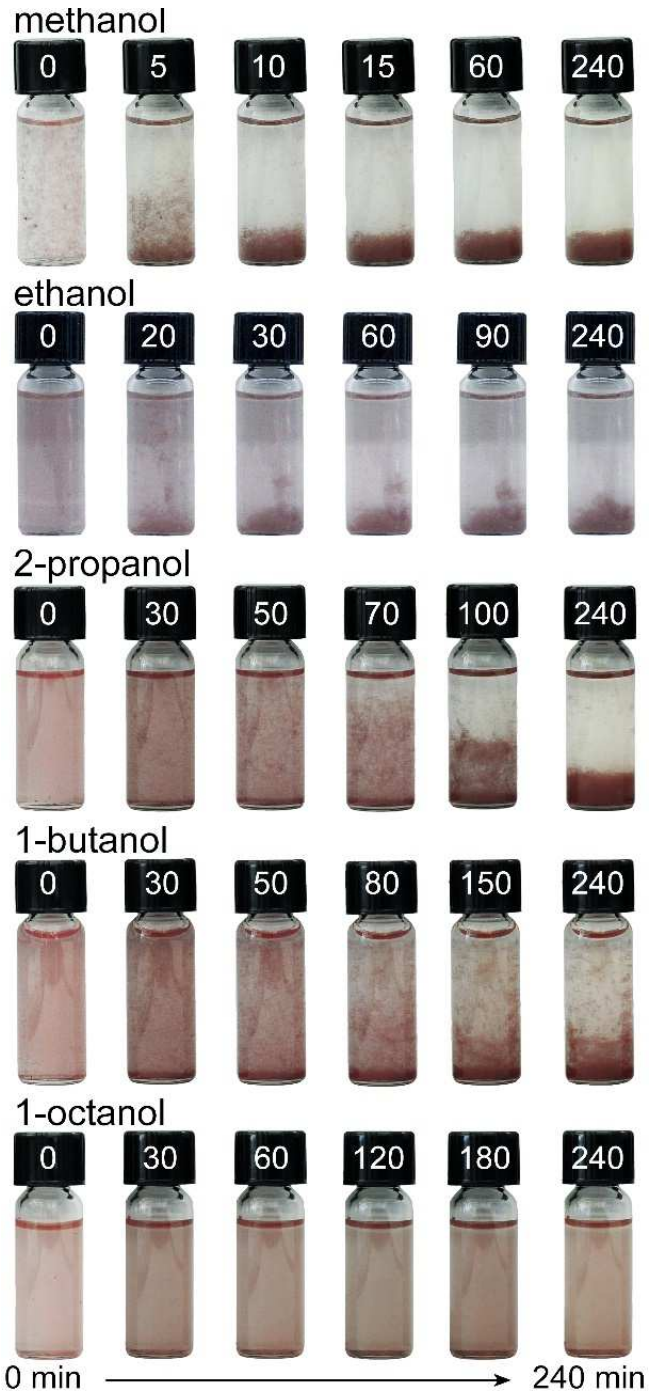

Figure 3.9. Time-resolved images of selenium nanowire dispersed in alcohol solutions, such as methanol, ethanol, 2-propanol, 1-butanol, and 1-octanol, respectively. The number labelled on the cap of each vial corresponds to time, in min, at which the photograph was taken.

For ease of comparison, the time-resolved spectral data for each sample of nanowires was normalized with respect to the absorbance at t = 0 min (1 min after

sample agitation). The results are plotted as an average of 3 separate experiments and the error bars reflect ± 1 standard deviation (Figure 3.10). We evaluated the colloidal stability of selenium nanowires for a series of aliphatic alcohols. In the absence of peptizing agent, these alcohols function as the dispersing medium as well as the stabilizers for the nanowires. Since selenium (ρ: 4.81 g/cm^3) has higher density then the alcohols (ρ: ~0.8 g/cm^3), gravitational forces will eventually lead to these nanowires settling out of solution. Suspensions of selenium nanowires settled out of the media at different rates. This difference is observed in the amount the selenium nanowires that settled out of the solution as determined by the amount of decrease in absorbance over a period 240 min (Figure 3.10). The sedimentation of nanowires is correlated to a gradual decrease in absorbance intensity at 400 nm. Differences observed between these results for aliphatic alcohols are attributed to the solvents interactions with the selenium and other solvent properties, such as viscosity and density (Table 3.1). Figure 3.10 confirmed that the colloidal stability of the nanowire dispersions increases with an increase in chain length of the alcohol (*i.e.*, in the order of increasing colloidal stability: methanol < ethanol < 2-propanol < 1-butanol < 1-octanol). In addition, the hydrocarbon chain length for these alcohols has a noticeable influence on each solvent's ability to achieve a uniform dispersion of the selenium nanowires. For example, the images (Figure 3.9 – methanol at 0 min) indicated that nanowires dispersed in methanol form small red flocculates in comparison to the relatively homogenously red solution of samples dispersed in other alcohols at t = 0 min.

Table 3.1 Density and Viscosity of Aliphatic Alcohols and Polar Aprotic Solvents

category	solvent	ρ (g/cm^3)	η (mPa·s)
aliphatic alcohol	methanol	0.79	0.55
	ethanol	0.79	0.28
	2-propanol	0.78	2.04
	1-butanol	0.81	2.95
	1-octanol	0.83	7.29
polar aprotic	chloroform	1.48	0.58
	dichloromethane	1.32	0.41
	acetone	0.78	0.31
	ethyl acetate	0.90	0.46

**abbreviations: ρ = density and η = viscosity*

The colloidal stability of the selenium nanowires in these aliphatic alcohols was reflected in the settling rate and mechanism of sedimentation for the nanowires. The rate

of change in intensity (or concentration of selenium) over time for MeOH (Figure 3.10 – ♦; solid diamond) is an exponential decay; the normalized absorbance value decreased sharply in the first 20 min of monitoring before leveling off. Selenium nanowires dispersed in EtOH (Figure 3.10 – ∆; open triangle), *i*PA (Figure 3.10 – ●; solid circle), 1-ButOH (Figure 3 – ○; open circle) and 1-OctOH (Figure 3.10 – ■; solid square) each exhibited a more linear decay in absorbance intensity, although at different settling rates, over the same period of time. The rate of decrease in absorbance intensity was translated into the amount of selenium (in weight) per min for ease of comparison. Both time-resolved photograph and spectroscopy suggested that 1-OctOH was the best alcohol (of those analyzed) to create a stable and uniformly dispersed solution of selenium nanowires. Selenium nanowires were settling from 1-OctOH at a rate of 0.009 µg of selenium per min (Se/min). We did, however, observe evidence for the formation of small amounts of flocculate, which was not observable in the time-resolved photography (Figure 3.9). The time-resolved spectroscopy data suggested flocculation of nanowires by the slight increase in absorbance value recorded at t = 180 min in Figure 3.10. Selenium nanowires dispersed in 1-ButOH was the second most stable dispersion with the nanowires settling out of the solution in 2 stages at rates of 0.17 and 0.2 µg Se/min, respectively. Nanowires dispersed in *i*PA and EtOH also exhibited 2 stages of nanowire sedimentation. In the first stage, selenium nanowires dispersed in *i*PA and EtOH settled at a higher rate of 0.32 and 0.54 µg of Se/min, respectively. The second phase of sedimentation rate was 1.5 and 5.5 times slower at rates of 0.2 and 0.1 µg Se/min for dispersions in *i*PA and EtOH, respectively. Both time-resolved spectroscopy and photography suggested that the selenium nanowires settled out of 1-ButOH, *i*PA and EtOH before observable flocculates became observable by eye. Selenium nanowires were unstable in MeOH (Figure 3.10) as documented by the sharp drop in the normalized absorbance intensity within the first 20 min. The nanowires settled from MeOH at a rate of 4.2 µg Se/min, which was significantly faster than when dispersed in the other alcohols. The rate of sedimentation in MeOH slowed to 0.21 and 0.005 µg Se/min in the time period between 20-80 min and 90-240 min, respectively. These observed slower sedimentation rates may correspond to the sedimentation of medium to short aspect-ratio selenium nanowires, since shorter aspect-ratio selenium nanowires are more colloidally stable than high-aspect-ratio selenium nanowires (Figure 3.8).

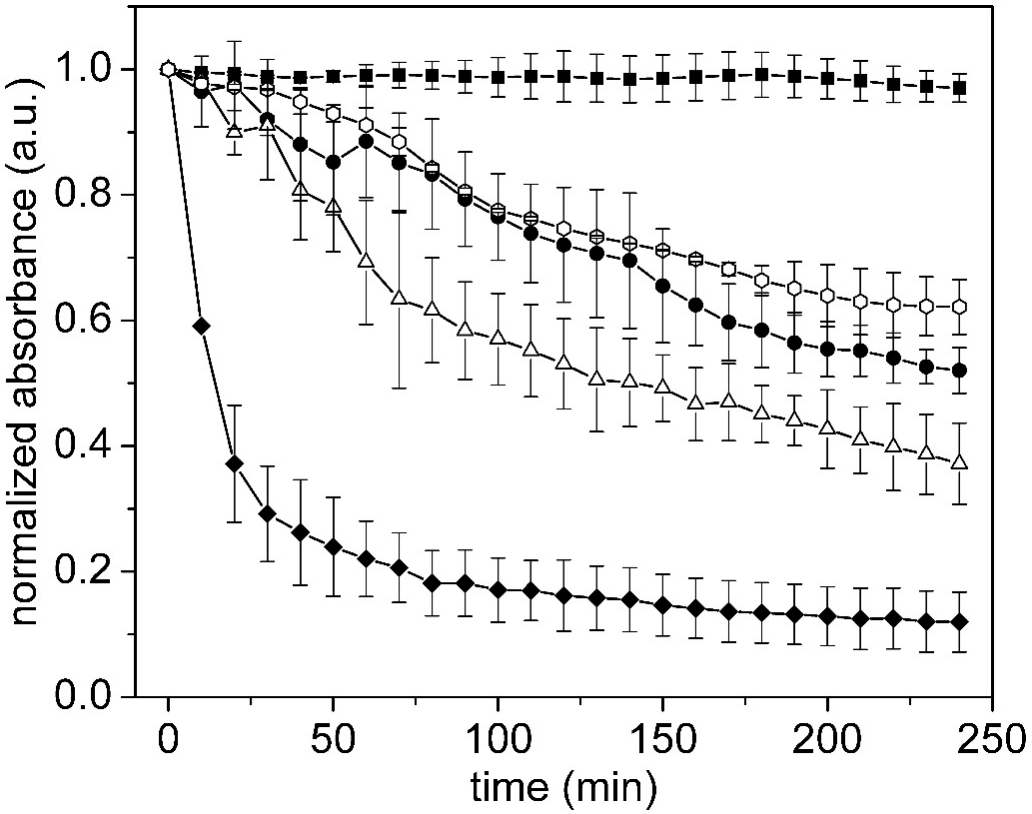

Figure 3.10. A measure of colloidal stability of selenium nanowire dispersions in a series of aliphatic alcohols was monitored as a function of change in absorbance at 400 nm over time using a UV-visible spectrometer. Selenium nanowires were suspended in 1-octanol (■; solid square), 1-butanol (○; open circle), 2-propanol (●; solid circle), ethanol (Δ; open triangle), and methanol (♦; solid diamond), respectively.

All alcohol dispersants, except 1-OctOH, exhibited sedimentation of selenium nanowires in 2 or 3 stages. A fast initial sedimentation rate was always followed by a slower rate of sedimentation. We hypothesize that this is due to the polydisperse length of selenium nanowires in the sample. A result of having a polydisperse length of selenium nanowires within a sample, the higher aspect-ratio selenium nanowires may settle at a higher rate in comparison to those of lower aspect-ratios.[87] Furthermore, sometimes higher absorbance values were observed in Figure 3.10 at later time points in comparison to the earlier time points. This phenomenon is observed around 40 min in EtOH, and ~60 min and ~160 min in *i*PA. We attribute the increase in absorbance values to the formation of flocculates of the selenium nanowires forming in the path of the transmitted light. The sedimentation rate of selenium nanowires dispersed in aliphatic alcohols are tabulated in (Table 3.2).

Table 3.2 Tabulated Sedimentation Rates in Aliphatic Alcohols.

	sedimentation rates (μg/min)*		
solvent	stage 1	stage 2	stage 3
1-octanol	0.009 (0-240 min)	N/A	N/A
1-butanol	0.17 (0-170 min)	0.20 (180-240 min)	N/A
2-propanol	0.32 (0-160 min)	0.20 (170-240 min)	N/A
ethanol	0.54 (0-140 min)	0.10 (150-240 min)	N/A
methanol	4.2 (0-20 min)	0.21 (30-80 min)	0.005 (90-240 min)

**sedimentation rates of specified time range in parentheses*

3.3.3. Monitoring the Colloidal Stability of Selenium Nanowire Dispersions in Polar Aprotic Solvents

Some chemical reactions, out of necessity, require polar aprotic solvents. For example, a polar aprotic solvent was used to increase both colloidal stability and the dielectric constant of reaction media to prevent electrostatic charge induced flocculation of selenium nanowires.[47] Time-resolved photography was used to provide a visual comparison, such as whether the dispersant was successful in uniformly dispersing the selenium nanowires. This photography series also provided further insight into how selenium nanowires were flocculating and settling out of the dispersing medium (Figure 3.11). Polar aprotic solvents, except chloroform and dichloromethane, were able to achieve uniform dispersions of the selenium nanowires. Small flocculates were observable in the chloroform and dichloromethane dispersions at t = 0 min. Through time-resolve photography we noticed that as these small flocculates started to settle to the bottom of the vials as they also grew in size. In the absence of obvious flocculates in the acetone dispersion selenium nanowires continued to settle out of solution as suggested by the increase in brick red intensity at the bottom of the vial. The nanowire sediment observed in acetone was compact in comparison the loosely packed collection of selenium nanowires found in other aliphatic alcohols and polar aprotic solvents. It took selenium nanowires dispersed in ethyl acetate a little longer to develop noticeable flocculates. The first evidence of formation of selenium nanowires flocculation in ethyl

acetate was detected at t = 10 min. These flocculates in ethyl acetate did not grow significantly in size before settling in comparison to selenium nanowire flocculates formed in chloroform and dichloromethane.

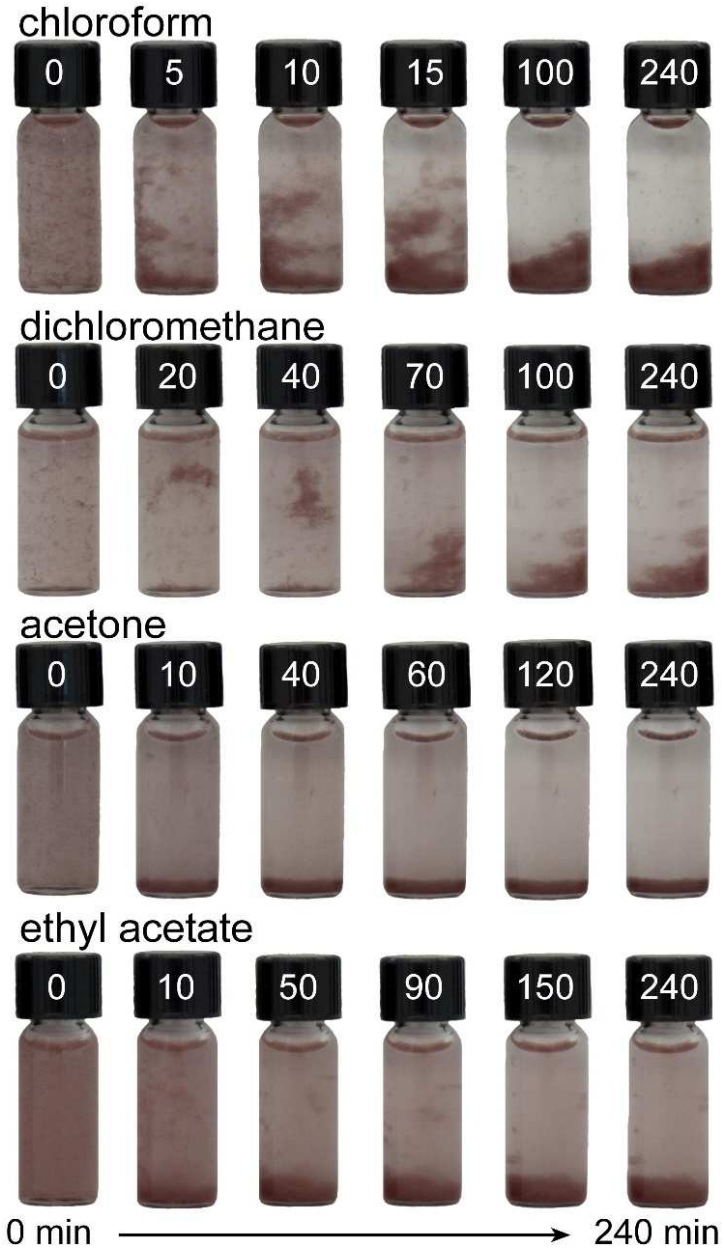

Figure 3.11 Time-resolved images of selenium nanowires dispersed in polar aprotic solvents: chloroform, dichloromethane, acetone, and ethyl acetate. The time, in min, at which each photograph was taken is labelled on the cap of each vial.

Time-resolved spectroscopy provided quantitative information that allowed a direct comparison of the colloidal stability of selenium nanowires in different polar aprotic solvents. We were able to determine that selenium nanowires have the best colloidal stability in ethyl acetate, followed by acetone, dichloromethane, and chloroform (Figure 3.12). This assessment was based on the amount of decrease in normalized absorbance intensity with respect to t = 0 min after 240 min of monitoring by UV-Vis spectroscopy. The normalized absorbance of selenium nanowire dispersions in chloroform decayed exponentially, which was a hallmark of colloid instability. The selenium nanowires settled out of chloroform in 2 stages. In the first stage, destabilized selenium nanowires, usually high-aspect-ratio nanowires, flocculated and quickly settled out of the medium at a rate of 2.5 µg Se/min. This assessment coincided with the trends observed by time-resolved photography (Figure 3.11 – chloroform). When most of the high-aspect-ratio nanowires had settled from the dispersant, the spectroscopic observations followed the settling of the remaining shorter aspect-ratio selenium nanowires. These shorter aspect-ratio selenium nanowires had a sedimentation rate of 0.07 µg Se/min. Selenium nanowires dispersed in dichloromethane indicated that the sedimentation occurred in 3 stages. In the first stage, there was a slow decrease in the absorption intensity at 400 nm with a sedimentation rate of 0.59 µg Se/min. It was evident from the time-resolved photography images (Figure 3.11 – dichloromethane) that during this period the selenium nanowires formed observable flocculates. If the flocculates were formed outside of the path of the transmitted light, we expected to observe a decrease in absorbance intensity at 400 nm. The formation of flocculates would cause a decrease in the surrounding nanowire concentration. The second stage of nanowire sedimentation was almost twice as fast as the rate observed in the first stage. Selenium nanowires settled at a speed of 0.96 µg Se/min. This accelerated decay rate can be correlated to the sedimentation of large flocculates of selenium nanowires. The last stage of nanowire sedimentation was attributed to the sedimentation of shorter aspect-ratio nanowires, which are more buoyant than the higher aspect-ratio nanowires (Figure 3.8). These shorter nanowires slowly settled out of the medium, at a rate of 0.14 µg Se/min, over time due to gravitational forces.

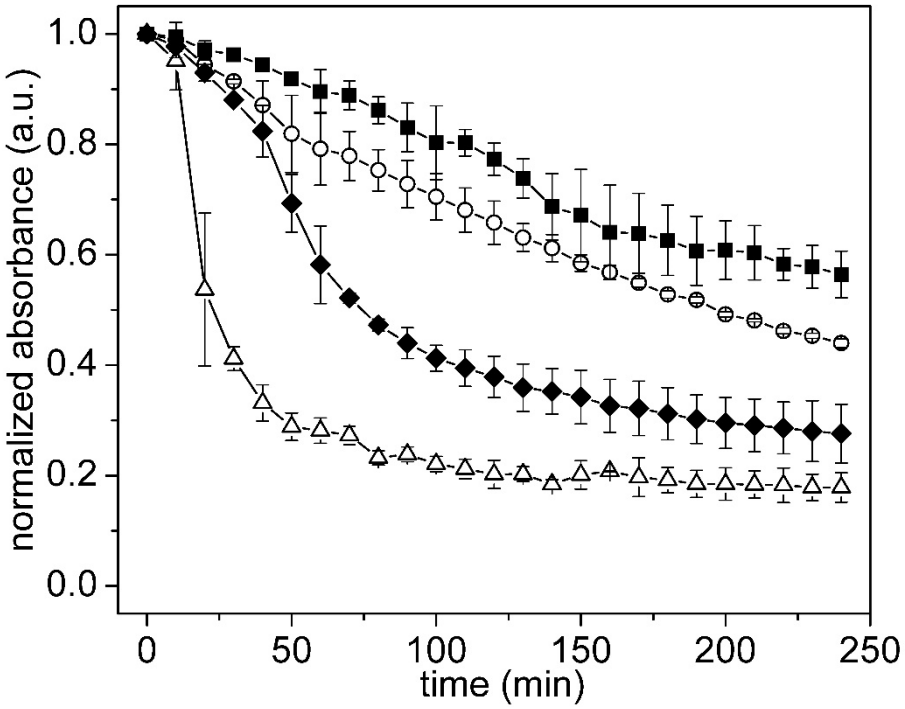

Figure 3.12. Colloidal stability of selenium nanowire dispersions in polar aprotic solvents were monitored as a function of change in absorbance at 400 nm over time using a UV-visible spectrometer. Selenium nanowires are suspended in ethyl acetate (■; solid square), acetone (○; open circle), dichloromethane (♦; solid diamond), and chloroform (Δ; open triangle), respectively. "Reprinted with permission from Cambridge publication."[87]

Sedimentation of selenium nanowire dispersions in acetone also had 3 distinct settling rates. The observed rates of sedimentation in acetone were 0.49, 0.29 and 0.17 µg Se/min between 0 to 60 min, 70 to 200 min and 210 to 240 min, respectively. These rates of sedimentation did not vary significantly in contrast to the variations observed in chloroform and dichloromethane. The selenium nanowires were relatively stable in acetone and settled out of solution largely due to gravitational forces acting on individual nanowires or very small flocculates. Time-resolved photography revealed the absence of large flocculates in the sample. The nanowires in acetone largely settled as individual nanowires forming compact layers at the bottom of the vial. We hypothesize that there were 3 different aspect-ratios of selenium nanowires in the medium. Therefore, we observed 3 separate sedimentation rates, which began with the sedimentation of the highest aspect-ratio nanowires and ended with sedimentation of the most buoyant shorter aspect-ratio nanowires. The trends observed for dispersion of nanowires in ethyl

acetate closely resembled those of the acetone sample. The sedimentation rate in ethyl acetate was, however, higher between 120 and 140 min at 0.57 µg Se/min relative to the initial and final sedimentation rates of 0.26 and 0.14 µg Se/min, respectively. This accelerated sedimentation rate between 120 and 140 min was attributed to formation and sedimentation of selenium nanowire flocculates. The sedimentation rate of selenium nanowires dispersed in polar aprotic solvents are tabulated in Table 3.3.

Table 3.3 Tabulated Sedimentation Rates in Polar Aprotic Solvents.

	sedimentation rates (µg/min)*		
solvent	stage 1	stage 2	stage 3
ethyl acetate	0.26 (0-110 min)	0.57 (120-140 min)	0.14 (150-240 min)
acetone	0.49 (0-60 min)	0.29 (70-200 min)	0.17 (210-240 min)
dichloromethane	0.59 (0-40 min)	0.96 (50-80 min)	0.14 (90-240 min)
chloroform	2.5 (0-40 min)	0.07 (50-240 min)	N/A

**sedimentation rates of specified time range in parentheses*

Both time-resolved spectroscopy and photography revealed that favorable interactions between the surfaces of selenium nanowires and the dispersing medium are key factors to achieve colloidal stability. The solvent's density and viscosity had a smaller influence on the colloidal stability. Instead a solvents' density and viscosity had a greater impact on the rate of sedimentation of the selenium nanowires or flocculates. Colloidal stability is determined by how well the solvent molecules adsorb onto the surfaces of selenium nanowires. These adsorbed solvent molecules on the surfaces of the selenium nanowires prevented the flocculation of these nanowires through steric stabilization (Figure 3.13a,b). Steric stabilization improved the colloidal stability of the selenium nanowires, and facilitated the formation of more uniform dispersions. For example, selenium nanowires dispersed in methanol, chloroform, and dichloromethane exhibited relatively fast sedimentation rates, because these solvents were unable to interact strong enough with the non-polar surfaces of individual selenium nanowires to prevent them from interacting with neighboring nanowires. Usually, these interacting nanowires form flocculates and settle out of solution. Solvents with longer hydrocarbon chains had sufficient van der Waals interactions with the surfaces of selenium nanowires to minimize nanowire-nanowire interactions (Figure 3.13c,d). These nanowires will,

however, eventually settle out of the dispersant due to gravitational forces. Density and viscosity of the alcohols and organic solvents studied in these experiments are listed in Table 3.1. Although alcohols have a similar density, their viscosity increases with increasing chain length of the aliphatic alcohol. The increased viscosity implies an impeded movement of the nanowires in the suspending medium. The selenium nanowires settle at a slower rate in a more viscous solvent, as indicated in Figure 3.10. Colloidal stability of the selenium nanowires is enhanced when the dispersing medium is composed of longer hydrocarbon chains and a higher viscosity.

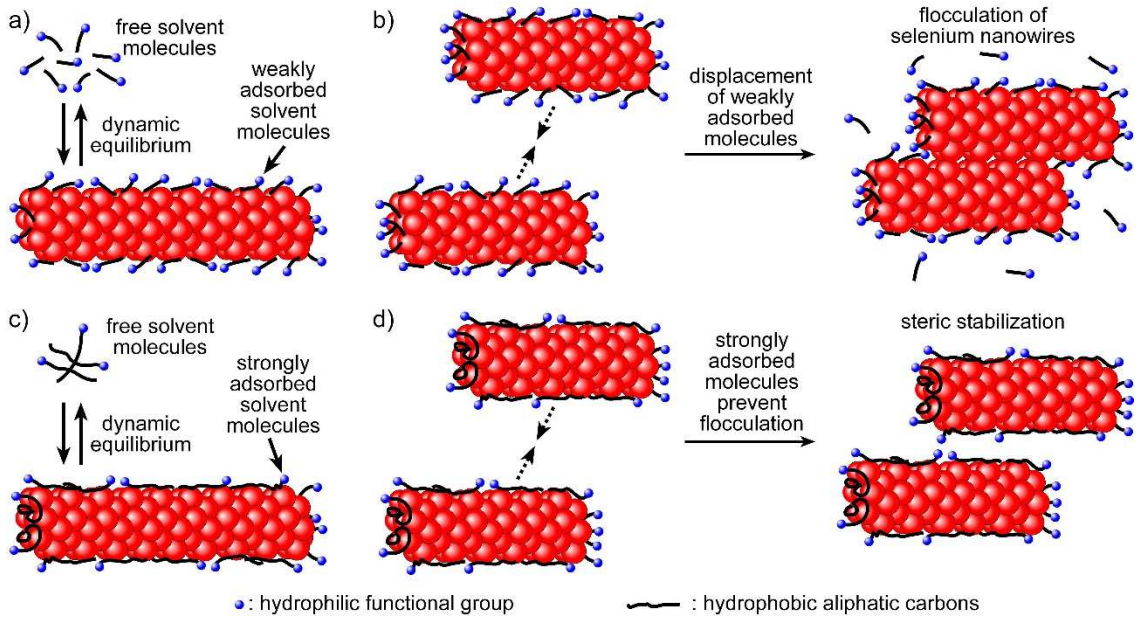

Figure 3.13 Schematics depicting (a,b) poorly and (c,d) well steric stabilized selenium nanowires.

3.3.4. Monitoring the Colloidal Stability of Polymer Assisted Selenium Nanowire Dispersions

A dispersing medium's physical properties, such as polarity, viscosity and density, are able to facilitate the formation of a uniform dispersion of selenium nanowires and to keep the nanowires from settling. The most important aspect of the dispersant is, however, its ability to form favorable interactions with the surfaces of selenium nanowires. Selenium nanowires produced from the same synthesis and dispersed in *i*PA and acetone exhibited similar sedimentation rates (Figure 3.10 and Figure 3.12). We hypothesize that *i*PA, despite being more viscous than acetone, does not interact

favorably with the surfaces of the selenium nanowires to provide sufficient steric stabilization. As a result, selenium nanowires dispersed in *i*PA are unstable and quickly form flocculates that settled at a faster rate than that for individual selenium nanowires. Solvent molecules that interact favorably with the surfaces of selenium nanowires are able to uniformly disperse the nanowires, and prevent the nanowires from forming flocculates that have accelerated sedimentation rates.

Figure 3.14 Photographs of (a) as-synthesized selenium nanowires that are heavily entangled. (b) Attempts for manual agitation to form a homogenous dispersion were unsuccessful. (c) After poly(vinylpyrrolidone) (PVP) was introduced to the sample, the aggregated selenium nanowires was successfully dispersed upon manual agitation, as indicated by the homogenous texture.

Colloidal stability of selenium nanowires in specific organic solvents is a function of the chemical structure and properties of each solvent. These solvents' properties can be augmented by introducing additives, such as polymers to enhance the nanowires' colloidal stability. Polymers can provide steric and/or electrostatic stabilizations, depending on their chemical constituents. A stabilizing agent such as poly(vinylpyrrolidone) (PVP), consists of a non-polar hydrocarbon backbone that would facilitate adsorption onto the hydrophobic surfaces of the selenium nanowires through non-covalent interactions. Selenium nanowires passivated with PVP would become hydrophilic because the protruding pyrrolidone groups along the hydrocarbon backbones are polar. The surface bound PVP molecules would be able to provide steric stabilization to selenium nanowires by increasing inter-nanowire distances, and decrease the chances of direct nanowire-nanowire interactions. Poly(vinylpyrrolidone) molecules are capable of dispersing entangled selenium nanowires. High-aspect-ratio selenium nanowires synthesized from sonochemically initiated route reported in the previous Chapter (e.g., 0.25 mg *a*-Se in 1 mL of abs. EtOH) form an entangled mesh (Figure

3.14a) that cannot be dispersed through manual agitation. The entangled cluster of selenium nanowires was separated into several smaller clusters upon manual agitation, but further agitation would not result in a uniformly dispersed sample (Figure 3.14b). The van der Waals between the selenium nanowires in these bundles were too great to be overcome by the shear forces produced during shaking. After PVP was added to this aggregated sample of selenium nanowires, the nanowires could be easily dispersed by manual agitation. The resulting dispersion produced a uniform color throughout the sample (Figure 3.14c). This study suggests that the PVP molecules facilitated the uniform dispersion of selenium nanowires by minimizing the inter-nanowire van der Waals interactions. We hypothesized that PVP molecules would adsorb onto the exposed surfaces of selenium nanowires, and between the selenium nanowires during agitation while the nanowires were separated briefly due to the applied shear forces. Excess PVP molecules quickly adsorb onto the exposed surfaces, thus separating the bundled selenium nanowires (Figure 3.15).

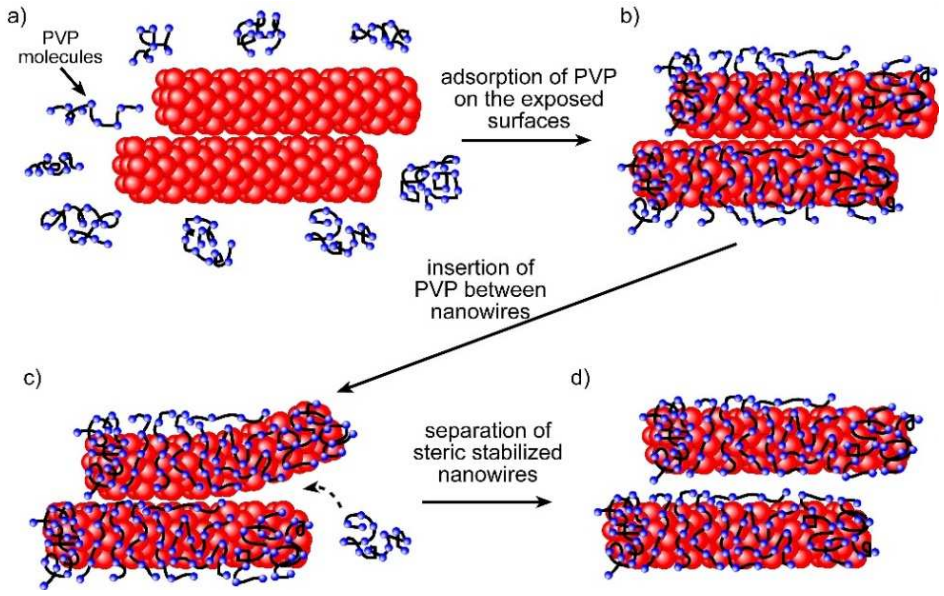

Figure 3.15 A proposed process of separating bundled selenium nanowires through the addition of PVP.

Addition of PVP also leads to an increase in the viscosity and density of these solvents resulting in a decrease in mobility of selenium nanowires in the dispersing media. These attributes effectively slow down the sedimentation rate of selenium nanowires. Three dispersions of selenium nanowires in EtOH, each sample containing a

different molecular weight of PVP stabilizer, were monitored by time-resolved spectroscopy. The molecular weight of the PVP molecules were 10.3k, 55k, and 360k, respectively. Each contained 10 mg of PVP per mL of EtOH. Literature reports have demonstrated that as the molecular weight of a polymer increases, the viscosity of the solvent containing the same weight fraction of polymer also increases.[89-90] Increased viscosity is a result of the increased interactions between polymer chains. Interactions such as van der Waals attractions and entanglements can lead to a decrease in the mobility of the dissolved polymer molecules. Herein, we will investigate the influence of polymer chain length (or molecular weight) on the colloidal stability of selenium nanowires.

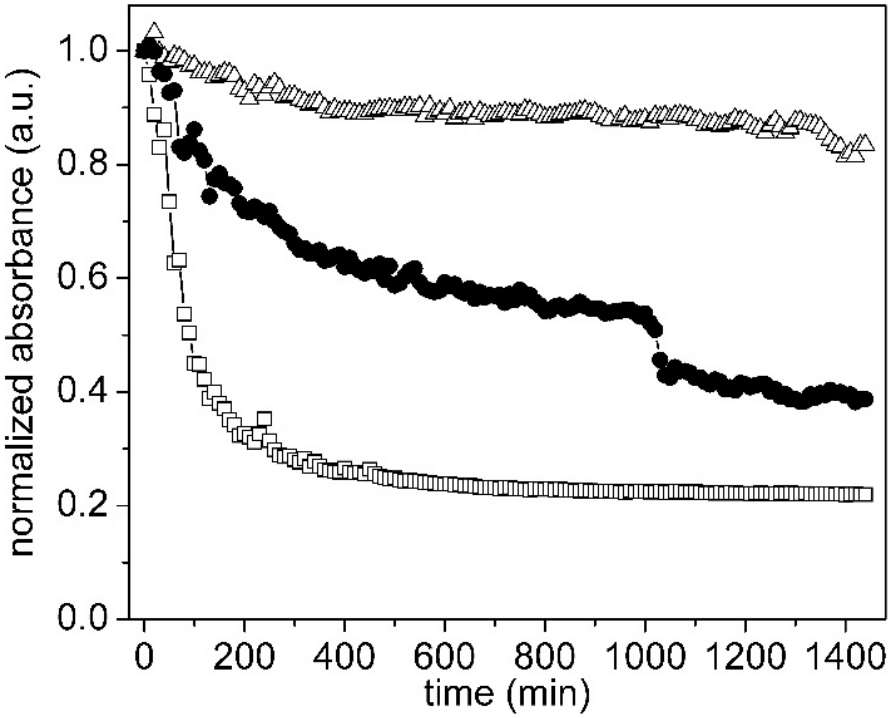

Figure 3.16. Suspensions of selenium nanowires in ethanol were stabilized by PVP of 3 different molecular weights. Their colloidal stability was monitored as a function of change in absorbance at 400 nm over time using a UV-visible spectrometer. Selenium nanowires are suspended in ethanol containing a concentration of 10 mg/mL of 360k PVP (Δ; open triangle), 55k PVP (●; solid circle), or 10.3k PVP (□; open square), respectively.

The colloidal stability of sterically stabilized selenium nanowires was monitored by a decay in absorbance intensity as a function of time for 3 different molecular weights

of PVP added to separate dispersions of selenium nanowires in ethanol. The molecular weight of these polymers were 10.3k, 55k, and 360k g/mol, or $PVP_{10.3k}$, PVP_{55k}, and PVP_{360k}, respectively. To examine the long term colloidal stability of the sterically stabilized selenium nanowires, we monitored the suspensions of nanowires over a period of 24 h (Figure 3.16). Selenium nanowires dispersed in EtOH containing the highest molecular weight PVP (i.e., PVP_{360k}) exhibited the best colloidal stability, followed by those nanowires sterically stabilized by PVP_{55k}. The selenium nanowires were least stable in the lowest molecular weight PVP (i.e., $PVP_{10.3k}$). Selenium nanowires stabilized by $PVP_{10.3k}$ were settling quickly over the first 150 min period of monitoring, losing ~70% of nanowires to colloidal instability. These nanowires settled out of solution in 3 stages. The fastest sedimentation rate was observed in the first stage at a rate of 0.59 µg Se/min. After the initial sedimentation, the rate of nanowire sedimentation slowed to 0.06 and 0.004 µg Se/min, respectively. Selenium nanowires dispersed in EtOH containing PVP_{55k} settled out of the dispersant in 4 stages, at rates of 0.15, 0.02, 0.34, and 0.02 µg Se/min, respectively. Higher aspect-ratio selenium nanowires were settling out of the solution during the first stage of sedimentation, leaving behind sterically stabilized medium and low aspect-ratio selenium nanowires. At approximately 1000 min into the spectroscopy study some of these medium aspect-ratio selenium nanowires formed into a flocculate that quickly settled out of the solution over a period of 40 min. The remaining ~40% of the selenium nanowires subsequently settled out of the solution due to gravitational forces. Over a period of 1440 min, only ~15% of the selenium nanowires settled out from the PVP_{360k} stabilized sample. Selenium nanowires dispersed in EtOH with PVP_{360k} settled out of the medium in 2 stages, at rates of 0.04 and 0.01 µg Se/min, respectively. A time-resolved spectroscopy analysis suggested that the highest molecular weight polymer, PVP_{360k}, was best at stabilizing selenium nanowires of any aspect-ratio. The PVP_{55k} was more suited to stabilizing the medium- to low-aspect-ratio nanowires, while $PVP_{10.3k}$ was ineffective at keeping the selenium nanowires of medium- to high-aspect-ratios in the dispersing medium. The sedimentation rate of selenium nanowires dispersed in EtOH containing different molecular weights of PVP is tabulated in Table 3.4.

Table 3.4 Tabulated Sedimentation Rates of Selenium Nanowires Stabilized by PVP

	sedimentation rates (μg/min)*			
polymer	stage 1	stage 2	stage 3	stage 4
PVP_{360k}	0.04 (0-420 min)	0.01 (430-1440 min)	N/A	N/A
PVP_{55k}	0.15 (0-310 min)	0.02 (320-1000 min)	0.34 (1010-1050 min)	0.02 (1060-1440 min)
$PVP_{10.3k}$	0.59 (0-130 min)	0.06 (140-360 min)	0.004 (370-1440 min)	N/A

**sedimentation rates of specified time range in parentheses*

Polymers with the appropriate functional groups can uniformly disperse the entangled, as-synthesized selenium nanowires. The colloidal stability of these nanowires can be further enhanced by choosing high molecular weight polymers. Each sample contained the same weight fraction of PVP, and the difference in observed colloidal stability is attributed to differences in the polymer's chain length. We hypothesize that the selenium nanowires exhibited an exceptional colloidal stability in 1-octanol because the alcohol molecules adsorbed onto the surfaces of selenium nanowires are difficult to displace and the solution has a high viscosity. Selenium nanowires steric stabilized by PVP of different chain lengths, which are much longer than the 1-octanol, should be able to adsorb more strongly on the nanowire's surfaces. These strongly adsorbed PVP molecules would effectively shield the selenium nanowires from approaching to close to each other by steric stabilization (Figure 3.15). The selenium nanowires' exceptional colloidal stability observed in the sample containing PVP_{360k} could be due to a combination of steric stabilization, as well as a higher solvent viscosity. The solution containing dissolved PVP_{360k}, had increased inter-polymer attractions and entanglements that made it the most viscous in comparison to solutions containing $PVP_{10.3k}$ and PVP_{55k}.[90] Hence, selenium nanowires settled out of the solution at a significantly slower rate when stabilized with PVP_{360k}. A time-resolved spectroscopy analysis suggested that the $PVP_{10.3k}$ was unable to stabilize both high- and medium-aspect-ratio selenium nanowires. The selenium nanowire's colloidal stability in EtOH (i.e., 0.54 μg Se/mL) or $PVP_{10.3k}$ assisted (i.e., 0.59 μg Se/mL) dispersions were similar, suggesting that $PVP_{10.3k}$ dissolved in EtOH does not increase the overall viscosity of the mixture in comparison to EtOH. In summary, shorter chain lengths of PVP, which

provided a similar degree of steric stabilization, were unable to keep the well-dispersed selenium nanowires in solution because their solution viscosities were lower in comparison to solutions containing the high molecular weight polymer.

3.3.5. Reaction at the Surfaces of Selenium Nanowires

To demonstrate the importance of achieving a well-dispersed sample of selenium nanowires, we explored the impact on using the selenium nanowires as a template and analyzing the uniformity of the product. Selenium nanowires dispersed in EtOH in the presence and in the absence of PVP were reacted with hexachloroplatinic acid (H_2PtCl_6).[71] Hexachloroplatinic acid readily reacts with the selenium nanowire templates (Eqn. 3.1-3.3) to yield platinum nanoparticles attached to the surfaces of the nanowires (Se@Pt-NP). The overall standard electrochemical cell potential of this reaction is positive, indicating that the reaction would be spontaneous. The reaction mixtures were refluxed for 12 h to increase the rate of diffusion of reagents for the reactions.

$$[PtCl_6]^{2-} + 4e^- \rightarrow Pt + 6Cl^- \qquad E^o = 1.435\ V \qquad \text{(Eqn. 3.1)}$$

$$Se + 3H_2O \rightarrow H_2SeO_3 + 4e^- + 4H^+ \qquad E^o = -0.74\ V \qquad \text{(Eqn. 3.2)}$$

$$Se + [PtCl_6]^{2-} + 3H_2O \rightarrow Pt + H_2SeO_3 + 6Cl^- + 4H^+ \qquad E^o_{cell} = 0.695\ V \qquad \text{(Eqn. 3.3)}$$

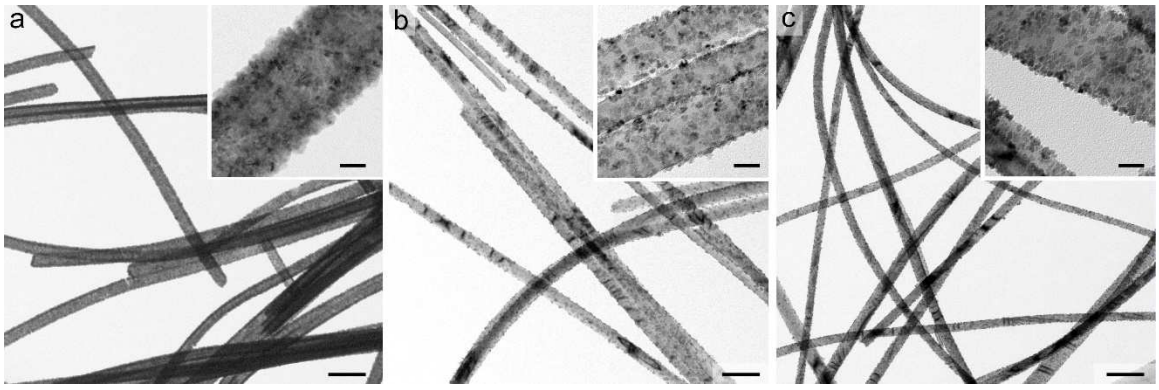

Figure 3.17 Transmission electron microscopy analysis of the electrochemical reactions between hexachloroplatinic acid and selenium nanowires dispersed in EtOH in the absence (a,b) and in the presence (c) of PVP. Scale bars are 200 nm and inset scale bars are 20 nm.

Since the platinum nanoparticles are tightly bound to the surfaces of the selenium nanowires, the observed density and uniformity of platinum nanoparticles on the surfaces of the selenium nanowires could be correlated with the exposure of the selenium to dissolved H_2PtCl_6. For ease of assessment, the concentration of selenium nanowires in the reaction was twice the concentration of H_2PtCl_6. A reaction that consisted of well-dispersed selenium nanowires should yield lightly decorated Se@Pt-NP nanostructures and the platinum nanoparticle density should be similar between different nanowires. Electron microscopy analysis revealed that the reaction carried out in the absence of PVP lacked uniformity in the resulting nanostructures. The product comprised of a mixture of hollow Pt nanoshells (Figure 3.17a) and Se@Pt-NP (Figure 3.17b). The electron microscopy analysis suggested that the aggregated selenium nanowires had non-uniform exposure to the platinum precursor. Selenium nanowires on the surfaces of the aggregates had access to more of the H_2PtCl_6 than those nanowires deep within the core of the aggregates (Figure 3.2). Selenium nanowires, which were exposed to an excess of H_2PtCl_6, were completely consumed by the electrochemical process, producing hollow Pt shells instead of selenium nanowires decorated with platinum nanoparticles. In order to uniformly transform or convert selenium nanowires to its corresponding selenium nanostructures decorated with metal nanoparticles, a reaction was performed in the presence of PVP. The addition of PVP facilitated the dispersion of the entangled selenium nanowires, and produced Se@Pt-NP decorated with similar densities throughout the reaction mixture (Figure 3.17c).

3.3.6. Monitoring the Colloidal Stability of Polymer and Surfactant Assisted Dispersions of Selenium Nanowire inWater

Selenium nanowires are hydrophobic (Figure 3.5). They have a tendency to flocculate in either an aqueous medium or solvents that have a high water content. This limits the techniques available to handle, process, and manipulate these nanowires. Typically, surfactants are used to disperse hydrophobic materials in aqueous solutions. A surfactant is an amphiphilic molecule that consists of a hydrophilic head group and a hydrophobic tail group. The use of surfactants could shield, or minimize, the unfavorable interactions between the hydrophobic surfaces of the selenium nanowires and water molecules. We hypothesize that the hydrophobic component of the surfactant molecules

would preferentially adsorb onto the surfaces of the selenium nanowires. The hydrophilic functionality of the surfactants would remain in the aqueous environment, screening the hydrophobic surfaces from interaction with the water molecules (Figure 3.18). In addition, the adsorbed surfactant molecules would prevent flocculation of the selenium nanowires through steric stabilization in a similar fashion as described in Figure 3.15. In order to uniformly transform or convert selenium nanowires into its corresponding metal selenide nanostructures, the sample must be uniformly dispersed in the aqueous media. Performing template-engaged transformation of selenium nanowires could be extended to other metal selenides through reaction in aqueous media, such as to form silver selenides.[34, 91]

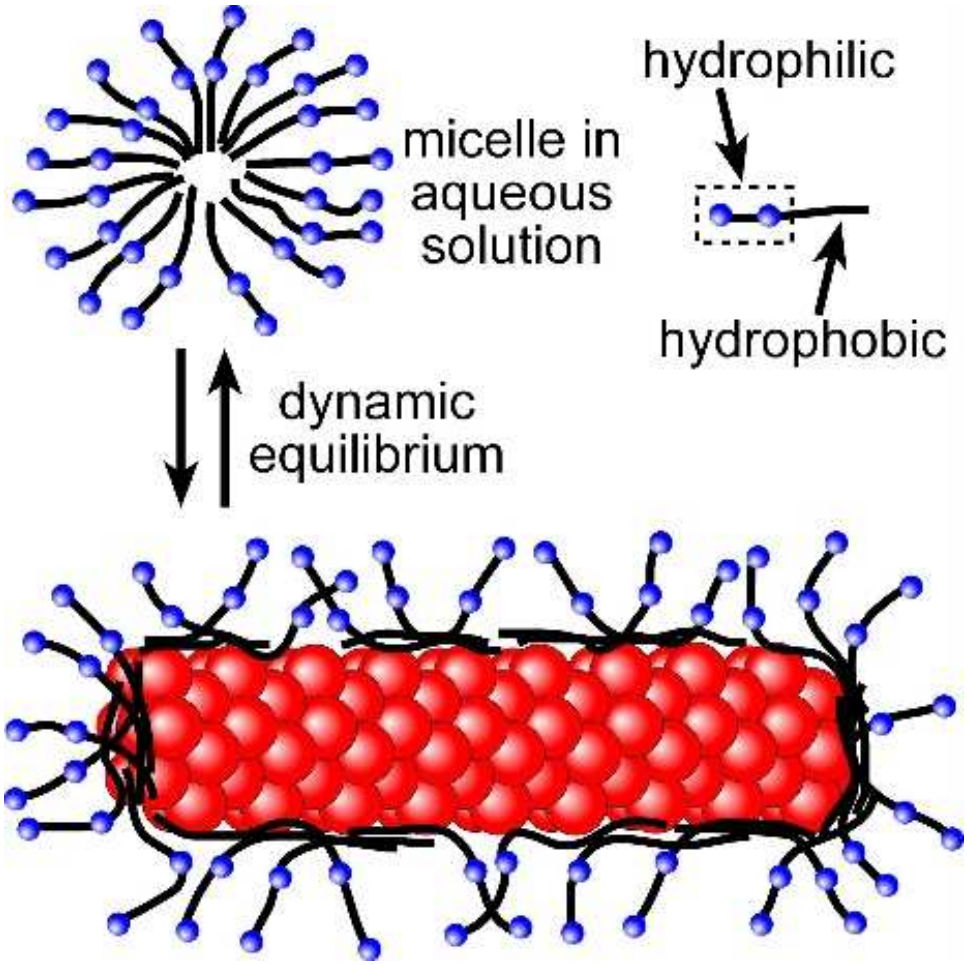

Figure 3.18 Depiction of the proposed interactions between surfactant molecules and the surfaces of selenium nanowires in aqueous solutions.

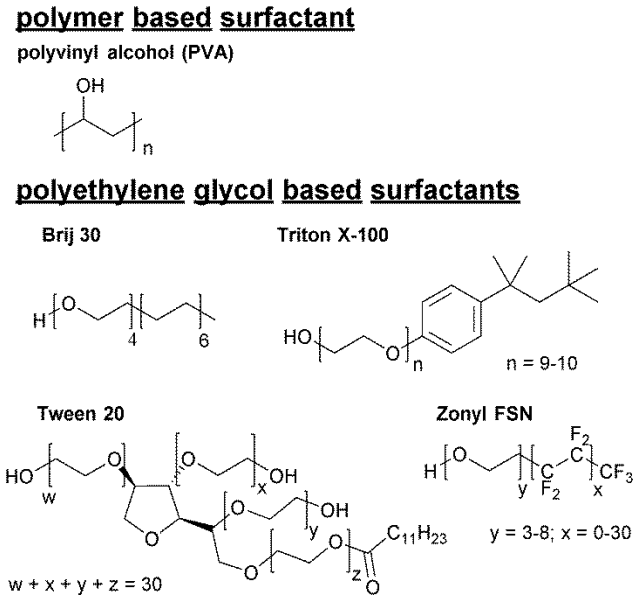

Figure 3.19 Chemical structures of polyvinyl alcohol and polyethylene glycol based surfactants used to disperse selenium nanowires in aqueous solutions.

We examined both polyvinyl alcohol and polyethylene glycol based surfactants for dispersing and stabilizing selenium nanowires in aqueous solutions (Figure 3.19). Time-resolved photography (Figure 3.20) studies revealed that these surfactants were able to assist in the uniform dispersion of selenium nanowires in aqueous solutions. The aqueous solutions contained either 0.1% (w/w) PVA, or 10 ppm (v/v) of the polyethylene glycol based surfactants. A low concentration of surfactants was used to avoid the formation of micelles, which would interfere with the time-resolved photography and spectroscopy analyses. The homogenous red colored solutions observed at t = 0 min is a hallmark of well-dispersed selenium nanowires. Interestingly, all surfactant stabilized selenium nanowires dispersed in aqueous solutions did not form observable flocculates over the 240 min. The red coloration of the sample of selenium nanowires stabilized by polyvinyl alcohol (PVA) did not change noticeably over the 240 min. This suggests that the colloidal stability of PVA stabilized selenium nanowires is maintained for more than 240 min. In contrast, color gradients were observed at the menisci of the other solutions (e.g., containing Brij 30, TWEEN 20, Triton X-100, or Zonyl FSN) as the selenium nanowires settled out of the media. For those nanowires that eventually settled out of the solutions, they form a compact layer at the bottom of the vials (i.e., Figure 3.20 – Triton X-100 and Zonyl FSN at 240 min).

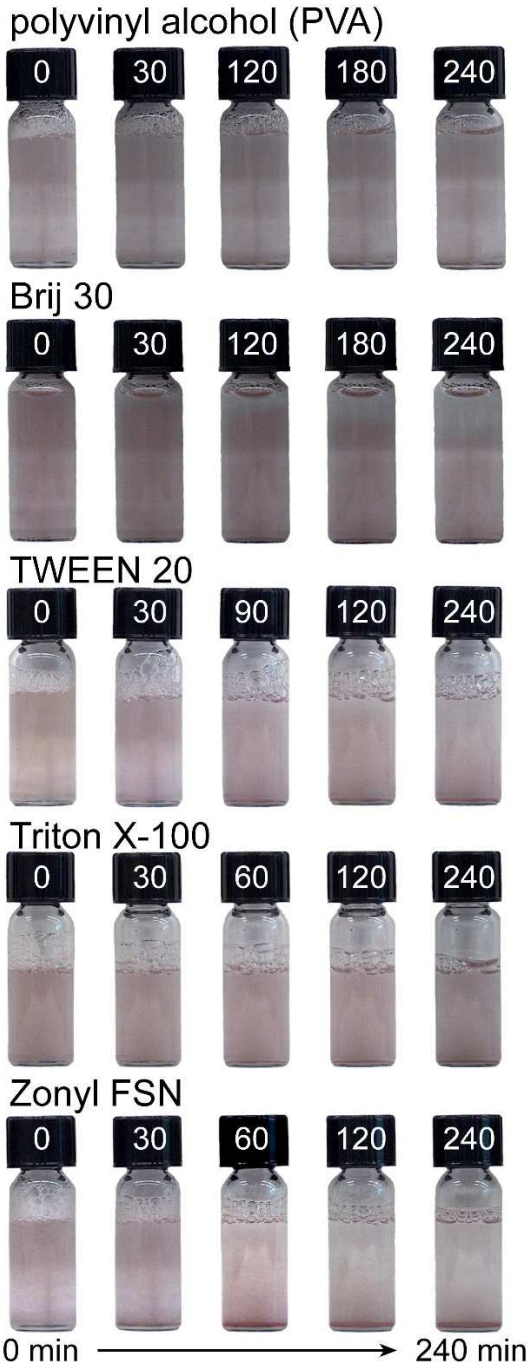

Figure 3.20 Time-resolved photography images of surfactant stabilized selenium nanowires dispersed in aqueous solutions containing PVA, Brij 30, TWEEN 20, Triton X-100, or Zonyl FSN. The time, in min, at which each photograph was taken is labelled on the cap of each vial.

Further verification by time-resolved spectroscopy also supported the observation that the selenium nanowires stabilized by PVA had a colloidal stability for

periods of time greater than 240 min (Figure 3.21 – ■; solid square). Only ~3% of the selenium nanowires settled from the solution after 4 h of monitoring. We noticed that there was an increase in the normalized absorbance intensity at ~30 min into the time-resolved spectroscopy study. We believed that microscopic flocculates were formed during this period because we did not observe the presence of selenium nanowire clusters in the time-resolved photography study (Figure 3.20 – PVA). These microscopic flocculates did not settle out of the solution at a high rate as would normally occur for flocculates of selenium nanowires suspended in organic media. After the formation of flocculates, the nanowires settled in 2 stages, at rates of 0.06 and 0.01 µg Se/mL. Polyethylene glycol based surfactants Brij 30 and TWEEN 20 shared similar trends in the time-resolved spectroscopy study (Figure 3.21 – ○&Δ; open circle and triangle, respectively). These solutions of selenium nanowire also had initial increases in their absorbance intensities before the nanowires started to settle out of the solution. This observed phenomenon suggested that the selenium nanowires were flocculating in the path of the incident light. Once, again these flocculates were microscopic because we were unable to see them in the photographs (Figure 3.20 – Brij 30 and TWEEN 20). The flocculates formed in the Brij 30 and TWEEN 20 solutions were settling from the solution at a rate of 0.07 µg Se/mL. Interestingly, the sample dispersed in solution containing Brij 30 formed further flocculates, which was correlated to another increase in the absorbance intensity between 80 and 120 min in the time-resolved spectroscopy analysis. Following the second flocculation, the selenium nanowires started to settle 3 times faster than the first sedimentation rate. This signifies that the Brij 30 was unable to stabilize these flocculates against the gravitational forces. Selenium nanowires dispersed in solution containing TWEEN 20 did not have a second increase in the absorbance intensity. Instead, the rate of sedimentation steadily increased for these nanowires to 0.19 µg Se/mL, suggesting that the flocculates were settling out of the solution.

Dispersions of selenium nanowires stabilized by Triton X-100 or Zonyl FSN settled out of the solution in 2 stages (Figure 3.21 – ●&♦; solid circle and diamond, respectively). Nanowires stabilized by Triton X-100 settled from the solution at rates of 0.14 and 0.80 µg Se/mL, respectively. The Zonyl FSN stabilized nanowires settled at rates of 0.33 and 0.11 µg Se/mL, respectively. Higher rates of sedimentation were

observed in the first stage for both the Triton X-100 and Zonyl FSN stabilized sample, indicating that the high-aspect-ratio nanowires were possibly the first to settle out of the solutions. The more buoyant lower aspect-ratio selenium nanowires subsequently settled out of the solutions due to gravitational forces. The sedimentation rate of selenium nanowires dispersed in aqueous solutions containing surfactants are tabulated in Table 3.5.

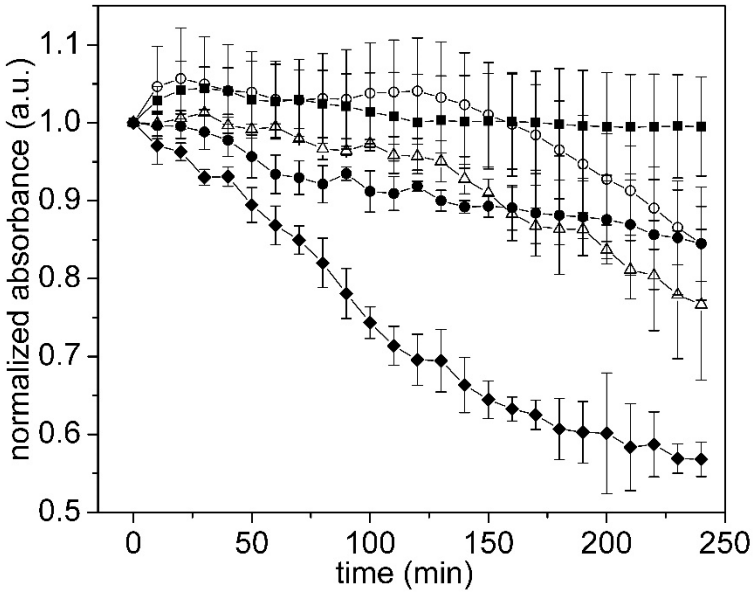

Figure 3.21 Surfactant and polymer assisted dispersion of selenium nanowires as monitored over time by UV-visible spectroscopy. Selenium nanowires are dispersed in aqueous solution containing 0.1% (w/v) of PVA – polyvinyl alcohol (■; solid square), 10 ppm (v/v) of Brij 30 (○; open circle), 10 ppm (v/v) of Triton X-100 (●; solid circle), 10 ppm (v/v) of TWEEN 20 (△; open triangle), and 10 ppm (v/v) Zonyl FSN – fluorosurfactant (♦; solid diamond), respectively. Their corresponding molecular structures are shown in Figure 3.19.

The addition of PVA has achieved superior stabilization of nanowires in comparison to other amphiphilic surfactants that contain long hydrophobic and hydrophilic chains (Figure 3.19 and Figure 3.21). The PVA polymer imparted a greater stability to the nanowires than dispersions in organic solvents or aqueous solutions containing small surfactant molecules. We attribute the improved nanowire stabilization in aqueous solutions by PVA to the increased viscosity of the solution due to multiple and regular interactions of each polymer with the surfaces of selenium nanowires and the surrounding non-adsorbed polymer molecules. Selenium nanowire dispersions in

polyethylene glycol based surfactants, such as Brij 30, Triton X-100, and TWEEN 20 all exhibited a similar colloidal stability (Figure 3.21). It is difficult to assess which of the 3 samples has the greatest colloidal stability because their data points at t = 240 min lie within 1 standard deviation of normalized absorbance intensity from each other. We attributed the similarity in colloidal stability of these samples to the chemical structures of these surfactants. These three surfactants each have an aliphatic hydrocarbon tail and long polyethylene glycol chain(s). Interestingly, Zonyl FSN was unable to stabilize the selenium nanowire dispersions in comparison to non-fluorosurfactants. We believed that this anomaly could be attributed to the unique chemical structure of Zonyl FSN with a polyethylene glycol chain and a fluorinated carbon chain (Figure 3.19). We hypothesize that the surfaces of selenium nanowires were unable to interact favorably with the fluorinated carbon chain of Zonyl FSN. This study indicated that the length and the amount of branching of the aliphatic hydrocarbon or the length of polyethylene glycol chains are not of great importance to the colloidal stability of the selenium nanowires. Surfactants with a relatively short hydrophobic tail, such as Triton X-100 (8 carbons, including aromatic carbons; Figure 3.19), was sufficient to interact with the surfaces of selenium nanowires to provide steric stabilization. Colloidal stability of selenium nanowires in different solvent environments could be further improved by the addition of surfactants and polymers containing the appropriate functional groups.

Table 3.5 Tabulated Sedimentation Rates in Surfactant Stabilized Selenium Nanowires in Aqueous Solutions

	sedimentation rates (μg/min)*	
solvent	stage 1	stage 2
polyvinyl alcohol (PVA)	0.06 (30-130 min)	0.01 (140-240 min)
Brij 30	0.07 (20-70 min)	0.21 (130-240 min)
Triton X-100	0.14 (0-60 min)	0.80 (70-240 min)
TWEEN 20	0.07 (0-120 min)	0.19 (130-240 min)
Zonyl FSN	0.33 (0-150 min)	0.11 (160-240 min)

**sedimentation rates of specified time range in parentheses*

3.4. Conclusions

In summary, we have systematically examined the colloidal stability of selenium nanowires in a variety of organic and aqueous media. We determined that selenium nanowires with smaller aspect-ratios take longer to settle out of solution in comparison to those with higher aspect-ratios. In an attempt to account for sample variability, such as a variation in aspect-ratios that could contribute differences in the colloidal stability of selenium nanowires, time-resolved photography and spectroscopy analyses were acquired for all solutions. In addition the selenium nanowires used in these studies were from the same synthetic batch. We have identified that organic solvents comprised of long aliphatic hydrocarbons are able to uniformly disperse the selenium nanowires, while providing viscous environments capable of suspending the nanowires for long periods of time. Favorable interactions between the nanowires and the dispersing media was one of the key factors to obtain homogenous dispersions of selenium nanowires, while solvents that are viscous and that interact favorably with the surfaces of selenium nanowires produced samples with the highest colloidal stability. The colloidal stability of the nanowires could also be enhanced through the addition of surfactants or polymers to provide steric stabilization. In addition, surfactants and polymers were used to facilitate dispersion of selenium nanowires in aqueous solutions. We have also demonstrated that uniformity of Se@Pt nanostructures prepared from selenium templates is directly influenced by how well the selenium nanowires are dispersed in solution. Performing the reaction with a poorly dispersed sample of selenium nanowires leads to the formation of non-uniform and undesired products, such as hollow Pt nanoshells instead of platinum decorated selenium nanowires.

3.5. Future Directions in Dispersing Selenium Nanowires in Solution

One of the possible ways to enhance the colloidal stability of selenium nanowires dispersed in aqueous environments, would be to coat them with charged surfactant molecules. For instance, selenium nanowires can be coated with charged amphiphilic molecules, such as sodium dodecyl sulfate (SDS) or cetyl trimethylammonium bromide (CTAB) (Figure 3.22). These surfactants, or a mixture of surfactants, may further

improve the colloidal stability and dispersibility of the selenium nanowires through electrostatic stabilization. In addition, the incorporation of specific charges at or near the surface of the nanowires when dispersed in aqueous solutions will be important for further work on the assembly and processing of individual nanowires.

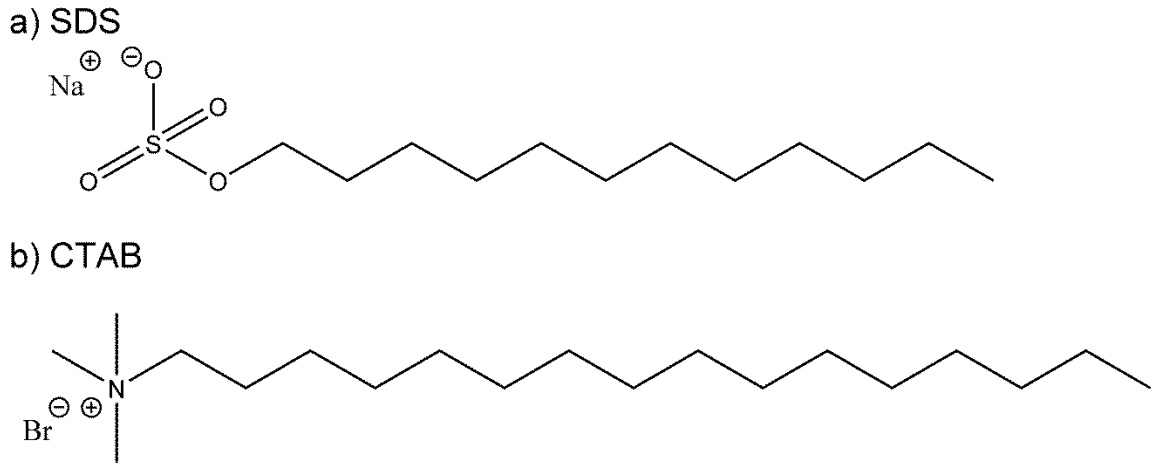

Figure 3.22 Chemical structures of (a) negatively and (b) positively charged surfactants.

4. Electrokinetic Assembly of Selenium and Silver Nanowires into Macroscopic Fibers†

4.1. Introduction to Assembly of Metal and Semiconductor Nanowires

Synthetic techniques can produce nanostructures with a diverse set of shapes and an equally diverse range of dimensions and compositions.[18, 92-98] Harnessing these materials for their nanoscale properties requires the ability to handle and manipulate the materials. Although much attention has been given to the manipulation of many nanoscale materials,[22, 99-107] some structures have received relatively little attention. One type of structure that requires further development of techniques for their assembly are solution-phase synthesized nanowires.[21] Some attention has been given to the assembly of carbon nanotubes, another highly anisotropic nanostructure. These nanotubes can be assembled during or after synthesis.[108-112] One lesson to learn from the previous work on manipulating nanoscale materials is the importance of developing techniques that can be appropriately scaled in order to assemble nanostructures in parallel for a range of concentrations. The challenge is to extend this concept to nanowires that require solution-based techniques for manipulation. Our goal is to develop appropriate

† Synthesis of selenium nanowires and electrokinetic assembly both selenium and silver nanowires were carried out by Michael C. P. Wang. Michael C. P. Wang, also, performed all the microscopy, spectroscopy, and powder diffraction analyses. Dr. Xin Zhang measured the IV responses of fibers of selenium. Elham Majidi synthesized the silver nanowires and modified their surfaces with 1-dodecanethiol. Kevin Nedelec performed electric field simulations by COMSOL using finite element method. The "Electrokinetic Assembly of Selenium and Silver Nanowires into Macroscopic Fibers" manuscript was co-written by Michael C. P. Wang and Professor Byron D. Gates. "Reprinted Journal Article with permission from Electrostatic Assembly of Selenium and Silver Nanowires into Macroscopic Fibers," Wang, M. C. P.; Majidi, E.; Gates B. D. *ACS Nano,* **2010***, 4,* 2607-2614. Copyright 2010 American Chemical Society."[21] The review article "Directed Assembly of Nanowires" was co-written by Michael C. P. Wang and Professor Byron D. Gates. The contents of this publication were reproduced with the permission of the ScienceDirect, and co-authors.,[87]

techniques to direct nanowires into assemblies that span over large distances (>5 cm) within a few minutes for further manipulation and utilization of these materials.

The challenge of directing the assembly of synthetic nanowires increases as the length (or aspect-ratio) of these structures also increases. This correlation is attributed to an increased flexibility and fragility of these nanostructures.[113] Nanowires with a small aspect-ratio are relatively stiff structures, but nanowires with high-aspect-ratios (e.g., 1:1,000; diameter/length) are flexible and easily entwine with other nanowires (Figure 4.1). This process of self-entanglement can be avoided by dilution of the nanowire suspensions. However, assembly of nanowires one-by-one or in low quantities is inefficient and/or impractical for many applications. A number of approaches can be implemented to assemble nanowires.[21] These assembly techniques are either driven by molecular forces,[48, 114-118] electrostatic interactions,[119-124] shear forces,[103-104, 106, 110, 125-140] magnetic forces,[141-146] or electrokinetic forces.[147-158] Ideally, the technique for directing the assembly of nanowires would be independent of the material composition, scalable over multiple lengths, and applicable to a wide range of nanowire concentrations.

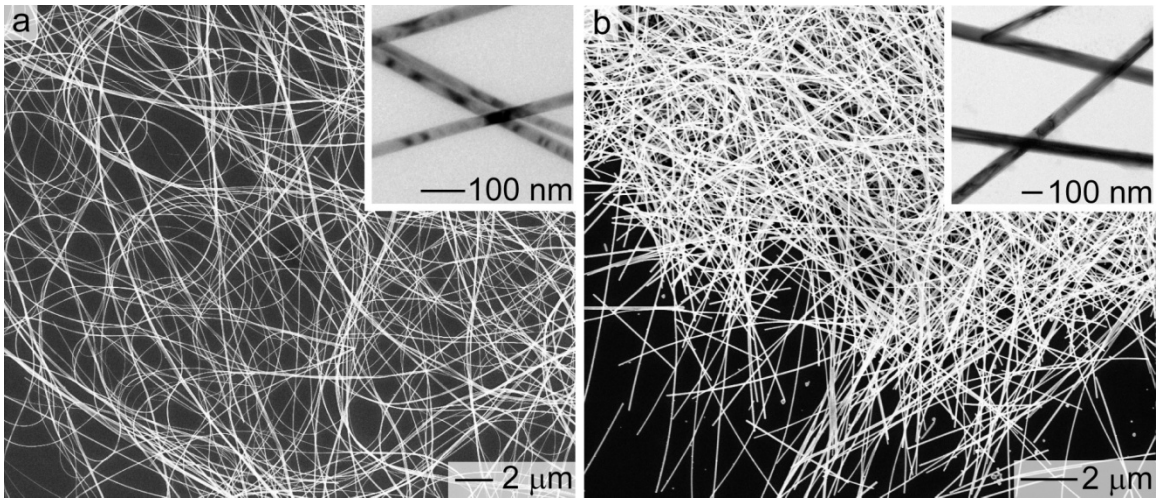

Figure 4.1 Scanning electron microscopy (SEM) and inset transmission electron microscopy (TEM) images of the as-synthesized (a) trigonal selenium and (b) face-centered cubic silver nanowires.

Many nanowires can be processed as a colloidal solution. Handling the nanowires as a solution is very convenient because these structures can be processed in a manner similar to most liquids. Also, the concentration of nanostructures can be adjusted through dilution or solvent evaporation. This suspension of nanowires can be

cast onto a substrate. Nanowires can be adhered to the engineered surfaces through target-recognition or biorecognition in random orientations.[114-117] The strength of the interactions between the nanowire and the substrate determines both the adhesion of the nanowire to the substrate and the final orientation that will be adopted by this structure upon removal of the solvent. Interactions between the nanowire and the substrate can be enhanced through van der Waals and hydrogen bonding interactions. For example, a colloidal solution containing nanowires, whose surfaces are modified with single-stranded deoxyribonucleic acid (ssDNA), is cast onto a substrate that had been patterned with complementary DNA (cDNA) molecules on its surfaces. The ssDNA modified nanowires are directed to the location on the substrate with the corresponding cDNA through DNA hybridization (Figure 4.2).[115-117]

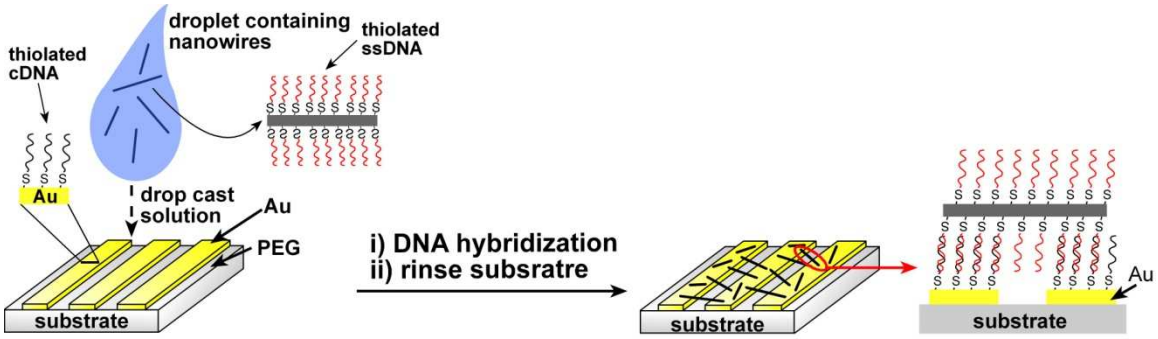

Figure 4.2 Assembly of nanowires can be directed by the biorecognition of complementary DNA. A suspension of nanowires whose surface is modified with single-stranded DNA (ssDNA) is cast onto a surface patterned with the complementary DNA strands (cDNA) and poly(ethylene glycol) (or PEG). Nanowires bind to the substrate through hybridization of ssDNA with cDNA.

Biorecognition is an efficient method to assemble nanoscale materials. It can be used to facilitate the adhesion of nanowires onto various surfaces, but this technique, currently, lacks the ability to direct the alignment of the nanowires during the assembly process. A further complication can be the reliance of this technique on the integrity of the biomolecules used in these examples. This process for directing the assembly of nanowires is, however, simple and can be easily adapted to many materials. Further modifications to this technique could utilize regioselective surface modification of nanowires using biotin-avidin linkages[114] or block-copolymer modifications,[48] which have been pursued for end-to-end assembly of nanostructures. Another alternative is to take

advantage of hydrophobic surface modifications that have been used to assemble composite nanowires into inverse micelle structures when immersed in aqueous environments.[118]

Better nanowire alignment can be achieved by imparting shear forces on to the nanowires during the assembly process. A shear force is created by the motion of a fluid or solid object against a second fluid or solid object. This motion can be achieved by a number of means, such as the wetting/dewetting of surfaces or the mechanical movement of two surfaces in opposing directions. In either case, a force is generated that is parallel to the direction of movement. This force can be used to redirect the orientation of nanowires that are either suspended in a solution or fixed to a substrate. The new orientation of the nanowires will be parallel to the direction of the shear force. For instance, shear force directed alignment of nanowires during the assembly process has been demonstrated through the use of an evaporating liquid droplet (Figure 4.3a)[126, 129, 137] and within a microfluidic channel.[127, 130, 133-134] Nanowires deposited onto a substrate will reorient with the direction of fluid flow to minimize the fluid drag. Density of nanowires can be controlled by changing the concentration of nanowires within the suspended liquid. Repeating this process after realigning the microfluidic channels can be used to create layer-by-layer assemblies of nanowires with complex geometries.[130, 133] The density of the aligned nanowires can be improved by adapting Langmuir-Blodgett (LB) techniques to assemble the nanowires.[104, 125, 135-136, 159] Nanostructures suspended at an air-liquid interface can be assembled into dense films through compression within an LB trough (Figure 4.3b). The nanowires adopt a close-packed organization to minimize the energy of the system during compression. Dip coating is used to transfer the nanostructures from the air-liquid interface onto a solid substrate. The wires can adhere to this substrate through van der Waals interactions as it is drawn in a vertical direction through the layer of compressed nanowires. A shear force is created along the vertical direction as the solvent withdraws from the surfaces of the substrate, leading to alignment of the nanowires along the same direction (Figure 4.3b, step 3). Density of the deposited nanowires is controlled by speed of withdrawing the substrate from the LB trough and the pressure applied to the assembly within the LB trough. Limitations of this technique include reorganization of the nanowires during dip coating that leads to overlapping features and gaps within the dense arrays of nanowires.[135] Hierarchical

structures can also be produced by repeating the assembly process after changing the orientation of the substrate onto which the nanowires are being transferred.[138]

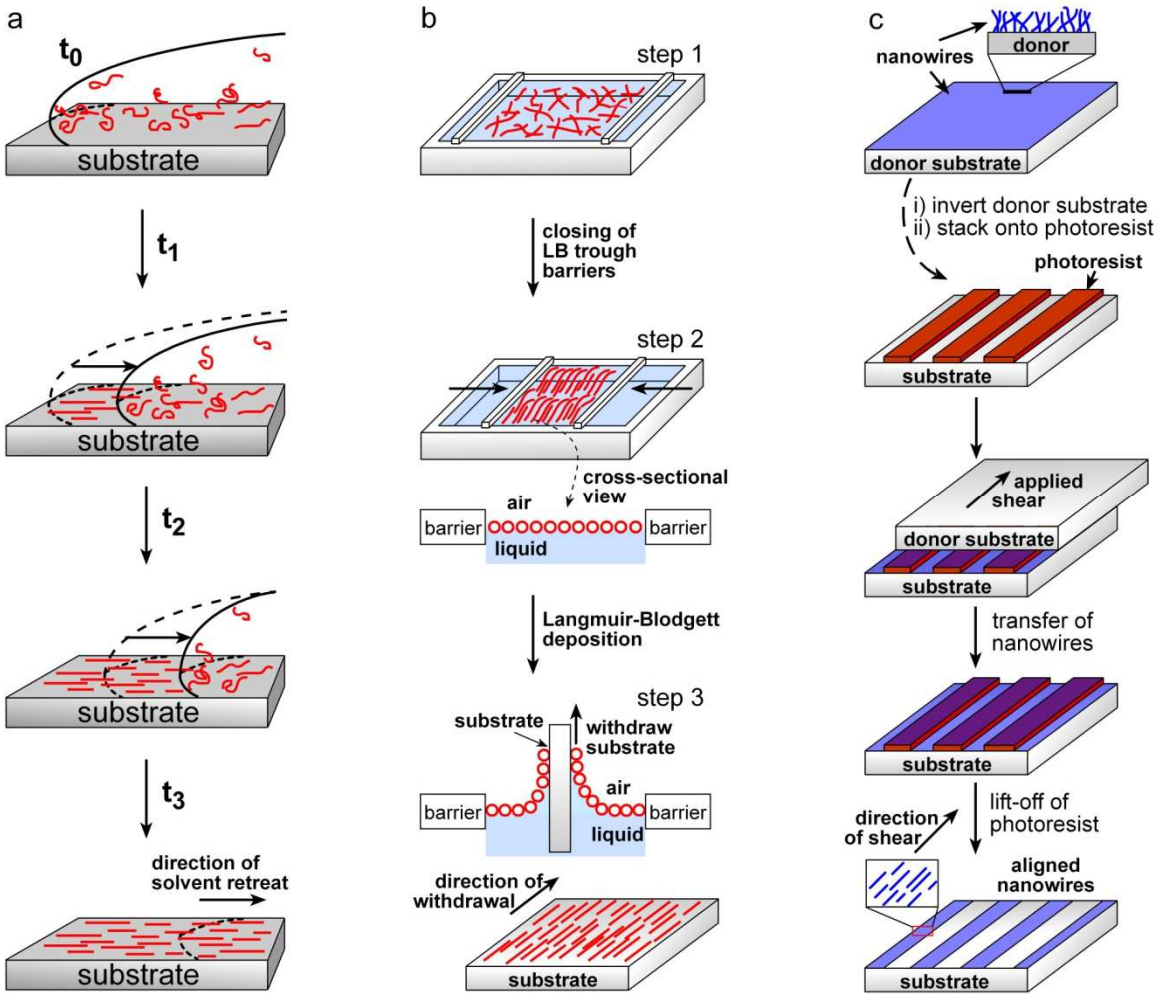

Figure 4.3 (a) Shear forces from evaporation of a droplet can align nanowires with an orientation parallel to the fluid flow. (b) Nanowires can be assembled at an air-liquid interface within a Langmuir-Blodgett (LB) trough and transferred by dip-coating. (a) Mechanically applied shear forces will reorient nanowires along the direction of the applied force. Nanowires can be patterned by masking the substrate with photoresist.

Shear force can also be generated from the mechanical movement of two contacting surfaces by one sliding across another. This mechanically generated force can direct the assembly of vertically grown nanowires into arrays with an orientation parallel to the direction of the applied force (Figure 4.3c). A pattern can be imposed on the assembled arrays of nanowires by lift-off or similar lithographic patterning of these

nanostructures.[131] Nanowires with a crossed-wire configuration can be achieved by assembling the wires in two, orthogonal directions.[128] This assembly technique can be scaled-up for high throughput. One approach is to create a shear force using a rolling substrate.[139] A common limitation for techniques relying on a shear force to assemble nanowires is the balance of the interacting forces. A minimum force is required to reorient the nanowires, and these structures must adhere to the substrate while maintaining their integrity.

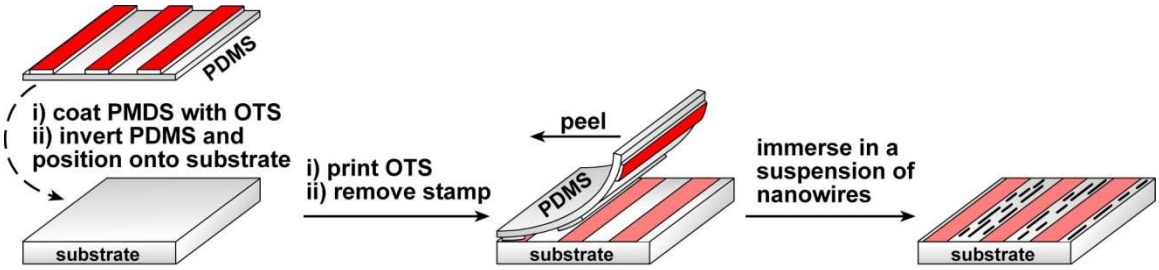

Figure 4.4 Nanowires can be assembled by electrostatic interactions. The negative charge of silica can attract ammonium-terminated nanowires. This negative charge can be selectively masked by patterning octadecyltrichlorosilane (OTS) by microcontact printing (μ-CP) with a polydimethylsiloxane (PDMS) stamp.

Assembly of nanowires can be driven by electrostatic interactions.[119-124] These interactions rely on either the inherent polarizability of the nanostructure or a surface modification of this material to adopt a specific charge. One example is the negative charge of silicon oxide at pH 7, can attract nanowires with a positive charge (e.g., nanowires coated with an amine-terminated functionality).[119-120] The negative charge of silica can be partially masked by the selective patterning with a dielectric layer. An example of this modification is the printing of a methyl-terminated alkylsilane onto substrates of silicon oxide by microcontact printing (μ-CP) as shown in Figure 4.4. Silicon nanowires functionalized with 3-aminopropyltriethoxysilane (APTES) adhere to the unmasked silica (Figure 4.4). Electrostatic interactions can assist the assembly of nanowires. This process can be driven by either passive or active (applied) electrostatic interactions, which are easily scalable over large areas. Simple structures are quickly assembled by these electrostatic interactions, but orientation of the nanowires can be easily altered by shear forces upon solvent evaporation.

Magnetic field can also direct the alignment of nanowires in a colloidal solution that are susceptible to magnetization (Figure 4.5).[141-146] This assembly technique has been limited to nanowires composed of ferromagnetic and superparamagnetic materials. The process of assembly can be guided by external magnetic fields, but the uniformity of the assembled patterns and control over positioning of the nanowires both improve when magnets are incorporated onto the substrate. This alignment depends on the magnetic field lines and their shape. Nanowires assembled onto these substrates will often form chain-like structures extending from this magnet along the magnetic field lines.[141] A complex geometry, which can assemble the nanowires into crossed-wire configurations and hierarchical structures, is also possible by positioning the magnets beneath the receiving substrate.[142] A major limitation of this technique is the requirement that the nanowire being assembled must respond to a magnetic field.

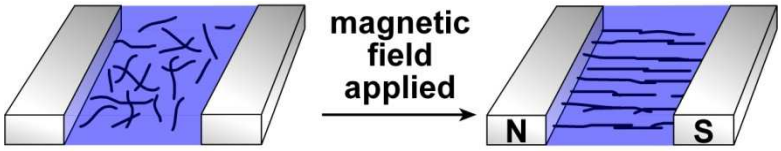

Figure 4.5 Magnetically susceptible nanowires can be aligned within a magnetic field.

Another area that has been explored for the parallel assembly of nanowires over large areas of a substrate is through the use of electrokinetic forces. Nanowires can adopt a polarization within an applied electric field. These structures align with a minimum energy configuration within the applied field, such as along the field lines (Figure 4.6). Electrokinetic assembly is a promising approach to manipulating nanowires. Directing the assembly of nanostructures within an electric field has a number of benefits and limitations. Materials can assemble based on polarization of the material and/or the interactions of charge on the material within an applied electric field.[99, 111, 150, 155, 160-165] The electric field direct the assembly of the materials and can, therefore, be used to assemble multiple nanostructures in a parallel process. In addition, the process can be reversible if electrochemical degradation of the sample is avoided during the assembly process. This ability to reconfigure the assembled nanostructures can be useful for optimizing their positions by cycling between assembly and dispersion processes. The field lines can also be directed over distances much larger than the largest dimension of the nanostructures. These properties have been used to assemble nanowires of metals,

semiconductors and dielectric materials over distances of a few micrometers,[150, 155, 162-163] but for highly anisotropic nanostructures only carbon nanotubes have been assembled over larger distances through the use of electrokinetics.[109, 112] We demonstrate herein the ability to use electrokinetics to direct the assembly of solution-phase synthesized nanowires over large distances (>5 cm).

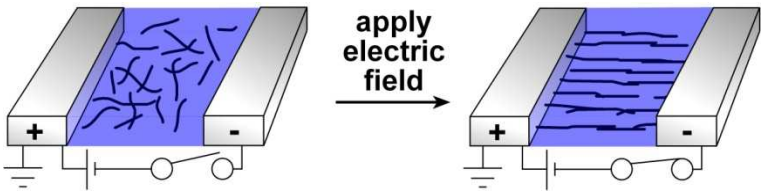

Figure 4.6 Polarization of nanowires in an electric field can direct the alignment of these structures.

4.2. Experimental Section

Nanowires used in the studies on electrokinetic assembly were synthesized by solution-phase techniques. Selenium nanowires were synthesized from a solid-solution-solid transformation using amorphous selenium powder. Silver nanowires are produced via the polyol method as discussed below.

4.2.1. Synthesis of Selenium Nanowires

In brief, to synthesize amorphous selenium, 2.73 g (21.1 mmol) of selenious acid (H_2SeO_3, 98%; Sigma-Alrich) was dissolved in 100 mL of 18.0 MΩ·cm water (produced via a Millipore water filtration system) in a 250 mL round bottom flask. The H_2SeO_3 solution was chilled with an ice-water bath. This solution was reduced with 3 mL (61.1 mmol) of hydrazine (N_2H_4, 50-60% in water; Sigma-Aldrich), which was introduced over a 2 min period drop-by-drop into the reaction solution under magnetic stirring. After a total reaction time of 15 min, the red precipitate was collected by vacuum filtration onto a PVDF membrane (catalogue number: VVLP04700; Millipore). The filtrate was rinsed with 200 mL of ice-cold high purity water to remove residual N_2H_4. The resulting red solid was stored in a desiccator in darkness at 22℃. Selenium nanowires were produced by sonicating (Branson Model 1510) for 20 s a dispersion of 1 mg of amorphous selenium powder in 1 mL of ethanol (EtOH, 95%; Commercial Alcohols) within a sealed 1 dram

glass vial. The nanowires grow over a period of 12 h while this sonicated solution was stored in darkness at 22℃. After centrifugation at 1,500 rpm for 15 min, the ethanol solution was decanted and replaced with hexanes. This solvent exchange process was repeated at least three times to remove trace amounts of ethanol. The final solution of selenium nanowires was used for the electrokinetic assembly studies.

4.2.2. Synthesis and Surface Modification of Silver Nanowires

In the polyol synthesis of silver nanowires, 220 mg of polyvinylpyrrolidone (PVP_{55k}, M*w*: 55 k; Sigma-Aldrich) dissolved in 5 mL of ethylene glycol (EG, ≥99%; Sigma-Aldrich) was heated to 120°C with an oil bath while N_2 (g) was blown over the top of the solution at 2 mL/min to remove water vapor. When the solution reached 120°C, 1 mL of an ethylene glycol solution containing 0.024 mg platinum (II) chloride ($PtCl_2$, 99.99+%; Aldrich) was added dropwise into the reaction mixture. The reaction proceeded under an atmosphere of N_2 (g) for 1 h, before adding a solution of 50 mg of silver nitrate ($AgNO_3$, 99+%; Sigma-Aldrich) and 220 mg of PVP_{55k} dissolved in 7.5 mL of ethylene glycol. The later solution was introduced into the reaction mixture at 2 mL/min via a syringe pump. After the addition of this solution, the reaction temperature was increased at 1.8°C/min to 160°C. Upon reaching this temperature the N_2 (g) flow was removed and the reaction flask was capped to prevent the accumulation of dust in the solution. The reaction was held at this temperature for 1 h, resulting in formation of silver nanowires. This solution of nanowires was diluted with 20 mL of acetone (Anachemia; Lab Grade) and purified at least 3 times via centrifugation at 3,000 rpm for 10 min, decantation of the supernatant, and re-dispersion in ethanol. The purified silver nanowires were coated with self-assembled monolayers of an alkanethiol. A solution of 0.5 mL 1-dodecanethiol (≥98%; Aldrich) and 1 mL purified silver nanowires in acetone contained within a 2 mL centrifuge tube was vortexed overnight. Excess alkanethiol is removed by purification of the nanowires by at least three processes of centrifuging, decanting, and washing the modified nanowires with hexanes (≥98.5%; Anachemia).

4.2.3. Materials Characterization Techniques

All optical images were taken with an HP Photosmart 945 digital camera and all color images in the main body of the manuscript were altered to grey scale using Adobe Photoshop CS3 Extended software.

Scanning electron microscopy (SEM) images were acquired with Strata DB235 FESEM operating at 5 kV. Samples for SEM analysis were prepared by either drop-casting a solution of nanowires or otherwise positioning the sample of interest onto a 1 cm^2 piece of silicon wafer. Bright field transmission electron microscopy (TEM) images were obtained with a Tecnai G^2 STEM operating at 200 kV. These TEM samples were prepared by drop-casting or dip-coating solutions of nanowires onto a 300 mesh copper grid coated with formvar/carbon (catalogue number: FCF300_CU_50; Cedarlane Laboratories Limited).

X-ray diffraction (XRD) patterns were acquired with a Rigaku diffractometer using Cu Kα radiation (λ = 0.15418 nm). Copper X-rays were generated from a copper target by electron bombardment at 42 kV and 40 mA. A 0.5-mm collimator was placed between the X-ray source and the sample. Samples for X-ray analysis were prepared by casting a suspension of nanowires from EtOH onto a glass slide and drying the sample under vacuum. A fiber of selenium nanowires was fixed on a glass capillary by Dow Corning™ high-vacuum grease (Thermo Fisher Scientific Inc.; catalogue number: 146355D). Electrokinetically assembled silver nanowires were collected on a piece of ~1x1 cm^2 glass slide.

X-ray photoelectron spectroscopy analysis was performed using a Kratos Analytical Axis ULTRA spectrometer containing a DLD spectrometer using a monochromatic aluminum source (AlKα, 1486.6 eV) operating at 150 W (10 mA emission current and 15 kV HT). Analysis was conducted on a 700 x 300 μm^2 area of the sample. High resolution scans were obtained at a 25 meV step size with a dwell time of 300 ms per step, a pass energy of 20 eV, and averaged over 2 scans. Energy scale linearity was calibrated using Al and Mg X-ray sources on Argon sputter cleaned gold and copper substrates. The calibration procedure was performed in accordance to the ISO 15472 international procedure. XPS samples were prepared by drop-casting dispersions of selenium and silver nanowires onto a 1 cm^2 polished Si/SiOx substrate.

The Kratos charge neutralizer was used during analysis of a fiber of selenium that was fixed on a Si/SiOx substrate with conductive copper tape (catalogue number: 77800; Electron Microscopy Sciences) and the electrokinetically assembled silver nanowires were collected on a piece of ~1x1 cm^2 glass slide.

Zeta potential measurements of selenium nanowires were acquired in ethanol using a Malvern Instruments Zetasizer Nano ZS system and disposable capillary cell (catalogue number: DTS1060C; Malvern Instruments).

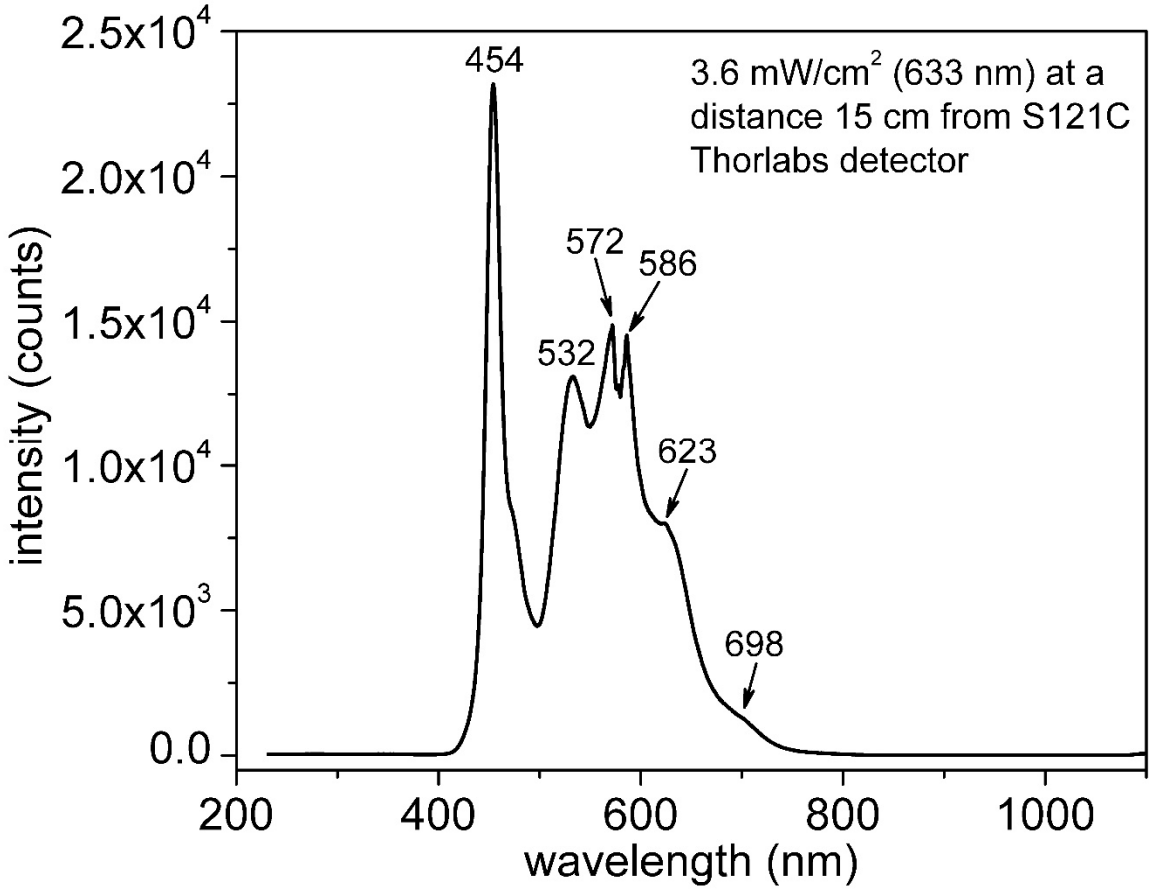

Figure 4.7 Emission spectrum of ringlight light emitting diodes (LEDs) with a fluence of 3.6 mW/cm^2 at 633 nm as measured at a distance of 15 cm from the detector.

Conductivity measurement of selenium nanowire fibers was performed on a Cascade Microtech, Inc. M150 probe station equipped with a Leica Stereo Zoom microscope and an Aglient BI500A semiconductor device analyzer. The fibers of selenium nanowires were irradiated with a Leica ringlight light emitting diodes (LEDs;

color temperature of 5000 K). The emission spectrum of the LEDs (Figure 4.7) was obtained on a Mightex Systems High-Resolution High-Stability Spectrometer (HRS-Series). These LEDs have a maximum fluence of 3.6 mW/cm^2 at a distance of 15 cm from the detector. Fluence of the LEDs was measured with a S121C detector (Thorlabs, Inc.) at a wavelength of 633 nm. Signal from the S121C detector was read out from a PM100A Handheld Optical Power Meter (Thorlabs, Inc.) Tungsten probes were placed in direct contact with the selenium fibers and the current collected from -3 to 3 V at 50 mV increments both in the absence of light and during illumination at various intensities from the LEDs of the microscope. Three consecutive measurements were made for each sample. The reported values are the average of the three measurements.

4.2.4. Electrokinetic Assembly Techniques

Care was taken to avoid the presence of dust within the solutions containing the dispersions of nanowires. Hexanes were initially filtered through a syringe filter containing a PTFE membrane with 0.2 μm holes (catalogue number: AP-4225; Acrodisc). Open solutions of nanowires were kept in an environment that was cleaned to minimize the presence of dust, and all dispersions were analyzed immediately after placement into rinsed glassware. These solutions were capped with a thoroughly rinsed watch glass upon completion of each study.

Nanowires dispersed in hexanes were contained in glass or plastic vials for small scale assemblies (e.g., over distances up to 1 cm). This assembly can be driven by the accumulation of charge on the exterior of the vials from a Zerostat® anti-static gun (product number: Z108812-1EA; Sigma-Aldrich) held next to the vial. Alternatively, similar assemblies of nanowires can be achieved using a high voltage power supply (Spellman High Voltage DC Supply; with an operating range of 0.1–30 kV) that is connected by copper or platinum wire leads attached to the exterior of the vial. Larger scale assemblies were performed with dispersions of nanowires contained in a glass Petri dish that was suspended in air with either a single clamp or hollow glass supports. The electrodes used for these assemblies were either copper or platinum wires (~1 mm in diameter, 2 to 3 cm in length; ≥99.9%; Sigma-Aldrich), or a stainless steel mesh with open circular holes (Small Parts Inc.). The high voltage power supply is connected to these electrodes *after* positioning the wire or mesh within the suspension of nanowires.

WARNING: use extreme caution when working with high voltages. The system under study should be appropriately grounded, and the working and ground electrodes should be at least 3 cm apart while performing the electrokinetic assembly to avoid arcing. Sparks created from electrode arcing could easily initiate combustion of the hexanes. Extreme care should be taken when performing large-scale assembly of nanowires in an open dish of hexanes.

4.2.5. Modeling of Electric Field

Simulated spatial distributions of the electric field and gradients were performed with COMSOL Multiphysics 3.5 using the constitutive relation, $D = \varepsilon_0 * \varepsilon_r * E$ for two spherical electrodes immersed in water contained within a glass Petri dish. Water was used as the solvent for this simulation as we were not able to model low dielectric constant solutions, such as hexane. Scaling for this simulation was identical to that for the experimental conditions. The two opposing spherical gold electrodes (each with a radius of 0.65 cm) were spaced 4.6 cm apart (center-to-center distance) within the glass Petri dish. This dish had a volume of $\pi r^2 h$, where r = 4.25 cm and h = 1.3 cm. Physical properties of water (at a temperature of 293 K) entered into the model include: relative permittivity, ε_r = 80.1; conductivity, $\sigma = 5.5 \times 10^{-6}$ S/m; and viscosity, η = 1.003 mPa•s. Physical properties of gold has a relative permittivity of ε_r = 6.9.[166] In addition, ε_o is the electric permittivity of free space (ε_o = 8.85E-12 F/m). In addition, potentials of +5000 and 0 V under DC conditions were applied to the working and ground electrodes, respectively.

4.3. Results and Discussion

Electrokinetic assembly of nanostructures requires a dispersion of either polarizable or charged materials.[167] Assembly proceeds by either dielectrophoresis or electrophoresis.[167-168] In order to design a general system for assembly, we chose a low dielectric constant solution to suspend the nanostructures. This type of solution will maximize the response of our system to applied electric fields. The first systems we tested were the response of suspensions of selenium and silver nanowires (detailed syntheses of the nanowires are described in the Experimental Section) to static electric fields established by externally applied charges. A number of methods can generate charge to create this external electric field, such as Van de Graaf generators, Tesla coils, and piezoelectric charge generators. The later method ionizes air molecules and is often used to dispel electrostatic charge accumulated within dry chemical powders.[169] We use a commercially available Zerostat® anti-static gun to apply charge to the exterior of vessels containing dispersions of nanowires (Figure 4.8a,d). The initial dispersion of ~50-μm long selenium nanowires, which have a zeta potential of -54.3 ± 2.3 mV, are attracted to the wall of the vessel when positive ions are generated (Figure 4.8b,b').[170] These selenium nanowires collect into fibers extending from the region nearest to the nozzle of the anti-static gun where positive ions are generated after the trigger is squeezed. Selenium nanowires were repelled from this interface when negative ions are subsequently produced by the Zerostat® anti-static gun (Figure 4.8c,c'). This process is reversible and can be repeated multiple times. Dispersions of ~10-μm long silver nanowires with a zeta potential of 43.3 ± 5.0 mV exhibited an equal and opposite response to the charge accumulated on the vessel; these metal nanowires are repelled by positive charge accumulation (Figure 4.8d,d') and attracted to the side of the vessel with a subsequent generation of negative ions (Figure 4.8e,e'). In both systems the assembled nanowires appear to align with electric field extending from the charge accumulated on the exterior of the container to the nearest ground, such as the table top.

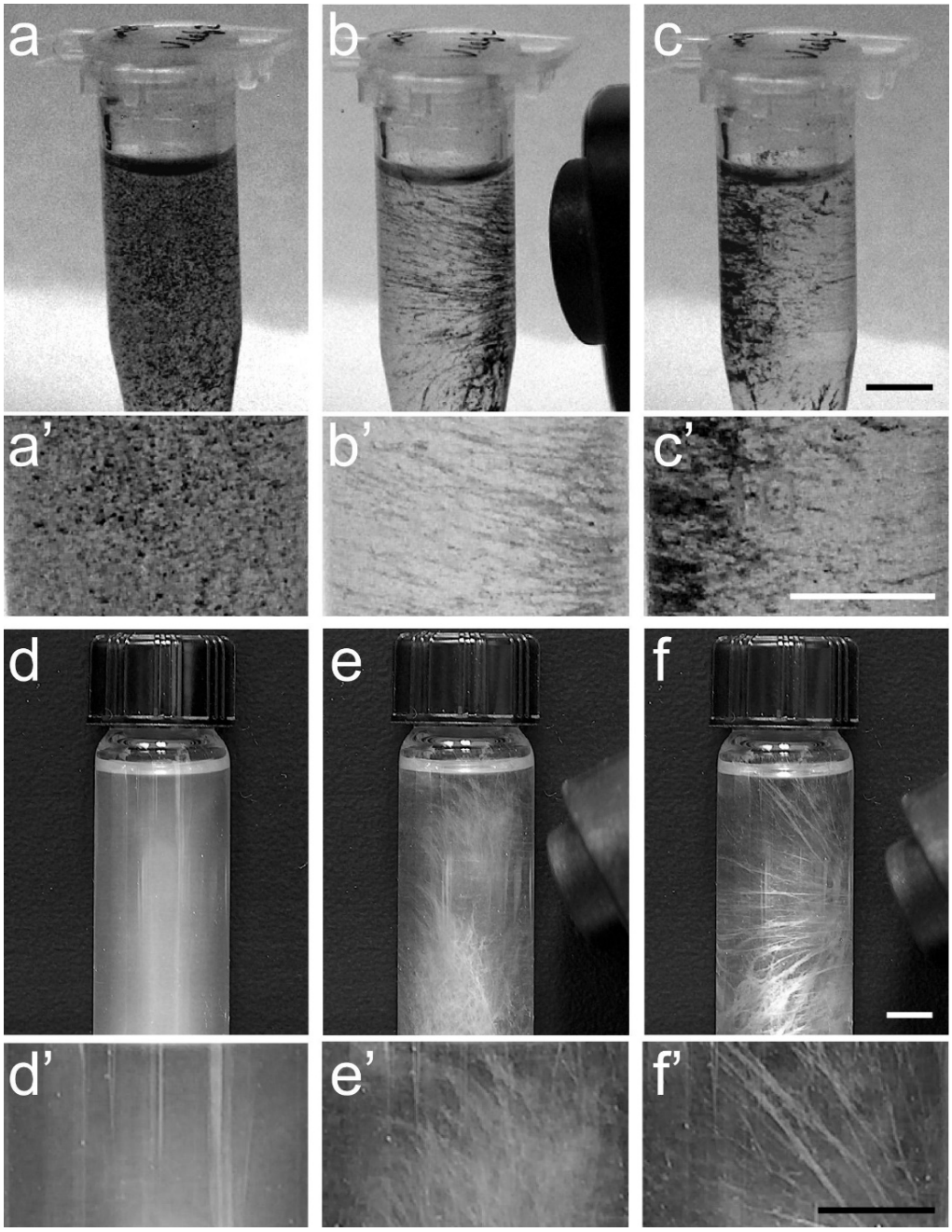

Figure 4.8 Optical images show that dispersions of (a) selenium and (d) silver nanowires in hexanes (b,c,e,f) align with electric field created after the exterior of the plastic or glass vial is exposed to charged ions generated from a handheld Zerostat® anti-static gun. (a'-f') Higher magnification images are below each corresponding optical image. All scale bars are 0.5 cm.

The solvent plays an important role in the electrokinetic assembly of the nanowires into macroscopic fibers. Solvent properties that influence the dispersion of

nanowires within a solvent also influence their assembly into fibers. These properties include dielectric constant, viscosity, polarity of the medium and of the suspended material, and zeta potential of the dispersed nanostructures.[164-165] It is anticipated that viscosity plays a minor role in the ability to form fibers from dispersed nanowires. We screened a number of solvents with similar viscosities. These solvents had very different solvent polarities and dielectric constants. Our studies revealed that dielectric constant of the solvent played a dominate role in determining whether dispersed nanowires would successfully assemble into a visible macroscopic fiber (Table 4.1). When isolating fibers of nanowires from a low dielectric constant solvent, we prefer to use a solvent with both low boiling point and low vapour pressure. It is desirable that the solvent evaporate as soon as the fiber is removed from the assembly medium. From the low dielectric solvents that we screened, hexanes was chosen as the preferred solvent for assembly of the fiber-like structures. This choice was dictated by a combination of macroscopic fiber stability in each solvent, vapour pressure, and boiling point of the solvent.

Table 4.1 Solvent Dependence for the Assembly of Nanowires into Macroscopic Fibers*[171-172]

solvent	ε_r	P'	forms fiber?
hexanes	1.89	0	yes
hexafluorobenzene	2.02	0	yes
1,4-dioxane	2.2	4.8	yes
carbon tetrachloride	2.23	1.6	yes
toluene	2.37	2.4	yes
diethyl ether	4.34	2.8	yes
chloroform	4.8	4.1	no
tetrahydrofuran	7.6	4	no
ethanol	25.3	5.2	no
acetonitrile	37.5	5.8	no

Abbreviations: ε_r = dielectric constant and P'= solvent polarity.

Selenium and alkanethiol modified silver nanowires dispersed within low dielectric constant solvents (i.e., dielectric constants $\leq$4.34) could assemble into macroscopic fibers under an applied electric field. A similar method of assembly was

reported by Kamat *et al.*[109] Kamat introduced extrinsic charges onto the surfaces of their materials through the addition of an ionic surfactant in order to polarize their material under applied electric fields. In comparison to our study, Kamat *et al.* were able to assemble their material into linear bundles along electric field in a relatively high dielectric constant solvent. In our system both selenium and silver nanowires were assembled into macroscopic fibers without the addition of charged surfactants. The assembly of nanowires in our system relies on a combination of material polarization and dispersion in the solvent. Low dielectric constant solvents were required in our method of nanowire assembly. Insulating properties of these low dielectric constant solvents prevented the loss of charge or screening of polarization from the nanowires within the applied electrostatic field.

Electrokinetic assembly was driven by the electric field strength and the polarizability of the nanowires dispersed in a medium of a lower dielectric constant than the nanowires. Polarization of metallic nanowires most likely proceeded by the displacement of free electrons away from the negatively charged electrode in the presence of an applied electric field, while the positive charges migrated in the opposite direction. Semiconducting nanowires were polarized in a similar fashion, but charges on a semiconducting nanowire could also originate from oxidation of the surface atoms, accumulation of static charges as nanowires moved against each other, accumulated through solvent mediated charge transfer, and photon induced charge separation.[173-174] Induced polarization due to charge separation and/or accumulated excess charges facilitated the directed alignment and assembly of both silver and selenium nanowires in the applied electric field. In addition, polarized nanowires dispersed in an electric field experience electrophoretic forces that cause them to move toward the region of the highest field strength.[167-168] These polarized nanowires subsequently assembled into centimeter long fibers in solution through induced dipole-dipole interactions.

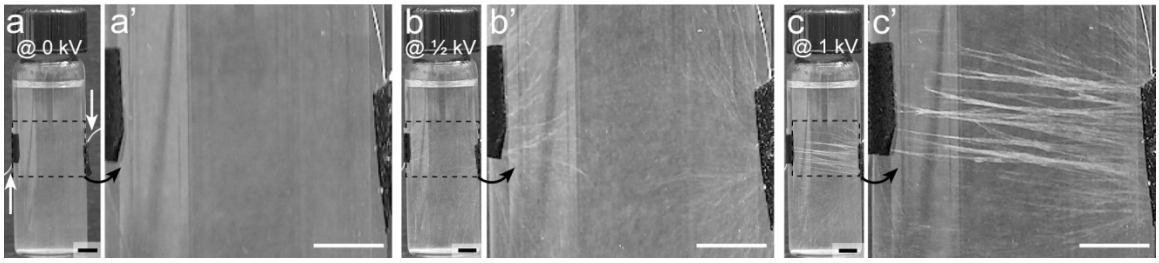

Figure 4.9 Optical images of silver nanowires assembled into fibers by electrokinetic processes. (a,a') Silver nanowires dispersed in hexanes align with electric fields (b-c') created using an external power supply. Electrodes from this power supply are in contact with opposite sides of the glass vial at the positions indicated by the white arrows in (a). All scale bars are 0.4 cm.

Fine tuning the response of the assembled system requires the use of a variable power supply to control the strength of the applied electric field. The distance covered by the assembled nanowires and the density of the nanowires collected within the electric field should scale with the strength of the applied electric field. The type of power supply necessary to direct the assembly of nanostructures within a low dielectric constant solution can be estimated from the electrostatic potential used in the previous study (e.g., 2 to 5 kV for a Zerostat® anti-static gun). Electrodes from a high voltage DC power supply connected to opposing sides of a glass vial can establish electric field within the container for directing the organization of nanostructures. The silver nanowires assemble into macroscale fibers extending from the walls of the container. These fibers of assembled silver nanowires span the diameter of the vial between the two external electrodes (Figure 4.9). Increasing the applied electric field strength from 0.33 MV/m in Figure 4.9b to 0.67 MV/m in Figure 4.9c increases both the length and quantity of assembled fibers between the two electrodes. Lengths of the fibers are limited by the distance between the two electrodes, or the distance to a second, more efficient source of ground (Figure 4.10). When a dispersion of selenium nanowires are assembled in a vial that is in contact with two sources of ground, the assembled structures will extend from the working electrode to the nearest or the more efficient source of ground. In order to manipulate the geometry of assemblies the systems need to be isolated from unwanted grounding sources.

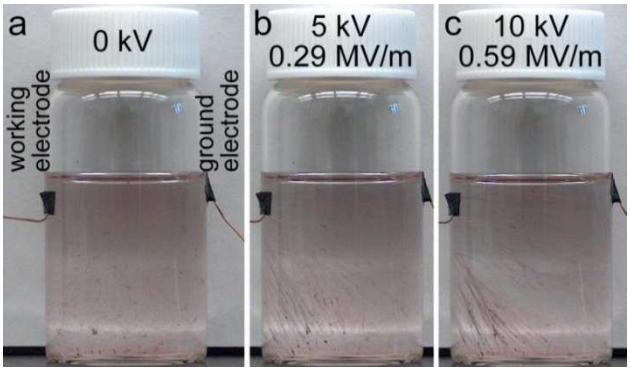

Figure 4.10 (a) When electric fields are applied to suspensions of selenium nanowires, (c,d) these materials assemble into fiber-like structures that extend from the working electrode to the nearest ground, in this case the table beneath the glass vial.

There are few options to isolate a system containing high voltage field lines from external, unwanted grounding sources. One of the best electric insulators is air. A simple method for insulating our system is to suspend it in air. A number of insulating containers of either plastic or glass could be used to contain the dispersions of nanowires during the assembly process. A simple and inexpensive container is an open glass dish, such as a glass Petri dish or crystallizing dish. This set-up can be easily viewed from above or from the side with minimal distortion. The new container is also convenient for assessing the dynamics of the assembling nanowires. In this configuration the choice of electrode is important in order to avoid unwanted electrochemical reactions between the nanowires and the electrode. For example, although copper wires can be used to direct assembly within the solution, the nanowires and/or the electrodes can potentially react electrochemically with each other during this process. Platinum wires are the preferred choice for directing the assembly of both selenium and silver nanowires. Material in solution starts to assemble into fiber-like structures extending from these electrodes as soon as an electric field of sufficient magnitude is applied to the solution. Under an electric field strength of 1.7 MV/m these fibers will grow to lengths of ~1 cm in <30 s and continue to grow in both length and width as more nanowires accumulate along the electric field over time (Figure 4.11). The fibers and field lines can extend in all directions from a single working electrode (Figure 4.11a). Fibers can also form between electrodes with orientations along the applied field lines (Figure 4.11b,f). As the magnitude of the electric field increases, the assembled fibers of selenium nanowires are directed to the regions of the highest field strength (Figure 4.11c,d). A fiber ~7 cm in length was

assembled under an electric field strength of 2.1 MV/m (Figure 4.11e). With the appropriate concentration of the selenium nanowires and electric field strength longer fibers can be assembled in the low dielectric constant solvents.

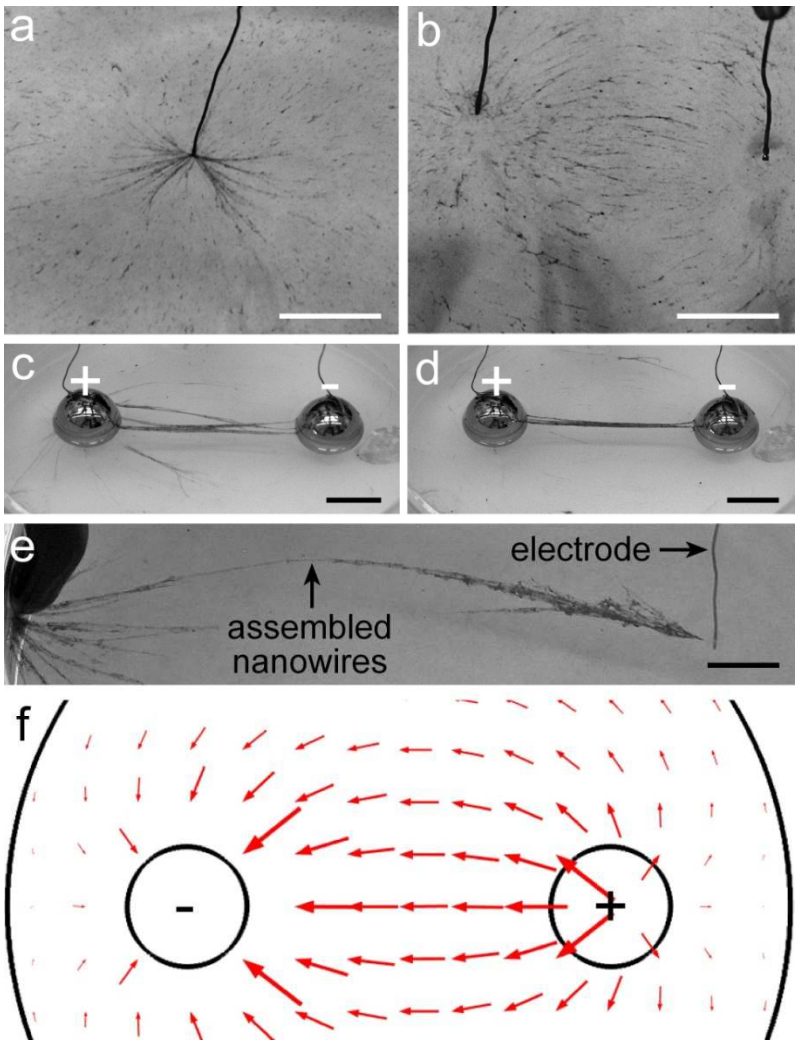

Figure 4.11 Selenium nanowires assemble into fibers along electric field generated in a solution of hexanes. Visible fibers are observed extending (a) from the working electrode, or (b) between two electrodes in close proximity. (c,d) Increasing the field strength (e.g., from 1.6 MV/m in c to 3.3 MV/m in d) drives the assembly of the nanowires into a single fiber. (e) A fiber ~7 cm in length is assembled under a potential of 2.1 MV/m. (f) Simulated electric field using a COMSOL finite element method. Arrows indicate the direction of the field lines and the sizes of these arrows represent the magnitude of the electric field strength. Scale bars are 1 cm.

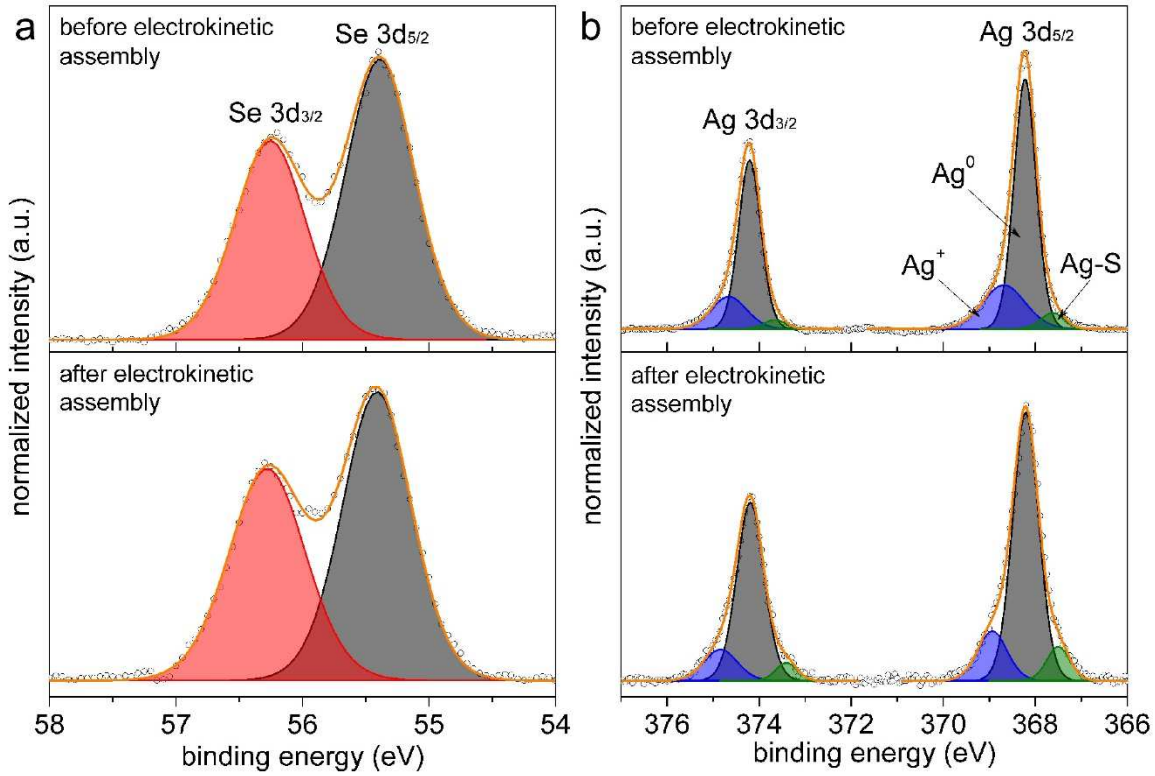

Figure 4.12 (a) X-ray photoelectron spectroscopy (XPS) data for the selenium nanowires both before (top) and after (bottom) electrokinetic assembly within hexane at an electric field strength of 3.3 MV/m. (c) XPS analysis of silver nanowires before (top) and after (bottom) electrokinetic assembly within hexane at an electric field strength of 0.67 MV/m.

Increasing the electric field strength concentrates the nanowires into a single fiber spanning the shortest path between the working and ground electrodes. The onset of assembly for both selenium and silver nanowires into macroscopic fibers was visually observed for field strengths >0.30 MV/m, and fibers of appreciable length (>1 cm) are seen at ~0.50 MV/m. The assembled fibers continue to gather nanowires from solution until reaching ~9 MV/m. At this electric field strength fiber-like structures were observed to shuttle back-and-forth between the two electrodes. It is likely that these bundles of selenium or silver nanowires may react with the electrodes. However, analysis by XPS indicated the chemical states of the assembled fibers did not change in comparison to the dispersed silver and selenium nanowires (Figure 4.12). In addition, matching XRD patterns between the assembled fiber of selenium nanowires and randomly dispersed selenium nanowires deposited onto glass substrates further suggested that no reaction

had occurred between the electrode and the selenium or silver nanowires during the electrokinetic assembly process (Figure 4.13a). Both diffraction patterns are well matched to the XRD pattern for the *t*-Se standard (PDF 42-1425). The XRD pattern for assembled fibers of silver nanowires also indicated no change in the crystal structure in comparison to randomly oriented silver nanowires on glass substrates (Figure 4.13b). Both diffraction patterns match the silver standard with a face-centered cubic (FCC) geometry (PDF 4-783).

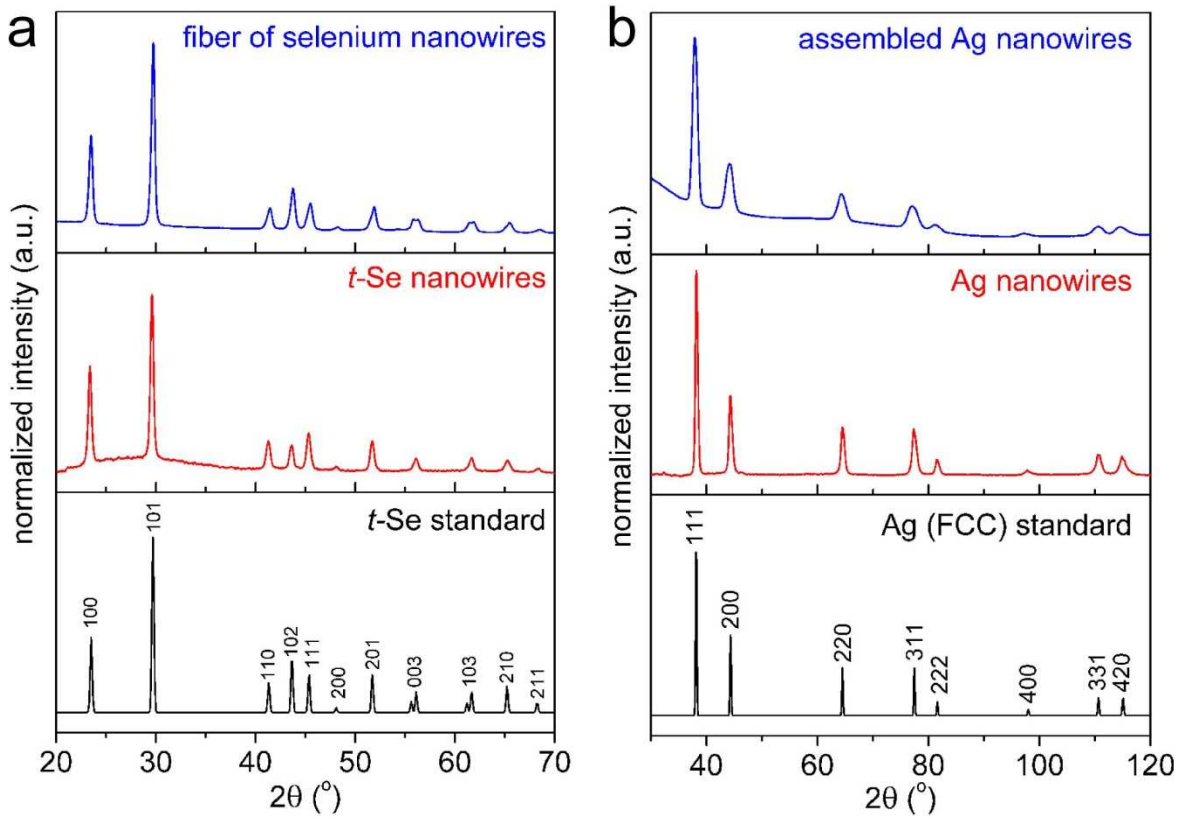

Figure 4.13 X-ray diffraction (XRD) patterns of (a, top) fiber of selenium nanowire removed from the electrokinetic assembly process, (a, middle) randomly oriented selenium nanowires on a glass substrate, (a, bottom) trigonal selenium (t-Se) reference standard (PDF- 42-1425). (b) Diffraction pattern of corresponding silver nanowires (b – top) after assembly, (b, middle) prior to assembly, and (b, bottom) face-centered cubic silver reference standard (PDF 4-783), respectively.

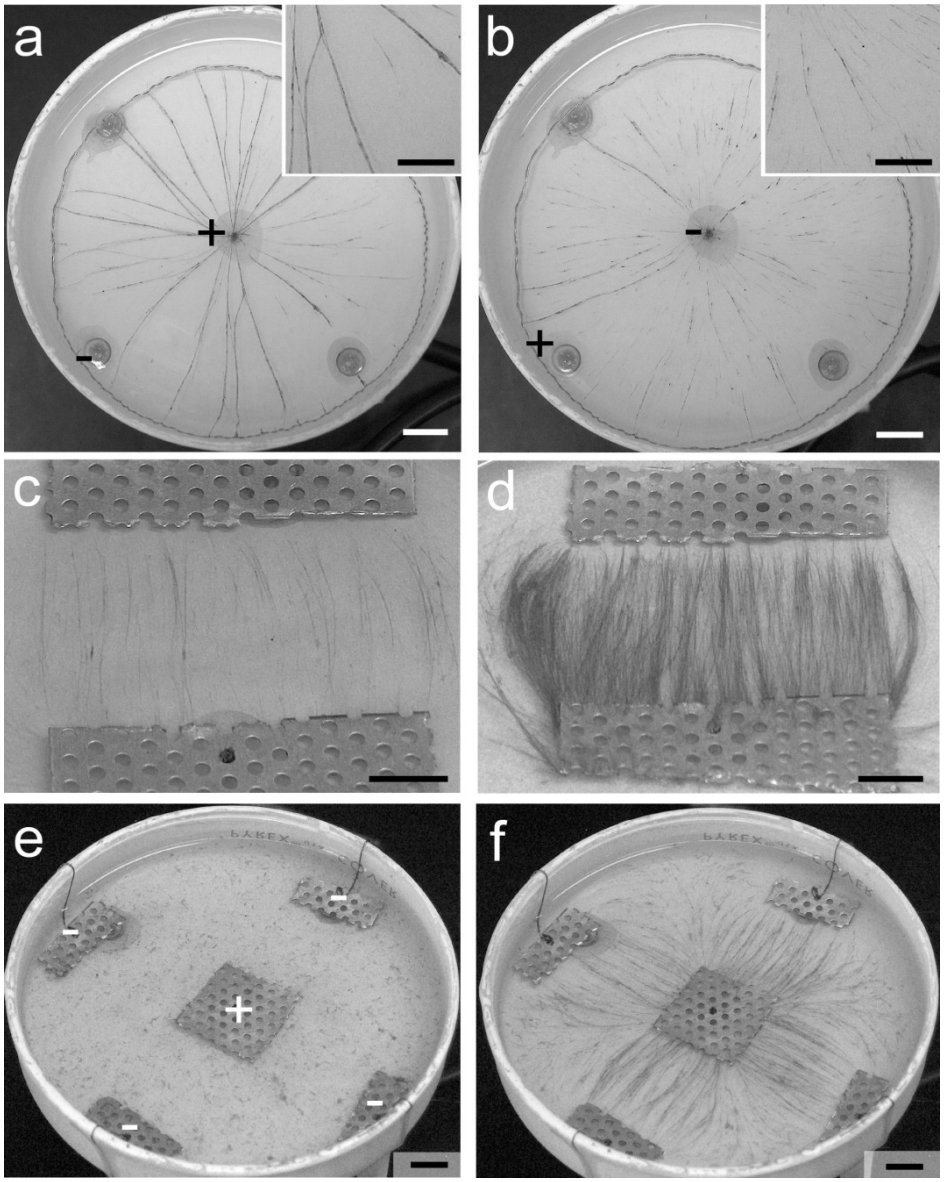

Figure 4.14 Optical images of selenium nanowires assembled into fibers with a radial pattern extending from (a) a point and (b) ring electrode within a glass Petri dish. The inset images of (a,b) showed differences in the density and the diameter. Different amount of selenium nanowires (c) ~5 μg and (d) ~120 μg are assembled between stainless steel mesh electrodes. (e,f) The geometry and relative positions of the working and ground electrodes can be used to align nanowires into fibers of different orientation. The electrical contact with the central electrode is made through a hole in the bottom of the glass dish. All scale bars are 1 cm.

To further demonstrate the versatility and scalability of the system, we pursued a number of different electrode configurations for directing the nanowires into arrays of

fibers. The fibers form along the electric field in solution, which seek the path of least resistance between the working and ground electrodes. Parallel assembly of nanowires into multiple fibers can be achieved by increasing the area of either the working or ground electrodes (Figure 4.14). In an electrode geometry where a point electrode located in the middle of a petri-dish is surrounded by a ring electrode is used to study the effect of working electrode surface area on the electrokinetic assembly process. Electrokinetic assemblies were performed on a dispersion containing ~50 µg of selenium nanowires in ~40 mL of hexanes, with equal electric field strength, but opposite polarity of the electrodes. Under an applied electric field strength of 1.16 MV/m the selenium nanowires assembled into fibers that radiate from the point and ring electrode (Figure 4.14a,b). Optical images suggest that thicker selenium fibers are produced when an electric field emanates from a single point such as the electrode geometry in Figure 4.14a, where the central electrode is the working electrode. In contrast, numerous slender fibers assembled when the field gradient converges into a central ground electrode, in this instance the ring electrode served as the working electrode instead (Figure 4.14b). A close inspection of the two scenarios suggests there are ~5 times fewer fibrous structures over 6 cm^2 in the later scenario (Figure 4.14a – inset versus Figure 4.14b – inset). Electrodes fabricated from a stainless steel mesh demonstrate a few important considerations in the design of these larger electrodes in order to create desired patterns from the assembled fibers (Figure 4.14c-f). Density of fibers assembled between the mesh electrodes is non-uniform across the width of the electrodes and is mostly attributed to the periodic shape of the mesh electrode. Flat protrusions of the working electrode collect a dense array of fibers along its length. Gaps between the organized fibers correspond to the recesses at the edge of the mesh electrode. Nanowires collect primarily along the regions of the highest electric field strength, which correspond to the shortest distances between the electrodes. Therefore, density of fibers can be controlled by the periodicity of the metal protrusions extending from the working electrode. The number of assembled fibers depends on the concentration of nanowires in solution. Density of the fibers increases proportional to increases in the nanowire concentration. A small number of fibers of selenium nanowires with narrow diameters were assembled from a ~40 mL hexanes containing ~5 µg of selenium nanowires at an electric field strength of 2 MV/m (Figure 4.14c). Under the same electric field strength, the assembled fibers increased both in number as well as their diameter when the

concentration of suspended nanowires was increased to ~120 µg in an equivalent volume of hexanes (Figure 4.14d).

The electrokinetic assembly of nanowires is a reversible process. This means that the assembled fibers of selenium or silver nanowires can be redispersed by agitating the low dielectric constant solution in the absence of an electric field. Then the dispersed nanowires can be assembled into fiber structures, again, in the presence of an electric field. To demonstrate, a round-bottom flask containing a suspension of selenium nanowires dispersed in a low dielectric constant solvent (Figure 4.15a) was assembled into centimeter long fibers under an electric field strength of 9.6 MV/m (Figure 4.15b). In the absence of an electric field, fibers of selenium nanowires can be redispersed through manual agitation of the solution (Figure 4.15c). In the presence of an electric field the dispersed nanowires assembled into centimeter long fibers, again (Figure 4.15d).

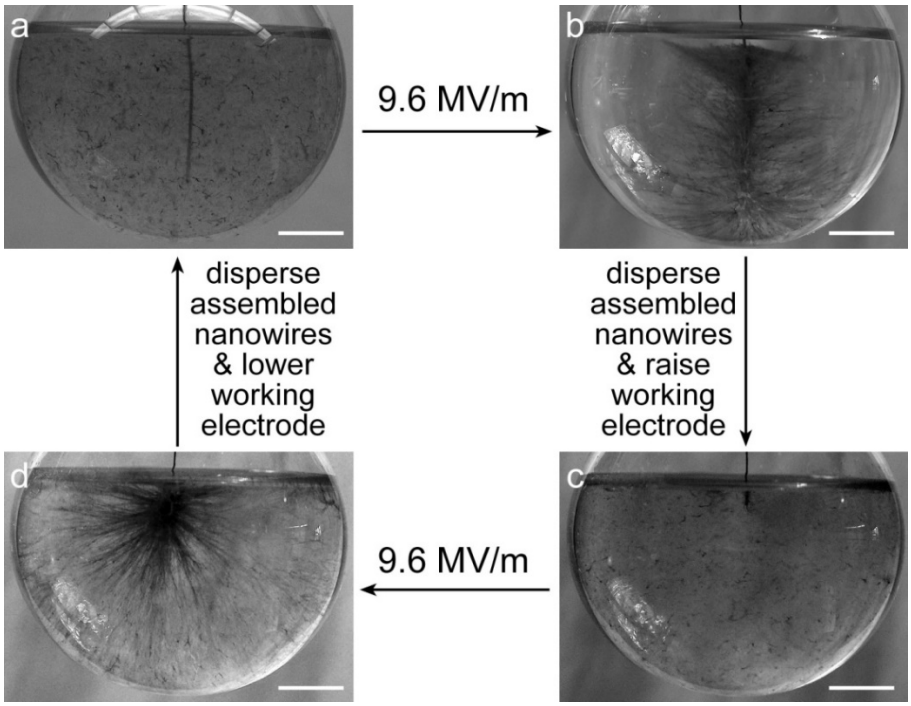

Figure 4.15 Optical image of (a) a suspension of dispersed selenium nanowires and a Cu working electrode in a round-bottom flask. (b,d) The selenium nanowires are assembled into fibers that extend from the working electrode at 9.6 MV/m. (c) In the absence of an electric field the selenium nanowires can be redispersed through manual agitation. Scale bars are 1 cm.

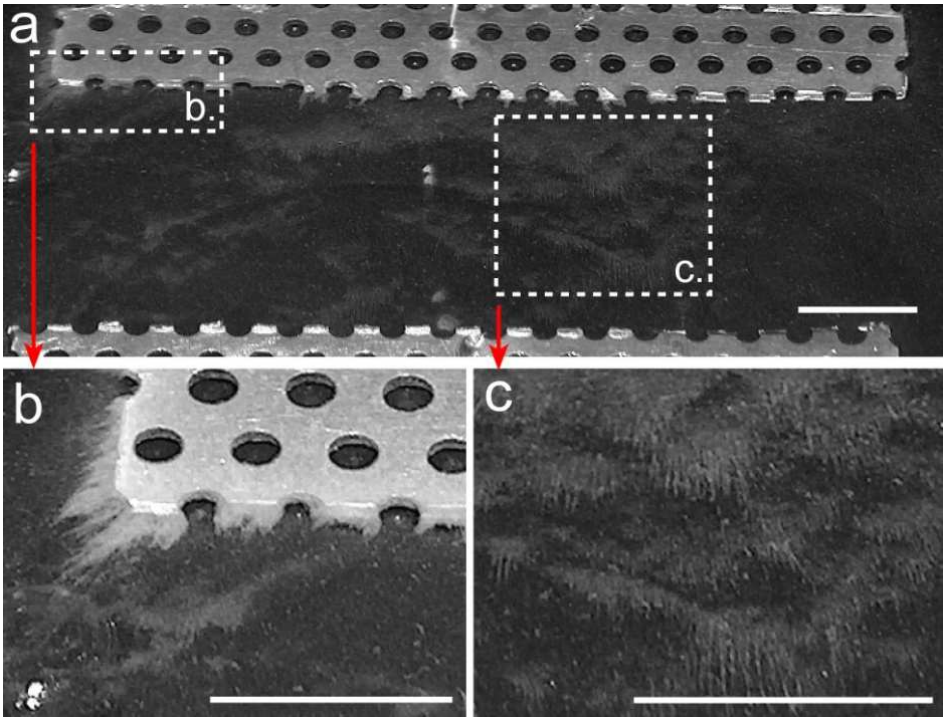

Figure 4.16 Optical images of silver nanowires assembled into fibers between two mesh electrodes. (a) Silver nanowires assembled between two electrodes of stainless steel mesh with electric field strength of 0.04 MV/m. (b) The assembled nanowires form dense fibers extending from the sharp edges of the ground electrode, and (c) also assemble into aligned fibers between the two electrodes extending in the direction of the field lines. All scale bars are 1 cm.

The open glass dishes were useful for assembling long fibers of selenium nanowires. Extending this to the assembly of silver fibers presented a larger challenge. Although these metal nanowires assembled into long fibers (>1 cm) within glass vials, in the open glass dish the silver nanowires formed short fibers (Figure 4.16). One of the primary reasons for our inability to form long silver fibers in the open dish was the interaction of the silver nanowires with the surfaces of the glass dish. The silver nanowires had a positive surface charge and assembled on the negative electrode. However, the negative charge of the glass also attracted these nanowires, and could be one of the reasons short fibers of silver nanowires irreversibly collected on the bottom of the glass dish (Figure 4.16c). Despite our attempts to protect the glass surface with a coating of 1H,1H,2H,2H-perfluorodecyltrichlorosilane, the metal nanowires irreversibly adhered to the surfaces of the glass dish. However, the nanowires collected within the region between two electrodes did align with the direction of the applied electric field.

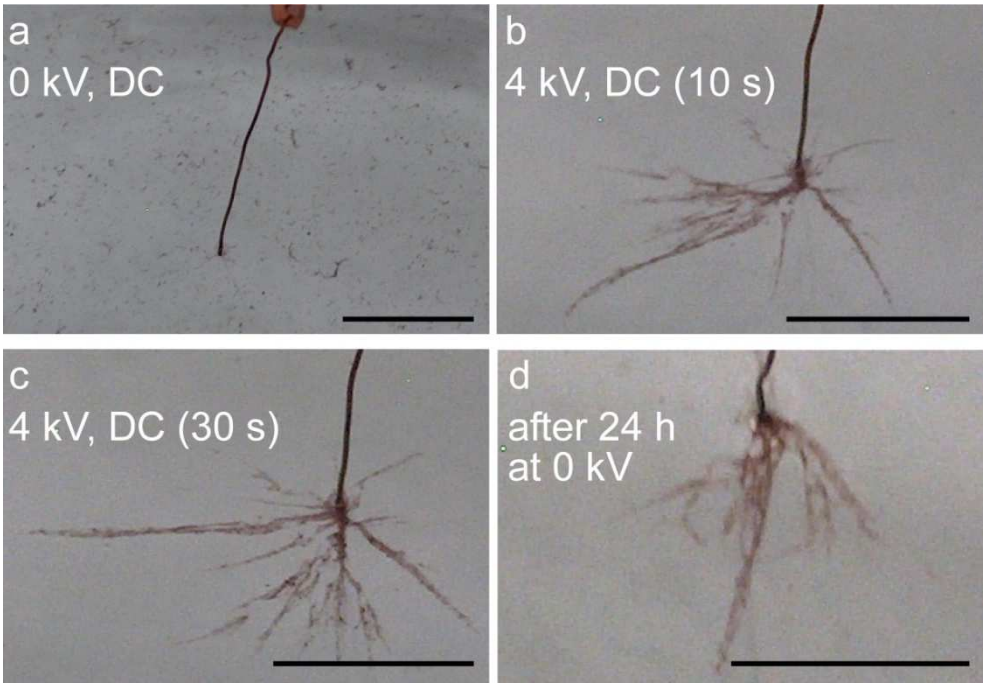

Figure 4.17 Time-resolved optical images of fibers assembled from selenium nanowires. (a) A dispersion of selenium nanowires assembles at the working electrode. (b) After 10 s and (c) 30 s of an applied electric potential of 4 kV, selenium nanowires assemble into fibers extending in multiple directions from the tip of the working electrode. (d) These suspended fibers remain intact and attached to the working electrode for >24 h after removing the applied electric potential. Scale bars are 1 cm.

Electrokinetic assembly of nanowires can form very long and stable fibers. Nanowires can be assembled into fibers with lengths >7 cm that are suspended in solution (Figure 4.11e). These fibers are stable upon removal of the applied electric field. The suspended fibers stay in contact with the electrode and remain intact except for distortions imparted by Brownian motion and gravitational forces on these dense materials (Figure 4.17). If the aspect-ratio of the nanowires is significantly decreased the nanostructures assembled into a very different arrangement. These shorter nanowires will also assemble within the applied electric field, but the observed assemblies are no longer simple fiber-like structures. Selenium nanowires with lengths of ~1 μm assemble into thick bundles extending from the working electrode (Figure 4.18). These bundles do not form the long fibers that were observed for the assemblies of 50-μm long nanowires. Higher resolution imaging is required to further understand the interactions between the 50 μm nanowires within the observed fibers.

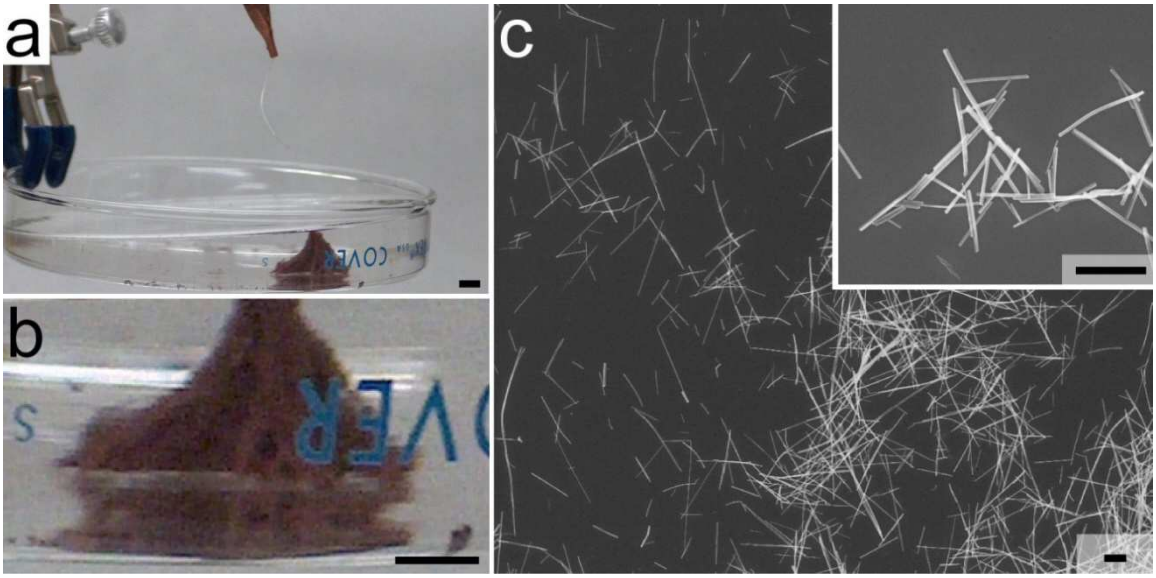

Figure 4.18 (a,b) Optical images of a mountain-like structure assembled by electrokinetic processes from selenium nanowires with lengths of ~1 µm. These structures grew by assembly of the short nanowires collected at the working electrode under field strengths of 5 MV/m. (c) Scanning electron microscopy (SEM) images of the original selenium nanowires with average lengths of 1.08 ± 0.44 µm. Scale bars in a and b are 0.5 cm, and in c are 1 µm.

A simple technique to remove the selenium fibers from solution is to use the ground electrode to lift-out the fiber while the power supply is in operation. The process of lifting-out the fiber from the assembly solution is similar to fishing. Fibers of selenium will move toward the ground electrode when it is lowered into the low dielectric constant medium. Once a fiber of selenium is in contact with the ground electrode, the electrode is quickly removed from the solution, taking the assembled fiber of selenium with it. (*Warning: use extreme caution when dipping the ground electrode into a combustible medium, the ground electrode should be at least 3 cm apart while performing the electrokinetic assembly and during the process of removing assembled selenium fiber to avoid arcing. Sparks created from electrode arcing could easily initiate combustion of the hexanes.*) The low surface tension of hexanes minimizes potential distortions to the fiber during a quick solvent evaporation (~1 s). Scanning electron microscopy (SEM) analysis suggests that the fibers are held together by entangled nanowires (Figure 4.19a,b). The nanowires interact with each other in solution through van der Waals and electrostatic forces, and possibly through material polarization within the applied electric field. If the fibers of selenium nanowires were not removed from solution prior to evaporation of the

bulk solvent the structure of the fiber looked very different. The nanowires within the fiber collapsed into a two-dimensional structure due to reorganization during solvent evaporation over a period of 12 h (Figure 4.20). These structures were sheets of randomly oriented nanowires with an outline in the shape of the original fiber. The collapsed structure strongly adhered to and could not be removed from the substrate.

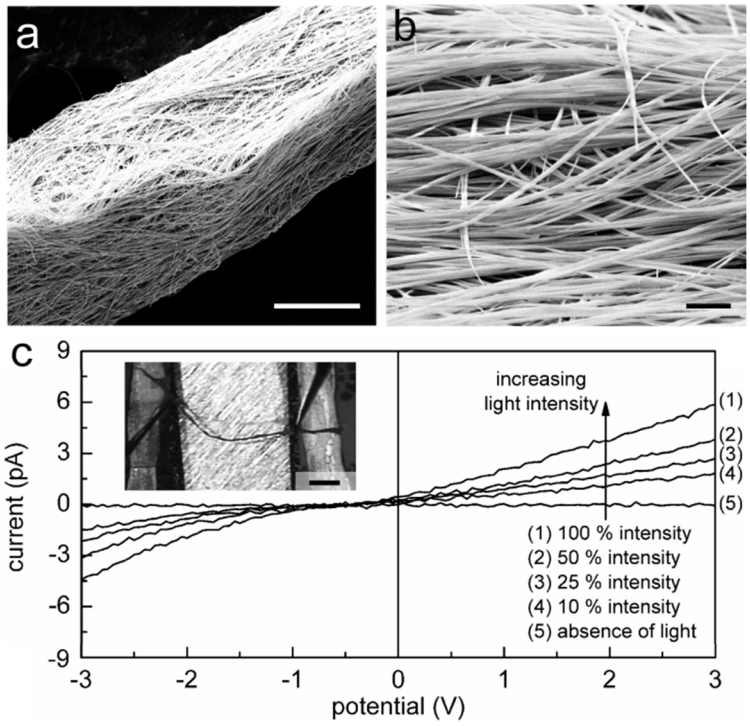

Figure 4.19 (a,b) Single fibers can be isolated from the solution and imaged by SEM. (c) These fibers exhibit increased conduction as a function of the intensity of light from LEDs used to illuminate the sample (Figure 4.7). The inset shows an optical image of the selenium fiber on a glass substrate with a tungsten probe in contact with either end of the fiber. Scale bars are 20 μm in a, 2 μm in b, and 1 mm in c.

The free-standing selenium fibers exhibited photoconductive properties. The fiber was insulating in the absence of light (Figure 4.19c), but became conducting with white light illumination producing peak currents of -4.4 to 5.8 pA at -3 and 3 V, respectively. The observed current under white light illumination was non-symmetric around 0 V, possibly due to charge accumulation on the fiber. The current passing through the selenium fiber is considerably lower in comparison to that reported by Liao *et al.* for a single selenium nanowire (~100 nm in diameter) over a distance of ~500 nm.[70] There are at least three possible explanations for the relatively low conductivity of our

assembled fibers. One reason is the low intensity of the LED light source used in these studies (i.e., 3.6 mW/cm^2 at 633 nm, Figure 4.7) relative to that of Liao *et al*. (i.e., 514 nm output from an Ar ion laser).[70] In addition, the mobility of charge carriers decreases for nanowires with smaller diameters (our nanowires have diameters between 20 and 60 nm in comparison to ~90 nm nanowire diameter reported by Liao *et al.*).[175-176] A third possible explanation for the relatively low photoconductivity of the assembled fibers of selenium is the increased resistance due to the long (~4 mm) and discontinuous pathway for electronic transport along the fiber. Furthermore, electrons are scattered at the nanowire-to-nanowire interfaces while they are moving between different strands of nanowires when they are traveling to the drain electrode (Figure 4.21).[177-178]

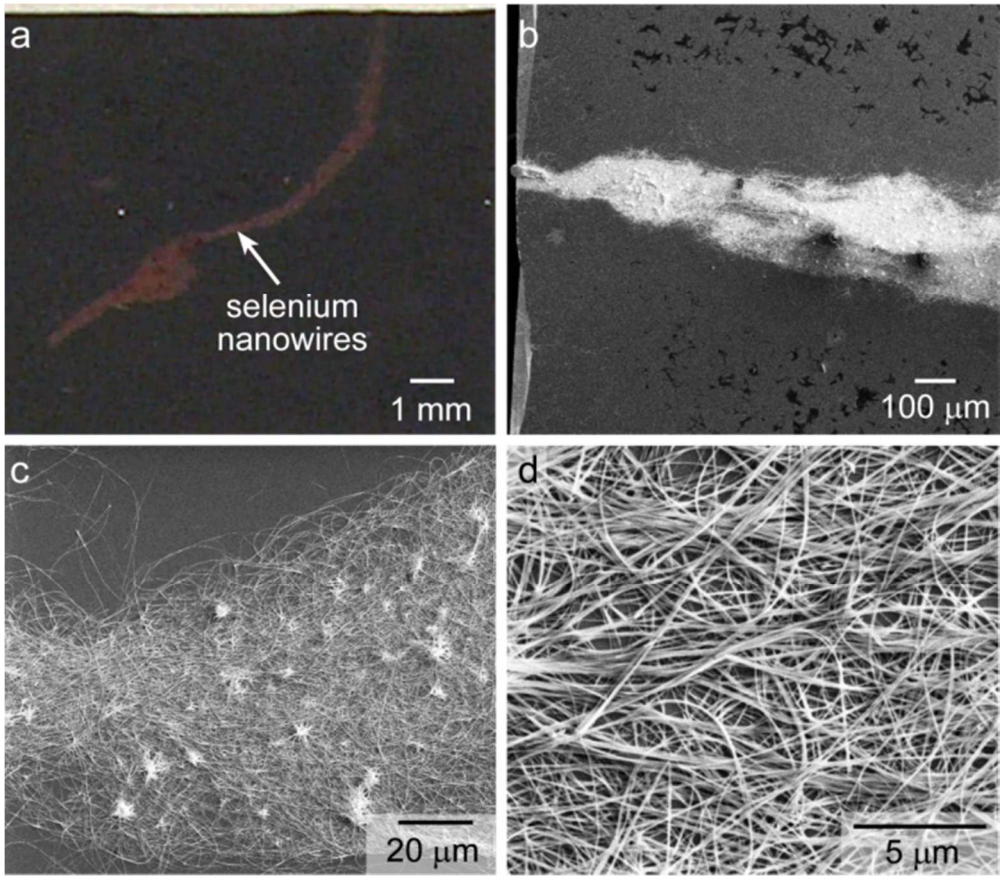

Figure 4.20 (a) Optical image of a collapsed fiber assembled from selenium nanowires supported on a silicon substrate. (b-d) SEM images of the sample in (a) revealed that the selenium structure was composed of randomly oriented selenium nanowires and did not retain the original shape of the fiber.

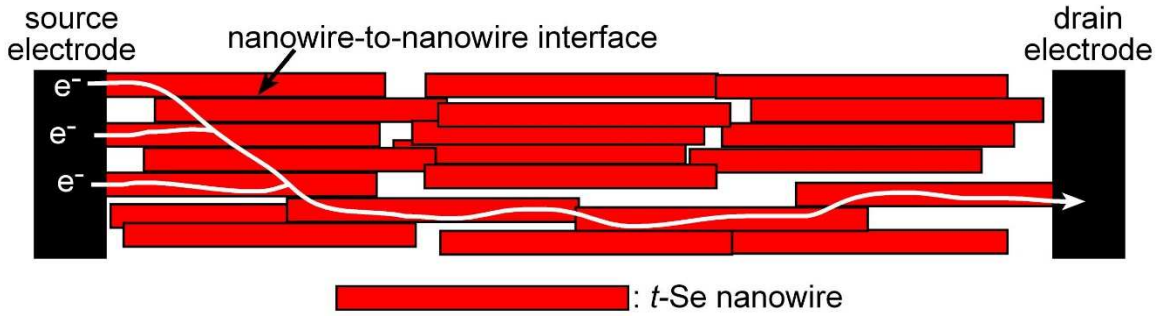

Figure 4.21 Electrons moving through a fiber composed of selenium nanowires are scattered at the nanowire-to-nanowire interfaces.

Fibers of selenium nanowires isolated from solution exhibited the ability to reversibly bend in response to electrostatic charges brought into proximity to these fibers. A free-standing fiber bends relative to the magnitude of the electrostatic charge. One method of introducing charge onto the fibers is through the use of a ZeroStat® anti-static gun. A free-standing selenium fiber deflects away from the source of the charge; the fiber can move either up or down depending on the relative position of the external charge (Figure 4.22a-d). The fiber is repelled from the external charge independent of the polarity of the applied charges (i.e., negatively or positively charged ions). This is an indication that there was a saturation of charge accumulated on the surfaces of the fiber (Figure 4.22a,b). Each fiber was electrically insulated from ground, leading to a quick accumulation of charge and a fast response (or actuation) of the fiber. These charged fibers were attracted to either an electrical ground or oppositely charged material (Figure 4.22c,d). The actuated fibers exhibited a high range of flexibility (reversibly bending over angles of at least 154°; see Figure 4.23) and a moderate resistance to breaking (remaining predominately intact after bending >200 times; Figure 4.22e). Analysis by SEM revealed the presence of some fractured nanowires at the bend in the fiber after being reversibly bend >200 times. These fractured nanowires are predominately located near the center of the fiber (Figure 4.22f).

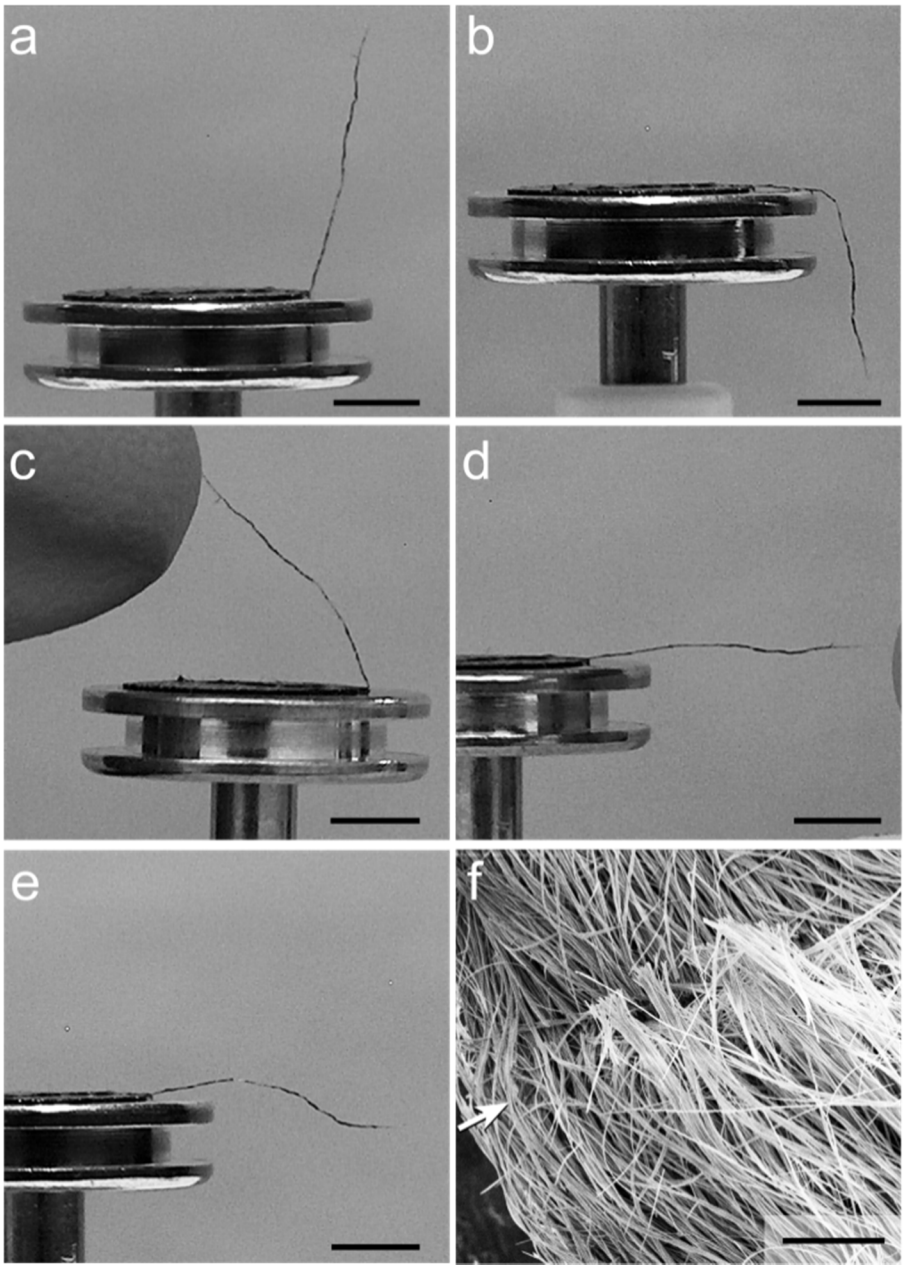

Figure 4.22 (a-e) Optical images of a selenium fiber partially supported on carbon tape upon an aluminum mount that is electrically insulated from ground. (a,b) This fiber is repelled by charged ions produced from a ZeroStat® anti-static gun. (c,d) This same fiber is attracted to electrical ground or oppositely charged materials. (e) After bending the fiber >200 times by steering the fiber with electrostatic charges the fiber remains intact, but (f) SEM analysis reveals fractured nanowires along the bend in the fiber (indicated by the white arrow). Scale bars in a-e are 1 cm and in f is 10 μm.

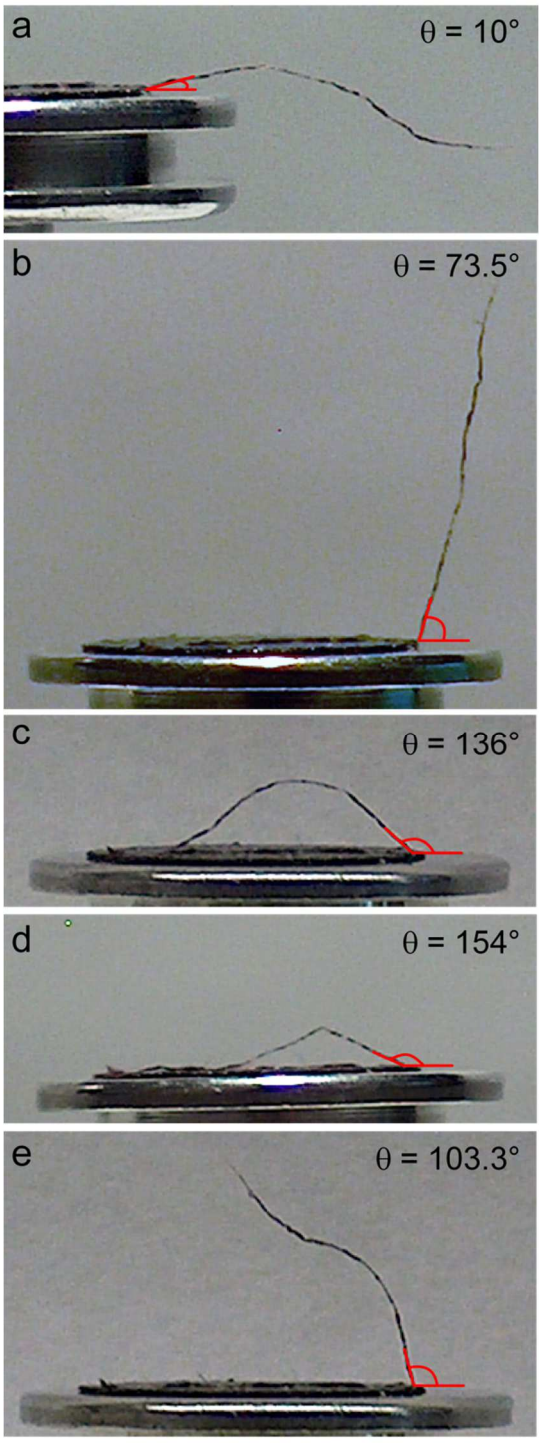

Figure 4.23 (a-d) Optical images of a free-standing fiber of selenium nanowires that was bent by actuating the fiber with electrostatic charges. The fiber was bent up to angles of at least 154°. (e) This fiber remained intact after repeated bending. Scale bar is 1 mm.

4.4. Conclusions

We have developed a technique for assembling nanowires of semiconductors and metals into macroscopic fibers directed along electric field when suspended in low dielectric solvents. We have determined that selenium and silver nanowires dispersed in a solvent with a dielectric constant <4.34 can be assembled into macroscopic fibers in the presence of an electric field. This electrokinetic assembly is dominated by electrophoretic movement of the suspended nanowires. The assembly process is simple to implement, fast, and reversible. Multiple nanowires can be assembled in a parallel process over distances much greater than the length of the individual nanowires. Anisotropic structures extending over ~7 cm are assembled from dispersions of nanowires within 1 min of applying an electric potential to the solvent. These fiber-like structures can be isolated from solution, or re-dispersed with manual aggitation as a suspension of individual nanowires, which can be assembled into another fiber. Fibers of selenium nanowires are able to retain their polarization for >24 h after the electric field is removed. Silver nanowires, on the other hand, are unable to remain assembled as fibers after the electric field is removed. Both assembled structures of selenium and silver have retained their crystal structure as well as surface chemical state(s). The morphology of the individual nanowires is also retained after the electrokinetic assembly process. We are able to isolate free-standing fibers of selenium nanowires with the ground electrode, while under the presence of an electric field. Free-standing fibers of selenium nanowires are mechanically flexible and photoconductive. Photoconductivity of the fibers of selenium nanowires is ~100 times lower than a single selenium nanowire device reported by other literature. We have attributed 1) a weaker irradiation intensity (i.e., LED lighting versus an Ar ion laser), 2) a ~2 times narrower selenium nanowire diameter, and 3) an increase in the resistance of the fibers of selenium nanowire due to electron scattering as the electrons hop from nanowire-to-nanowire could be one of the potential contributing factors that resulted in the significant decrease in our observed photoconductivity. Overall, electrokinetic techniques are versatile and scalable for directing the assembly of solution-phase synthesized nanowires that may otherwise be difficult to organize.

4.5. Future Directions in Electrokinetic Assembly of Selenium and Silver Nanowires

Electrokinetic assembly can be extended to directing the alignment of individual nanowires over micron-scale lengths[148, 151, 155-158, 179] as well as to purify solution-phase synthesized nanowires. Most solution-phase syntheses are able to produce nanowires of uniform diameter. It is, however, more challenging to synthesize nanowires of similar lengths as the aspect-ratio increases. Nanowires of different lengths are formed because nucleation is not instantaneous, growth is diffusion-limited, and these nanowires are competing for limited amount of reagents. As a result, most solution-phase syntheses yield nanowires with a polydisperse aspect-ratio and zero-dimensional (0D) nanoparticles as common byproducts. The presence of these 0D particles, in a sample to be assembled into a 2D array, can disrupt the packing of nanowires, resulting in packing defects.[103, 136] There are a few techniques such as cross-flow separation,[180] diafiltration,[181] density gradient sorting,[182] and gel electrophoresis[183] have been developed to sort nanostructures. We believe that electrokinetic assembly can be used both as a purification and sorting technique to isolate nanowires of different aspect-ratios from one another and to separate the nanowires from 0D nanoparticles.

To perform electrokinetic assembly at the micron scale, microelectrodes with a few micrometers of separation between each other can be fabricated using photolithography or electron beam lithography techniques on insulating substrates, such as quartz, silica, or borosilicate glass. These electrodes would then be protected with silicon nitride to prevent shorting of the electrodes during the assembly process. The geometry of these electrodes can be optimized by performing electric field simulations using COMSOL finite element methods. The electric field simulation will provide information on the location(s) of the highest electric field strengths, in which the nanowires will be collected and oriented parallel to the direction of the electric field. As an example, an interdigitated electrode geometry (Figure 4.24a) has highest electric field strength along the length of the electrodes, therefore, nanowires will align perpendicularly between the length of the electrodes. In contrast, the highest electric field strength is located between the tips of electrodes. Nanowires will align in between the tips of the electrodes and orient parallel to the length of the electrodes in an end-to-end electrode geometry (Figure 4.24b).

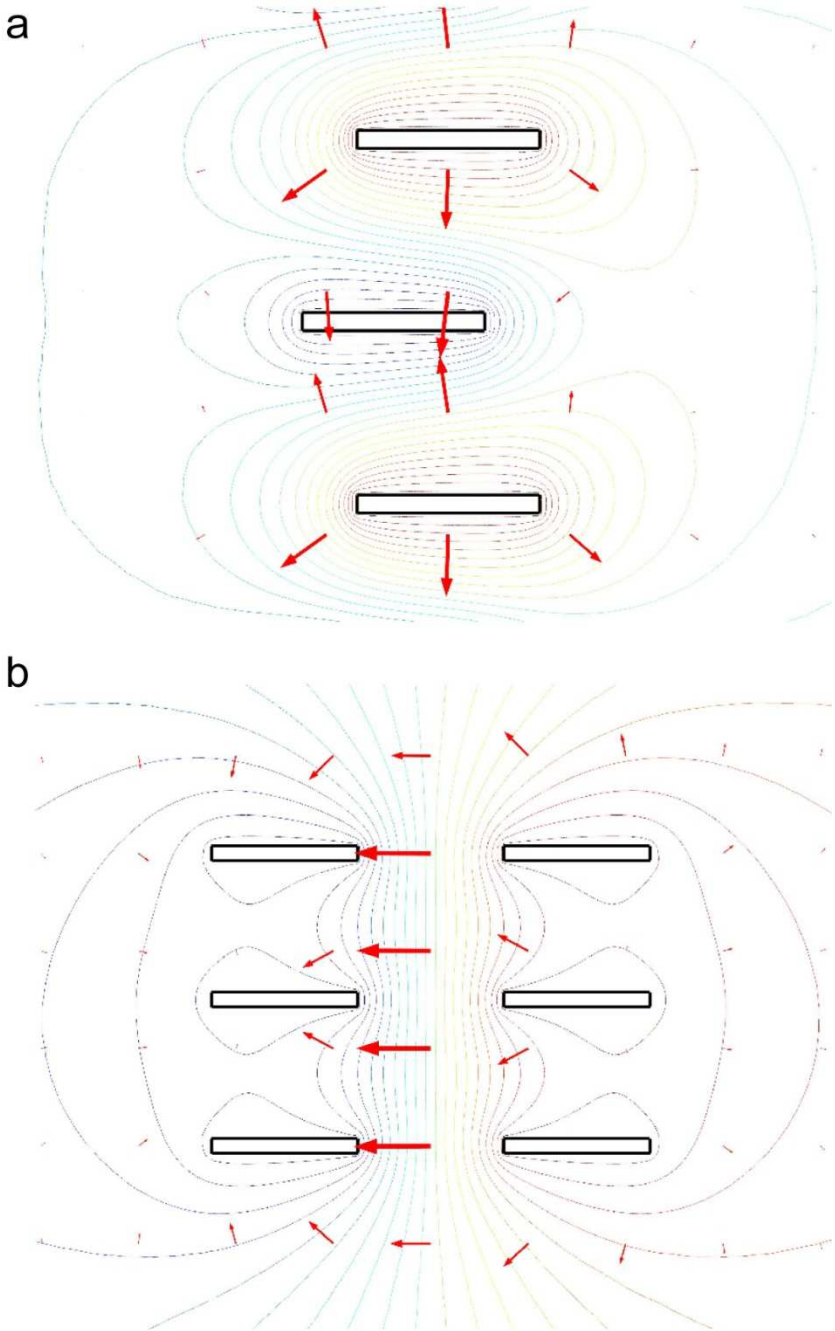

Figure 4.24 Electric field simulation using COMSOL finite element methods. The electric field vector and strength are expressed in arrow and contour plots, respectively, of an (a) interdigitated and (b) end-to-end electrode geometry.

Substrates patterned with an array of electrodes via photolithography or electron beam lithography techniques would be coupled to flow cells, which are coupled in tandem. Each substrate would be patterned with electrodes of different spacing

designed specifically to trap nanowires of certain lengths or 0D nanoparticles. These substrates are connected to their own power supplies to permit changing of electric field strength within each flow cell (Figure 4.25a). A suspension of nanowire would be mechanically pumped through the flow cells. Each flow cell would be under different applied electric field strengths, which has been optimized to capture nanowires of certain lengths. A nanowire purification setup would be similar to the schematic drawn in Figure 4.25b. The direction of fluid flow should be parallel to the orientation of the assembled nanowires to minimize the removal of trapped nanowires due to strong hydrodynamic forces. We hypothesize that the selective removal of nanowires of certain lengths from a suspension or solution is possible when the separation distance between electrodes and the length of the nanowires are approximately equal. These electrokinetically bound nanowires of similar lengths can be subsequently removed from the substrate in the absence of an electric field by solvent rinsing.

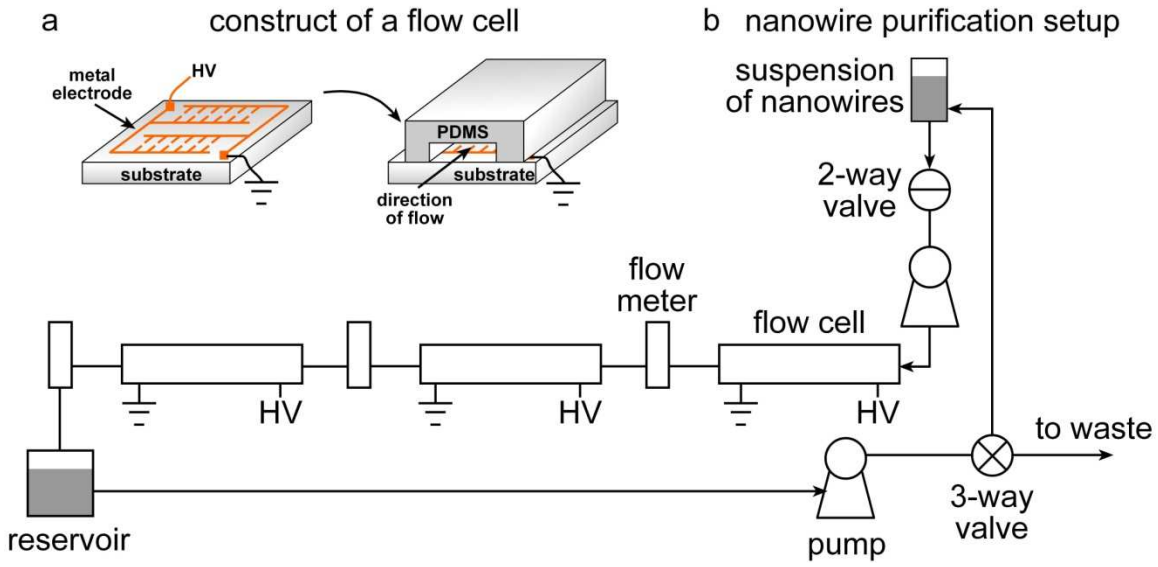

Figure 4.25 (a) An array of microelectrodes on a solid substrate is coupled to a polydimethylsiloxane (PDMS) substrate. The PDMS substrate contains prefabricated channels through which a suspension of nanowires is directed by fluid flow induced by a pressure differential. The direction of the fluid flow is parallel to the direction of the highest electric field strength located between the end-to-end registered electrodes. (b) A schematic showing a potential setup for nanowire purification.

5. Synthesis of Trigonal Selenium Nanowires Encapsulated in Polystyrene (*t*-Se@PS) by Surface-Initiated Atom Transfer Radical Polymerization‡

5.1. Motivations to Encapsulate Selenium Nanowires with Polystyrene

As a functional component of many materials, elemental selenium is used in the synthesis of various selenides and composites that have a wide range of applications. For example, it is used to synthesize metal selenides of various properties, such as luminescent materials,[33, 59, 62-63] phase-change memory materials,[64] and energy harvesting materials.[65-66] Selenium is also used as a key component in electromagnetic radiation sensors,[57, 67-70, 184] xerography,[55] biomedicine,[72-73] antimicrobial agent,[74] and mercury capturing sorbents.[76] The performance of selenium in these devices is inherently influenced by its surface chemistry, crystal structure, oxidation state, and structural integrity.

Oxidation is a process describing an increase in the oxidation state of matter.[52] Oxidation of a solid material, typically, occurs at the air-solid or liquid-solid interphases where oxygen or other oxidants are available. When oxidation occurs in the presence of moisture, ions from the oxidized materials are solubilized by water as hydrated ion complexes. These ion complexes are, subsequently, transformed within the presence of water to form corresponding oxides. These newly formed oxide species are less soluble in water in comparison to the corresponding ion complexes and precipitated from water, leaving deposits that can easily delaminate from the surfaces of solid materials. A solid

‡ Experiments were carried out by Michael C. P. Wang and the manuscript was co-written by Michael C. P. Wang and Professor Byron D. Gates. The contents of this publication were reproduced with the permission of the Royal Society of Chemistry and co-authors.[47]

material could eventually degrade completely to its corresponding oxides or ionic complexes after a prolonged process of oxidation, dissolution, and precipitation. The progression of this material degradation is commonly referred to as corrosion. For corrosion to occur a material is first oxidized. The relative reduction potentials of substances are the deterministic factor that dictates whether electrochemical reactions will proceed spontaneously. For example, oxygen, with a reduction potential of 1.23 V under acidic conditions, is a strong oxidant capable of oxidizing most zerovalent metals and semiconductors, including selenium.[23, 52] In reactions between these metals/semiconductors and oxygen, the overall standard electrochemical cell potentials (E^{o}_{cell}) are always positive (Eqn. 5.1), indicating these processes will occur spontaneously.

$$E^{o}_{cell} = E^{o}_{red.}(cathode) - E^{o}_{oxd.}(anode) \quad \text{(Eqn. 5.1)}$$

The E^{o}_{cell} is directly correlated to the Gibbs free energy (Eqn. 5.2), where ΔG^{o} is the standard Gibbs free energy, n is the number of moles of electrons transferred per mole of reaction, and F is the Faraday constant. A positive E^{o}_{cell} value equates to a negative Gibbs free energy, which suggests such that a reaction is thermodynamically favorable.[52]

$$\Delta G^{o} = -nFE^{o}_{cell} \quad \text{(Eqn. 5.2)}$$

A well-known example of corrosion is the oxidation of iron to iron rust in the presence of oxygen and moisture.[185] Oxidation of the iron leads to the formation of iron oxides (e.g., $Fe_2O_3 \bullet nH_2O$) and pitting of the material at its surfaces.[52] As oxidation progresses, these pits propagate into cracks within the iron substrate.[186] The defect riddled iron substrate would eventually have a decreased structural integrity in comparison to a non-oxidized iron substrate.[187] Oxidation and corrosion can also have a great impact on the properties and long-term utility of nano-scale materials. In some cases corrosion can have a more pronounced impact on nanostructures than in their bulk counterparts.[188-191] Oxidation does not always lead to corrosion of the underlying material. Oxides of aluminum,[192] and silicon[193] protect the underlying material from further oxidation and corrosion.

For nano-scale materials, the ratio of surface-area-to-volume is larger than that of bulk materials. Surface chemistry of nanostructures plays a significant role in the performance and integrity of these functional materials. Since most oxidation processes have a negative Gibbs free energy, the formation of oxides is thermodynamically favourable.[52] Many metals and semiconductors oxidize when left for extended periods of time in an environment containing oxygen and moisture. Magnetite (Fe_3O_4) nanoparticles, for example, decrease in saturation of magnetization as they oxidize into maghemite (γ-Fe_2O_3).[194] Another example is the oxidation of silicon based nanowires and quantum dots (QDs) into Si/SiOx core–shell nanostructures.[19, 195-201] Researchers have demonstrated that oxidation of the Si QDs will lead to a decrease in their photoluminescence intensity and an increase in the bandgap energy.[200] Some nanomaterials, such as these Si containing particles, form self-limiting layers of oxide that protect the nanostructure from further oxidation.[19] However, little is known about the surface chemistry of trigonal selenium (*t*-Se) nanostructures and how its surface chemistry evolves over time under ambient conditions in the presence of acid vapour. We hypothesize that native selenium could contain one of these three types of surface chemistries: the surface selenium atoms could terminate in 1) dangling bonds (i.e non-bonding electrons available on Se (Figure 5.1a); 2) selenium-hydride bond (Se-H, Figure 5.1b), and 3) selenium oxides (i.e., Se-OH or Se-O-Se; Figure 5.1c depicts the Se-OH surface chemistry) or a mix of these surface chemistries. We seek to identify the chemical state(s) associated with the surface chemistry of surfaces of *t*-Se nanostructures and to analyze the effect of oxidation on these materials. In addition, we are interested in developing techniques to impede corrosion of the selenium nanostructures.

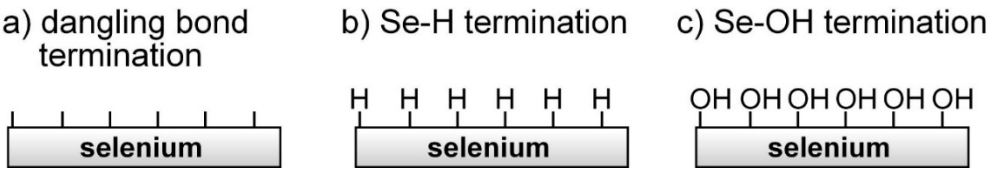

Figure 5.1 Possible surface chemistries of native trigonal selenium nanowires with terminal groups that could be present as (a) dangling bonds, (b) Se-H, and (c) Se-OH. Sticks in (a) represent non-bonding electrons.

The process of corrosion occurs only when materials are exposed to both oxidants and moisture. Corrosion, therefore, can be prevented if one of the principle

elements is shielded from interacting with the material. There are a number of well-developed processes designed to impede corrosion of metals and semiconductors. Most strategies involve making a composite material in which a passivation layer is deposited to protect the surfaces of interest. Techniques such as electrodeposition[202-203] and surface passivation with monomeric or polymeric molecules[204-207] have been implemented with great success to retard oxidation, or to selectively protect an underlying material. More recently, surface initiated atom transfer radical polymerization (SI-ATRP) has been used to graft polymers onto the surfaces of various materials.[208-215] Modifying the surfaces of a nanostructured material with a polymer film allows researchers to tailor its surface properties, such as its tribology,[216-217] wettability,[218-219] biocompatibility,[220-221] and corrosion resistance.[222-224] Covalently linking polymers to the surfaces of nanostructures is a preferred strategy because physically adsorbed polymers can easily detach from these surfaces (Figure 5.2a). Polymers can be *grafted onto* various surfaces by forming covalent bonds between the polymers and the reactive groups on the surfaces of the nanostructures (Figure 5.2b). This method does, however, have difficulty achieving high grafting densities because the adsorbed polymers effectively shield some of the reactive surface sites. This grafting technique will produce porous and non-uniform polymer coatings. On the other hand, surface-initiated atom transfer radical polymerization (SI-ATRP) offers the ability to control the functionality, density and thickness of the polymer coating. Rather than grafting bulky polymers onto the surfaces of a material, chain propagation occurs at the reactive sites in a SI-ATRP (Figure 5.2c). Polymers *grafted from* the surfaces of a substrate by this atom transfer radical polymerization are, therefore, better suited to the preparation of polymer coatings of higher quality and density.

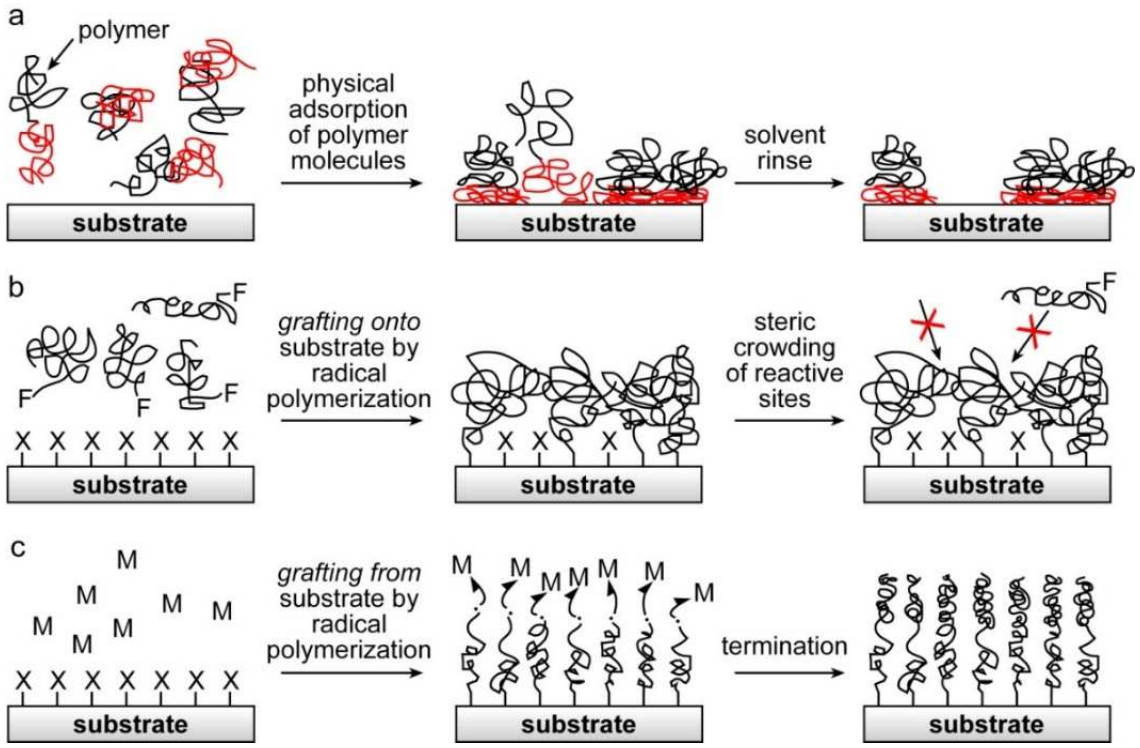

Figure 5.2 Strategies of passivating surfaces of a substrate through (a) preferential physisorption of the red portion of a copolymer, (b) covalently linking a polymer to the surfaces via radical polymerization, and (c) polymers are grown on the substrate surface by a surface-initiated polymerization. X denotes an initiating group, F denotes the appropriate functional group that could react with radicals and M is a monomer, both of which will react with a radical species.

Most surfaces do not possess the appropriate functional groups to undergo surface-initiated polymerization. Additional chemical modifications to these surfaces are necessary. These surfaces are typically modified with initiator-bearing self-assembled monolayers (Figure 5.3). The initiator covered surfaces are then immersed in a solution of monomer and catalyst, which subsequently converts the initiators into radicals to start the polymerization process.[208-209] Since the initiators all reside on the surfaces of the material to be encapsulated with the polymer, the polymerization is confined to the surfaces of the substrate.

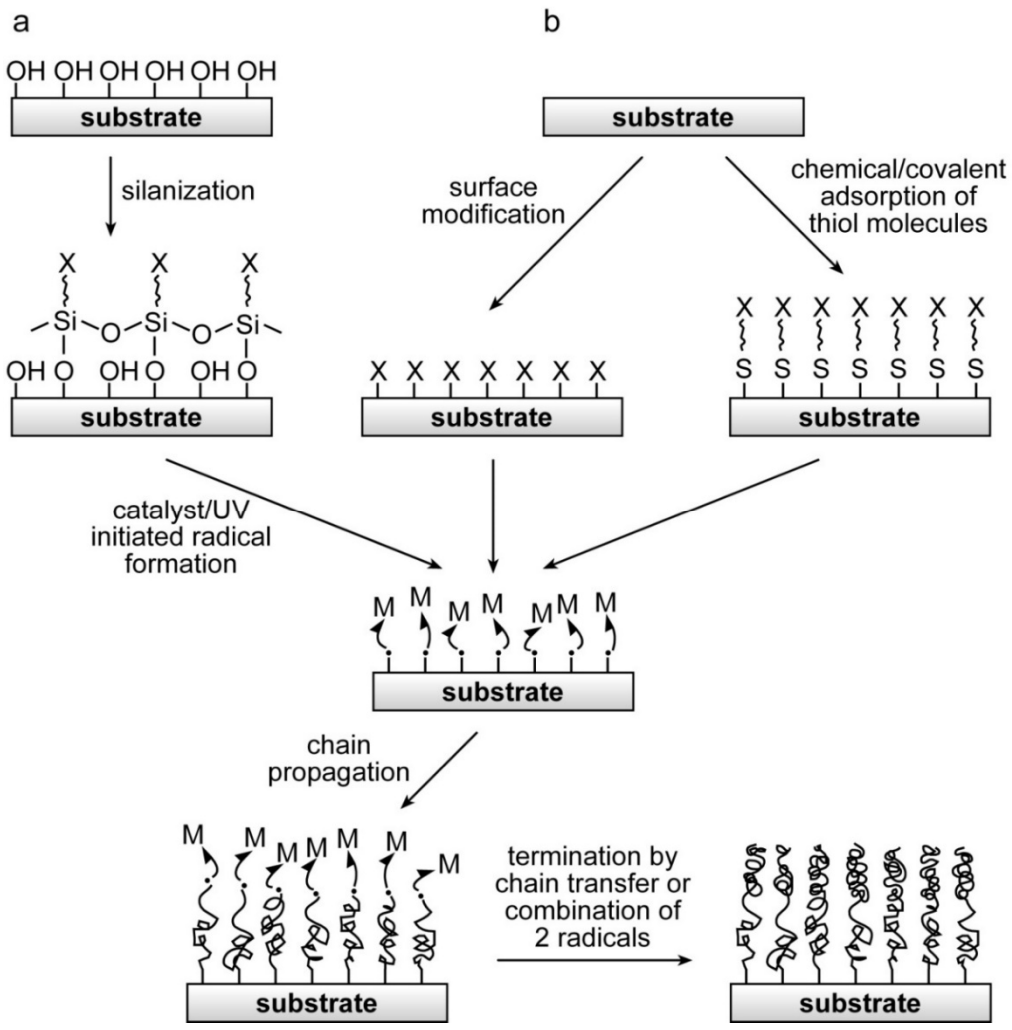

Figure 5.3 Surfaces of (a) oxides and (b) polymer or non-oxide inorganic substrates are modified with initiating groups using the appropriate chemistry prior to surface-initiated atom transfer radical polymerization. X denotes an initiating group and M denotes a monomer that will react with a radical species.

This chapter reports the synthesis of a novel semiconductor-polymer material consisting of anisotropic *t*-Se nanowires encapsulated in a sheath of polystyrene (*t*-Se@PS) by SI-ATRP processes without the need for further modification to the surface chemistry of the as-synthesized *t*-Se nanostructures. The PS layer acts as a moisture barrier to impede the corrosion of the *t*-Se nanostructures. The resulting *t*-Se@PS nanostructure was characterized by scanning transmission electron microscopy (STEM), electron diffraction, and X-ray photoelectron spectroscopy (XPS). The quality of the PS coating was examined by immersing the *t*-Se@PS in various oxidizing solutions. The

semiconductor-polymer nanomaterial was subsequently analyzed by transmission electron microscopy for corrosion damage. In addition, as a frame of reference the surface states of the *t*-Se nanowires were analyzed by surface sensitive techniques such as XPS and SIMS after exposure to oxygen containing environment and an etchant. The crystallinity and structure of these *t*-Se nanowires were investigated by STEM and electron diffraction techniques before and after exposure to corrosive conditions.

5.2. Experimental Section

Anisotropic nanostructures of single crystalline *t*-Se were synthesized by a hydrothermal process without the assistance of surfactants, which are commonly used to facilitate the formation of many other anisotropic nanostructures.[18, 225] Surfactants are used in other syntheses to prevent the nanostructures from aggregating, and serve as protective barriers between the nanostructures' surfaces and the surrounding chemical environment. The absence of surfactants or other coatings on the surfaces of the selenium nanostructures expose its surfaces to corrosive damage by oxygen and moisture.

5.2.1. Synthesis of One-Dimensional Trigonal Selenium Nanostructures.

One-dimensional selenium nanostructures were synthesized from amorphous selenium colloids. The selenium colloids were synthesized by reducing selenious acid with hydrazine. For example, 2.73 g (21.1 mmol) of selenious acid (H_2SeO_3; 98%; Sigma-Aldrich) was dissolved in 100 mL of 18 MΩ•cm water (purified with Barnstead Nanopure DIamond Life Science water filtration system) with magnetic stirring in a 250 mL round bottom flask. The solution was cooled to ice-water temperatures before slowly adding 3 mL (61.1 mmol) of ice cooled reducing agent, hydrazine (N_2H_4; 50-60%; Sigma-Aldrich). Hydrazine was introduced in a drop-by-drop manner into the reaction solution under magnetic stirring over a period of 2 min. The reaction was allowed to proceed for another 15 min while at ice-water temperatures before the brick red precipitate was collected by vacuum filtration onto a PVDF filter membrane with an average pore size of 0.1 µm (catalogue number VVLP04700; Millipore). The filtrate was

rinsed with 200 mL of deionized water to remove residual hydrazine. The filtered precipitate of selenium colloids was stored in a plastic petri-dish wrapped in aluminum foil and freeze dried in a Savant Modulyo lyphoilizer (Thermo Scientific) at -50°C and 100 mbar for 12 h.

Anisotropic *t*-Se nanostructures were synthesized from amorphous selenium colloids by a solvochemical method. Selenium colloids (1 mg) were combined with ethanol (EtOH; 2 mL; 95%; Commercial Alcohols) in a 2 dram glass vial (Thermo Scientific™; catalogue number: B7999-2). The selenium colloids were dispersed in the EtOH by immersion of the vial for 20 s in a sonication bath (Branson Model 1510). The solution was then placed in a dark cabinet maintained at 22°C to allow the reaction to reach completion over a period of ~12 h. The resulting nanostructures are single crystalline as characterized by selected area electron diffraction.[31]

5.2.2. Synthesis of Trigonal Selenium Nanowires Encapsulated in Polystyrene (t-Se@PS)

Selenium nanostructures dispersed in EtOH (2 mL; 233 mg/mL) were separated from solution via centrifugation (13,500 rpm for 15 min). The solvent was decanted and replaced with dichloromethane (DCM; 99%; Caledon) to re-disperse the selenium nanostructures. This process was repeated twice in total to remove residual ethanol. Finally, selenium was re-dispersed in 10 mL of DCM, which was combined with 10 mL of styrene (99%; Sigma), and 10 mL of hexanes (>98.5%; EMD Millipore) in a three-necked round bottom UV reactor. Nitrogen was bubbled via a glass pipette through the reaction mixture for 10 min while cooling the solution to ice-water temperatures. Then the glass pipette was elevated above the reactants to maintain the inert atmosphere over the next 6 h of UV irradiation. The UV light source was a mercury pencil lamp (Oriel Instruments Model 6035; see Figure 5.4 for its emission spectrum) powered by a DC power supply (Oriel Instruments Model 6060). The final product, *t*-Se@PS, was purified by centrifugation (13,500 rpm for 15 min) and rinsed with a solution of 1:1 hexanes to EtOH (v:v) after decanting the original solvent. The product was purified three times in total, before it was redispersed in EtOH.

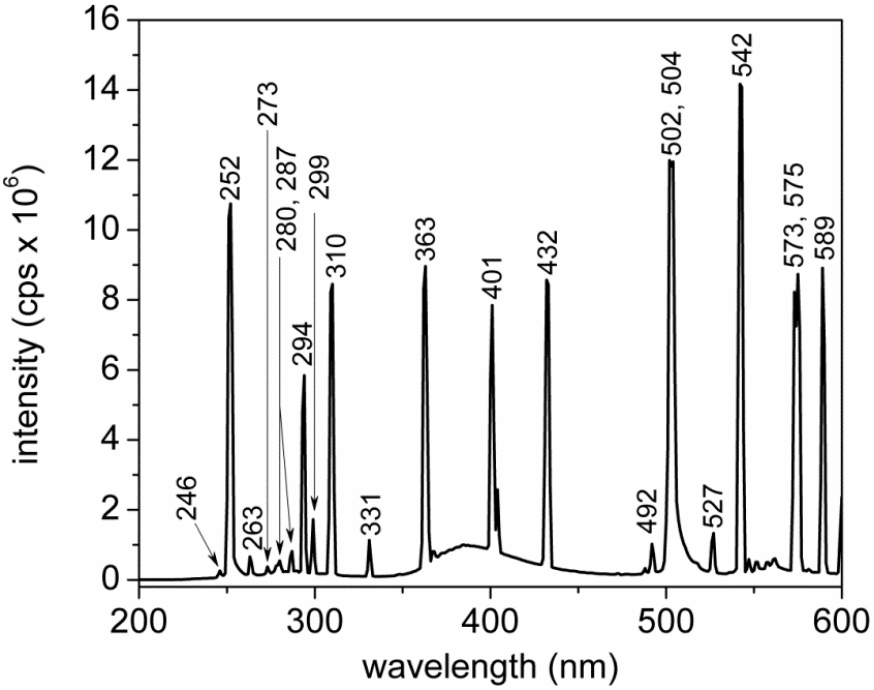

Figure 5.4 A spectrofluorometer was used to acquire the photoemission spectrum of the mercury pen lamp used to initiate the polymerization of styrene on the surfaces of selenium nanostructures. Reproduced from Ref. 46 with permission from The Royal Society of Chemistry.

5.2.3. Materials Characterization Techniques

Transmission electron microscopy (TEM) images, energy-dispersive X-ray spectroscopy (EDS) and selected area electron diffraction (SAED) data were obtained with either an FEI Tecnai G^2 F20 scanning TEM (STEM) with a field emission gun thermionic source operating at 200 kV, or a Hitachi 8000 STEM with a lanthanum hexaboride thermionic source operating at 200 kV. For TEM analysis, samples were prepared by drop-casting or dip-coating solutions of nanostructures onto a 300 mesh copper grid coated with formvar/carbon (catalogue number: FCF300_CU_50; Cedarlane Laboratories Ltd.). To test the resistance of the *t*-Se@PS nanowires to oxidation and corrosion, these samples were immersed into either a 1% or 30% aqueous solution of hydrogen peroxide (H_2O_2; Caledon) before they were drop-cast onto TEM grids. Selenium samples without surface passivation by PS were prepared by dipping a TEM grid containing *t*-Se nanostructures into 1% H_2O_2 for 5 s before the sample was flash frozen on a block of aluminum that had been cooled to liquid nitrogen temperatures. The frozen solution was removed by lyophilization before TEM analysis. Hydrogen peroxide

readily oxidized the *t*-Se nanowires forming water soluble species, such as selenious acid (H_2SeO_3) and selenic acid (H_2SeO_4).

Nanowires of *t*-Se@PS were immersed in nitric acid (68-70% HNO_3; Anachemia) to test these polymer coated semiconductor core-shell nanowires' ability to resist corrosion against ionic etchants. First, the *t*-Se@PS material dispersed in EtOH was collected via centrifugation (8,500 rpm for 15 min). The material was rinsed with 1 mL of DI water for a total of 3 times to remove residual EtOH. Then 1 mL of 30% of HNO_3 was added into the centrifuge tube containing the *t*-Se@PS nanowires. The polymer coated semiconductor core-shell nanowires were immersed in the ionic etchant at RT for 1 h before decanting the solution. The products were rinsed with 1 mL of DI water 3 times to remove residual acid before redispersing the nanostructures in 1:1 EtOH to hexanes (v:v) for TEM sample preparation. As a control, concentrated HNO_3 was added to a sample of *t*-Se nanowires after removal of the EtOH under vacuum. Concentrated HNO_3 dissolved the *t*-Se nanowires in ~10 min (Eqn. 5.3-5.5; see Figure 5.5).[226]

$$NO_3^- + 4H^+ + 3e^- \rightarrow NO + 2H_2O \qquad E^o = 0.957\ V \qquad \text{(Eqn. 5.3)}$$

$$Se + 3H_2O \rightarrow H_2SeO_3 + 4e^- + 4H^+ \qquad E^o = -0.74\ V \qquad \text{(Eqn. 5.4)}$$

$$3Se + 4HNO_3 + H_2O \rightarrow 3H_2SeO_3 + 4NO \qquad E^o_{cell} = 0.217\ V \qquad \text{(Eqn. 5.5)}$$

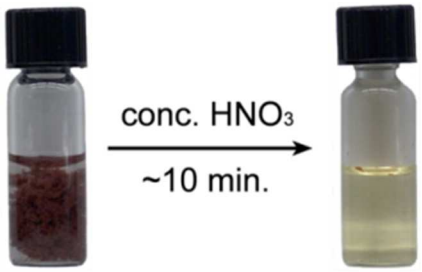

Figure 5.5 Anisotropic trigonal selenium nanowires dissolved in concentrated nitric acid (70% HNO_3) produced a transparent solution of selenious acid and nitric oxide.[226] Reproduced from Ref. 46 with permission from The Royal Society of Chemistry.

X-ray photoelectron spectroscopy (XPS) analysis was carried out on a Kratos Analytical Axis Ultra DLD spectrometer using a monochromatic aluminum source (AlKα, 1486.6 eV) operating at 150 W (10 mA emission current and 15 kV HT). Analysis was conducted on a 700 x 300 μm^2 area of the sample. High resolution scans were obtained

at a 25 meV step size with a dwell time of 1000 ms per step, a pass energy of 20 eV, and averaged over 4 scans. Energy scale linearity was calibrated using Al and Mg X-ray sources on Argon sputter cleaned gold and copper substrates. The calibration procedure was performed in accordance to the ISO 15472 international procedure (see Appendix C for further detail). XPS samples were prepared by drop-casting dispersions of *t*-Se or *t*-Se@PS onto a ~1 cm^2 polished Si/SiOx substrates. The as-synthesized *t*-Se sample (Figure 5.6a) cast on the Si/SiOx was left at ambient conditions (RT, and ~1 atmosphere) in a plastic petri-dish (VWR; catalogue number: 89038-968) for a month before XPS analysis to assess oxidation of the *t*-Se nanostructures (Figure 5.6b). Selenium oxide was removed by immersing the *t*-Se nanostructures deposited on a Si/SiOx substrate in a bath of 1% hydrofluoric acid (diluted from 48% non-buffered HF, EMD Millipore) for 2 min (Figure 5.6c).

Secondary ion mass spectrometry (SIMS) was carried out on a Hiden Analytical Ltd. instrument equipped with an IG20 gas ion gun and a triple quadrupole MAXIM mass spectrometer. Samples were sputtered with 5 keV Argon ions that were used to produce positive and negative ions species. SIMS samples were prepared by drop-casting dispersions of *t*-Se and *t*-Se@PS onto a ~1 cm^2 Au (100–nm thick) coated Si substrate or onto a ~1 cm^2 polished Si/SiOx substrate. Mass spectra were acquired at a mass increment of 0.01 amu at a dwell time of 100 ms per 0.01 amu. Multiple mass spectra were acquired from each sample, but only the best data is presented.

Photoemission spectrum of the mercury pen lamp was recorded on a PTI Quantamaster spectrofluorometer. The mercury pen lamp emission spectrum between wavelength of 200 to 600 nm was acquired with a slit width of 2-nm and at a scan rate of 60 nm/s. Data were acquired at a detector potential of 1079 V.

Optical absorption measurements (UV-vis spectroscopy) were performed with a Varian Cary 300 Bio spectrophotometer system. Samples were dispersed in or diluted with acetonitrile (Spectro grade; Caledon Lab) contained within a 1 cm path length quartz cell (catalog number: 100-10-40, Type 100-QS, Hellma Analytics). Selenium nanowires were sonicated for 30 s to achieve a uniformly dispersed solution prior to acquiring the optical absorption measurements. It is crucial to obtain a uniform dispersion to minimize scattering of incident radiation.

5.3. Results and Discussion

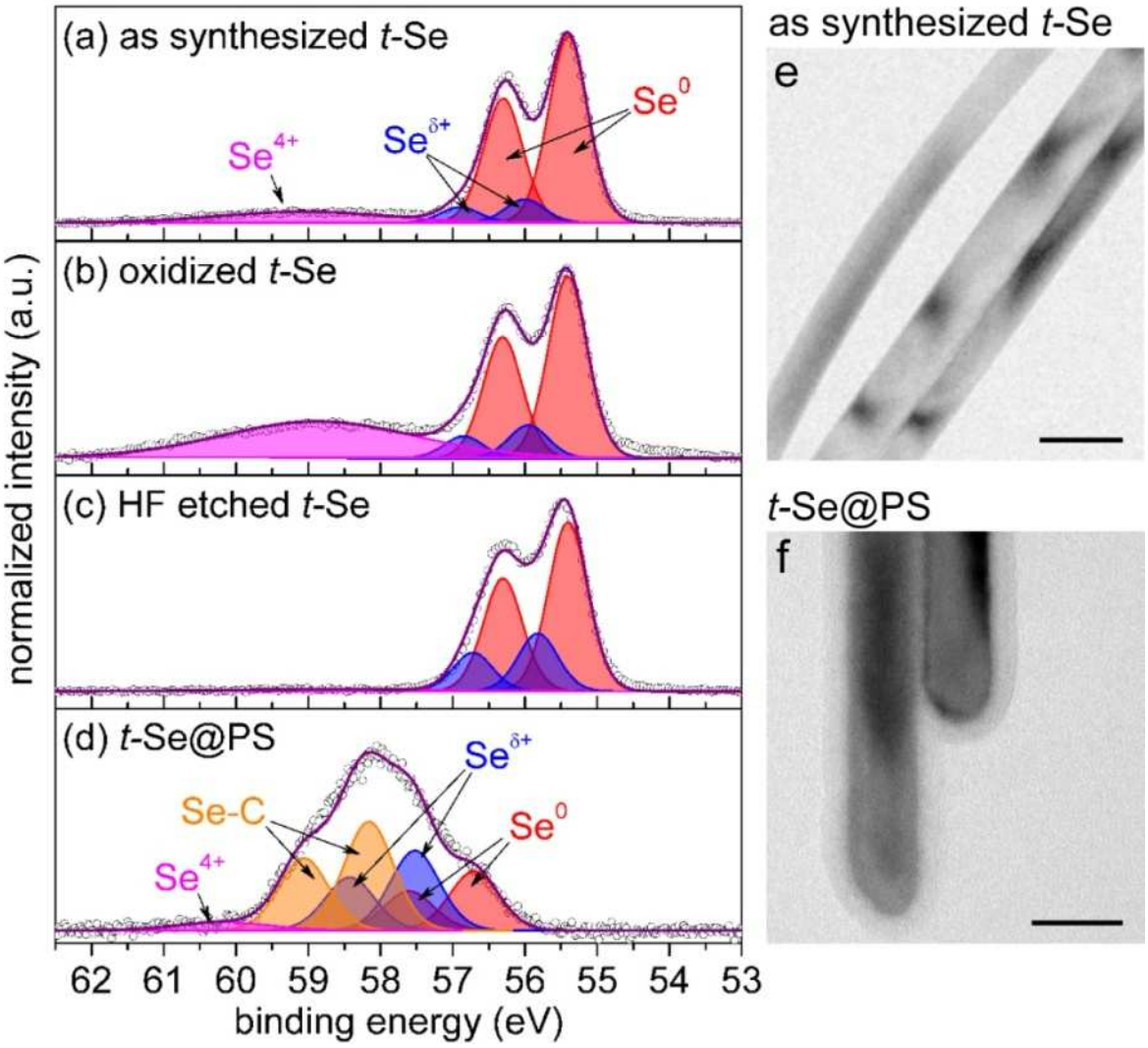

Figure 5.6 High resolution Se 3d photoelectron emission spectra with de-convolution for (a) as-synthesized t-Se nanowires, (b) oxidized t-Se nanowires, (c) HF etched t-Se nanowires, and (d) t-Se nanostructures encapsulated in a sheath of polystyrene (t-Se@PS). Corresponding transmission bright field electron microscopy images are displayed for the (e) as-synthesized t-Se nanowires and (f) t-Se nanowires coated with a low contrast layer of polymer. Scale bars are 40 nm. Reproduced from Ref. 46 with permission from The Royal Society of Chemistry.

X-ray photoelectron spectroscopy was used to elucidate the chemical states at the surfaces of the as-synthesized trigonal selenium nanowires, trigonal selenium wires oxidized under ambient conditions, and hydrofluoric acid etched anisotropic selenium

nanostructures (Figure 5.6a-c). The doublet colored in red are the emission peaks (Se $3d_{3/2}$ and Se $3d_{5/2}$) from elemental selenium (Se^0). Doublet colored in blue has a higher binding energy in comparison to that of elemental selenium, indicating that these species of selenium ($Se^{\delta+}$) atoms exist next to an electron withdrawing neighbor, such as water molecules. Fragments (O^- and OH^-) of water molecules were detected in secondary ion mass spectrometry (SIMS) analysis of both as-synthesized and HF etched samples, suggesting that the surfaces of trigonal selenium nanostructures were covered with water molecules (Figure 5.7). In addition, the SIMS spectrum of the as-synthesized selenium nanowires (Figure 5.7a) had mass fragments that correspond to the oxides of selenium (SeO^-, SeO_2^-, and SeO_3^-) in comparison to the HF etched sample (Figure 5.7b). This surface oxide was detected in XPS as a broad singlet at ~59 eV, which corresponds to Se^{4+} species.[227] Quantitative chemical state analysis revealed an increase in surface oxide concentration when the as-synthesized trigonal selenium nanostructures were left in an environment containing oxygen and moisture. The surface oxides of selenium can be removed by immersing the sample into a solution of HF (Figure 5.6c and Figure 5.7b).

To inhibit corrosion of the *t*-Se nanowires (Figure 5.6e), PS was grafted onto its surfaces by a radical initiated reaction. It was well known that monomers of styrene undergo free-radical polymerization upon exposure to ultraviolet irradiation or to heat.[228] According to the XPS analysis, the selenium 3d photoelectron emission spectrum of *t*-Se@PS (Figure 5.6d) broadened and shifted to higher binding energy (BE) than that of observed for the *t*-Se (Figure 5.6a). The increase in peak width is attributed to the formation of Se-C bonds, which have BEs of 58.2 and 59.1 eV. To our knowledge, this is the first time that Se-C bonds are observed on selenium nanostructures. In addition, all of the peaks are shifted to higher binding energies, which is a result of scattering of the emitted photoelectrons as they traverse through the layer of polystyrene. Binding energy of the emitted photoelectrons is calculated according to Eqn. 5.4,

$$BE = h\upsilon - KE - \Phi inst. \qquad \text{(Eqn. 5.4)}$$

where BE is binding energy of the ejected photoelectrons, hυ is the energy of the irradiation source, KE is the kinetic energy of the ejected photoelectrons, and Φinst. is the work function of the instrument. A photoelectron removed from the Se $3d_{5/2}$ orbital of

an elemental selenium sample using an Al X-ray source at 0 eV Φinst. has a kinetic energy of 1431.3 eV. The corresponding inelastic mean free path (IMFP) of the photoelectron in PS is ~4.3 nm (Figure 5.8).[229-230] The following equation (Eqn. 5.5) was proposed by Tanuma *et al.* to calculate the IMFP (λ) as a function of electron energy (E):

$$\lambda = \frac{E}{E_p^2[\beta \ln(\gamma E) - \left(\frac{C}{E}\right) + \left(\frac{D}{E^2}\right)]} \qquad \text{(Eqn. 5.5)}$$

where

$$\beta = -0.1 + \frac{0.944}{\left(E_p^2 + E_g^2\right)^{0.5}} + 0.069\rho^{0.1}$$

$$\gamma = 0.191\rho^{-0.5}$$

$$C = 1.97 - 0.91U$$

$$D = 53.4 - 20.8U$$

$$U = \frac{E_p^2}{829.4} = \frac{N_v \rho}{M}$$

E_p is the free-electron plasmon energy, ρ is the material density, N_v is the number of valence electrons of carbon, M is the molecular weight, and E_g is the bandgap energy. Since the average thickness of the PS coating is ~10-nm, the photoelectrons emitted from the orbital will be scattered multiple times before they exit the polymer (Figure 5.8 – inset). Therefore, a decrease in the KE of the emitted photoelectron due to scattering from the polymer coating would translate into an increase in the observed BE according to Eqn. 5.4.

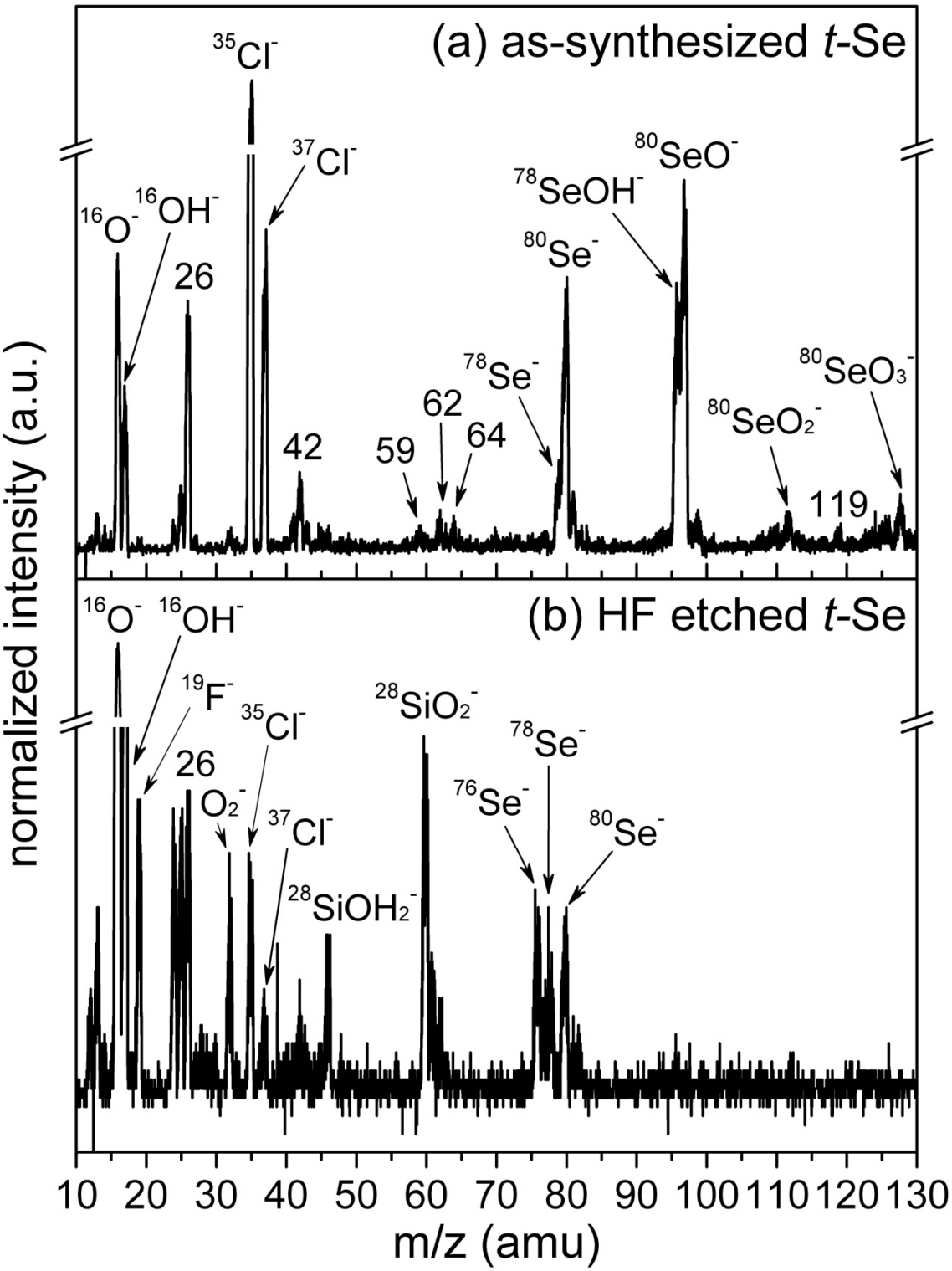

Figure 5.7 Secondary ion mass spectrometry (SIMS) analysis of (a) as-synthesized t-Se nanowires and (b) HF etched t-Se nanowires. Reproduced from Ref. 46 with permission from The Royal Society of Chemistry.

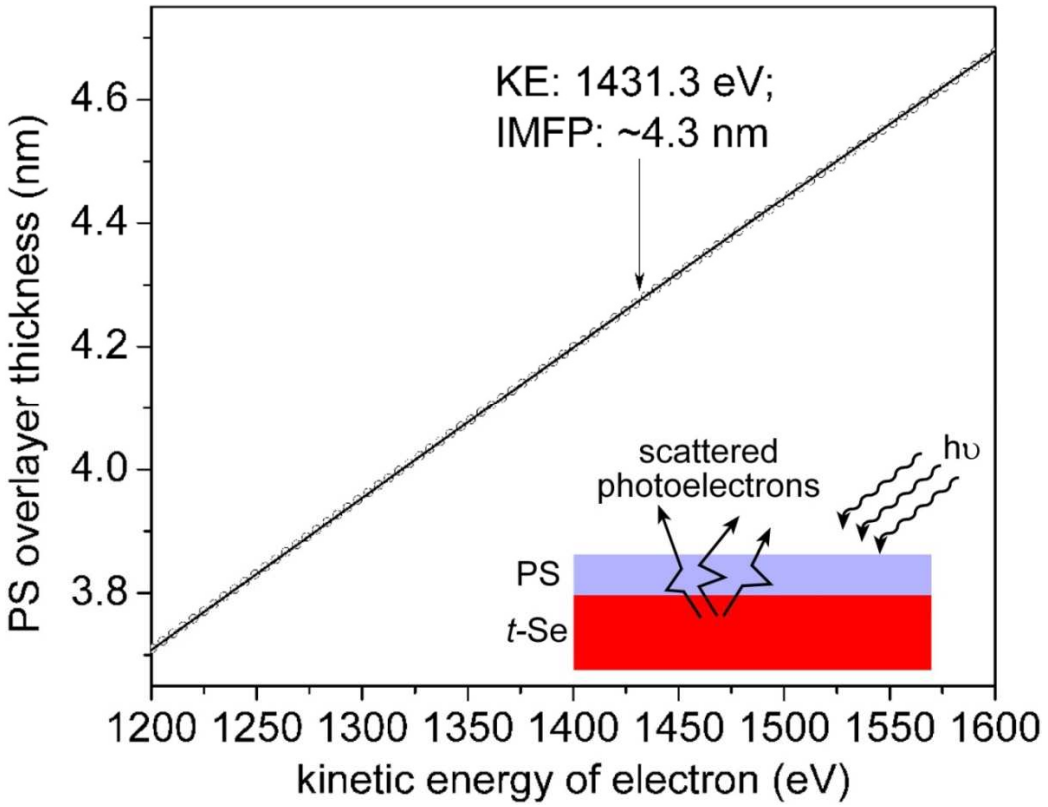

Figure 5.8 Calculated inelastic mean free path (IMFP) of an electron emitted from the Se 3d5/2 orbital in polystyrene (PS).[229] (Inset) A schematic showing the scattering of emitted photoelectrons in the PS overlayer.

In the absence of the selenium nanowires, polymerization of styrene produced only spherical colloids (Figure 5.9a). Surface initiated atom transfer radical polymerization of styrene conducted in the presence of the anisotropic *t*-Se at ice-water temperatures, produced a polymer coated semiconductor core-shell material (*t*-Se@PS). The styrene radicals preferentially reacted at the surfaces of *t*-Se nanowires. Bright field transmission electron microscopy (TEM) analysis revealed that the nanostructures were encapsulated in a ~10-nm thick layer of low contrast material (Figure 5.6f). In addition, electron diffraction analysis performed on an individual nanowire indicated that *t*-Se core remained single crystalline (Figure 5.9b and c). The acquired electron diffraction pattern was matched to a simulated single crystal diffraction pattern of *t*-Se in [200] down pole produced by CrystalMaker© (Figure 5.9d).

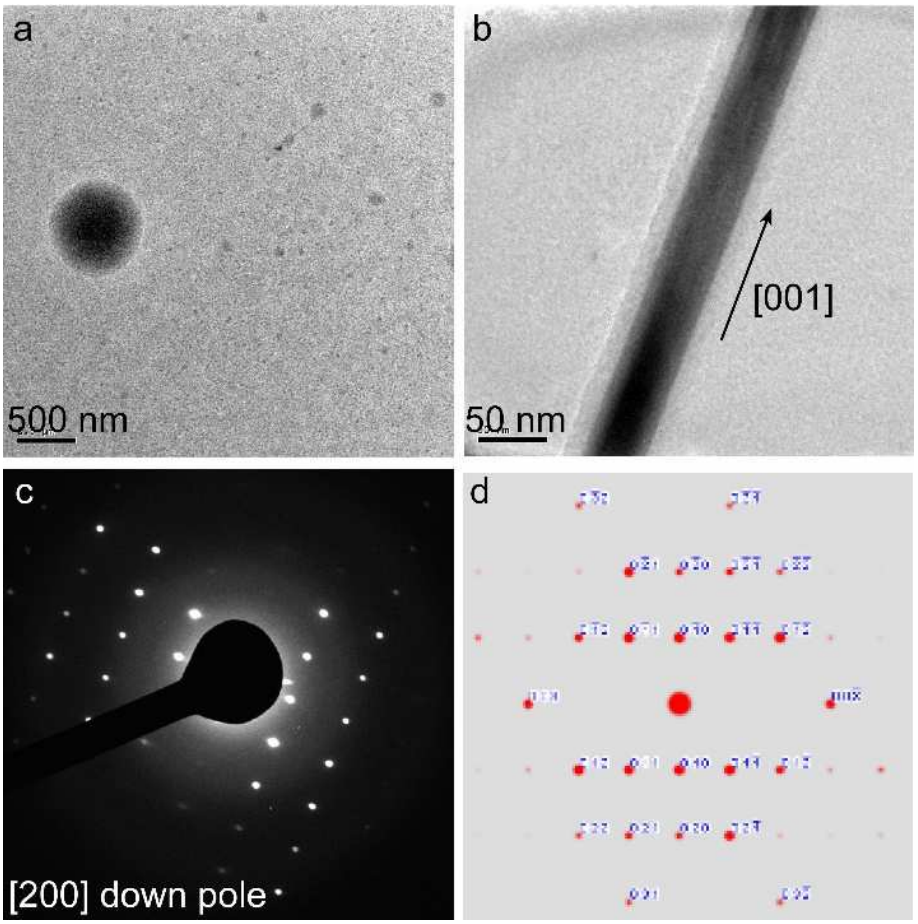

Figure 5.9 Bright field TEM microscopy image of (a) polydispersed polystyrene colloids produced from the UV initiated radical polymerization in the absence of one-dimensional t-Se nanostructures. (b) A t-Se@PS nanowire and its corresponding (c) electron diffraction pattern. (d) A simulated single crystal diffraction pattern of similar crystal orientation as in (b) produced using CrystalMaker©. Reproduced from Ref. 46 with permission from The Royal Society of Chemistry.

Radical initiated polymerization of styrene was carried out at ice-water temperatures to minimize the formation of undesirable by-products and to prevent *t*-Se nanowires from thermal degradation. The formation of polystyrene colloids and polymerization encapsulating multiple *t*-Se nanowires were observed when the reaction was conducted at elevated reaction temperatures (Figure 5.10a,b). Electron microscopy analysis also indicated that *t*-Se@PS nanowires formed at elevated temperatures also suffered from heat related damage. Surfaces of the damaged *t*-Se nanowires were no longer smooth, and appeared to be roughened and jagged (Figure 5.10c). Due to Rayleigh instability[231] *t*-Se nanowires were partially melted at elevated reaction

temperatures, although they were below the melting point of bulk selenium, 221°C.[23] Another possible contributing factor to melting of the nanowires is the relative high absorption coefficient of *t*-Se at UV and visible wavelengths in the electromagnetic spectrum (Figure 5.10d). The absorbed energy leads to bond vibration and possible breaking of Se–Se bonds. This phenomenon was minimized by performing the reaction in an ice-water bath.

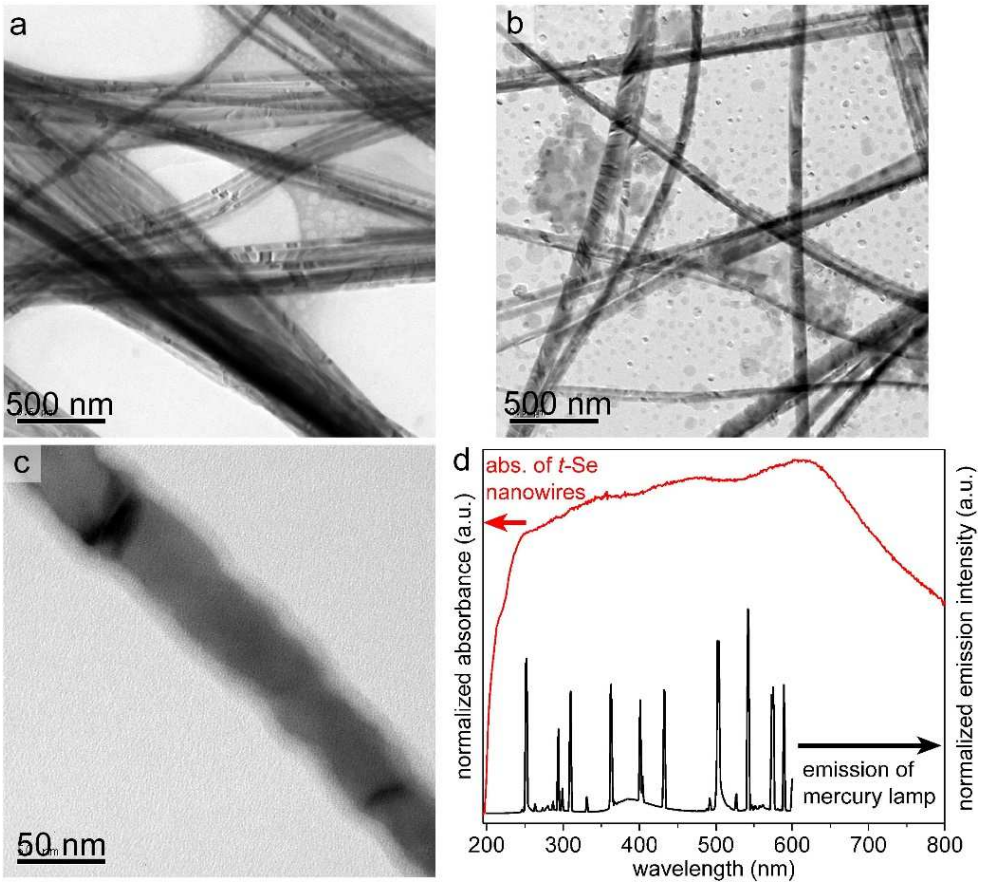

Figure 5.10 Radical initiated polymerization performed without controlling the reaction temperature can produce undesired by-products, such as (a) polystyrene coating that encapsulated multiple t-Se nanowires, (b) polystyrene colloids in the presence of t-Se nanowires, and (c) heat induced degradation of the t-Se nanostructures. (d) UV-vis absorption spectrum of t-Se (red line) absorbs most of the electromagnetic radiation produced by the mercury lamp (black line) that was used in radical initiated polymerization. Scale bars in (a) and (b) are 500 nm; and 50 nm in (c). Reproduced from Ref. 46 with permission from The Royal Society of Chemistry.

The SI-ATRP process could have been initiated by photolysis of Se-Se bonds on the surfaces of *t*-Se nanostructures, producing selenium radicals. These radicals could serve as initiators for styrene polymerization (Scheme 5.1a). It is also possible to initiate the polymerization of PS by light. Light induces styrene to undergo free-radical polymerization in which styrene radicals are generated in a bimolecular radical-forming process (Scheme 5.1b).[232] In both proposed mechanisms, the styrene radicals would be able to react non-specifically with the *t*-Se nanostructures, hence, grafting PS onto their surfaces. We believe that SI-ATRP occurs predominantly via the pathway in Scheme 5.1a pathway because the majority of the PS observed by electron microscopy is associated with the surfaces of the selenium nanostructures as a thin (~10-nm thick) sheath of polymer. Scheme 5.1b indicates that free-living PS radicals would be produced in large quantity before they are grafted onto the surfaces of the *t*-Se nanowires. The latter would also produce a large quantity of PS that is not associated with the *t*-Se surfaces (See Experimental Section on the Synthesis of *t*-Se@PS Nanostructures and Figure 5.11). In latter instance, we should have observed a significant quantity of PS colloids, but at ice-water temperatures we observed neither free PS colloids nor the decoration of the surfaces of *t*-Se with PS colloids. The predominate structure in these cases were the selenium nanostructures encapsulated in a thin layer of PS.

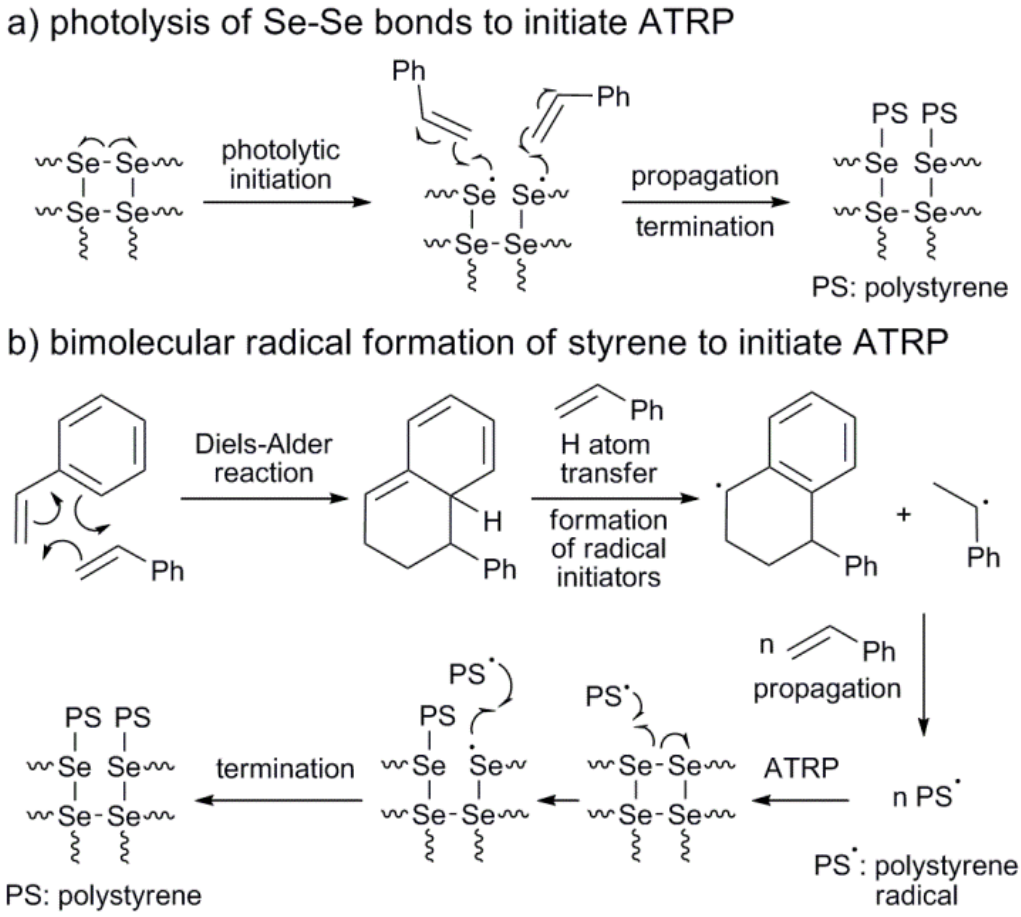

Scheme 5.1 Grafting of polystyrene (PS) onto the surfaces of selenium nanowires by surface initiated atom transfer radical polymerization (SI-ARTP) could follow either of these possible mechanisms: (a) photolysis of Se-Se bonds generating selenium radicals that initiated chain propagation to form PS at the nanostructures' surfaces; or (b) radicals of PS, which were created from the photolysis of styrene monomers,[232] reacted with the surface selenium atoms. Note: These surfaces of selenium nanostructures are shown as a two dimensional projection of the SI-ATRP process. Reproduced from Ref. 46 with permission from The Royal Society of Chemistry.

As a control experiment, ~10 to 50–nm PS colloids were first synthesized by UV initiated polymerization of styrene in the absence of *t*-Se nanowires while under constant magnetic stirring, nitrogen purged conditions, and at an ice-water temperature. Throughout 6 h of UV irradiation, the reaction mixture was kept under a nitrogen atmosphere and at the ice-water temperatures. Then *t*-Se nanowires was introduced into the reaction flask and the reaction mixture was left at room temperature (RT) for 15 h before it was purified by the method described in the Experimental Section in the

Synthesis of Trigonal Selenium Nanowires Encapsulated in Polystyrene (*t*-Se@PS). Bright field TEM images revealed that this control sample contains micrometer and nanometer sized PS colloids (Figure 5.11a) mixed together with *t*-Se@PS nanostructures (Figure 5.11b). Some of the polymer coated semiconductor core-shell nanostructures have large PS colloids attached to their surfaces (Figure 5.11c).

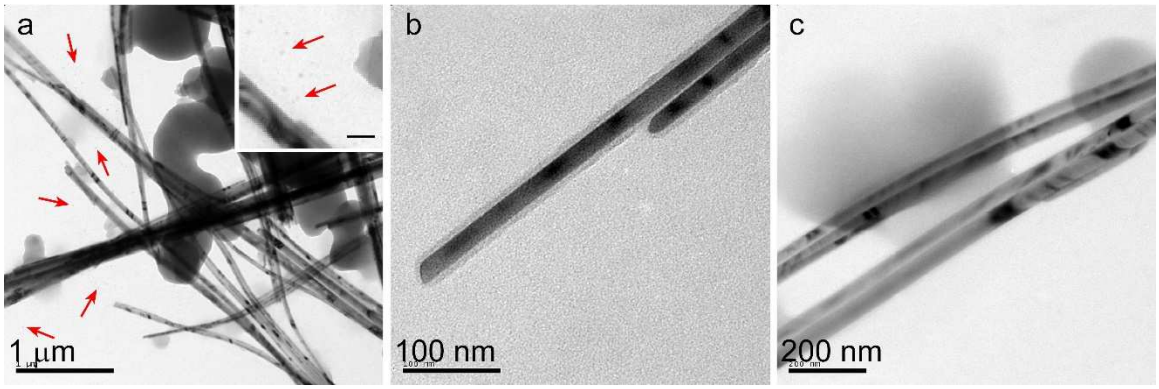

Figure 5.11 Bright field TEM images demonstrated that the control reaction of exposing the styrene to UV for 6 h and then combining this solution with t-Se nanowires produced (a) micrometer and nanometer (red arrows and inset) sized PS colloids along with (b) t-Se@PS Reproduced from Ref. 46 with permission from The Royal Society of Chemistry.

The *t*-Se@PS nanostructures were subject to immersion in nitric acid (HNO_3) and separately in hydrogen peroxide (H_2O_2) to determine the ability of these polymer coated semiconductor core-shell materials to resist corrosion. To provide a frame of reference, freshly synthesized 1D *t*-Se nanostructures (Figure 5.12a, inset) were exposed to a similar oxidative environment. After immersion in H_2O_2, the samples were flash frozen and lyophilized to prepare them for TEM analysis. Electron microscopy indicates extensive corrosion to freshly synthesized *t*-Se nanostructures when immersed into a 1% H_2O_2 solution for 5 s (Figure 5.12a). Selenium was oxidized by H_2O_2, leading to the formation of selenium salts such as selenious acid (H_2SeO_3) and selenic acid (H_2SeO_4). The electrochemical reactions may have proceeded by oxidation of *t*-Se into H_2SeO_3 (Eqn. 5.6), which was further oxidized into H_2SeO_4 by the excess H_2O_2 (Eqn. 5.7).

$$2H_2O_2 + Se \leftrightarrow H_2SeO_3 + H_2O \qquad E^o_{cell} = 1.036\ V \qquad \text{(Eqn. 5.6)}$$

$$H_2SeO_3 + H_2O_2 \leftrightarrow SeO_4^{2-} + H_2O + 2H^+ \qquad E^o_{cell} = 0.625\ V \qquad \text{(Eqn. 5.7)}$$

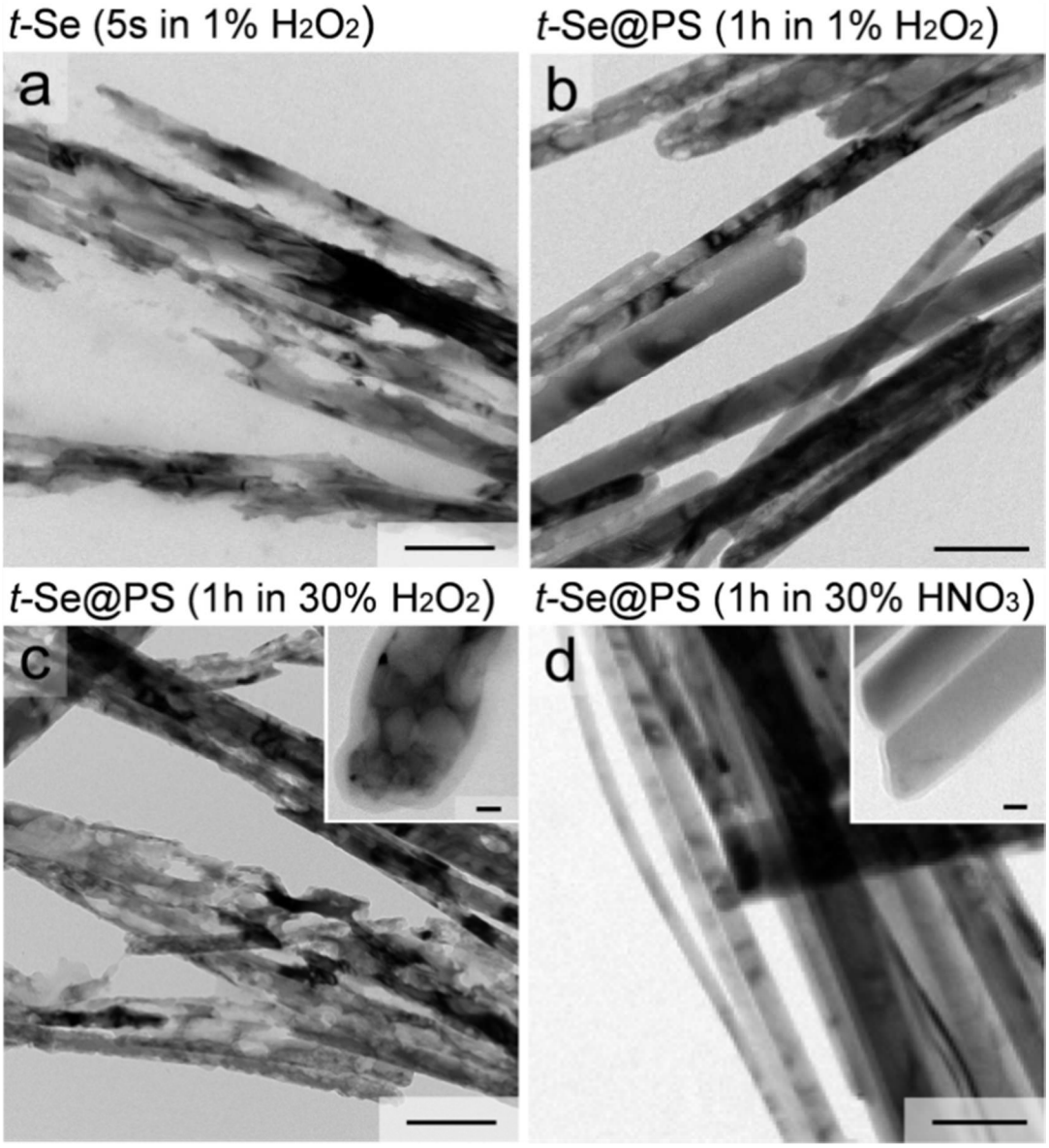

Figure 5.12 Bright field transmission electron micrographs of (a) t-Se nanowires immersed for 5 s in 1% H_2O_2, (b) t-Se@PS nanowires immersed in 1% H_2O_2 for 1 h, (c) t-Se@PS nanowires immersed in 30% H_2O_2 for 1 h, and (d) t-Se@PS nanowires immersed in 30% HNO_3 for 1 h. Scale bars are 200 nm; the inset scale bars are 20 nm. Reproduced from Ref. 46 with permission from The Royal Society of Chemistry.

These salts of selenium were, subsequently, dissolved in the presence of moisture. The *t*-Se@PS was able to withstand the same oxidative conditions up to 1 h with minimal pitting (Figure 5.12b). Bright field TEM images revealed severe etching and pitting were observed for the *t*-Se core material (Figure 5.12c) when the *t*-Se@PS was

immersed in a 30% H_2O_2 solution for 1 h. Figure 5.12c – inset indicates the polymer encapsulated *t*-Se corroded in a non-uniform manner providing evidence of defects in the polymer sheath along the length of the 1D nanostructures that allowed H_2O_2 to seep through and attack the underlying surfaces of selenium. These defects in the PS encapsulation could arise from oxidation of the polystyrene. Oxidation of the polystyrene would lead to polymer swelling, hence the formation of defects leading to penetration of H_2O_2 to the core material. On the other hand, *t*-Se@PS nanowires demonstrated superior corrosion resistance against 30% HNO_3; the TEM images revealed that there is no pitting on the surfaces of *t*-Se nanowires after 1 h exposure (Figure 5.12d). This indicates that the PS has uniformly encapsulated the *t*-Se nanowires.

High resolution C 1s spectrum of prior exposure to a 30% H_2O_2 solution for 1 h revealed the presence of two carbon species (Figure 5.13a). The signal centered at 284.6 eV corresponds to C-C and C-H in the aliphatic polymer backbone and phenyl rings of the polystyrene coating on *t*-Se, while the peak centered at 285.8 eV is attributed to C-O species. Impurities in EtOH, which was used to purify the *t*-Se@PS nanowires, could have contributed to the observed C-O species. The π-π^* electronic transition of the phenyl rings were not detected by XPS.[233] We believe the signal intensity of the π-π^* electronic transition was below the limit of detection of XPS, because only a relatively small quantity of *t*-Se@PS nanowires was prepared. After *t*-Se@PS nanowires were immersed in a solution of 30% H_2O_2 for 1 h, we observed the presence of higher oxidation state species of carbon in the C1s spectrum (Figure 5.13b), indicating the polystyrene coatings on the *t*-Se nanostructures were oxidized by H_2O_2. These species starting from the highest binding energy corresponds to carbonate esters (RO-**C**(O)OR), carboxylic acid (**C**OOH), and other carbonyls (**C**=O). This evidence suggested that the polystyrene coating was oxidized by the presence of H_2O_2, leading to the formation of hydrophilic species in the polymer film that subsequently allowed H_2O_2 to penetrate through the polymer layer and resulted in the corrosion of the *t*-Se core.

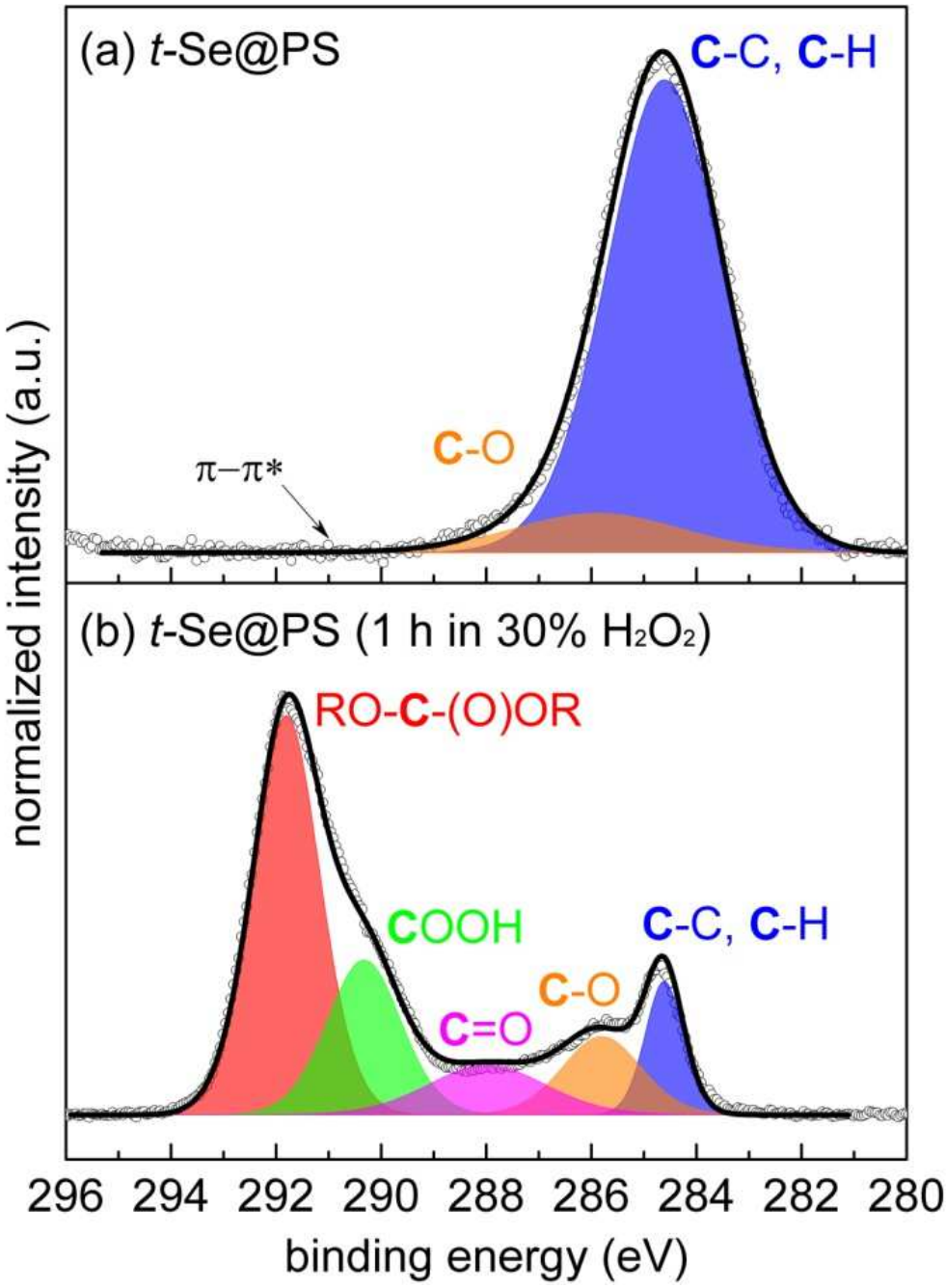

Figure 5.13 High resolution C 1s X-ray photoelectron spectroscopy of t-Se@PS (a) before and (b) after exposing to a solution of 30% H_2O_2 for 1 h.

5.4. Conclusions

In conclusion, analyses by XPS and SIMS have indicated that water molecules residing on the surfaces of the selenium nanowires interact with the surface selenium

atoms to form additional chemical states ($Se^{\delta+}$) that have not been reported previously. Also, storing *t*-Se nanowires under ambient conditions will lead to their oxidation, leading to the formation of selenium oxides. Secondary ion mass spectrometry analysis suggests selenium oxides exist on the surfaces of the selenium nanowires in both dehydrated (SeO_2) and hydrated forms (SeOH and H_2SeO_3). Oxidation then leads to corrosion of the material, which becomes pitted and fragmented, under humid or acidic conditions. We have demonstrated that the surfaces of the selenium nanostructures can be encapsulated with a thin layer of polystyrene formed by a surface initiated atom transfer radical polymerization. The reaction was performed at ice-water temperatures to minimize the formation of PS colloids, to control the rate of polymerization, to decrease the chance of forming a PS coating that contains multiple selenium nanowires as well as to avoid thermal degradation of the selenium nanowires. The XPS spectrum of *t*-Se@PS nanowires possesses an additional chemical state in comparison to *t*-Se, suggesting Se-C formation during the SI-ATRP process. This encapsulating layer of polystyrene dramatically increases the resilience of selenium nanostructures towards corrosion. The *t*-Se@PS is able to withstand an environment of 30% HNO_3 for 1 h or more without noticeable corrosion to the *t*-Se core. Under extremely oxidizing environments the polystyrene coating is oxidized, such as by H_2O_2 leading to polymer swelling and allowing the oxidant to penetrate through the PS coating. The resulting material is a semi-porous and hollow *t*-Se@PS nanowire.

5.5. Future Directions in Synthesis of Trigonal Selenium Nanowires Encapsulated in Polystyrene by Surface-Initiated Atom Transfer Radical Polymerization

This work can be extended to encapsulation of other polymers, copolymers, or block copolymers on the surfaces of *t*-Se nanowires. One improvement could be to minimize the oxygen permeability of the encapsulating layer and, thus, improve the oxidation resistance of the core selenium nanostructure. A copolymer such as vinylidene chloride in a mixture of acrylates, methacrylates, acrylonitrile, and vinylcarboxylic acids has a much lower oxygen permeability coefficient of 0.07 $nmol•(m•s•GPa)^{-1}$ than PS, which has an oxygen permeability of 765 $nmol•(m•s•GPa)^{-1}$. Copolymer of vinylidene chloride encapsulation should perform considerably better in preventing the oxidation of

the *t*-Se core in comparison to PS coating. Also, the water vapor transmission of the vinylidene chloride copolymer (0.012 nmol•(m•s)$^{-1}$) is comparable to that of the PS (0.002 nmol•(m•s)$^{-1}$), indicating that vinylidene chloride should be capable of providing sufficient protection against moisture permeation to prevent corrosion of the *t*-Se core.[234-235]

This technique can, also, be adopted in the encapsulation other nanoscale materials, such as silicon nanoparticles encapsulated with polymer to minimize oxidation. One example would be the encapsulation of Si QDs with a low oxygen permeability polymer[234, 236] formed by SI-ATRP. Silicon QDs are susceptible to oxidation transforming them into silica, which do not exhibit any fluorescence properties. Encapsulating Si QDs with a low oxygen permeable polymer is, therefore, very desirable. Surfaces of an as-synthesized Si QD can be etched briefly with hydrofluoric acid to remove the SiOx species and to transform the surface chemistry of the nanoparticles into a Si-H termination. Silicon surfaces with hydrogen termination are capable of reacting with alkene species via a photochemical process.[237] Silicon QDs are generally passivated with self-assembled monolayers (SAMs) to prevent them from oxidizing. Although these Si QDs are protected by SAMs, they are still susceptible to oxidation.[238] We believe Si QDs encapsulated in a polymer with low oxygen permeability as-synthesized through an SI-ATRP process will increase the oxidation resistance of these fluorescent nanoparticles and thus improve their stability and utilization as *in situ* contrast agents.

The polymer coating on *t*-Se@PS can, also, be further modified via chemical reactions to tailor the surfaces with the appropriate functional groups for subsequent modification or to increase the colloidal stability of the material in specific media. For example, the phenyl moieties on the PS can be modified with sulfate or nitrate functional groups to facilitate the colloidal stability and processability of *t*-Se@PS in aqueous environments.[239] Polystyrene can also be modified with hydroxyl groups before it is coated with another layer of material. For example, the hydroxyl terminated surfaces could be encapsulated in silica via a sol-gel process.[239-241] The silica coating should further improve the corrosion resistance of *t*-Se@PS in H_2O_2.

6. Surface-Initiated Atom Transfer Radical Polymerization Induced Transformation of Selenium Nanowires into Copper Selenide@Polystyrene Core–Shell Nanowires[§]

6.1. Motivations to Synthesize Copper Selenide Nanowires from Selenium Nanowires and to Encapsulate Copper Selenide Nanowires with Polystyrene

A significant research effort has been put into studying copper selenides because they have a wide range of applications in fields that include gas sensing[242], thermal electrics[243], nonlinear optics[244], therapeutics[245], and photovoltaics[246]. Researchers have been recently focusing on synthesizing copper selenide nanostructures with controlled shapes and sizes to tune their optoelectronic properties.[59, 242, 247-257] Copper selenides are a desirable material for photovoltaic applications because they can be easily doped with other metals to enhance their solar conversion efficiency.[258] In addition, recent studies have shown that copper selenide nanostructures could be useful in photothermal therapy because these materials are both less expensive and have superior photothermal efficiencies in contrast to gold nanostructures.[66, 245] However, metal chalcogenides have not been widely adopted in theranostics applications because of their lethality in biological systems.[259] It is desirable to passivate the copper selenides with a material that would prevent the dissolution of these toxic substances *in vivo*. In addition, the passivating layer can be tailored with the appropriate functional group(s) to increase the colloidal stability of the nanostructure in various media, making the material

[§] Experiments were carried out by Michael C. P. Wang and the manuscript was co-written by Michael C. P. Wang and Professor Byron D. Gates. "Reprinted Journal Article with permission from Surface-Initiated Atom Transfer Radical Polymerization-Induced Transformation of Selenium Nanowires into Copper Selenide@Polystyrene Core-Shell Nanowires, Wang, M. C. P.; Gates, B. D. *ACS Appl. Mater. Interfaces*, **2013**, *5*, 9546-9553. Copyright 2013 American Chemical Society."[61]

easier to handle and process for subsequent steps such as device integration or assembly. Polymer encapsulation of nanowires has been shown to increase the corrosion resistance and ease of handling of the core material.[47] Polymer encapsulated copper selenide nanowires may, therefore, be less lethal in biological systems when used in theranostics applications and may improve their stability and ease of processing for other applications. There are, however, no previous demonstrations of coating copper selenide nanostructures with a thin encapsulating sheath of polymer.

Herein, we report a method to synthesize copper selenide nanowires that are simultaneously encapsulated with a thin layer of polystyrene (PS) by surface-initiated atom transfer radical polymerization (SI-ATRP). This process is demonstrated using selenium nanowires dispersed in styrene in the presence of a copper substrate covered with a native oxide. X-ray photoelectron spectroscopy suggested that styrene radicals facilitated the reduction of Cu^{2+} species to Cu^{1+} and Cu^{0} and that both of which reacted spontaneously with the selenium nanowire templates to produce cuprous (Cu_2Se) and cupric selenide (CuSe) nanowires.

There are many synthetic approaches to make copper selenide nanostructures. One of the most commonly reported procedures relies on the coreduction of either salts or organometallic precursors of copper and selenium in the presence of solvated ligands.[247-248, 255] Most of these reports have focused on the synthesis of 0D,[248] 2D or 3D nanostructures of copper selenides, such as triangular or hexagonal plates,[248] discs,[247] and cubes.[255] Another approach is to transform amorphous and crystalline selenium structures into copper selenide crystals by the mutual diffusion of copper and selenium atoms. Two-dimensional copper selenide ribbons and discs have been prepared at room temperature by a solid-state chemical reaction between thin films or particles of selenium and copper deposited on top of each other under vacuum.[260-266]

In general, there have been fewer articles published on the synthesis of one-dimensional (1D) nanostructures of copper selenide. One-dimensional copper selenide nanostructures have been synthesized by both solution-phase and gas-phase techniques.[250-251, 253] High-aspect-ratio copper selenide nanowires can be grown under vacuum through chemical vapor deposition (CVD), but this technique requires a careful choice of precursors.[250] Low-aspect-ratio copper selenide nanorods have been

electrochemically grown within the pores of an anodized alumina membrane.[251, 253] This electrodeposition method can easily yield anisotropic nanostructures, but the technique is limited by low throughput in comparison to more easily scalable solution-based syntheses. Some solution-phase syntheses can produce 1D copper selenide nanostructures with both an increased aspect-ratio and an increased yield. One approach to the solution-based synthesis of 1D copper selenide nanostructures uses hydrothermal and solvothermal techniques.[242-243, 252, 255] These syntheses can be performed in the absence of surfactants that are commonly used to promote the anisotropic growth of metallic 1D nanostructures.[267-268] A preformed structural template can also guide the formation of copper selenide nanorods in solution, as Alivisatos *et al.* demonstrated through the use of cadmium selenide nanorods with diameters below 10 nm.[59] This reaction involved the exchange of cations that reside within the nanorod template (i.e., Cd^{2+}) with the desired cation (i.e., Cu^{2+}). This template-engaged route to copper selenide is limited by the ion-exchange process and diffusion kinetics within the solid material, which restricts the ability to synthesize copper selenide nanostructures of larger diameters without the use of high temperatures. As an alternative approach, Yang *et al.* reported the synthesis of copper selenide nanotubes from a template of trigonal selenium nanotubes.[257] In their synthesis, a mild reducing agent was used to convert Cu^{2+} into Cu^{+}, which reacted spontaneously with the Se^{0} nanotubes to produce copper selenide nanotubes in an aqueous environment.

In this chapter, we report a template-engaged method to directly convert selenium nanowires into polystyrene encapsulated cuprous and cupric selenide core–shell (CuSe-Cu_2Se@PS) nanowires. This transformation occurs under ambient conditions via a series of reactions initiated by atom transfer radical polymerization. The CuSe-Cu_2Se@PS has the potential of being corrosion resistant, similar to *t*-Se@PS.[47] Scanning transmission electron microscopy, electron energy loss spectroscopy, X-ray powder diffraction, and X-ray photoelectron spectroscopy techniques are used to characterize the composition, purity, and crystallinity of the CuSe-Cu_2Se@PS products. The bandgap of the CuSe-Cu_2Se@PS was determined by UV–vis absorption spectroscopy.

6.2. Experimental Section

Copper selenide nanowires were synthesized from templates of selenium nanowires. These sacrificial selenium nanowires were grown by solution-phase techniques following the Ostwald ripening of amorphous selenium colloids via a sonication-induced solvothermal process.[47]

6.2.1. Synthesis of Selenium Nanowires

Amorphous selenium was prepared by first dissolving 2.73 g (21.1 mmol) of selenious acid (H_2SeO_3, 98%; Sigma-Aldrich) in 100 mL of 18.2 MΩ·cm water (purified using a Barnstead NANOpure DIamond Life Science water filtration system) contained within a 250 mL round-bottomed glass flask. This solution was cooled in an ice-water bath for 20 min before introducing the reducing agent hydrazine (N_2H_4, 50–60% in water; Sigma-Aldrich). An ice-water chilled solution of hydrazine, 3 mL (61.1 mmol), was introduced drop-by-drop into the reaction solution under constant magnetic stirring over a period of 2 min. After 15 min of continuous stirring, the brick-red precipitate was collected by vacuum filtration onto a PVDF membrane with an average pore size of 0.1 µm (catalogue number: VVLP04700; Millipore). The filtrate was rinsed with 200 mL of 18.2 MΩ·cm water to remove residual N_2H_4. The resulting red solid was stored in a plastic petridish wrapped in aluminum foil and freeze dried in a Savant Modulyo lyophilizer (Thermo Scientific) at -50℃ and 100 mbar for 12 h. This red solid was characterized as amorphous selenium particles by XRD and elemental analysis.

A solvochemical route was used to synthesize the selenium nanowires from the amorphous selenium particles. In brief, a dispersion containing 1 mg of amorphous selenium powder in 2 mL of ethanol (EtOH, 95%; Commercial Alcohols) dispersed in a 2 dram glass vial was sonicated for 20 s. The solution was then placed in a dark cabinet maintained at 22℃ to allow the reaction to reach completion over a period of ~12 h.

6.2.2. Synthesis and Purification of Copper Selenide@Polystyrene Core-Shell Nanowires

An ethanol solution containing selenium nanowires was drop cast onto a piece of copper plate (~0.5 cm x 1 cm^2) coated with a layer of native oxide. Ethanol was evaporated under vacuum, leaving a dried sample of selenium nanowires on the copper substrate. Subsequently, the copper substrate with selenium nanowires was placed in a 5 mL screw capped glass vial containing 1.5 mL of styrene, which had been passed through an alumina column to filter off the chemical inhibitors in the solution. The reaction vial was kept at room temperature under ambient light. The progress of the transformation into copper selenide@polystyrene was initially monitored by observing the slow transformation of the dark red selenium nanowires into black copper selenide nanowires.

The crude product dispersed in styrene was collected by decanting, isolated by centrifugation at 3,000 rpm for 5 min and rinsed with EtOH. This purification procedure was performed a total of 3 times to remove residual styrene. A solution of ethanol containing the crude product, which consisted of a mixture of cuprous and cupric selenide@polystyrene and selenium nanowires, was transferred to a Schlenk tube. The solvent was subsequently removed under vacuum. To remove selectively the excess starting material (unreacted selenium nanowires), the Schlenk tube (fitted with a cold finger) was heated at 300℃ for 12 h. Thermal evapo ration under vacuum to remove residual selenium nanowires was performed with a similar setup with the side-arm of the Schlenk tube coupled to the vacuum gas manifold of a Schlenk line. The Schlenk line was coupled to a Welch® DuoSeal® (Model 1400) vacuum pump. The sample was heated at 160℃ for 12 h under vacuum. Evaporated s elenium collected onto the cold finger located above the sample. The purified product was redispersed in ethanol.

6.2.3. Transformation of Selenium Nanowires into Copper Selenide Nanowires

Copper selenide nanowires without polystyrene encapsulation was produced by drop casting selenium nanowires onto a Cu^{1+} and Cu^0 enriched Cu/CuOx substrate that had been used to synthesize the polystyrene coated copper selenide nanowires. The reaction was completed when dark red selenium nanowires had turned into black copper

selenide. The reaction took approximately 1–3 months. A Cu substrate containing higher concentrations of Cu^{1+} species on the surface would have a faster reaction rate, whereas diffusion of Cu^0 atoms into selenium nanowire templates took significantly longer (~3 months), because the rate of reaction is limited by Cu atom's rate of diffusion.

6.2.4. Materials Characterization Techniques

Scanning electron microscopy (SEM) images and energy-dispersive X-ray spectroscopy (EDS) data were acquired with an FEI Strata DB235 FESEM operating at 15 kV. Samples for SEM analysis were prepared by drop casting a solution of nanowires onto a piece of approximately 1 cm^2 silicon wafer. Transmission electron microscopy (TEM) images, energy-dispersive X-ray spectroscopy (EDS), and selected area electron diffraction (SAED) data were obtained with either an FEI Tecnai G^2 F20 scanning TEM (STEM) with a field emission gun thermionic source operating at 200 kV or a Hitachi 8000 STEM with a lanthanum hexaboride thermionic source operating at 200 kV. Analysis by electron energy loss spectroscopy (EELS) was carried on the Tecnai G^2 F20 STEM equipped with a Gatan GIF 2000 imaging filter. The spectrometer had an energy resolution of 1.1 eV that was calculated from the full-width at half-maximum of the zero loss peak obtained with a 2 mm aperture and a detector setting of 0.1 eV/channel. For TEM and EELS analysis, the samples were prepared by drop-casting or dip-coating solutions of nanowires onto a 300 mesh copper grid coated with formvar/carbon (catalogue number: FCF300-CU-50; Cedarlane Laboratories Ltd.) or onto a Quantifoil holey carbon copper grid (catalogue number: Q225-CS7; Cedarlane Laboratories Ltd.). Nickel TEM grids coated with silicon monoxide (catalogue number: D20515; Soquelec International) and carbon (catalogue number: CF-150-Ni; Electron Microscopy Sciences) were used in the STEM – EDS analysis for the elemental composition of the copper selenide nanostructures.

X-ray diffraction (XRD) patterns were acquired with a Rigaku diffractometer using Cu Kα radiation (λ = 0.15418 nm). Copper X-rays were generated from a copper target by electron bombardment at 42 kV and 40 mA. A 0.5-mm collimator was placed between the X-ray source and the sample. Samples for X-ray analysis were prepared by casting a suspension of nanowires from EtOH onto a glass slide and drying the sample under

vacuum. Quantitative Rietveld phase analysis was performed with Materials Analysis Using Diffraction (MAUD) program (Appendix B).

Optical absorption measurements (UV-vis spectroscopy) were performed with a Varian Cary 300 Bio spectrophotometer system. Samples of nanowires were dispersed into ethanol contained within a 1 cm path length quartz cell (catalog number: 100-10-40, Type 100-QS, Hellma Analytics). Each solution of nanowires was sonicated for 30 s to achieve a uniformly dispersed solution prior to acquiring the optical absorption measurements. It is crucial to obtain a uniform dispersion to minimize scattering of incident radiation.

X-ray photoelectron spectroscopy (XPS) analysis was carried out on a Kratos Analytical Axis Ultra DLD spectrometer using a monochromatic aluminum source (Al Kα, 1486.6 eV) operating at 150 W (10 mA emission current and 15 kV HT), with the exception that the aluminum source was operated at 65 W (5 mA emission current and 15 kV HT) when analyzing the polystyrene films to minimize sample charging. Analyses were conducted on a 700 µm x 300 µm area of the samples. High resolution scans were obtained at a 50 meV step size with a dwell time of 1000 ms per step and a pass energy of 20 eV. The Kratos charge neutralizer was used during analysis of insulating samples. Energy scale linearity was calibrated using Al and Mg X-ray sources on Argon sputter cleaned gold and copper substrates. The calibration procedure was performed in accordance with ISO 15472 international procedure. XPS analyses were performed on polystyrene (Aldrich, M_w *ca.* 280,000 by GPC), CuSe-Cu_2Se@PS, a copper substrate prior to the surface-initiated atom transfer radical polymerization, as well as a copper substrate that has been used to convert selenium nanowires into cuprous and cupric selenide@polystyrene nanowires. All spectra have been calibrated with respect to the peak position of the C–C signal of C1s at 284.6 eV. Vision 2 Processing software (version 2.2.7) was used to analyze and perform curve fitting on the XPS spectra.

6.3. Results and Discussion

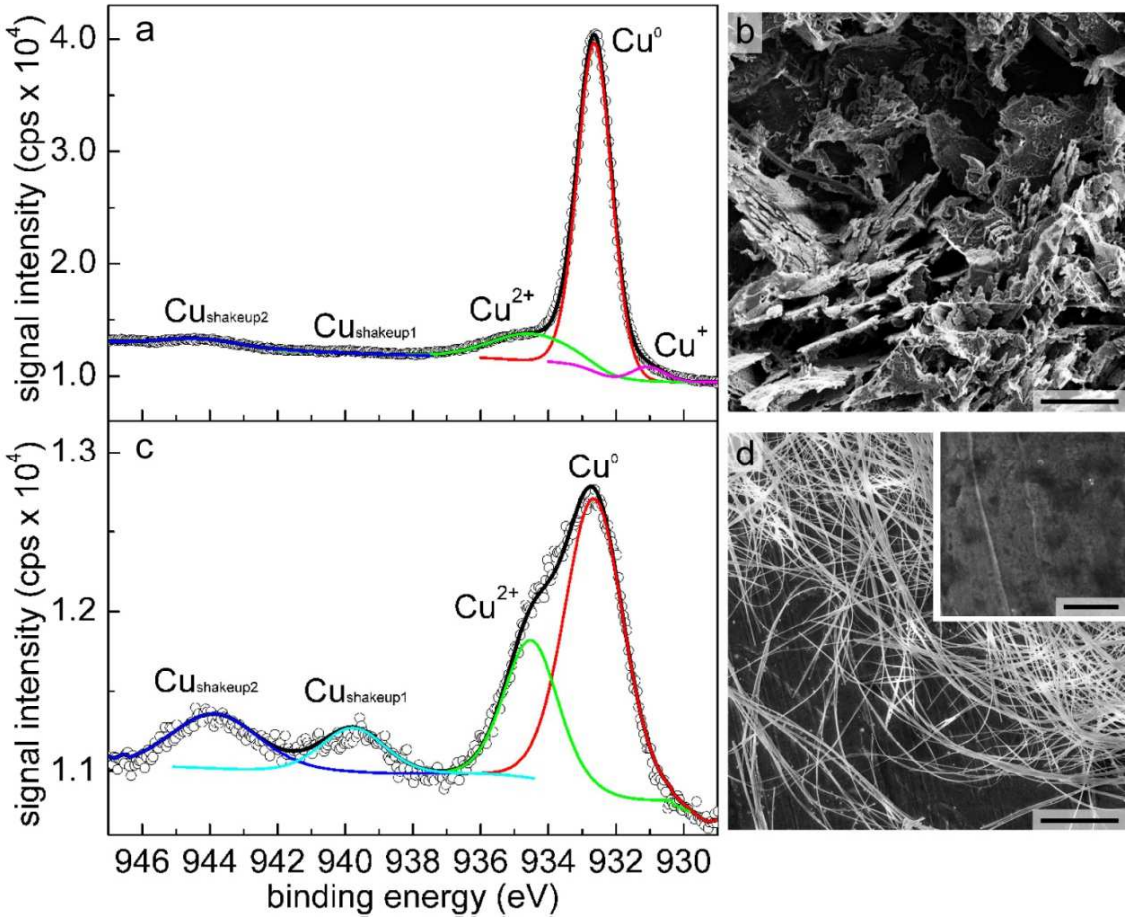

Figure 6.1 (a, c) Cu2p3/2 high resolution X-ray photoelectron spectroscopy (XPS) analysis of the Cu/CuOx substrate and selenium nanowires immersed in (a) styrene and (c) EtOH. (b) SEM analysis of the Cu/CuOx substrate after immersing in styrene with the selenium nanowires. The Cu/CuOx substrate's topography is no longer smooth, indicating a reaction with the Cu/CuOx substrate.[262] (d) SEM analysis of selenium nanowires deposited on a Cu/CuOx substrate immersed in EtOH for 3 months. (d – inset) High magnification SEM analysis revealed that surfaces of the Cu/CuOx substrate are relatively smooth after 3 months. Scale bars are 5 µm and the inset scale bar is 1 µm.

Copper selenide nanowires encapsulated in a sheath of polystyrene (CuSe-Cu_2Se@PS) are synthesized from selenium nanowires. The selenium nanowires transform into copper selenide by a series of reactions initiated by the formation of styrene free radicals. Monomers of styrene are converted to free radicals either by

exposure to heat or UV irradiation.[228] These free radicals of styrene are able to reduce some of the Cu^{2+} species on the surfaces of a Cu/CuOx substrate to Cu^{1+} species, as indicated by X-ray photoelectron spectroscopy (XPS) analysis (Figure 6.1a and c).[269] It has been documented that Cu^{1+} species react spontaneously with selenium to produce cuprous selenide (Cu_2Se).[75, 257] The concentration of Cu^0 at the surface increased for a Cu/CuOx substrate that had been immersed in styrene in comparison to a Cu/CuOx sample spectrum acquired in the absence of styrene. This result suggests that styrene radicals are capable of reducing Cu^{2+} species into Cu^0. Prior literature reports that selenium particles in physical contact with Cu^0 undergo a solid-state reaction to produce cupric selenide (CuSe) by the mutual diffusion of Cu and Se atoms.[261-263] Scanning electron microscopy (SEM) analysis revealed that the surfaces of the Cu/CuOx substrate immersed in a mixture of styrene and selenium nanowires became rough. The new structures included discs and ribbons, suggesting the formation of copper selenides (Figure 6.1b).[261, 263, 266] In addition, free radicals of styrene would initiate polymerization of styrene monomers to encapsulate both the starting materials[21] and the newly formed copper selenide nanowires. In the absence of styrene, the selenium nanowires and Cu/CuOx substrate did not transform into copper selenide nanowires. Both transmission electron microscopy (TEM) and X-ray diffraction (XRD) analyses did not indicate the presence of copper selenide nanowires. The morphology could indicate the occurrence of a reaction. The selenium nanowires morphology remained unchanged (Figure 6.2a). X-ray diffraction pattern of the selenium nanowires deposited on Cu/CuOx substrate in the absence of styrene does not contain diffraction patterns that correspond to copper selenides (Figure 6.2b). Analysis by XPS confirmed the presence of Cu^{2+} species and an absence of Cu^{1+} species on the surfaces of Cu substrate (Figure 6.1c). Moreover, SEM analysis revealed that the surfaces of the Cu substrate had remained unchanged, suggesting that no chemical reaction had occurred (Figure 6.1d). We believe that a layer of CuO and $Cu(OH)_2$ overlayers[269] on the Cu/CuOx substrate served as a barrier to inhibit the mutual diffusion of Cu and Se atoms.

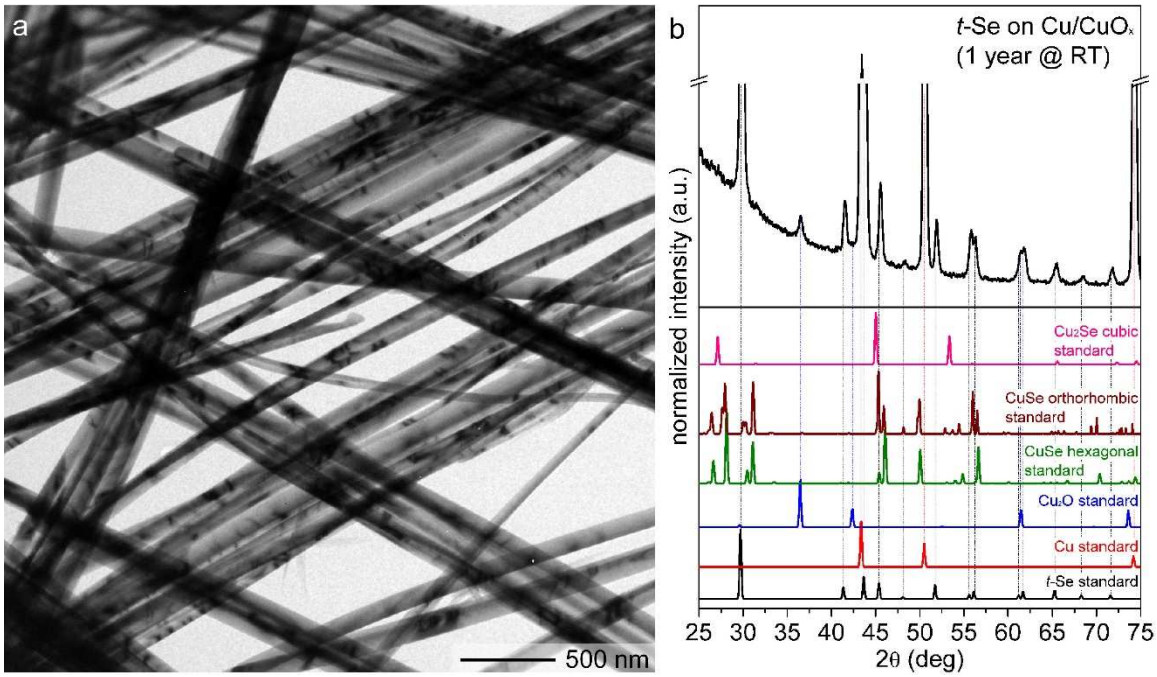

Figure 6.2 Transmission electron microscopy analysis revealed that selenium nanowires remained unchanged after they were kept in an ethanol solution containing a copper substrate for 3 months. X-ray diffraction analysis indicated that only the starting materials (trigonal selenium nanowires (t-Se) and Cu/CuO_x substrate) are present in a sample stored in ethanol for 1 year.

To synthesize copper selenide@polystyrene nanowires, a sample of selenium nanowires deposited on a Cu/CuOx substrate was immersed into styrene. Transmission electron microscopy analysis (Figure 6.3a) reveals that the 1D nanostructures of selenium initially have a uniform diameter along their growth direction of [001]. Bend contours along the length of the nanowires can also be observed in the bright-field TEM image. These features are a hallmark of high-aspect-ratio single crystalline 1D nanomaterials. Selected area electron diffraction (SAED) analysis (Figure 6.3a inset) performed on a single selenium nanowire produced a pattern of diffraction spots that correlates to single crystal selenium with a hexagonal symmetry. In this case, the collimated electron beam passed through the selenium nanowire perpendicular to the [210] zone axis. After the reaction mixture is left at room temperature under ambient lighting for a period of 3 months, the selenium nanowires and the Cu/CuOx substrate exhibited a noticeable change in their coloration. The nanowires turned dark grey in color, in contrast to the dark brick-red color of the selenium nanowires, whereas the

shiny orange-toned Cu/CuOx substrate changed to a dull red. Analysis by TEM (Figure 6.3b) indicates that the newly formed anisotropic nanostructures have a different morphology than the starting material. These nanowires have nonuniform diameters with multiple bends along the length of the nanowire and are encapsulated in a low-contrasting polystyrene sheath similar to selenium@polystrene nanowires prepared by a surface-initiated atom transfer radical polymerization.[47]

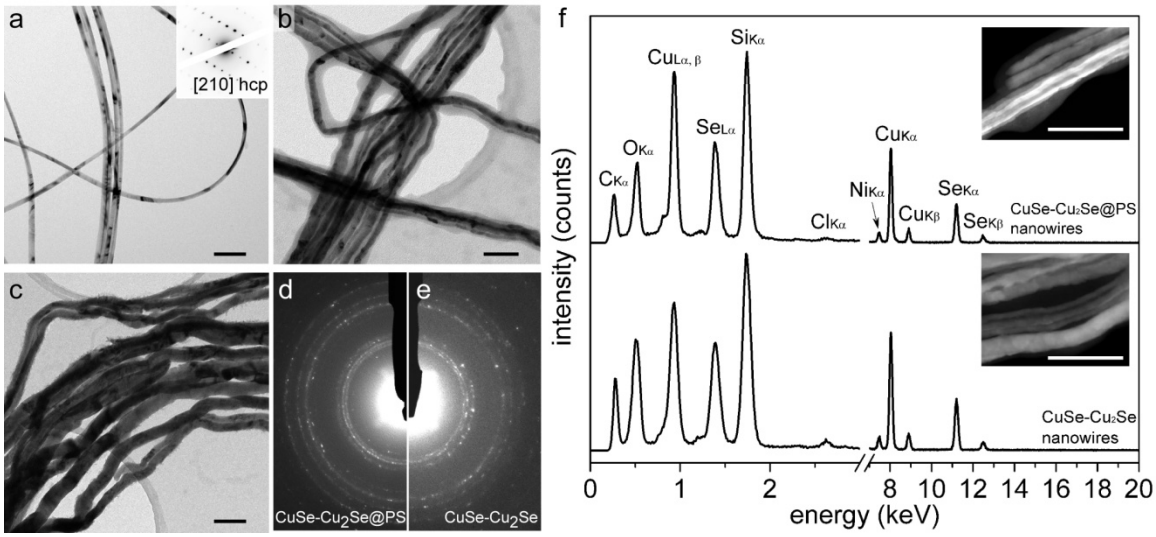

Figure 6.3 (a, inset) Corresponding transmission electron microscopy (TEM) and selected-area electron diffraction (SAED) pattern of the 1D selenium templates. (b) TEM analysis revealing the presence of a new species of polycrystalline nanowires encapsulated in a low-contrasting material after prolonged incubation of both a Cu substrate and t-Se nanowires in a solution of styrene. (c) TEM of copper selenide nanowires without polymer encapsulation formed by reacting Cu^{+} species on a Cu substrate with selenium nanowires. (d, e) Electron diffraction patterns of these $Cu_{1.75\pm0.04}Se$@PS and $Cu_{1.63\pm0.04}Se$ nanowires. (f) Elemental analysis by energy dispersive X-ray spectroscopy (EDS) on a scanning transmission electron microscope (STEM) of the polystyrene-encapsulated copper selenide nanowires (top inset) and uncoated copper selenide nanowires (bottom inset) deposited on SiOx-coated Ni grids. Scale bars are 200 nm.

X-ray photoelectron spectroscopy was employed to determine the composition of the polymer coating on the copper selenide nanowires. A high-resolution C_{1s} photoemission spectrum of the copper selenide@polystyrene nanowires indicated the presence of a π–π^* electronic transition that is a signature of unsaturated or aromatic carbon species. This peak corresponds to the phenyl rings of the polystyrene (Figure

6.4a).[233] The thickness of the polystyrene coating is nonuniform along the length of the copper selenide nanowires. Nodules of PS are present along the length of these nanowires (Figure 6.4e and f). This nonuniformity is attributed to the fact that SI-ATRP was performed at room temperature. The rate of polymerization is proportional to local variation in reactivity along the selenium nanowire templates. Polystyrene colloids produced as a byproduct of the reaction can be removed by isolating the polystyrene-encapsulated copper selenide nanowires via centrifugation at 3000 rpm followed by decanting the supernatant. A higher temperature can be used to accelerate the transformation of selenium to copper selenide nanowires, but the rate of styrene polymerization also increases. The resulting product is a viscous and tacky mass.

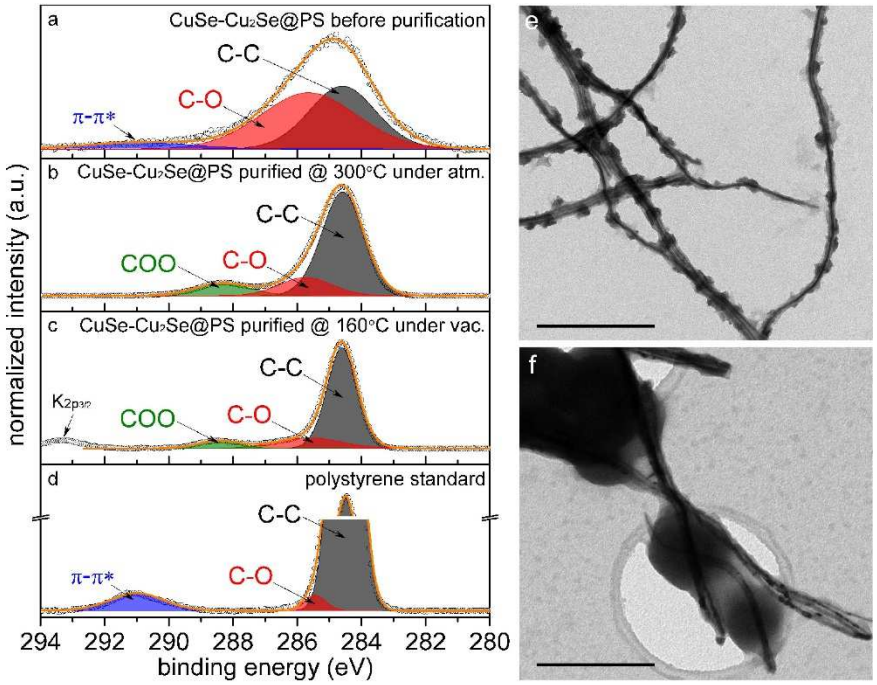

Figure 6.4 High resolution C1s photoemission spectra of (a) CuSe-Cu_2Se@PS prior to thermal purification to remove residual selenium nanowires, (b) after thermal evaporation of selenium nanowires at 300℃ under atmospheric pressure for 12 h, (c) after thermal evaporation of selenium nanowires at 160℃ under vacuum for 12 h, and (d) polystyrene standard. (e, f) Transmission electron microscopy revealed that polystyrene nodules are observed on some of the copper selenide@polystyrene nanowires. The scale bars are 1 μm.

Copper selenide nanowires without polystyrene encapsulation (Figure 6.3c) can also be produced by drop casting selenium nanowires onto a Cu^{1+} and Cu^0 enriched

Cu/CuOx substrate (Figure 6.1a) that had been used to synthesize the polystyrene coated copper selenide nanowires. This reaction was facilitated by an increase in the surface concentration of Cu^{1+} and Cu^0 on the Cu/CuOx substrate from the presence of styrene radicals, as indicated by the XPS analysis. The Cu^{1+} and Cu^0 species on the surfaces of the Cu/CuOx substrate can react with the selenium nanowires by two possible mechanisms. The Cu^{1+} species on the surfaces of the Cu/CuOx substrate can react electrochemically[75, 257] to produce cuprous selenide (Cu_2Se). In addition, copper selenides (CuSe and Cu_2Se) can be formed through solid-state reactions between Cu^0 and Se^0, as reported in previous literature.[261-263] The newly formed copper selenide nanowires, both with or without the polymer coating, no longer exhibit the bend contours and have an increased contrast in the TEM images. These changes indicate the formation of a polycrystalline material that has a higher density than selenium. The electron diffraction patterns obtained from multiple copper selenide nanowires indicate similar crystal lattices for nanowires with and without the polymer coating (Figure 6.3d and e). Elemental analysis by energy dispersive X-ray spectroscopy (EDS) performed by STEM on an area containing a collection of copper selenide nanowires confirmed that these new nanostructures are composed of copper and selenium (Figure 6.3f). Elemental composition analyses were extracted from these EDS spectra shown in Figure 6.3f using TEM Imaging & Analysis software provided by FEI Company (version 4.2 SP1). The bare copper selenide nanowires have an average composition of $Cu_{1.63\pm0.04}Se$, and the polystyrene-encapsulated copper selenide core–shell nanowires have an average composition of $Cu_{1.75\pm0.04}Se$@PS. In addition, spot EDS analyses performed along the length of individual $Cu_{1.75\pm0.04}Se$@PS nanowire revealed a larger variation in composition between Cu and Se in comparison to the $Cu_{1.63\pm0.04}Se$ (Figure 6.5). Variation in the ratio of Cu/Se observed in $Cu_{1.75\pm0.04}Se$@PS nanowires could be due to the formation of the polystyrene layer, which occurs simultaneously to the electrochemical transformation of selenium into copper selenide. The polystyrene coating could impede the selenium nanowires from reacting uniformly with the Cu^{1+} species or there may be an uneven supply of reactive Cu species along the length of the selenium nanowire because some sections of the nanowire are dispersed in the styrene and not in physical contact with the Cu substrate. Poor physical contact would result in a nonuniform product for a solid-state chemical reaction.

CuSe-Cu_2Se@PS nanowires

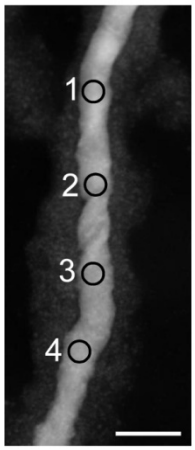

spot	Cu at. %	Se at. %	Cu/Se ratio
1	17.45	13.58	1.3
2	14.91	8.53	1.7
3	16.07	10.66	1.5
4	17.85	12.56	1.4

CuSe-Cu_2Se nanowires

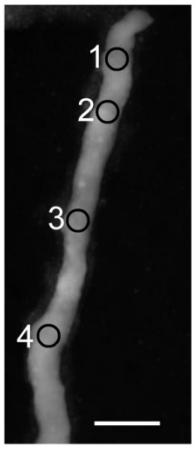

spot	Cu at. %	Se at. %	Cu/Se ratio
1	20.66	12.24	1.7
2	19.48	11.64	1.7
3	19.01	11.85	1.6
4	18.13	11.01	1.6

Figure 6.5 Elemental analysis by energy dispersive X-ray spectroscopy was conducted at different positions along the length of polystyrene encapsulated copper selenide (CuSe-Cu_2Se@PS) and copper selenide (CuSe-Cu_2Se) nanowires. The analyzed spots on the nanowires are circled and labeled on the scanning transmission electron microscopy high-angle annular dark field images, while their corresponding atomic concentrations (%) are tabulated next to these images. Scale bars are 100 nm.

These polycrystalline 1D nanostructures have an average core diameter of 76 ± 21 nm (Figure 6.6), which is ~2.6 times larger than the average diameter of selenium nanowires at 29 ± 9 nm. Because the copper selenide nanowires retain the anisotropic form of the template nanowires, the mechanism of transformation is unlikely to proceed solely by reduction of Se^0 into Se^{2-} before it reacts with the reactive copper species. The complete reduction of selenium would have resulted in the formation of copper selenide colloids.[247-248] The reaction may instead have proceeded through an electrochemical

process in which Cu^{1+} ions diffused into the selenium nanowires as well as through a solid-state reaction in which Cu^0 atoms diffused into the selenium in contact with the Cu substrate.[75, 91, 257, 261, 263, 266] The combination of both processes lead to the transformation of selenium nanowires into cupric and cuprous selenide nanowires.

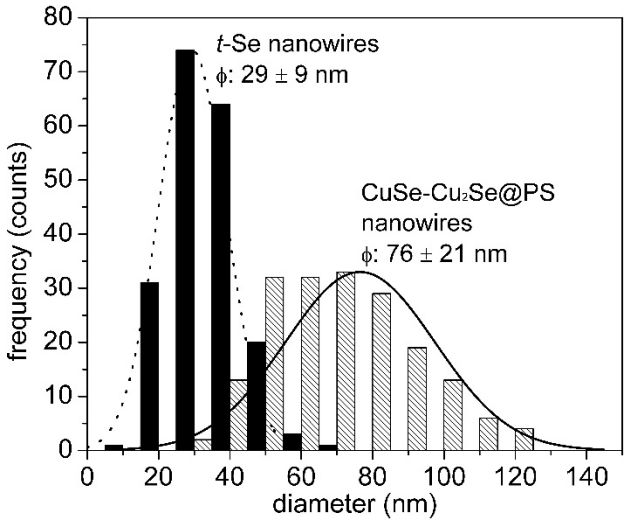

Figure 6.6 The transformed nanowires of copper selenide@polystyrene (CuSe-Cu_2Se@PS) have a larger core diameter in comparison to the starting material of trigonal selenium (t-Se). Average diameters were calculated from ~200 nanowires.

Copper selenide and copper selenide@polystyrene nanowires were further investigated with alternative TEM imaging modes to analyze the crystalline domains within these nanostructures. Under higher magnification TEM in the bright-field imaging mode (Figure 6.7a and c) in which the (000) diffraction spot is used to acquire the image, features such as grain boundaries and Moiré fringes are easily identifiable. The specific size of each grain and the orientation of these grains are difficult to discern from the bright-field image. Different regions of the sample that have similar crystal orientations and therefore jointly contribute to specific electron beam diffractions can be distinguished using a dark-field imaging mode. For example, other individual diffraction spots can be used to produce an image that distinguishes the size and distribution of grains within the $Cu_{1.75\pm0.04}$Se@PS and $Cu_{1.63\pm0.04}$Se nanowires that contribute to this diffraction (Figure 6.7b and d). This analysis suggests that the crystalline domains within the copper selenide nanowire have lateral dimensions from approximately 2 to 50 nm.

Additional confirmation of the phase and purity of copper selenide nanowires was sought using X-ray spectroscopy.

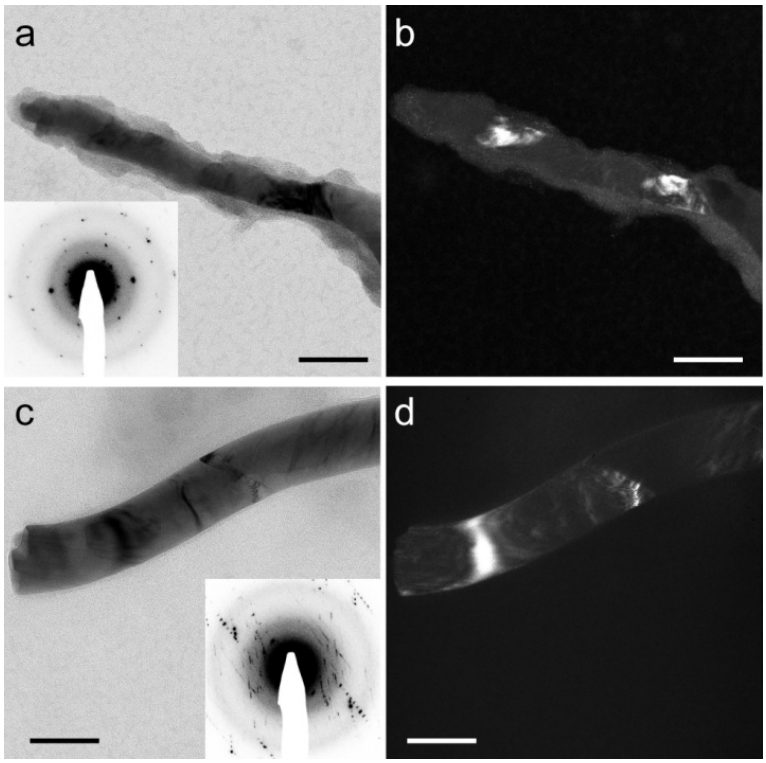

Figure 6.7 (a, c) Grain boundaries and Moiré fringes are observable in a bright-field TEM image of a copper selenide@polystyrene nanowire (CuSe-Cu_2Se@PS NW) and copper selenide nanowire (CuSe-Cu_2Se NW), respectively, obtained using the (000) diffraction spot. (b, d). Dark-field images acquired from the same region of each sample reveal the size and frequency of grains within each nanowire that have a similar orientation to one another. Scale bars are 100 nm.

We investigated the phase of the anisotropic copper selenide by powder XRD analysis. The acquired diffraction pattern (Figure 6.8) contains a set of overlapping diffraction peaks. Some of these diffractions arise from unreacted selenium nanowires, which correlate to PDF#: 42-1245. Other peaks coincide with hexagonal copper selenide (CuSe, PDF#: 01-072-8417 34-171), cubic copper selenide (Cu_2Se, PDF#: 46-1129), and orthorhombic copper selenide (CuSe, PDF#: 86-1239). After one month of reaction, the reaction product consists of ~43% copper selenide nanowires and ~57% selenium nanowires. The powder XRD pattern was studied by a quantitative Rietveld phase analysis through a Materials Analysis Using Diffraction (MAUD) program (Appendix B).[270]

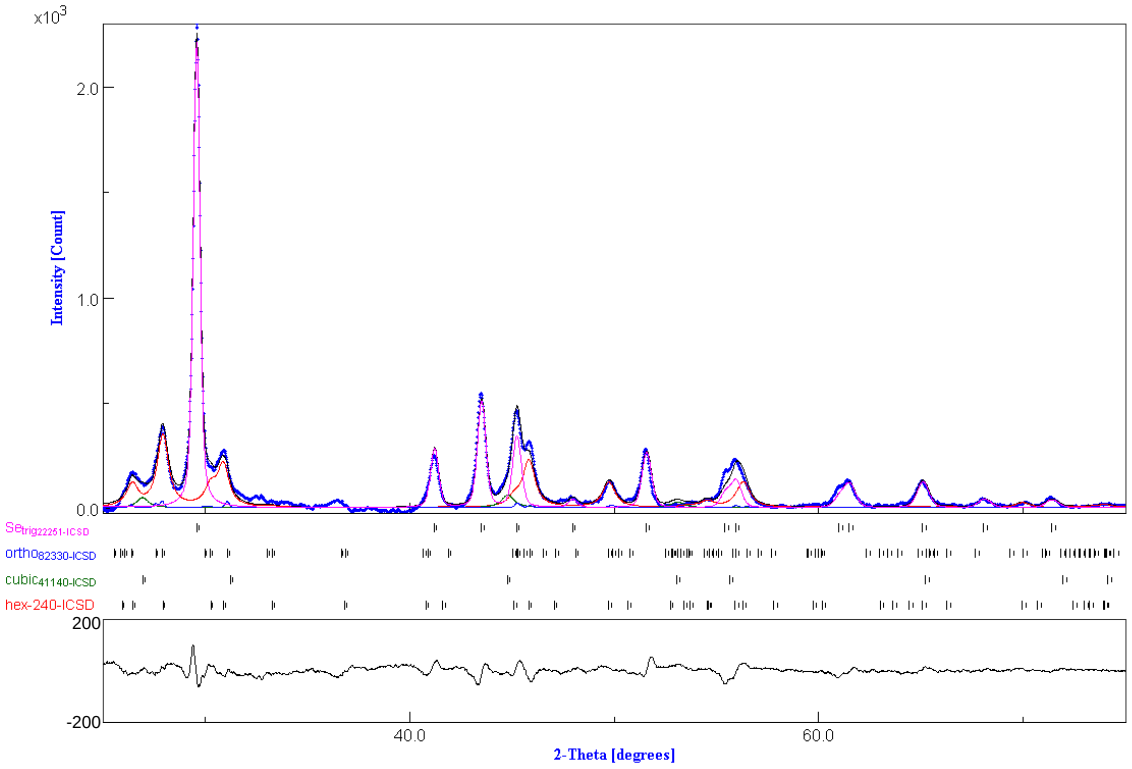

Figure 6.8 Quantitative analysis of powder XRD pattern of the crude product after 1 month of reaction is composed of selenium (pink, 57%), orthorhombic copper selenide (blue, 1%), cubic copper selenide (green, 7%), and hexagonal copper selenide (red, 35%). A linear combination of the four fits is shown in black. The bottom plot represents the residual ($R_{expt.}$ = 2%) of the curve fitting.

The presence of selenium nanowires in the product diminishes with increasing reaction time. After 3 months, ~97% of selenium nanowires were converted to copper selenide nanowires (Figure 6.9). Optical characterization of the as-synthesized nanowires, such as by UV-vis absorption spectroscopy, could lead to an erroneous interpretation of the electronic transitions of these copper selenide nanowires due to the presence of unreacted selenium nanowires. Therefore, the unreacted selenium nanowires must be selectively removed from the sample. Selenium can be dissolved in a number of solvents, such as hydrazine[49] and carbon disulfide,[271] but these chemicals might also influence the composition of the copper selenide nanowires. Hence, an alternative method of was sought to selectively remove residual selenium from the as-synthesized mixture.

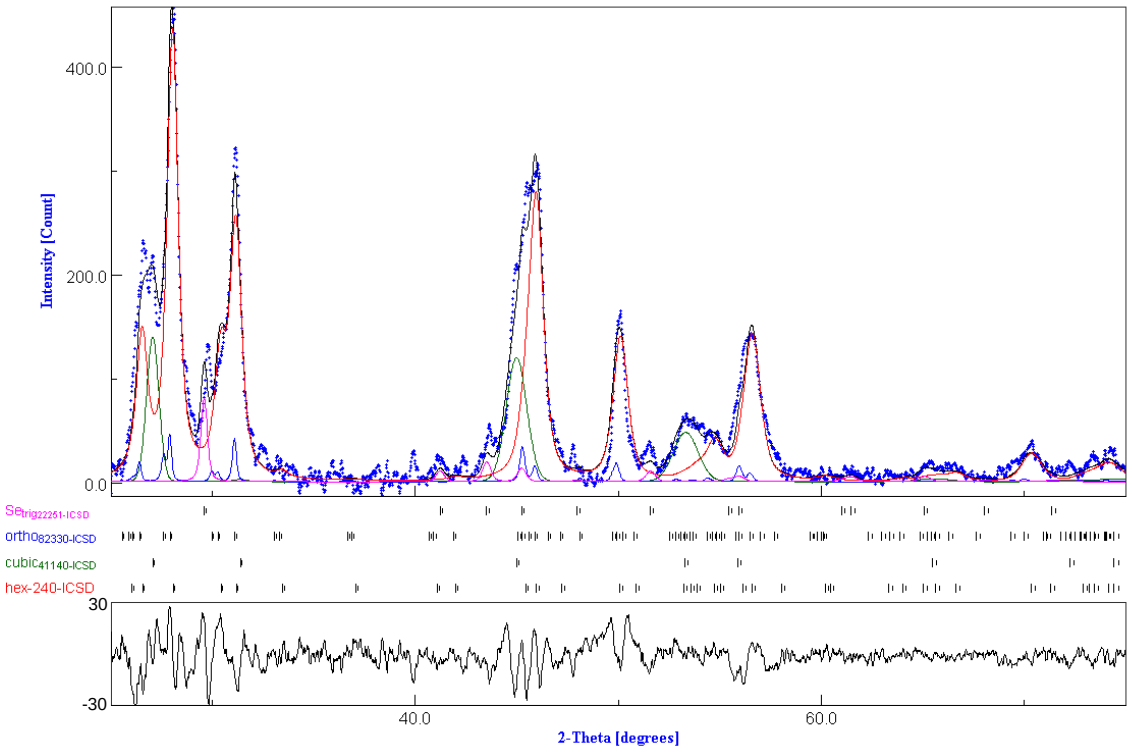

Figure 6.9 Quantitative analysis of powder XRD pattern of the crude product after 3 months of reaction is composed of selenium (pink, 3%), orthorhombic copper selenide (blue, 4%), cubic copper selenide (green, 26%), and hexagonal copper selenide (red, 67%). The blue dotted trace represents the raw data and the black trace is the linear combination of the four components. The bottom plot represents the residual ($R_{expt.}$ = 2%) of the curve fitting.

Differential scanning calorimetry studies of selenium and copper selenide indicate these materials have very different melting and decomposition temperatures. Selenium melts at 221℃,[56] whereas the copper selenide decomposes to β-$Cu_{2-x}Se$ at 380℃.[254] By operating between these two temperature ranges, it is possible to selectively remove the unreacted Se from the crude product by thermal evaporation. One method of purification is to heat a batch of crude product at 300℃ in a Schlenk tube fitted with a cold finger under ambient pressure for 12 h. Subsequent analysis of the heat-treated samples by powder XRD (Figure 6.10) indicates the selective removal of selenium nanowires from the crude product because of the absence of trigonal selenium (*t*-Se) diffraction peaks. The purified product potentially consists of a mixture of three different phases of copper selenide. These phases are hexagonal (CuSe, PDF#: 01-072-8417 34-171), orthorhombic (CuSe, PDF#: 86-1239), and cubic (Cu_2Se, PDF#: 46-1129)

copper selenide (Figure 6.10). The thermally purified copper selenide nanowires are polycrystalline with an average domain size of 23 ± 13 nm, as approximated from the XRD data (Figure 6.10) using the Scherrer equation (See Appendix E).[272] In addition, HAADF-STEM images of the purified copper selenide nanowires (Figure 6.11) indicate that the anisotropic nanostructure remains intact after thermal treatment to selectively remove the unreacted selenium nanowire template.

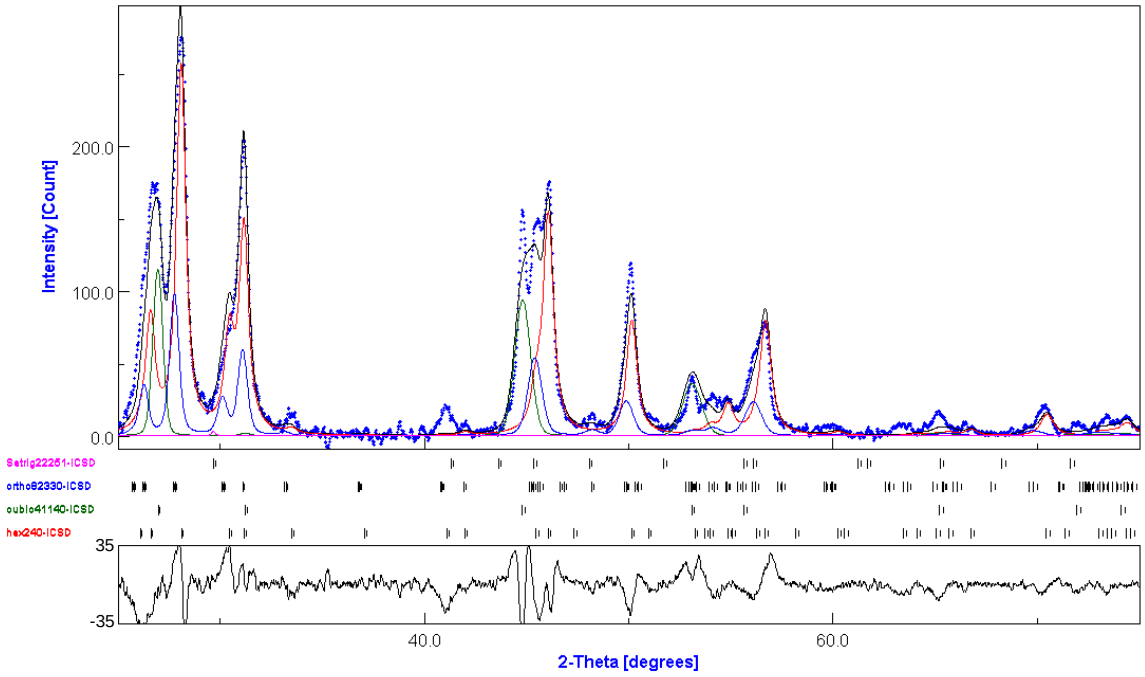

Figure 6.10 X-ray diffraction pattern depicting a sample of purified nanowires after the successful removal of selenium from the crude product by heating the sample at 300℃ for 12 h. The pure copp er selenide nanowires consist of a mixture of hexagonal (red; 53.4%; PDF#: 01-072-8417 34-171), orthorhombic (blue; 18.1%; PDF#: 86-1239), cubic (green; 28.4%; PDF#: 46-1129) phases, and trigonal selenium (pink; 0.1%. The blue dotted trace represents the raw data and the black trace is the linear combination of the three components. The quantitative analysis was approximated in Materials Analysis Using Diffraction (MAUD) software through the Rietveld method. The bottom plot represents the residual ($R_{expt.}$ = 2.7%) of the curve fitting.

Heating the PS beyond its decomposition temperature[39] could lead to carbonization of the polymer, converting the PS coating on the copper selenide nanowires into a mixture of amorphous carbon and graphite. High-angle annular dark-

field imaging through scanning transmission electron microscopy analysis of the copper selenide@polystyrene nanowires revealed a change in the density of the PS coating after the sample had been thermal purified (Figure 6.11). Prior to thermal purification to remove residual selenium nanowires the PS coatings were observed as the low contrast material that coated the surfaces of the nanowires (Figure 6.11a – inset). These low contrast coatings were also observed in the STEM images of thermally purified copper selenide@polystyrene nanowires, which were purified either at 300°C under atmospheric pressure or under vacuum at 160°C (insets of Figure 6.11b and Figure 6.11c, respectively). The STEM images revealed no observable difference in the copper selenide nanowires purified under either condition. Both purification methods had preserved the nanostructures' anisotropic shape while keeping the nanowires encapsulated in low contrasting material after thermal treatment to remove residual selenium nanowires.

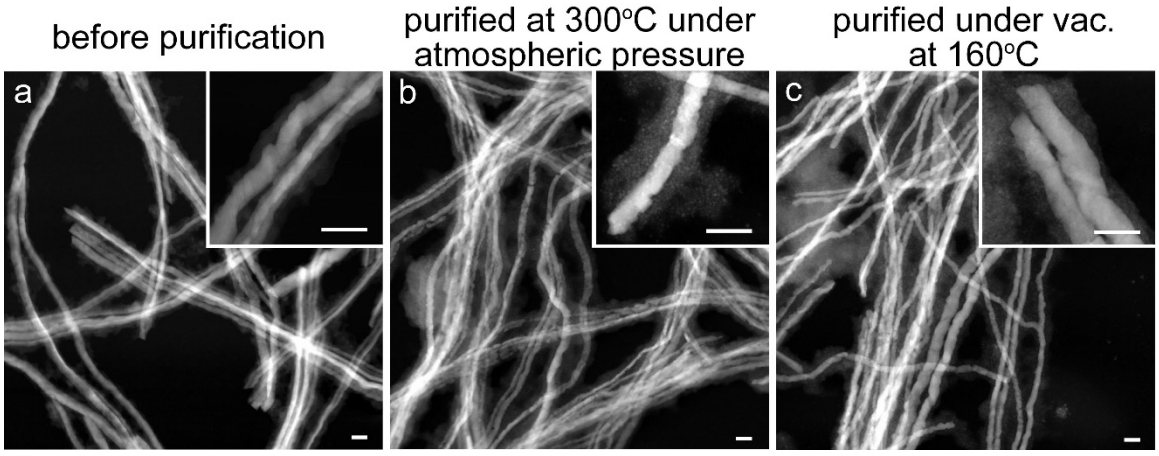

Figure 6.11 High angle annular dark field (HAADF) imaging by scanning transmission electron microscopy (STEM) analysis of copper selenide@polystyrene nanowires (CuSe-Cu_2Se@PS) (a) before thermal purification, (b) thermally purified at 300 °C under atmospheric pressure for 12 h, and (c) thermally purified at 160 °C under vacuum for 12 h. Scale bars are 100 nm.

After the sample was thermally purified at 300 °C, the chemical state of the PS coating on CuSe-Cu_2Se core-shell nanostructures was investigated by XPS. Analysis by XPS of these purified samples revealed the absence of the π–π^* transition at ~291 eV, indicating that the polymer coatings on the copper selenide nanowires had lost their aromaticity (Figure 6.4b and c). In addition, analysis by electron energy loss

spectroscopy of the carbon K-edge performed using a scanning transmission electron microscope suggested that the polymer coatings have similar chemical state as the amorphous carbon coating after the thermal purification process (Figure 6.12).

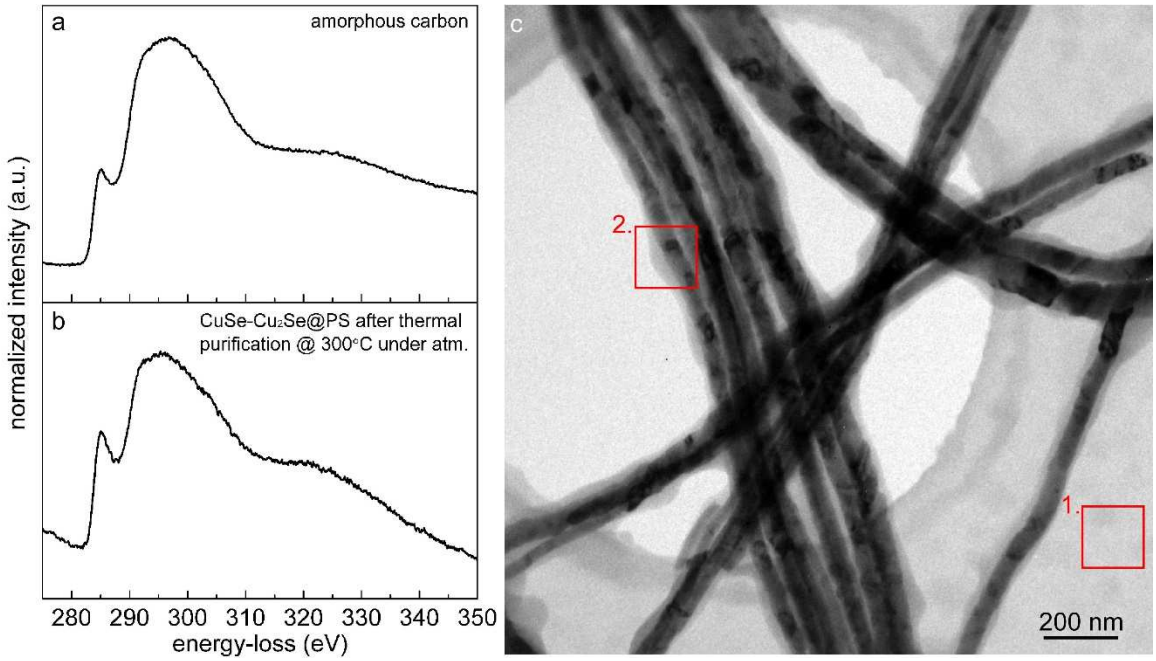

Figure 6.12 Analysis of the carbon K-edge by electron energy loss spectroscopy (EELS) for (a) amorphous carbon and (b) CuSe-Cu_2Se@PS nanowires after residual selenium nanowires were removed by thermal evaporation at 300 ℃ under atmospheric pressure. (c) TEM image of CuSe-Cu_2Se@PS nanowires supported on a holey carbon grid. The regions indicated by the red boxes correspond to the positions used for EELS analysis of amorphous carbon (box #1) and CuSe-Cu_2Se@PS nanowires (box #2).

Optoelectronic properties of selenium nanowires and purified copper selenide@polystyrene nanowires were characterized using UV-vis spectroscopy. Both materials have electronic transitions that can be excited in the UV-vis region of the electromagnetic spectrum. The UV-vis absorption spectrum of selenium nanowires (Figure 6.13a) spans from the UV to the near infrared (NIR) wavelengths of the electromagnetic spectrum, with three strongly absorbing peaks at 344, 437, and 559 nm, respectively. These peaks represent intramolecular and intermolecular electronic transitions.[28] The absorption spectrum of copper selenide (Figure 6.13b) indicates that the material can absorb a wide range of the photon energies, but it is most efficient at absorbing in the UV region of the electromagnetic spectrum. The purified CuSe-

Cu_2Se@PS nanowires have an absorption edge at 508 nm (2.44 eV) that corresponds to the direct bandgap energy. The bandgap energy falls in between that of the reported values of cubic (2.2 eV)[247] and hexagonal (2.0 and 2.8 eV)[250] copper selenide. The observed bandgap might be due to mixing of the bandgaps of the two different phases.

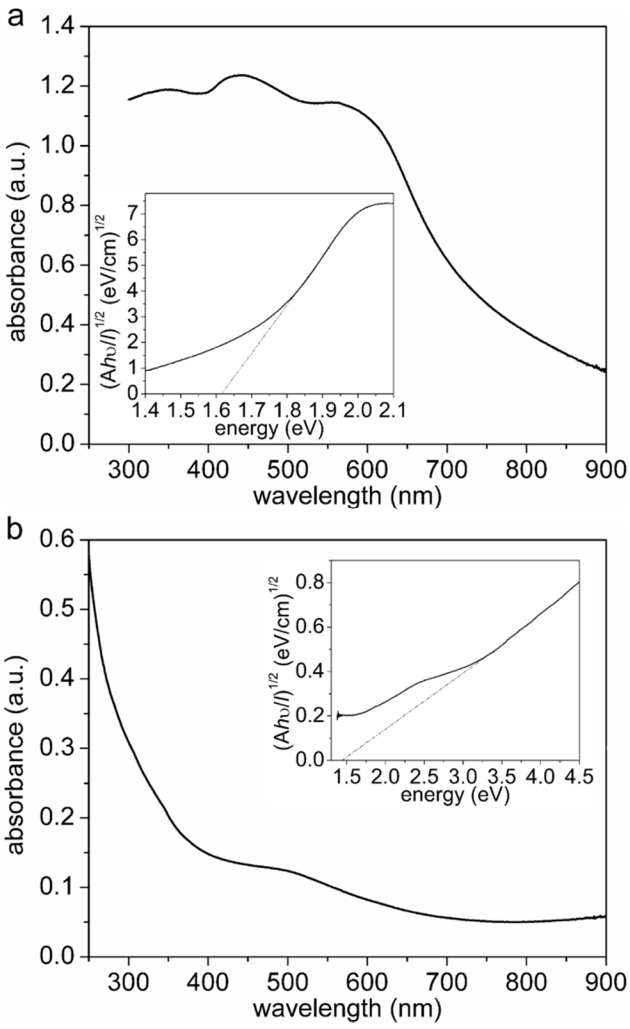

Figure 6.13 UV-vis absorption studies conducted on uniform dispersions of (a) selenium nanowires and (b) copper selenide@polystyrene nanowires (purified by heat treatment) as well as the corresponding plots used to estimate the indirect bandgap of each sample (a and b insets, respectively).

The inset plots of Figure 6.13a and b are used to estimate the indirect bandgap of the selenium and copper selenide nanowires using the formula: $(\alpha h\nu)^{1/2} = (Ah\nu/l)^{1/2} = (h\nu - E_g)$.[6] The absorption coefficient (α) can be calculated using the Beer–Lambert

equation from acquired absorbance *(*A) values and the known light path length (*l*). At the corresponding spectral wavelengths, the photon energy is calculated by multiplying frequency (*v*) of the wavelength of radiation by the Planck constant (*h*). The bandgap energy (E_g) of the material is estimated by determining the x–intercept of the steepest slope in a plot of $(Ahv/l)^{1/2}$ against *hv*. The estimated indirect bandgap of the selenium nanowires with an average diameter of 29 ± 9 nm is 1.61 eV, which closely matches the value of 1.65 eV previously reported on nanowires of a similar diameter.[28] The purified CuSe-Cu_2Se@PS nanowires have an indirect bandgap energy of 1.44 eV that is similar to reported literature values of 1.0–1.4 eV.[273]

6.4. Conclusions

This study was the first report of the direct conversion of selenium nanowires into cuprous and cupric selenide@polystyrene nanowires. This study demonstrated that the transformation of selenium to copper selenide proceeds readily under ambient conditions. The reaction was initiated by the surface-initiated atom transfer radical polymerization of styrene on the surfaces of the selenium nanowires or Cu/CuOx substrate. It is proposed that the styrene radical or polystyrene radicals subsequently reduced the Cu^{2+} oxide species to Cu^{1+} analogues and Cu^0. These copper species subsequently react either through an electrochemical or a solid-state process with the selenium nanowires. The single crystalline selenium nanowire templates were simultaneously converted into polycrystalline cuprous and cupric selenide nanowires encapsulated with a thin sheath of polystyrene. Transformation from single crystalline selenium templates into polycrystalline copper selenide@polystyrene nanowires was accompanied with an increase in the diameter of the copper selenide nanowires. These polycrystalline copper selenide nanowires coated with a thin sheath of polystyrene have an average composition of $Cu_{1.75\pm0.04}$Se@PS, as determined by EDS analysis on a collection of the nanostructures. Spot EDS analyses performed along the length of individual $Cu_{1.75\pm0.04}$Se@PS nanowire revealed a larger variation in Cu and Se composition, which could be due to the formation of the polystyrene layer that impedes the selenium nanowires from reacting uniformly with the Cu^{1+} species and prevents uniform physical contact between the selenium nanowires and the Cu/CuOx substrate required for a solid-state reaction. The as-synthesized product was purified by

selectively removing the unreacted selenium nanowires (~3% impurity) through a process of selective thermal evaporation that also transformed the polystyrene to an encapsulating layer of amorphous carbon. The purified CuSe-Cu_2Se@PS nanowires exhibited an indirect bandgap of 1.44 eV. This process could be readily extended to the formation and polymer encapsulation of other copper selenide nanostructures, but it may be adapted for the polymer encapsulation of other nanostructures.

6.5. Future Directions in Surface-Initiated Atom Transfer Radical Polymerization Induced Transformation of Selenium Nanowires into Copper Selenide@Polystyrene Core–Shell Nanowires

This work can be extended to the transformation of selenium nanowires into other metal selenides, binary metal selenide, or ternary metal selenide nanowires initiated by the SI-ATRP process. Indium and gallium selenide nanowires are particularly interesting because of their potential applications in photovoltaic devices once they are further transformed into $CuInSe_2$ and $CuIn_xGa_{(1-x)}Se_2$.[274-276] The syntheses of these metal selenides nanoparticles, usually, involves the co-reduction of the corresponding metal salts at high temperatures.[66, 277] Anisotropic nanostructures of indium and gallium selenides could be synthesized from selenium nanowire templates in this template-engaged process to provide a complementary synthetic route to cation/anion-exchange techniques to prepare copper selenides from cadmium selenides.[33, 241]

Another area of interest is to investigate the identity of the nanoparticles found on the surfaces of the CuSe-Cu_2Se@PS nanowires. These nanoparticle decorated CuSe-Cu_2Se@PS nanowires are only observed in samples from which the styrene had evaporated unintentionally. Styrene had evaporated from a loosely capped reaction vessel at RT and atmospheric pressure over a period of ~1 year. High resolution TEM imaging revealed these nanoparticles are single crystalline nanocrystals (Figure 6.14). Particle size analysis by TEM indicates these nanoparticles have an average diameter of 3 ± 0.8 nm. Future goals of this project include determining the elemental composition of the single crystalline nanoparticles by STEM-EDS and examining the possible mechanism in which these single crystalline nanoparticles were formed during the

chemical transformation of selenium nanowires into CuSe-Cu_2Se@PS nanowires. As control reactions, one of the three reactants (Cu/CuOx, selenium nanowires, and styrene) would be excluded from reaction. For example, Cu/CuOx substrate would be immersed in styrene for 6 months in the absence of selenium nanowires. As a control experiment, another portion of selenium nanowires would be kept in a solution of styrene in the absence of Cu/CuOx for the same duration. The supernatants of both solutions would then be analyzed by TEM and STEM-EDS to screen for the formation of the single crystalline nanoparticles at 1, 3, and 6 months of reaction time.

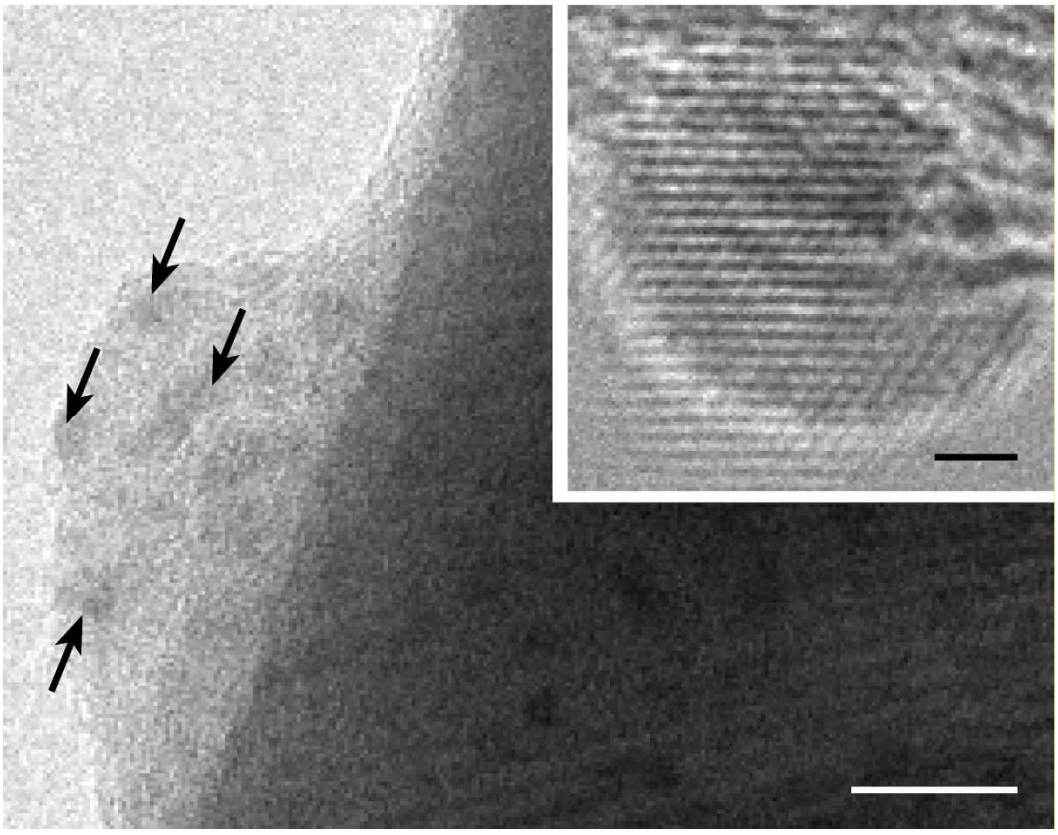

Figure 6.14 TEM analysis reveals the presence of single crystalline nanoparticles embedded and on the surfaces of the PS coating (highlighted by arrows). (Inset) The corresponding lattice fringe image of a nanoparticle adhered to the surfaces of the PS sheath. Scale bars are 10 nm and (inset) 1 nm, respectively.

7. Conclusions and Outlook

7.1. Conclusions

To recap, at the beginning of this thesis our goals were to address the following four challenges listed as questions to improve our understanding of the surface chemistry of selenium nanowires: 1) how can we synthesize selenium nanowires with a controlled diameter and length?; 2) how can we alter the surfaces of the selenium nanowires to facilitate colloidal stability and dispersion of the nanowires for easier processing and to facilitate a more uniform chemical reaction on these templates?; 3) how do we manipulate selenium nanowires en mass, as well as individually?; and 4) how do we prevent the chemical degradation of selenium? In short, we were able to address and resolve the challenges that we found in growing high-aspect-ratio nanowires, creating stable dispersions, manipulating the nanowires en mass, and preventing their chemical degradation. In addition, we were able to combine the new synthetic techniques with our acquired knowledge of selenium nanowire's surface chemistry to synthesize new classes of core-shell nanostructures (i.e., polystyrene coated selenium and polystyrene coated copper selenide nanowires).

In Chapter 2, we have demonstrated that sonochemically-induced synthesis of selenium nanowires grow by an Ostwald ripening process. The solubilized selenium atoms nucleate to form *t*-Se seeds, upon which subsequent recrystallization takes place. The selenium nanowires form as a result of preferential recrystallization on the high energy {001} facets of *t*-Se seeds. These selenium nanowires are single crystalline and grow preferentially along the <001> directions. We were able to tune the diameter of the selenium nanowires by adjusting the solubility of *a*-Se precursor in the growth medium via temperature regulation. Temperature was used to control the availability of solubilized selenium and the rate of nanowire growth. We have identified that the amorphous selenium colloids need to dissolve at a sufficient rate to supply the growth of high-aspect-ratio selenium nanowires, while an overabundance of dissolved selenium

would lead to the formation of low-aspect-ratio selenium nanorods. In addition, we have demonstrated that the solubilized selenium attach preferentially to the higher surface energy facets of the selenium nanowires by selectively inhibiting their axial growth. Addition of 11-hydroxyundecan-1-thiol during the growth of the selenium nanowires selectively inhibits the {001} facets from further recrystallization processes, forcing the selenium anisotropic nanostructures to grow radially. We have also determined that the concentration of *a*-Se colloid and water content in the growth medium have a direct impact on the success of sonochemically-induced transformation. High concentrations of both *a*-Se and water content in the growth medium lead to aggregation of the *a*-Se colloids, decreasing the solubility of *a*-Se. Large aggregates of *a*-Se colloids cannot dissolve fast enough to support the growth of selenium nanowires and, therefore, lower the chance of a successful sonochemically-induced transformation. Using the optimized parameters developed in this study, we are able to consistently produce selenium nanowires with average diameters of 29 ± 9 nm.

In Chapter 3, we have systematically examined the colloidal stability of selenium nanowires in a variety of organic and aqueous media. We have identified that organic solvents comprised of long aliphatic hydrocarbons are able to uniformly disperse the selenium nanowires, while providing viscous environments capable of keeping the nanowires suspended for long periods of time. Favorable interactions between the nanowires and the dispersing media was one of the key factors to obtain a homogenous dispersion of selenium nanowire. Solvents that are both viscous and can interact favorably with the surfaces of selenium nanowires provided the highest colloidal stability. The colloidal stability of the nanowires could also be enhanced through the addition of surfactants or polymers to provide steric stabilization. In addition, surfactants and polymers were used to facilitate the dispersion of otherwise hydrophobic selenium nanowires into aqueous solutions. We also have demonstrated that uniformity of platinum decorated selenium nanostructures (Se@Pt) prepared from selenium nanowire templates is directly influenced by how well the selenium nanowires are dispersed in solution. Performing the reaction with a poorly dispersed sample of selenium nanowires leads to the formation of undesired products, such as hollow Pt nanoshells, instead of platinum decorated selenium nanowires.

In Chapter 4, we have developed a technique for assembling nanowires of semiconductors and metals into macroscopic fibers directed along electric field when suspended in low dielectric solvents. This technique is capable of simultaneously assembling nanowires into an array of parallel fibers over distances much greater than the length of individual nanowires. The assembled fiber of selenium nanowires can extend over ~7 cm when assembled from dispersions of nanowires within 1 min of applying an electric potential to the solvent. These fibers of selenium nanowires can be isolated from solution, or re-dispersed as a suspension of individual nanowires in the absence of an electric field. These re-dispersed nanowires can be assembled into another fiber. Free-standing fibers of selenium nanowires are flexible and photoconductive. We have demonstrated that the electrokinetic assembly technique is versatile and scalable for directing the assembly of solution-phase synthesized nanowires that may otherwise be difficult to organize.

In Chapter 5, we have determined the chemical composition at the surfaces of as-synthesized selenium nanowires using a combination of surface sensitive techniques, such as X-ray photoelectron spectroscopy (XPS) and secondary ion mass spectrometry (SIMS). We are the first to report that water molecules residing on the surfaces of the selenium nanowires interact with the surface selenium atoms to give rise to an additional chemical state ($Se^{\delta+}$) observed through XPS and SIMS analyses. In addition, surface sensitive analysis techniques revealed that *t*-Se nanowires oxidize when stored under ambient conditions, resulting in the formation of selenium dioxides. The selenium dioxides are dissolved in the presence of moisture, leading to corrosion of the selenium nanowire, which becomes pitted and fragmented. To increase the corrosion resistance of selenium nanowires, we encapsulated the nanowires with a thin layer of polystyrene formed by a surface-initiated atom transfer radical polymerization process. The PS encapsulation served as a moisture barrier to prevent the dissolution of selenium oxides on the surfaces of selenium nanowires. The XPS spectrum of *t*-Se@PS nanowires contains a new chemical state in comparison to the uncoated *t*-Se, suggesting Se-C formation during the surface-initiated atom transfer radical polymerization process. This encapsulating layer of polystyrene dramatically increases the resilience (greater than 800 times more resilient to corrosion) of the selenium nanowires towards corrosion.

In Chapter 6, we have adopted the technology developed to increase the corrosion resistance of selenium nanowires to form copper selenide nanowires. We were able to directly convert selenium nanowires into cuprous and cupric selenide@polystyrene nanowires under ambient conditions. The reaction is initiated by the surface-initiated atom transfer radical polymerization of styrene on the surfaces of the selenium nanowires or a Cu/CuOx substrate. We proposed that the styrene radical or polystyrene radicals subsequently reduced the Cu^{2+} oxide species to Cu^{1+} analogues and Cu^{0}. These copper species subsequently react either through an electrochemical or a solid-state process with the selenium nanowires. The single crystalline selenium nanowire templates were simultaneously converted into polycrystalline cuprous and cupric selenide nanowires encapsulated with a thin sheath of polystyrene. These polycrystalline copper selenide nanowires coated with a thin sheath of polystyrene have an average composition of $Cu_{1.75\pm0.04}Se$@PS, as determined by energy-dispersive X-ray spectroscopy (EDS) of the nanostructures. Spot EDS analyses performed along the length of individual $Cu_{1.75\pm0.04}Se$@PS nanowires revealed a larger variation in Cu and Se composition, which could be due to the formation of the polystyrene layer that impedes the selenium nanowires from reacting uniformly with the Cu(I) species and prevents uniform physical contact between the selenium nanowires and the Cu/CuOx substrate required for a solid-state reaction. The as-synthesized product was purified by selectively removing the unreacted selenium nanowires (~3% impurity) through a process of selective thermal evaporation that also transformed the polystyrene into an encapsulating layer of amorphous carbon. The purified CuSe-Cu_2Se@PS nanowires exhibited an indirect bandgap of 1.44 eV. This process could be readily extended to the formation and polymer encapsulation of other copper selenide nanostructures, but it may also be adapted for the polymer encapsulation of other nanostructures.

7.2. Outlook

Nanoparticle catalysts that can be immobilized on solid supports are highly sought after because they can be easily isolated and recycled from heterogeneous reactions.[278] One of the challenges in heterogeneous catalysis is to maintain the colloidal stability of the heterogeneous catalysts in the reaction media. Aggregation of the nanoparticles or nanoparticles immobilized on a solid support would decrease the overall

active surface area of the catalyst, resulting in a decrease in the rate of reaction. Aggregation of the catalyst supports could be avoided by selectively functionalizing the support materials with the appropriate surface chemistry. Anisotropic selenium nanostructures could be used as sacrificial templates to produce porous materials containing nanoparticle catalysts. The surfaces of selenium nanowires can be decorated with nanoparticle when they are mixed with the appropriate transition metal salts, such as platinum, ruthenium, and palladium (Figure 7.1 – *t*-Se@M-NPs).[49, 71, 86] Subsequently, the nanoparticle decorated selenium nanowires could be encapsulated with a polymer (e.g., polystyrene or polyacrylonitrile) by surface-initiated atom transfer radical polymerization (Figure 7.1 – *t*-Se@M-NPs@PS).[47, 208] The surface chemistry of polymer encapsulation could be further modified to increase the colloidal stability of the catalyst support core-shell structures. The catalyst support core-shell structures can be fragmented by sonication to expose the selenium. Selenium could then be selectively removed by exposing the sample to a solution of nitric acid[47] or hydrazine[71] to yield a hollow polymer structure with nanoparticles supported on the inside walls (Figure 7.1 – M-NPs@PS). This synthesis would yield a new form of colloidal material that could be used trap oxygen gas when exposed to a dilute solution of hydrogen peroxide. One of the potential applications is to use the M-NPs@PS with trapped gases as contrast agent for non-invasive ultrasound or magnetic resonance imaging diagnostics and therapeutics.[279-280]

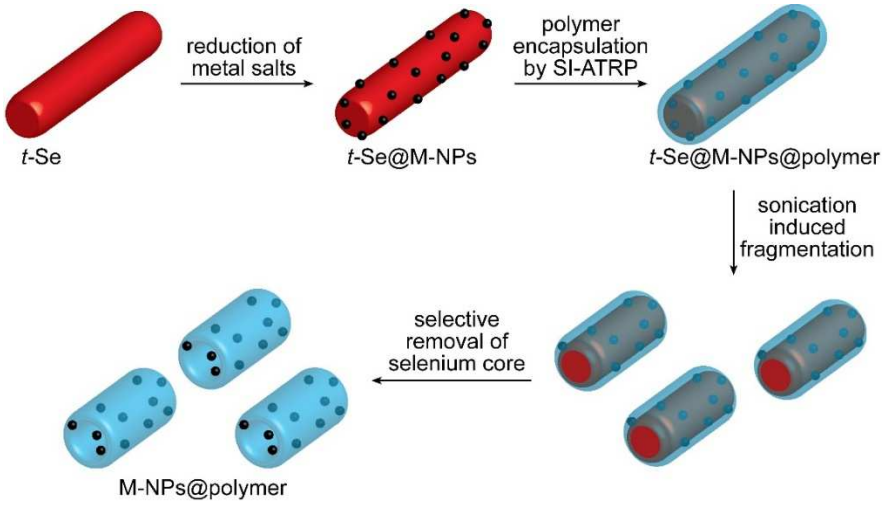

Figure 7.1 A schematic on the synthesis of hollow polymer tubes with metal nanoparticles (M-NPs) decorated on the inside from templates of trigonal selenium nanowires (t-Se).

References

(1) West, A. R., *Basic Solid State Chemistry*; 2nd ed.; John Wiley & Sons, Ltd: England, 1999.

(2) Smart, L. E.; Moore, E. A., *Solid State Chemistry an Introduction*; 3rd ed.; Taylor & Francis Group: Florida, 2005.

(3) Li, Y.; Qian, F.; Xiang, J.; Lieber, C. M. Nanowire Electronic and Optoelectronic Devices. *Mater. Today* **2006,** *9*, 18-27.

(4) Baliga, B. J., *Fundamentals of Power Semiconductor Devices*; Springer: Berlin, 2008.

(5) Numai, T., *Fundamentals of Semiconductor Lasers*; Springer: New York, 2004.

(6) Marwede, M.; Berger, W.; Schlummer, M.; Maurer, A.; Reller, A. Recycling Paths for Thin-Film Chalcogenide Photovoltaic Waste - Current Feasible Processes. *Renew. Energy* **2013,** *55*, 220-229.

(7) Kim, F. S.; Ren, G. Q.; Jenekhe, S. A. One-Dimensional Nanostructures of Pi-Conjugated Molecular Systems: Assembly, Properties, and Applications from Photovoltaics, Sensors, and Nanophotonics to Nanoelectronics. *Chem. Mater.* **2011,** *23*, 682-732.

(8) Hochbaum, A. I.; Yang, P. D. Semiconductor Nanowires for Energy Conversion. *Chem. Rev.* **2010,** *110*, 527-546.

(9) Miller, P.; O'Leary, T. Mediating Instruments and Making Markets: Capital Budgeting, Science and the Economy. *Account. Organ. Soc.* **2007,** *32*, 701-734.

(10) Veendrick, H. J. M., *Nanometer Cmos Ics: From Basics to Asics*; 1st ed.; Springer: New York, 2008.

(11) Kamata, Y. High-K/Ge Mosfets for Future Nanoelectronics. *Mater. Today* **2008,** *11*, 30-38.

(12) Khan, A.; Balakrishnan, K.; Katona, T. Ultraviolet Light-Emitting Diodes Based on Group Three Nitrides. *Nat. Photonics* **2008,** *2*, 77-84.

(13) Morkoc, H.; Strite, S.; Gao, G. B.; Lin, M. E.; Sverdlov, B.; Burns, M. Large-Band-Gap Sic, Iii-V Nitride, and Ii-Vi Znse-Based Semiconductor-Device Technologies. *J. Appl. Phys.* **1994,** *76*, 1363-1398.

(14) Dai, Q. Q.; Duty, C. E.; Hu, M. Z. Semiconductor-Nanocrystals-Based White Light-Emitting Diodes. *Small* **2010,** *6*, 1577-1588.

(15) McEvoy, A. J.; Castaner, L.; Markvart, T., *Solar Cells: Materials, Manufacture and Operation*; 2nd ed.; Academic Press: Oxford, 2012.

(16) Lutz, G., *Semiconductor Radiation Detectors*; 1st ed.; Springer: Verlag, 2007.

(17) Lu, W.; Lieber, C. M. Semiconductor Nanowires. *J. Phys. D: Appl. Phys.* **2006,** *39*, R387-R406.

(18) Xia, Y.; Yang, P.; Sun, Y. G.; Wu, Y. Y.; Mayers, B.; Gates, B.; Yin, Y.; Kim, F.; Yan, Y. Q. One-Dimensional Nanostructures: Synthesis, Characterization, and Applications. *Adv. Mater.* **2003,** *15*, 353-389.

(19) Hayden, O.; Agarwal, R.; Lu, W. Semiconductor Nanowire Devices. *Nano Today* **2008,** *3*, 12-22.

(20) Abouraddy, A. F.; Bayindir, M.; Benoit, G.; Hart, S. D.; Kuriki, K.; Orf, N.; Shapira, O.; Sorin, F.; Temelkuran, B.; Fink, Y. Towards Multimaterial Multifunctional Fibres That See, Hear, Sense and Communicate. *Nat. Mater.* **2007,** *6*, 336-347.

(21) Wang, M. C. P.; Gates, B. D. Directed Assembly of Nanowires. *Mater. Today* **2009,** *12*, 34-43.

(22) Lu, W.; Lieber, C. M. Nanoelectronics from the Bottom Up. *Nat. Mater.* **2007,** *6*, 841-850.

(23) *Crc Handbook of Chemistry and Physics*; 92nd ed.; CRC Press: Internet Version, 2012.

(24) Cherin, P.; Unger, P. The Crystal Structure of Trigonal Selenium. *Inorg. Chem.* **1967,** *6*, 1589.

(25) Nagata, K.; Ishibashi, K.; Miyamoto, Y. Raman and Infrared-Spectra of Rhombohedral Selenium. *Jpn. J. Appl. Phys.* **1981,** *20*, 463-469.

(26) Cherin, P.; Unger, P. Crystal Structure of Trigonal Selenium. *Inorg. Chem.* **1967,** *6*, 1589-&.

(27) Joannopoulos, J. D.; Schluter, M.; Cohen, M. L. Electronic-Structure of Trigonal and Amorphous Se and Te. *Phys. Rev. B* **1975,** *11*, 2186-2199.

(28) Gates, B.; Mayers, B.; Cattle, B.; Xia, Y. Synthesis and Characterization of Uniform Nanowires of Trigonal Selenium. *Adv. Funct. Mater.* **2002,** *12*, 219-227.

(29) Cheng, L.; Shao, M. W.; Chen, D. Y.; Wei, X. W.; Wang, F. X.; Hua, J. High-Yield Fabrication of T-Se Nanowires Via Hydrothermal Method and Their Photoconductivity. *J. Mater. Sci. - Mater. Electron.* **2008,** *19*, 1209-1213.

(30) Yu, D. B.; Jiang, T.; Wang, F.; Wang, Z. R.; Wang, Y.; Shi, W.; Sun, X. Q. Controlled Growth of Multi-Morphology Hexagonal T-Se Microcrystals: Tubes, Wires, and Flowers by a Convenient Lewis Acid-Assisted Solvothermal Method. *Crystengcomm* **2009,** *11*, 1270-1274.

(31) Gates, B.; Mayers, B.; Grossman, A.; Xia, Y. A Sonochemical Approach to the Synthesis of Crystalline Selenium Nanowires in Solutions and on Solid Supports. *Adv. Mater.* **2002,** *14*, 1749-1752.

(32) Yaman, M.; Khudiyev, T.; Ozgur, E.; Kanik, M.; Aktas, O.; Ozgur, E. O.; Deniz, H.; Korkut, E.; Bayindir, M. Arrays of Indefinitely Long Uniform Nanowires and Nanotubes. *Nat. Mater.* **2011,** *10*, 494-501.

(33) Moon, G. D.; Ko, S.; Min, Y.; Zeng, J.; Xia, Y.; Jeong, U. Chemical Transformations of Nanostructured Materials. *Nano Today* **2011,** *6*, 186-203.

(34) Gates, B.; Wu, Y. Y.; Yin, Y. D.; Yang, P. D.; Xia, Y. Single-Crystalline Nanowires of Ag2se Can Be Synthesized by Templating against Nanowires of Trigonal Se. *J. Am. Chem. Soc.* **2001,** *123*, 11500-11501.

(35) Ko, S.; Moon, G. D.; Jeong, U. Surface Energy-Controlled in-Plane Growth of T-Se Nanowires Transformed from a-Se Colloids. *Nanotechnology* **2008,** *19*, 345601.

(36) Cronemeyer, D. C. Hall and Drift Mobility in High-Resistivity Single-Crystal Silicon. *Phys. Rev.* **1957,** *105*, 522.

(37) Law, M.; Goldberger, J.; Yang, P. D. Semiconductor Nanowires and Nanotubes. *Annual Review of Materials Research* **2004,** *34*, 83-122.

(38) Maurice, V.; Marcus, P., *Electrochemistry at the Nanoscale*; Springer Science+Business Media: New York, 2009.

(39) Mondal, K.; Srivastava, S. K. A New Hydrothermal Route to Nano- and Microstructures of Trigonal Selenium Exhibiting Diverse Morphologies. *Mater. Chem. Phys.* **2010,** *124*, 535-540.

(40) Mayers, B. T.; Liu, K.; Sunderland, D.; Xia, Y. Sonochemical Synthesis of Trigonal Selenium Nanowires. *Chem. Mater.* **2003,** *15*, 3852-3858.

(41) Li, X. M.; Li, Y.; Li, S. Q.; Zhou, W. W.; Chu, H. B.; Chen, W.; Li, I. L.; Tang, Z. K. Single Crystalline Trigonal Selenium Nanotubes and Nanowires Synthesized by Sonochemical Process. *Cryst. Growth Des.* **2005,** *5*, 911-916.

(42) Ma, J. M.; Sun, C. S.; Lian, J. B.; Zheng, W. J. Inorganic and Organic Templates-Assisted Solvothermal Synthesis of Trigonal Selenium Microrods. *Cryst. Res. Technol.* **2009,** *44*, 391-394.

(43) Zhang, X. Y.; Cai, Y.; Miao, J. Y.; Ng, K. Y.; Chan, Y. F.; Zhang, X. X.; Wang, N. Formation and Phase Transformation of Selenium Nanowire Arrays in Anodic Porous Alumina Templates. *J. Cryst. Growth* **2005,** *276*, 674-679.

(44) Dalmaschio, C. J.; Ribeiro, C.; Leite, E. R. Impact of the Colloidal State on the Oriented Attachment Growth Mechanism. *Nanoscale* **2010,** *2*, 2336-2345.

(45) Zhang, Q.; Liu, S. J.; Yu, S. H. Recent Advances in Oriented Attachment Growth and Synthesis of Functional Materials: Concept, Evidence, Mechanism, and Future. *J. Mater. Chem.* **2009,** *19*, 191-207.

(46) Zhang, J.; Huang, F.; Lin, Z. Progress of Nanocrystalline Growth Kinetics Based on Oriented Attachment. *Nanoscale* **2010,** *2*, 18-34.

(47) Wang, M. C. P.; Gates, B. D. Synthesis of Selenium Nano-Composite (T-Se@Ps) by Surface Initiated Atom Transfer Radical Polymerization. *Chem. Commun.* **2012,** *48*, 8589-8591.

(48) Nie, Z.; Fava, D.; Kumacheva, E.; Zou, S.; Walker, G. C.; Rubinstein, M. Self-Assembly of Metal-Polymer Analogues of Amphiphilic Triblock Copolymers. *Nat. Mater.* **2007,** *6*, 609-614.

(49) Jeong, U. Y.; Herricks, T.; Shahar, E.; Xia, Y. Amorphous Se: A New Platform for Synthesizing Superparamagnetic Colloids with Controllable Surfaces. *J. Am. Chem. Soc.* **2005,** *127*, 1098-1099.

(50) Noorduin, W. L.; Vlieg, E.; Kellogg, R. M.; Kaptein, B. From Ostwald Ripening to Single Chirality. *Angew. Chem. Int. Ed.* **2009,** *48*, 9600-9606.

(51) Mobrhan-Shafiee, N. Developing an Efficient Approach to Fabricate Electric Contacts on Nanowires. Simon Fraser University, 2006.

(52) Housecroft, C. E.; Sharpe, A. G., *Inorganic Chemistry*; 2nd ed.; Prentice Hall: Upper Saddle River, NJ, 2005.

(53) Cheng, B.; Samulski, E. T. Rapid, High Yield, Solution-Mediated Transformation of Polycrystalline Selenium Powder into Single-Crystal Nanowires. *Chem. Commun.* **2003**, 2024-2025.

(54) Suslick, K. S. Sonochemistry. *Science* **1990,** *247*, 1439-1445.

(55) Mikla, V. I.; Mikla, V. V., *Amorphous Chalcogenides the Past, Present and Future*; 1st ed.; Elsevier: MA, 2012.

(56) Chen, Z. X.; Shen, Y. H.; Xie, A. J.; Zhu, J. M.; Wu, Z. F.; Huang, F. Z. L-Cysteine-Assisted Controlled Synthesis of Selenium Nanospheres and Nanorods. *Crystal Growth & Design* **2009,** *9*, 1327-1333.

(57) Luo, L. B.; Yang, X. B.; Liang, F. X.; Jie, J. S.; Li, Q.; Zhu, Z. F.; Wu, C. Y.; Yu, Y. Q.; Wang, L. Transparent and Flexible Selenium Nanobelt-Based Visible Light Photodetector. *Crystengcomm* **2012,** *14*, 1942-1947.

(58) Jeong, U. Y.; Camargo, P. H. C.; Lee, Y. H.; Xia, Y. Chemical Transformation: A Powerful Route to Metal Chalcogenide Nanowires. *J. Mater. Chem.* **2006,** *16*, 3893-3897.

(59) Son, D. H.; Hughes, S. M.; Yin, Y.; Alivisatos, A. P. Cation Exchange Reactions-in Ionic Nanocrystals. *Science* **2004,** *306*, 1009-1012.

(60) Xiong, Y. J.; Mayers, B. T.; Xia, Y. Some Recent Developments in the Chemical Synthesis of Inorganic Nanotubes. *Chem. Commun.* **2005**, 5013-5022.

(61) Wang, M. C. P.; Gates, B. D. Surface-Initiated Atom Transfer Radical Polymerization-Induced Transformation of Selenium Nanowires into Copper Selenide@Polystyrene Core-Shell Nanowires. *ACS Appl. Mater. Interfaces* **2013,** *5*, 9546-9553.

(62) Jeong, U.; Kim, J. U.; Xia, Y. Monodispersed Spherical Colloids of Se@Cdse: Synthesis and Use as Building Blocks in Fabricating Photonic Crystals. *Nano Lett.* **2005,** *5*, 937-942.

(63) Smyder, J. A.; Krauss, T. D. Coming Attractions for Semiconductor Quantum Dots. *Materials Today* **2011,** *14*, 382-387.

(64) Schoen, D. T.; Xie, C.; Cui, Y. Electrical Switching and Phase Transformation in Silver Selenide Nanowires. *Journal of the American Chemical Society* **2007,** *129*, 4116-4117.

(65) Zhao, Y. X.; Burda, C. Development of Plasmonic Semiconductor Nanomaterials with Copper Chalcogenides for a Future with Sustainable Energy Materials. *Energy & Environmental Science* **2012,** *5*, 5564-5576.

(66) Panthani, M. G.; Akhavan, V.; Goodfellow, B.; Schmidtke, J. P.; Dunn, L.; Dodabalapur, A.; Barbara, P. F.; Korgel, B. A. Synthesis of Cuins(2), Cuinse(2), and Cu(in(X)Ga(1-X))Se(2) (Cigs) Nanocrystal "Inks" for Printable Photovoltaics. *J. Am. Chem. Soc.* **2008,** *130*, 16770-16777.

(67) Bubon, O.; DeCrescenzo, G.; Rowlands, J. A.; Reznik, A. Amorphous Selenium (a-Se) Avalanche Photosensor with Metal Electrodes. *J. Non-Cryst. Solids* **2012,** *358*, 2431-2433.

(68) Bubon, O.; DeCrescenzo, G.; Zhao, W.; Ohkawa, Y.; Miyakawa, K.; Matsubara, T.; Kikuchi, K.; Tanioka, K.; Kubota, M.; Rowlands, J. A.; Reznik, A. Electroded Avalanche Amorphous Selenium (a-Se) Photosensor. *Curr. Appl. Phys.* **2012,** *12*, 983-988.

(69) Frey, J. B.; Belev, G.; Tousignant, O.; Mani, H.; Laperriere, L.; Kasap, S. O. Dark Current in Multilayer Stabilized Amorphous Selenium Based Photoconductive X-Ray Detectors. *J. Appl. Phys.* **2012,** *112*.

(70) Liao, Z. M.; Hou, C.; Zhao, Q.; Liu, L. P.; Yu, D. P. Gate Tunable Photoconductivity of P-Channel Se Nanowire Field Effect Transistors. *Appl. Phys. Lett.* **2009,** *95*, 093104-1-093104-3.

(71) Mayers, B.; Jiang, X. C.; Sunderland, D.; Cattle, B.; Xia, Y. Hollow Nanostructures of Platinum with Controllable Dimensions Can Be Synthesized by Templating against Selenium Nanowires and Colloids. *J. Am. Chem. Soc.* **2003,** *125*, 13364-13365.

(72) Carvalho, C. M. L.; Lu, J.; Zhang, X.; Arner, E. S. J.; Holmgren, A. Effects of Selenite and Chelating Agents on Mammalian Thioredoxin Reductase Inhibited by Mercury: Implications for Treatment of Mercury Poisoning. *FASEB J.* **2011,** *25*, 370-381.

(73) Jiang, L.; Yang, K. H.; Tian, J. H.; Guan, Q. L.; Yao, N.; Cao, N.; Mi, D. H.; Wu, J.; Ma, B.; Yang, S. H. Efficacy of Antioxidant Vitamins and Selenium Supplement in Prostate Cancer Prevention: A Meta-Analysis of Randomized Controlled Trials. *Nutr. Cancer* **2010,** *62*, 719-727.

(74) Tran, P. L.; Lowry, N.; Campbell, T.; Reid, T. W.; Webster, D. R.; Tobin, E.; Aslani, A.; Mosley, T.; Dertien, J.; Colmer-Hamood, J. A.; Hamood, A. N. An Organoselenium Compound Inhibits Staphylococcus Aureus Biofilms on Hemodialysis Catheters in Vivo. *Antimicrob. Agents Chemother.* **2012,** *56*, 972-978.

(75) Bai, Y.; Rong, F. X.; Wang, H.; Zhou, Y. H.; Xie, X. Y.; Teng, J. W. Removal of Copper from Aqueous Solutions by Adsorption on Elemental Selenium Nanoparticles. *J. Chem. Eng. Data* **2011,** *56*, 2563-2568.

(76) Lee, B.; Sarin, L.; Johnson, N. C.; Hurt, R. H. A Nano-Selenium Reactive Barrier Approach for Managing Mercury over the Life-Cycle of Compact Fluorescent Lamps. *Environ. Sci. Technol.* **2009,** *43*, 5915-5920.

(77) Grossiord, N.; Loos, J.; Regev, O.; Koning, C. E. Toolbox for Dispersing Carbon Nanotubes into Polymers to Get Conductive Nanocomposites. *Chem. Mater.* **2006,** *18*, 1089-1099.

(78) Penicaud, A.; Drummond, C. Deconstructing Graphite: Graphenide Solutions. *Acc. Chem. Res.* **2013,** *46*, 129-137.

(79) Quintana, M.; Vazquez, E.; Prato, M. Organic Functionalization of Graphene in Dispersions. *Acc. Chem. Res.* **2013,** *46*, 138-148.

(80) Maximova, N.; Dahl, O. Environmental Implications of Aggregation Phenomena: Current Understanding. *Curr. Opin. Colloid Interface Sci.* **2006,** *11*, 246-266.

(81) Karousis, N.; Tagmatarchis, N.; Tasis, D. Current Progress on the Chemical Modification of Carbon Nanotubes. *Chem. Rev.* **2010,** *110*, 5366-5397.

(82) Lu, K. L.; Lago, R. M.; Chen, Y. K.; Green, M. L. H.; Harris, P. J. F.; Tsang, S. C. Mechanical Damage of Carbon Nanotubes by Ultrasound. *Carbon* **1996,** *34*, 814-816.

(83) Sawawi, M.; Wang, T. Y.; Nisbet, D. R.; Simon, G. P. Scission of Electrospun Polymer Fibres by Ultrasonication. *Polymer* **2013,** *54*, 4237-4252.

(84) Huang, Y. Y.; Knowles, T. P. J.; Terentjev, E. M. Strength of Nanotubes, Filaments, and Nanowires from Sonication-Induced Scission. *Adv. Mater.* **2009,** *21*, 3945-3948.

(85) Wang, H. Dispersing Carbon Nanotubes Using Surfactants. *Curr. Opin. Colloid Interface Sci.* **2009,** *14*, 364-371.

(86) Jiang, X. C.; Mayers, B.; Wang, Y. L.; Cattle, B.; Xia, Y. Template-Engaged Synthesis of Ruse2 and Pd17se15 Nanotubes by Reacting Precursor Salts with Selenium Nanowires. *Chem. Phys. Lett.* **2004,** *385*, 472-476.

(87) Wang, M. C. P.; Gates, B. D. Stabilizing Dispersions of Large Quantities of Selenium Nanowires. *MRS Symposium Proceeding* **2009,** *1144*, LL18-25.

(88) Wang, M. C. P.; Zhang, X.; Majidi, E.; Nedelec, K.; Gates, B. D. Electrokinetic Assembly of Selenium and Silver Nanowires into Macroscopic Fibers. *ACS Nano* **2010,** *4*, 2607-2614.

(89) Holyst, R.; Bielejewska, A.; Szymanski, J.; Wilk, A.; Patkowski, A.; Gapinski, J.; Zywocinski, A.; Kalwarczyk, T.; Kalwarczyk, E.; Tabaka, M.; Ziebacz, N.; Wieczorek, S. A. Scaling Form of Viscosity at All Length-Scales in Poly(Ethylene Glycol) Solutions Studied by Fluorescence Correlation Spectroscopy and Capillary Electrophoresis. *Phys. Chem. Chem. Phys.* **2009,** *11*, 9025-9032.

(90) Pavlov, G. M.; Panarin, E. F.; Koreneeva, E. V.; Kurochkin, C. V.; Baikov, V. E.; Ushakova, V. N. Hydrodynamic Properites of Poly(1-Vinyl-2-Pyrrolidone) Molecules in Dilute Solution. *Makromol. Chem.* **1990,** *191*, 2889-2899.

(91) Gates, B.; Mayers, B.; Wu, Y. Y.; Sun, Y. G.; Cattle, B.; Yang, P.; Xia, Y. Synthesis and Characterization of Crystalline Ag2se Nanowires through a Template-Engaged Reaction at Room Temperature. *Adv. Funct. Mater.* **2002,** *12*, 679-686.

(92) Lu, X. M.; Rycenga, M.; Skrabalak, S. E.; Wiley, B.; Xia, Y. Chemical Synthesis of Novel Plasmonic Nanoparticles. *Annu. Rev. Phys. Chem.* **2009,** *60*, 167-192.

(93) Hu, J. Q.; Bando, Y.; Golberg, D. Novel Semiconducting Nanowire Heterostructures: Synthesis, Properties and Applications. *J. Mater. Chem.* **2009,** *19*, 330-343.

(94) Kuno, M. An Overview of Solution-Based Semiconductor Nanowires: Synthesis and Optical Studies. *Phys. Chem. Chem. Phys.* **2008,** *10*, 620-639.

(95) Zhang, W. X.; Yang, S. H. In Situ Fabrication of Inorganic Nanowire Arrays Grown from and Aligned on Metal Substrates. *Acc. Chem. Res.* **2009,** *42*, 1617-1627.

(96) Andrews, R.; Jacques, D.; Qian, D. L.; Rantell, T. Multiwall Carbon Nanotubes: Synthesis and Application. *Acc. Chem. Res.* **2002,** *35*, 1008-1017.

(97) Dai, H. J. Carbon Nanotubes: Synthesis, Integration, and Properties. *Acc. Chem. Res.* **2002,** *35*, 1035-1044.

(98) Xia, Y. N.; Yang, P. D.; Sun, Y. G.; Wu, Y. Y.; Mayers, B.; Gates, B.; Yin, Y. D.; Kim, F.; Yan, Y. Q. One-Dimensional Nanostructures: Synthesis, Characterization, and Applications. *Adv. Mater.* **2003,** *15*, 353-389.

(99) Hermanson, K. D.; Lumsdon, S. O.; Williams, J. P.; Kaler, E. W.; Velev, O. D. Dielectrophoretic Assembly of Electrically Functional Microwires from Nanoparticle Suspensions. *Science* **2001,** *294*, 1082-1086.

(100) Koh, S. J. Strategies for Controlled Placement of Nanoscale Building Blocks. *Nanoscale Res. Lett.* **2007,** *2*, 519-545.

(101) Hong, S.; Kim, T. H.; Lee, J.; Byun, K. E.; Koh, J.; Kim, T.; Myung, S. "Surface-Programmed Assembly" of Nanotube/Nanowire-Based Integrated Devices. *Nano* **2007,** *2*, 333-350.

(102) Heo, K.; Kim, C. J.; Jo, M. H.; Hong, S. Massive Integration of Inorganic Nanowire-Based Structures on Solid Substrates for Device Applications. *J. Mater. Chem.* **2009,** *19*, 901-908.

(103) Tao, A. R.; Huang, J. X.; Yang, P. D. Langmuir-Blodgettry of Nanocrystals and Nanowires. *Acc. Chem. Res.* **2008,** *41*, 1662-1673.

(104) Acharya, S.; Hill, J. P.; Ariga, K. Soft Langmuir-Blodgett Technique for Hard Nanomaterials. *Adv. Mater.* **2009,** *21*, 2959-2981.

(105) Mastrangeli, M.; Abbasi, S.; Varel, C.; Van Hoof, C.; Celis, J. P.; Bohringer, K. F. Self-Assembly from Milli-to Nanoscales: Methods and Applications. *J. Micromech. Microeng.* **2009,** *19*, 083001.

(106) Fan, Z. Y.; Ho, J. C.; Takahashi, T.; Yerushalmi, R.; Takei, K.; Ford, A. C.; Chueh, Y. L.; Javey, A. Toward the Development of Printable Nanowire Electronics and Sensors. *Adv. Mater.* **2009,** *21*, 3730-3743.

(107) Lu, W.; Lieber, C. M. Semiconductor Nanowires. *J. Phys. D: Appl. Phys.* **2006,** *39*, R387-R406.

(108) Zhang, Y. G.; Chang, A. L.; Cao, J.; Wang, Q.; Kim, W.; Li, Y. M.; Morris, N.; Yenilmez, E.; Kong, J.; Dai, H. J. Electric-Field-Directed Growth of Aligned Single-Walled Carbon Nanotubes. *Appl. Phys. Lett.* **2001,** *79*, 3155-3157.

(109) Kamat, P. V.; Thomas, K. G.; Barazzouk, S.; Girishkumar, G.; Vinodgopal, K.; Meisel, D. Self-Assembled Linear Bundles of Single Wall Carbon Nanotubes and Their Alignment and Deposition as a Film in a Dc Field. *J. Am. Chem. Soc.* **2004,** *126*, 10757-10762.

(110) Yu, G. H.; Cao, A. Y.; Lieber, C. M. Large-Area Blown Bubble Films of Aligned Nanowires and Carbon Nanotubes. *Nat. Nanotech.* **2007,** *2*, 372-377.

(111) An, L. B.; Cheam, D. D.; Friedrich, C. R. Controlled Dielectrophoretic Assembly of Multiwalled Carbon Nanotubes. *J. Phys. Chem. C* **2009,** *113*, 37-39.

(112) Annamalai, R.; West, J. D.; Luscher, A.; Subramaniam, V. V. Electrophoretic Drawing of Continuous Fibers of Single-Walled Carbon Nanotubes. *J. Appl. Phys.* **2005,** *98*.

(113) Huang, Y. Y.; Knowles, T. P. J.; Terentjev, E. M. Strength of Nanotubes, Filaments, and Nanowires from Sonication-Induced Scission. *Adv. Mater.* **2009,** *21*, 3945-3948.

(114) Chen, M.; Guo, L.; Ravi, R.; Searson, P. C. Kinetics of Receptor Directed Assembly of Multisegment Nanowires. *J. Phys. Chem. B* **2006,** *110*, 211-217.

(115) Kovtyukhova, N. I.; Mallouk, T. E. Nanowires as Building Blocks for Self-Assembling Logic and Memory Circuits. *Chemistry-a European Journal* **2002,** *8*, 4355-4363.

(116) Lee, J.; Wang, A. A.; Rheem, Y.; Yoo, B.; Mulchandani, A.; Chen, W.; Myung, N. V. DNA Assisted Assembly of Multisegmented Nanowires. *Electroanalysis* **2007,** *19*, 2287-2293.

(117) Mbindyo, J. K. N.; Reiss, B. D.; Martin, B. R.; Keating, C. D.; Natan, M. J.; Mallouk, T. E. DNA-Directed Assembly of Gold Nanowires on Complementary Surfaces. *Adv. Mater.* **2001,** *13*, 249-254.

(118) Ou, F. S.; Shaijumon, M. M.; Ajayan, P. M. Controlled Manipulation of Giant Hybrid Inorganic Nanowire Assemblies. *Nano Lett.* **2008,** *8*, 1853-1857.

(119) Heo, K.; Cho, E.; Yang, J.-E.; Kim, M.-H.; Lee, M.; Lee, B. Y.; Kwon, S. G.; Lee, M.-S.; Jo, M.-H.; Choi, H.-J.; Hyeon, T.; Hong, S. Large-Scale Assembly of Silicon Nanowire Network-Based Devices Using Conventional Microfabrication Facilities. *Nano Lett.* **2008,** *8*, 4523-4527.

(120) Kang, J.; Myung, S.; Kim, B.; Oh, D.; Kim, G. T.; Hong, S. Massive Assembly of Zno Nanowire-Based Integrated Devices. *Nanotechnology* **2008,** *19*.

(121) Kim, Y.-K.; Park, S. J.; Koo, J. P.; Kim, G. T.; Hong, S.; Ha, J. S. Control of Adsorption and Alignment of V2o5 Nanowires Via Chemically Functionalized Patterns. *Nanotechnology* **2007,** *18*.

(122) Myung, S.; Heo, K.; Lee, M.; Choi, Y. H.; Hong, S. H.; Hong, S. 'Focused' Assembly of V2o5 Nanowire Masks for the Fabrication of Metallic Nanowire Sensors. *Nanotechnology* **2007,** *18*.

(123) Myung, S.; Im, J.; Huang, L.; Rao, S. G.; Kim, T.; Lee, D. J.; Hong, S. H. "Lens" Effect in Directed Assembly of Nanowires on Gradient Molecular Patterns. *J. Phys. Chem. B* **2006,** *110*, 10217-10219.

(124) Myung, S.; Lee, M.; Kim, G. T.; Ha, J. S.; Hong, S. Large-Scale "Surface-Programmed Assembly" of Pristine Vanadium Oxide Nanowire-Based Devices. *Adv. Mater.* **2005,** *17*, 2361-2364.

(125) Acharya, S.; Panda, A. B.; Belman, N.; Efrima, S.; Golan, Y. A Semiconductor-Nanowire Assembly of Ultrahigh Junction Density by the Langmuir-Blodgett Technique. *Adv. Mater.* **2006,** *18*, 210-213.

(126) Deegan, R. D.; Bakajin, O.; Dupont, T. F.; Huber, G.; Nagel, S. R.; Witten, T. A. Contact Line Deposits in an Evaporating Drop. *Physical Review E* **2000,** *62*, 756-765.

(127) Duan, X. F.; Niu, C. M.; Sahi, V.; Chen, J.; Parce, J. W.; Empedocles, S.; Goldman, J. L. High-Performance Thin-Film Transistors Using Semiconductor Nanowires and Nanoribbons. *Nature* **2003,** *425*, 274-278.

(128) Fan, Z.; Ho, J. C.; Jacobson, Z. A.; Yerushalmi, R.; Alley, R. L.; Razavi, H.; Javey, A. Wafer-Scale Assembly of Highly Ordered Semiconductor Nanowire Arrays by Contact Printing. *Nano Lett.* **2008,** *8*, 20-25.

(129) Huang, J.; Fan, R.; Connor, S.; Yang, P. One-Step Patterning of Aligned Nanowire Arrays by Programmed Dip Coating. *Angew. Chem. Int. Ed.* **2007,** *46*, 2414-2417.

(130) Huang, Y.; Duan, X. F.; Wei, Q. Q.; Lieber, C. M. Directed Assembly of One-Dimensional Nanostructures into Functional Networks. *Science* **2001,** *291*, 630-633.

(131) Javey, A.; Nam, S.; Friedman, R. S.; Yan, H.; Lieber, C. M. Layer-by-Layer Assembly of Nanowires for Three-Dimensional, Multifunctional Electronics. *Nano Lett.* **2007,** *7*, 773-777.

(132) Jin, S.; Whang, D. M.; McAlpine, M. C.; Friedman, R. S.; Wu, Y.; Lieber, C. M. Scalable Interconnection and Integration of Nanowire Devices without Registration. *Nano Lett.* **2004,** *4*, 915-919.

(133) McAlpine, M. C.; Friedman, R. S.; Jin, S.; Lin, K. H.; Wang, W. U.; Lieber, C. M. High-Performance Nanowire Electronics and Photonics on Glass and Plastic Substrates. *Nano Lett.* **2003,** *3*, 1531-1535.

(134) McAlpine, M. C.; Friedman, R. S.; Lieber, D. M. Nanoimprint Lithography for Hybrid Plastic Electronics. *Nano Lett.* **2003,** *3*, 443-445.

(135) Park, J.; Shin, G.; Ha, J. S. Controlling Orientation of V(2)O(5) Nanowires within Micropatterns Via Icrocontact Printing Combined with the Gluing Langmuir-Blodgett Technique. *Nanotechnology* **2008,** *19*.

(136) Tao, A.; Kim, F.; Hess, C.; Goldberger, J.; He, R. R.; Sun, Y. G.; Xia, Y.; Yang, P. D. Langmuir-Blodgett Silver Nanowire Monolayers for Molecular Sensing Using Surface-Enhanced Raman Spectroscopy. *Nano Lett.* **2003,** *3*, 1229-1233.

(137) Wang, D. W.; Tu, R.; Zhang, L.; Dai, H. J. Deterministic One-to-One Synthesis of Germanium Nanowires and Individual Gold Nanoseed Patterning for Aligned Arrays. *Angew. Chem. Int. Ed.* **2005,** *44*, 2925-2929.

(138) Whang, D.; Jin, S.; Wu, Y.; Lieber, C. M. Large-Scale Hierarchical Organization of Nanowire Arrays for Integrated Nanosystems. *Nano Lett.* **2003,** *3*, 1255-1259.

(139) Yerushalmi, R.; Jacobson, Z. A.; Ho, J. C.; Fan, Z.; Javey, A. Large Scale, Highly Ordered Assembly of Nanowire Parallel Arrays by Differential Roll Printing. *Appl. Phys. Lett.* **2007,** *91*.

(140) Yu, G.; Li, X.; Lieber, C. M.; Cao, A. Nanomaterial-Incorporated Blown Bubble Films for Large-Area, Aligned Nanostructures. *J. Mater. Chem.* **2008,** *18*, 728-734.

(141) Hangarter, C. M.; Myung, N. V. Magnetic Alignment of Nanowires. *Chem. Mater.* **2005,** *17*, 1320-1324.

(142) Hangarter, C. M.; Rheem, Y.; Yoo, B.; Yang, E.-H.; Myung, N. V. Hierarchical Magnetic Assembly of Nanowires. *Nanotechnology* **2007,** *18*.

(143) Liu, M.; Lagdani, J.; Imrane, H.; Pettiford, C.; Lou, J.; Yoon, S.; Harris, V. G.; Vittoria, C.; Sun, N. X. Self-Assembled Magnetic Nanowire Arrays. *Appl. Phys. Lett.* **2007,** *90*.

(144) Ooi, C.; Yellen, B. B. Field Gradients Can Control the Alignment of Nanorods. *Langmuir* **2008,** *24*, 8514-8521.

(145) Rheem, Y.; Hangarter, C. M.; Yang, E.-H.; Park, D.-Y.; Myung, N. V.; Yoo, B. Site-Specific Magnetic Assembly of Nanowires for Sensor Arrays Fabrication. *IEEE Trans. Nanotechnol.* **2008,** *7*, 251-255.

(146) Yoo, B. Y.; Rheem, Y. W.; Beyermann, W. P.; Myung, N. V. Magnetically Assembled 30 Nm Diameter Nickel Nanowire with Ferromagnetic Electrodes. *Nanotechnology* **2006,** *17*, 2512-2517.

(147) Boote, J. J.; Critchley, K.; Evans, S. D. Surfactant Mediated Assembly of Gold Nanowires on Surfaces. *J. Exp. Nanosci.* **2006,** *1*, 125-142.

(148) Duan, X. F.; Huang, Y.; Cui, Y.; Wang, J. F.; Lieber, C. M. Indium Phosphide Nanowires as Building Blocks for Nanoscale Electronic and Optoelectronic Devices. *Nature* **2001,** *409*, 66-69.

(149) Evoy, S.; DiLello, N.; Deshpande, V.; Narayanan, A.; Liu, H.; Riegelman, M.; Martin, B. R.; Hailer, B.; Bradley, J. C.; Weiss, W.; Mayer, T. S.; Gogotsi, Y.; Bau, H. H.; Mallouk, T. E.; Raman, S. Dielectrophoretic Assembly and Integration of Nanowire Devices with Functional Cmos Operating Circuitry. *Microelectron. Eng.* **2004,** *75*, 31-42.

(150) Lee, J. W.; Moon, K. J.; Ham, M. H.; Myoung, J. M. Dielectrophoretic Assembly of Gan Nanowires for Uv Sensor Applications. *Solid State Commun.* **2008,** *148*, 194-198.

(151) Li, M.; Bhiladvala, R. B.; Morrow, T. J.; Sioss, J. A.; Lew, K.-K.; Redwing, J. M.; Keating, C. D.; Mayer, T. S. Bottom-up Assembly of Large-Area Nanowire Resonator Arrays. *Nat. Nanotech.* **2008,** *3*, 88-92.

(152) Liu, Y.; Chung, J.-H.; Liu, W. K.; Ruoff, R. S. Dielectrophoretic Assembly of Nanowires. *J. Phys. Chem. B* **2006,** *110*, 14098-14106.

(153) Marcus, M. S.; Shang, L.; Li, B.; Streifer, J. A.; Beck, J. D.; Perkins, E.; Eriksson, M. A.; Hamers, R. J. Dielectrophoretic Manipulation and Real-Time Electrical Detection of Single-Nanowire Bridges in Aqueous Saline Solutions. *Small* **2007,** *3*, 1610-1617.

(154) Small, W. R.; Paunov, V. N. Fabrication of Electrically Anisotropic Agarose Gels by Dielectrophoretic Assembly and Encapsulation of Silver Nanowires. *J. Mater. Chem.* **2008,** *18*, 2082-2084.

(155) Smith, P. A.; Nordquist, C. D.; Jackson, T. N.; Mayer, T. S.; Martin, B. R.; Mbindyo, J.; Mallouk, T. E. Electric-Field Assisted Assembly and Alignment of Metallic Nanowires. *Appl. Phys. Lett.* **2000,** *77*, 1399-1401.

(156) Zhou, R.; Chang, H.-C.; Protasenko, V.; Kuno, M.; Singh, A. K.; Jena, D.; Xing, H. Cdse Nanowires with Illumination-Enhanced Conductivity: Induced Dipoles, Dielectrophoretic Assembly, and Field-Sensitive Emission. *J. Appl. Phys.* **2007,** *101*.

(157) Wang, D. Q.; Zhu, R.; Zhou, Z. Y.; Ye, X. Y. Controlled Assembly of Zinc Oxide Nanowires Using Dielectrophoresis. *Appl. Phys. Lett.* **2007,** *90*.

(158) Motayed, A.; He, M. Q.; Davydov, A. V.; Melngailis, J.; Mohammad, S. N. Realization of Reliable Gan Nanowire Transistors Utilizing Dielectrophoretic Alignment Technique. *J. Appl. Phys.* **2006,** *100*.

(159) Wang, D. W.; Chang, Y. L.; Liu, Z.; Dai, H. J. Oxidation Resistant Germanium Nanowires: Bulk Synthesis, Long Chain Alkanethiol Functionalization, and Langmuir-Blodgett Assembly. *J. Am. Chem. Soc.* **2005,** *127*, 11871-11875.

(160) Vijayaraghavan, A.; Blatt, S.; Weissenberger, D.; Oron-Carl, M.; Hennrich, F.; Gerthsen, D.; Hahn, H.; Krupke, R. Ultra-Large-Scale Directed Assembly of Single-Walled Carbon Nanotube Devices. *Nano Lett.* **2007,** *7*, 1556-1560.

(161) Zhou, R. H.; Chang, H. C.; Protasenko, V.; Kuno, M.; Singh, A. K.; Jena, D.; Xing, H. Cdse Nanowires with Illumination-Enhanced Conductivity: Induced Dipoles, Dielectrophoretic Assembly, and Field-Sensitive Emission. *J. Appl. Phys.* **2007,** *101*, 073704.

(162) Kim, T. H.; Lee, S. Y.; Kim, H. G.; Kim, S. H.; Hong, C. H.; Hahn, Y. B.; Lee, S. K. Characteristics of Dielectrophoretically Aligned Uv-Blue Gan Nanowire Leds. *Journal of Nanoscience and Nanotechnology* **2008,** *8*, 268-273.

(163) Boote, J. J.; Evans, S. D. Dielectrophoretic Manipulation and Electrical Characterization of Gold Nanowires. *Nanotechnology* **2005,** *16*, 1500-1505.

(164) Besra, L.; Liu, M. A Review on Fundamentals and Applications of Electrophoretic Deposition (Epd). *Prog. Mater. Sci.* **2007,** *52*, 1-61.

(165) Velev, O. D.; Bhatt, K. H. On-Chip Micromanipulation and Assembly of Colloidal Particles by Electric Fields. *Soft Matter* **2006,** *2*, 738-750.

(166) Shklyarevskii, I. N.; Pakhmov, P. L. Separation of the Contribution of Free and Bound Electrons into Real and Imaginary Parts of the Dielectric Constant of Gold. *Opt Spektrosk.* **1973,** *34*, 163-166.

(167) Pohl, H. A. The Motion and Precipitation of Suspensions in Divergent Electric Fields. *J. Appl. Phys.* **1951,** *22*, 869-871.

(168) Pohl, H. A. Some Effects of Nonuniform Fields on Dielectrics. *J. Appl. Phys.* **1958,** *29*, 1182-1188.

(169) Wiles, J. A.; Grzybowski, B. A.; Winkleman, A.; Whitesides, G. M. A Tool for Studying Contact Electrification in Systems Comprising Metals and Insulating Polymers. *Anal. Chem.* **2003,** *75*, 4859-4867.

(170) Sakata, S.; Okada, T. Effect of Humidity on Hydrated Cluster-Ion Formation in a Clean Room Corona Discharge Neutrailzer. *J. Aerosol Sci* **1994,** *25*, 879-&.

(171) Skoog, D. A.; Holler, F. J.; Nieman, T. A., High-Performance Liquid Chromatography. In *Principles of Instrumental Analysis*, 5th ed.; Harcourt Brace & Company: Florida, 1998; p 743.

(172) Wohlfarth, C., Permittivity (Dielectric Constant) of Liquids. In *Crc Handbook of Chemistry and Physics*, 90th ed.; Lide, D. R.; Haynes, W. M., Eds. Taylor and Francis: New York, 2009; pp 148-169.

(173) Petchsang, N.; McDonald, M. P.; Sinks, L. E.; Kuno, M. Light Induced Nanowire Assembly: The Electrostatic Alignment of Semiconductor Nanowires into Functional Macroscopic Yarns. *Adv. Mater.* **2013,** *25*, 601-605.

(174) Schafer, S.; Wang, Z.; Zierold, R.; Kipp, T.; Mews, A. Laser-Induced Charge Separation in Cdse Nanowires. *Nano Lett.* **2011,** *11*, 2672-2677.

(175) Dayeh, S. A. Electron Transport in Indium Arsenide Nanowires. *Semicond. Sci. Technol. 25*, 024004.

(176) Talin, A. A.; Leonard, F.; Katzenmeyer, A. M.; Swartzentruber, B. S.; Picraux, S. T.; Toimil-Molares, M. E.; Cederberg, J. G.; Wang, X.; Hersee, S. D.; Rishinaramangalum, A. Transport Characterization in Nanowires Using an Electrical Nanoprobe. *Semicond. Sci. Technol. 25*, 024015.

(177) Kasap, S. O.; Capper, P., *Springer Handbook of Electronic and Photonic Materials*; Springer: New York, 2006.

(178) Guo, H. Z.; Lin, N.; Chen, Y. Z.; Wang, Z. W.; Xie, Q. S.; Zheng, T. C.; Gao, N.; Li, S. P.; Kang, J. Y.; Cai, D. J.; Peng, D. L. Copper Nanowires as Fully Transparent Conductive Electrodes. *Sci Rep* **2013,** *3*.

(179) Freer, E. M.; Grachev, O.; Duan, X.; Martin, S.; Stumbo, D. P. High-Yield Self-Limiting Single-Nanowire Assembly with Dielectrophoresis. *Nat. Nanotech.* **2010,** *5*, 525-530.

(180) Pradel, K. C.; Sohn, K.; Huang, J. Cross-Flow Purification of Nanowires. *Angew. Chem. Int. Ed.* **2011,** *50*, 3412-3416.

(181) Sweeney, S. F.; Woehrle, G. H.; Hutchison, J. E. Rapid Purification and Size Separation of Gold Nanoparticles Via Diafiltration. *J. Am. Chem. Soc.* **2006,** *128*, 3190-3197.

(182) Antaris, A. L.; Seo, J. W. T.; Brock, R. E.; Herriman, J. E.; Born, M. J.; Green, A. A.; Hersam, M. C. Probing and Tailoring Ph-Dependent Interactions between Block Copolymers and Single-Walled Carbon Nanotubes for Density Gradient Sorting. *J. Phys. Chem. C* **2012,** *116*, 20103-20108.

(183) Hanauer, M.; Pierrat, S.; Zins, I.; Lotz, A.; Sonnichsen, C. Separation of Nanoparticles by Gel Electrophoresis According to Size-and Shape. *Nano Lett.* **2007,** *7*, 2881-2885.

(184) Wang, K.; Chen, F.; Allec, N.; Karim, K. S. Fast Lateral Amorphous-Selenium Metal-Semiconductor-Metal Photodetector with High Blue-to-Ultraviolet Responsivity. *IEEE Trans. Electron Devices* **2010,** *57*, 1953-1958.

(185) Reardon, E. J. Zerolvalent Irons: Styles of Corrosion and Inorganic Control on Hydrogen Pressure Buildup. *Environ. Sci. Technol.* **2005,** *39*, 7311-7317.

(186) Malyshev, V. N. Corrosion Cracking of High-Strength Structural Steels at Large Depths in the Black Sea. *Prot. Met* **2000,** *36*, 199-201.

(187) *Handbook of Corrosion Data*; 2nd ed.; ASM International: 1997; Vol. 151, p 55-55.

(188) Kriegel, I.; Jiang, C. Y.; Rodriguez-Fernandez, J.; Schaller, R. D.; Talapin, D. V.; da Como, E.; Feldmann, J. Tuning the Excitonic and Plasmonic Properties of Copper Chalcogenide Nanocrystals. *J. Am. Chem. Soc.* **2012,** *134*, 1583-1590.

(189) Kong, D. S.; Cha, J. J.; Lai, K. J.; Peng, H. L.; Analytis, J. G.; Meister, S.; Chen, Y. L.; Zhang, H. J.; Fisher, I. R.; Shen, Z. X.; Cui, Y. Rapid Surface Oxidation as a Source of Surface Degradation Factor for Bi2se3. *ACS Nano* **2011,** *5*, 4698-4703.

(190) Janotta, M.; Rudolph, D.; Kueng, A.; Kranz, C.; Voraberger, H.-S.; Waldhauser, W.; Mizaikoff, B. Analysis of Corrosion Processes at the Surface of Diamond-Like Carbon Protected Zinc Selenide Waveguides. *Langmuir* **2004,** *20*, 8634-8640.

(191) Niu, Y.-F.; Guin, J.-P.; Rouxel, T.; Abdelouas, A.; Troles, J.; Smektala, F. Aqueous Corrosion of the Gese4 Chalcogenide Glass: Surface Properties and Corrosion Mechanism. *J. Am. Ceram. Soc.* **2009,** *92*, 1779-1787.

(192) Zumdahl, S. S., *Chemical Principles*; 3rd ed.; Houghton Mifflin Company: Boston, 1998.

(193) Khalilov, U.; Pourtois, G.; van Duin, A. C. T.; Neyts, E. C. Self-Limiting Oxidation in Small-Diameter Si Nanowires. *Chem. Mater.* **2012,** *24*, 2141-2147.

(194) Sun, S. H.; Zeng, H. Size-Controlled Synthesis of Magnetite Nanoparticles. *J. Am. Chem. Soc.* **2002,** *124*, 8204-8205.

(195) Nirmal, M.; Brus, L. Luminescence Photophysics in Semiconductor Nanocrystals. *Acc. Chem. Res.* **1999,** *32*, 407-414.

(196) Baran, M.; Khomenkova, L.; Korsunska, N.; Stara, T.; Sheinkman, M.; Goldstein, Y.; Jedrzejewski, J.; Savir, E. Investigation of Aging Process of Si-Siox Structures with Silicon Quantum Dots. *J. Appl. Phys.* **2005,** *98*.

(197) Li, H. S.; Lusk, M. T.; Collins, R. T.; Wu, Z. G. Optimal Size Regime for Oxidation-Resistant Silicon Quantum Dots. *ACS Nano* **2012,** *6*, 9690-9699.

(198) Ray, M.; Basu, T. S.; Jana, A.; Bandyopadhyay, N. R.; Hossain, S. M.; Pramanick, A. K.; Klie, R. F. Luminescent Core-Shell Nanostructures of Silicon and Silicon Oxide: Nanodots and Nanorods. *J. Appl. Phys.* **2010,** *107*.

(199) Pi, X. D.; Mangolini, L.; Campbell, S. A.; Kortshagen, U. Room-Temperature Atmospheric Oxidation of Si Nanocrystals after Hf Etching. *Phys. Rev. B* **2007,** *75*.

(200) Buttner, C. C.; Zacharias, M. Retarded Oxidation of Si Nanowires. *Appl. Phys. Lett.* **2006,** *89*.

(201) Ma, D. D. D.; Lee, C. S.; Au, F. C. K.; Tong, S. Y.; Lee, S. T. Small-Diameter Silicon Nanowire Surfaces. *Science* **2003,** *299*, 1874-1877.

(202) Barchi, L.; Bardi, U.; Caporali, S.; Fantini, M.; Scrivani, A. Electroplated Bright Alminium Coatings for Anticorrosion and Decorative Purposes. *Prog. Org. Coat.* **2010,** *67*, 146-151.

(203) Lebrini, M.; Fontaine, G.; Gengembre, L.; Traisnel, M.; Lerasle, O.; Genet, N. Corrosion Protection of Galvanized Steel and Electroplating Steel by Decanoic Acid in Aqueous Solution: Electrochemical Impedance Spectroscopy, Xps and Atr-Ftir. *Corros. Sci.* **2009,** *51*, 1201-1206.

(204) Ciampi, S.; Harper, J. B.; Gooding, J. J. Wet Chemical Routes to the Assembly of Organic Monolayers on Silicon Surfaces Via the Formation of Si-C Bonds: Surface Preparation, Passivation and Functionalization. *Chem. Soc. Rev.* **2010,** *39*, 2158-2183.

(205) Collins, G.; Holmes, J. D. Chemical Functionalisation of Silicon and Germanium Nanowires. *J. Mater. Chem.* **2011,** *21*, 11052-11069.

(206) Xia, Y.; Whitesides, G. M. Soft Lithography. *Annu. Rev. Mater. Sci.* **1998,** *28*, 153-184.

(207) Bajat, J. B.; Kacarevic-Popovic, Z.; Miskovic-Stankovic, V. B.; Maksimovic, M. D. Corrosion Behaviour of Epoxy Coatings Electrodeposited on Galvanized Steel and Steel Modified by Zn-Ni Alloys. *Prog. Org. Coat.* **2000,** *39*, 127-135.

(208) Barbey, R.; Lavanant, L.; Paripovic, D.; Schuwer, N.; Sugnaux, C.; Tugulu, S.; Klok, H. A. Polymer Brushes Via Surface-Initiated Controlled Radical Polymerization: Synthesis, Characterization, Properties, and Applications. *Chem. Rev.* **2009,** *109*, 5437-5527.

(209) Edmondson, S.; Osborne, V. L.; Huck, W. T. S. Polymer Brushes Via Surface-Initiated Polymerizations. *Chem. Soc. Rev.* **2004,** *33*, 14-22.

(210) Fristrup, C. J.; Jankova, K.; Hvilsted, S. Surface-Initiated Atom Transfer Radical Polymerization-a Technique to Develop Biofunctional Coatings. *Soft Matter* **2009,** *5*, 4623-4634.

(211) Cai, Q. J.; Fu, G. D.; Zhu, F. R.; Kang, E. T.; Neoh, K. G. Gaas-Polymer Hybrids Formed by Surface-Initiated Atom-Transfer Radical Polymerization of Methyl Methacrylate. *Angew. Chem. Int. Ed.* **2005,** *44*, 1104-1107.

(212) Kong, H.; Gao, C.; Yan, D. Y. Constructing Amphiphilic Polymer Brushes on the Convex Surfaces of Multi-Walled Carbon Nanotubes by in Situ Atom Transfer Radical Polymerization. *J. Mater. Chem.* **2004,** *14*, 1401-1405.

(213) Ohno, K.; Morinaga, T.; Koh, K.; Tsujii, Y.; Fukuda, T. Synthesis of Monodisperse Silica Particles Coated with Well-Defined, High-Density Polymer Brushes by Surface-Initiated Atom Transfer Radical Polymerization. *Macromolecules* **2005,** *38*, 2137-2142.

(214) Strozyk, M. S.; Chanana, M.; Pastoriza-Santos, I.; Perez-Juste, J.; Liz-Marzan, L. M. Protein/Polymer-Based Dual-Responsive Gold Nanoparticles with Ph-Dependent Thermal Sensitivity. *Adv. Funct. Mater.* **2012,** *22*, 1436-1444.

(215) Wang, L.; Wang, H. W.; Yuan, L.; Yang, W. K.; Wu, Z. Q.; Chen, H. Step-Wise Control of Protein Adsorption and Bacterial Attachment on a Nanowire Array Surface: Tuning Surface Wettability by Salt Concentration. *J. Mater. Chem.* **2011,** *21*, 13920-13925.

(216) Ishikawa, T.; Kobayashi, M.; Takahara, A. Macroscopic Frictional Properties of Poly(1-(2-Methacryloyloxy)Ethy1-3-Butyl Imidazolium Bis(Trifluoromethanesulfonyl)-Imide) Brush Surfaces in an Ionic Liquid. *ACS Appl. Mater. Interfaces* **2010,** *2*, 1120-1128.

(217) Sakata, H.; Kobayashi, M.; Otsuka, H.; Takahara, A. Tribological Properties of Poly(Methyl Methacrylate) Brushes Prepared by Surface-Initiated Atom Transfer Radical Polymerization. *Polym. J.* **2005,** *37*, 767-775.

(218) Kobayashi, M.; Terayama, Y.; Yamaguchi, H.; Terada, M.; Murakami, D.; Ishihara, K.; Takahara, A. Wettability and Antifouling Behavior on the Surfaces of Superhydrophilic Polymer Brushes. *Langmuir* **2012,** *28*, 7212-7222.

(219) Hutchings, L. R.; Narrianen, A. P.; Thompson, R. L.; Clarke, N.; Ansari, L. Modifying and Managing the Surface Properties of Polymers. *Polym. Int.* **2008,** *57*, 163-170.

(220) He, W. W.; Jiang, H. J.; Zhang, L. F.; Cheng, Z. P.; Zhu, X. L. Atom Transfer Radical Polymerization of Hydrophilic Monomers and Its Applications. *Polym. Chem.* **2013,** *4*, 2919-2938.

(221) Raynor, J. E.; Capadona, J. R.; Collard, D. M.; Petrie, T. A.; Garcia, A. J. Polymer Brushes and Self-Assembled Monolayers: Versatile Platforms to Control Cell Adhesion to Biomaterials. *Biointerphases* **2009,** *4*, FA3-FA16.

(222) Lu, G.; Li, Y. M.; Lu, C. H.; Xu, Z. Z. Corrosion Protection of Iron Surface Modified by Poly(Methyl Methacrylate) Using Surface-Initiated Atom Transfer Radical Polymerization (Si-Atrp). *Colloid. Polym. Sci.* **2010,** *288*, 1445-1455.

(223) Yuan, S. J.; Pehkonen, S. O.; Ting, Y. P.; Neoh, K. G.; Kang, E. T. Inorganic-Organic Hybrid Coatings on Stainless Steel by Layer-by-Layer Deposition and Surface-Initiated Atom-Transfer-Radical Polymerization for Combating Biocorrosion. *ACS Appl. Mater. Interfaces* **2009,** *1*, 640-652.

(224) Yuan, S. J.; Pehkonen, S. O.; Ting, Y. P.; Neoh, K. G.; Kang, E. T. Antibacterial Inorganic-Organic Hybrid Coatings on Stainless Steel Via Consecutive Surface-Initiated Atom Transfer Radical Polymerization for Biocorrosion Prevention. *Langmuir* **2010,** *26*, 6728-6736.

(225) Liang, H. W.; Liu, S.; Yu, S. H. Controlled Synthesis of One-Dimensional Inorganic Nanostructures Using Pre-Existing One-Dimensional Nanostructures as Templates. *Adv. Mater.* **2010,** *22*, 3925-3937.

(226) Wiberg, E.; Wiberg, N.; Holleman, A. F., *Inorganic Chemistry*; Academic Press: San Diego, 2001.

(227) Shenasa, M.; Sainkar, S.; Lichtman, D. Xps Study of Some Selected Selenium-Compounds. *J. Electron. Spectrosc. Relat. Phenom.* **1986,** *40*, 329-337.

(228) Allcock, H. R.; Lampe, F. W.; Mark, J. E., *Contemporary Polymer Chemistry*; Prentice Hall: Upper Saddle River, NJ, 2003.

(229) Tanuma, S.; Powell, C. J.; Penn, D. R. Calculations of Electron Inelastic Mean Free Paths .5. Data for 14 Organic-Compounds over the 50-2000 Ev Range. *Surf. Interface Anal.* **1994,** *21*, 165-176.

(230) Powell, C. J.; Jablonski, A., Nist Electron Inelastic-Mean-Free-Path Database, Version 1.2, Srd 71. National Institute of Standards and Technology, Gaithersburg, MD, 2010.

(231) Karim, S.; Toimil-Molares, M. E.; Balogh, A. G.; Ensinger, W.; Cornelius, T. W.; Khan, E. U.; Neumann, R. Morphological Evolution of Au Nanowires Controlled by Rayleigh Instability. *Nanotechnology* **2006,** *17*, 5954-5959.

(232) Kauffmann, H. F. Mechanism of the Photo-Polymerization of Styrene .1. Deactivation of Electronically Excited Styrene by Chemical Concentration Quenching Processes - Photo-Oligomers and Photopolymers. *Makromol. Chem.* **1979,** *180*, 2649-2663.

(233) Lock, E. H.; Petrovykh, D. Y.; Mack, P.; Carney, T.; White, R. G.; Walton, S. G.; Fernsler, R. F. Surface Composition, Chemistry, and Structure of Polystyrene Modified by Electron-Beam-Generated Plasma. *Langmuir* **2010,** *26*, 8857-8868.

(234) Kroschwitz, J. I., *Kirk-Othmer Encyclopedia of Chemical Technology*; 5th ed.; Wiley-Interscience: Chichester, Hoboken, NJ, 2004.

(235) Rharbi, Y.; Yekta, A.; Winnik, M. A. A Method for Measuring Oxygen Diffusion and Oxygen Permeation in Polymer Films Based on Fluorescence Quenching. *Anal. Chem.* **1999,** *71*, 5045-5053.

(236) Lu, X.; Winnik, M. A. Luminescence Quenching in Polymer/Filler Nanocomposite Films Used in Oxygen Sensors. *Chem. Mater.* **2001,** *13*, 3449-3463.

(237) Boukherroub, R.; Wayner, D. D. M. Controlled Functionalization and Multistep Chemical Manipulation of Covalently Modified Si(111) Surfaces. *J. Am. Chem. Soc.* **1999,** *121*, 11513-11515.

(238) Veinot, J. G. C. Synthesis, Surface Functionalization, and Properties of Freestanding Silicon Nanocrystals. *Chem. Commun.* **2006**, 4160-4168.

(239) Sperling, R. A.; Parak, W. J. Surface Modification, Functionalization and Bioconjugation of Colloidal Inorganic Nanoparticles. *Philos. Trans. R. Soc. A-Math. Phys. Eng. Sci.* **2010,** *368*, 1333-1383.

(240) Conradi, M.; Kocijan, A.; Zorko, M.; Jerman, I. Effect of Silica/Pvc Composite Coatings on Steel-Substrate Corrosion Protection. *Prog. Org. Coat.* **2012,** *75*, 392-397.

(241) Carbone, L.; Cozzoli, P. D. Colloidal Heterostructured Nanocrystals: Synthesis and Growth Mechanisms. *Nano Today* **2010,** *5*, 449-493.

(242) Xu, J.; Zhang, W. X.; Yang, Z. H.; Ding, S. X.; Zeng, C. Y.; Chen, L. L.; Wang, Q.; Yang, S. H. Large-Scale Synthesis of Long Crystalline Cu2-Xse Nanowire Bundles by Water-Evaporation-Induced Self Assembly and Their Application in Gas Sensing. *Adv. Funct. Mater.* **2009,** *19*, 1759-1766.

(243) Zhang, Y.; Hu, C. G.; Zheng, C. H.; Xi, Y.; Wan, B. Y. Synthesis and Thermoelectric Property of Cu2-Xse Nanowires. *J. Phys. Chem. C* **2010,** *114*, 14849-14853.

(244) Zolotovskaya, S. A.; Posnov, N. N.; Prokosin, P. V.; Yumashev, K. V.; Gurin, V. S.; Alexeenko, A. A. Nonlinear Properties of Phototropic Media on the Basis of Cuxse Nanoparticles in Quartz Glass. *Semiconductors* **2004,** *38*, 812-817.

(245) Hessel, C. M.; Pattani, V. P.; Rasch, M.; Panthani, M. G.; Koo, B.; Tunnell, J. W.; Korgel, B. A. Copper Selenide Nanocrystals for Photothermal Therapy. *Nano Lett.* **2011,** *11*, 2560-2566.

(246) Okimura, H.; Matsumae, T.; Makabe, R. Electrical Properties of Cu2−Xse Thin Films and Their Application for Solar Cells *Thin Solid Films* **1980,** *71*, 53-59.

(247) Choi, J.; Kang, N.; Yang, H. Y.; Kim, H. J.; Son, S. U. Colloidal Synthesis of Cubic-Phase Copper Selenide Nanodiscs and Their Optoelectronic Properties. *Chem. Mater.* **2010,** *22*, 3586-3588.

(248) Deka, S.; Genovese, A.; Zhang, Y.; Miszta, K.; Bertoni, G.; Krahne, R.; Giannini, C.; Manna, L. Phosphine-Free Synthesis of P-Type Copper(I) Selenide Nanocrystals in Hot Coordinating Solvents. *J. Am. Chem. Soc.* **2010,** *132*, 8912-8914.

(249) Deng, Z. T.; Mansuripur, M.; Muscat, A. J. Synthesis of Two-Dimensional Single-Crystal Berzelianite Nanosheets and Nanoplates with near-Infrared Optical Absorption. *J. Mater. Chem.* **2009,** *19*, 6201-6206.

(250) Hsu, Y. J.; Hung, C. M.; Lin, Y. F.; Liaw, B. J.; Lobana, T. S.; Lu, S. Y.; Liu, C. W. [Cu-4{Se2p((Opr)-Pr-I)(2)}(4)]: A Novel Precursor Enabling Preparation of Nonstoichiometric Copper Selenide (Cu2-Xse) Nanowires. *Chem. Mater.* **2006,** *18*, 3323-3329.

(251) Jagminas, A.; Juskenas, R.; Gailiute, I.; Statkute, G.; Tomasiunas, R. Electrochemical Synthesis and Optical Characterization of Copper Selenide Nanowire Arrays within the Alumina Pores. *J. Cryst. Growth* **2006,** *294*, 343-348.

(252) Li, D. P.; Zheng, Z.; Lei, Y.; Ge, S. X.; Zhang, Y. D.; Zhang, Y. G.; Wong, K. W.; Yang, F. L.; Lau, W. M. Design and Growth of Dendritic Cu2-Xse and Bunchy Cuse Hierarchical Crystalline Aggregations. *Crystengcomm* **2010,** *12*, 1856-1861.

(253) Statkute, G.; Tomasiunas, R. Copper Selenide Nanowires and Nanocrystallites in Alumina: Carrier Relaxation, Recombination, and Trapping. *J. Appl. Phys.* **2007,** *101*, 113715-1-113715-9.

(254) Vinod, T. P.; Jin, X.; Kim, J. Hexagonal Nanoplatelets of Cuse Synthesized through Facile Solution Phase Reaction. *Mater. Res. Bull.* **2011,** *46*, 340-344.

(255) Yu, R.; Ren, T.; Sun, K. J.; Feng, Z. C.; Li, G. N.; Li, C. Shape-Controlled Copper Selenide Nanocubes Synthesized by an Electrochemical Crystallization Method. *J. Phys. Chem. C* **2009,** *113*, 10833-10837.

(256) Chen, H. H.; Zou, R. J.; Wang, N.; Zhang, Z. Y.; Sun, Y. G.; Yu, L.; Tian, Q. W.; Chen, Z. G.; Hu, J. Q. Morphology-Selective Synthesis and Wettability Properties of Well-Aligned Cu(2-X)Se Nanostructures on a Copper Substrate. *J. Mater. Chem.* **2011,** *21*, 3053-3059.

(257) Zhang, S. Y.; Fang, C. X.; Tian, Y. P.; Zhu, K. R.; Jin, B. K.; Shen, Y. H.; Yang, J. X. Synthesis and Characterization of Hexagonal Cuse Nanotubes by Templating against Trigonal Se Nanotubes. *Cryst. Growth Des.* **2006,** *6*, 2809-2813.

(258) Kemell, M.; Ritala, M.; Leskela, M. Thin Film Deposition Methods for Culnse(2) Solar Cells. *Crit. Rev. Solid State Mater. Sci.* **2005,** *30*, 1-31.

(259) George, S.; Xia, T. A.; Rallo, R.; Zhao, Y.; Ji, Z. X.; Lin, S. J.; Wang, X.; Zhang, H. Y.; France, B.; Schoenfeld, D.; Damoiseaux, R.; Liu, R.; Lin, S.; Bradley, K. A.; Cohen, Y.; Nal, A. E. Use of a High-Throughput Screening Approach Coupled with in Vivo Zebrafish Embryo Screening to Develop Hazard Ranking for Engineered Nanomaterials. *ACS Nano* **2011,** *5*, 1805-1817.

(260) Hirota, Y.; Isshiki, T.; Okashita, K.; Shiojiri, M. High-Resolution Transmission Electron-Microscopy of Growth and Structures of Ag-Te and Cu-Se Crystals Produced by Solid-Solid Reactions. *J. Cryst. Growth* **1991,** *112*, 55-70.

(261) Kaito, C. Electron-Microscopic Studies of Growth of Cu-Se Crystals by Reaction of Selenium Films with Copper Fine Particles. *J. Cryst. Growth* **1974,** *24*, 563-567.

(262) Kaito, C.; Nonaka, A.; Kimura, S.; Suzuki, N.; Saito, Y. Size Effect on Solid-Solid Reaction Growth between Cu Film and Se Particles. *J. Cryst. Growth* **1998,** *186*, 386-392.

(263) Morikawa, H. Growth of Copper Selenide Crystals Produced by Solid-State Reaction. *Jpn. J. Appl. Phys.* **1970,** *9*, 607-614.

(264) Shiojiri, M.; Kaito, C.; Saito, Y.; Teranishi, K.; Sekimoto, S. High-Resolution Electron-Microscopic Study of the Growth of Cu-Se Crystals by a Solid-Solid Reaction. *J. Cryst. Growth* **1981,** *52*, 883-886.

(265) Ouchi, A.; Bastl, Z.; Bohacek, J.; Orita, H.; Miyazaki, K.; Miyashita, S.; Bezdicka, P.; Pola, J. Room-Temperature Reaction between Laser Chemical Vapor Deposited Selenium and Some Metals. *Chem. Mater.* **2004,** *16*, 3439-3445.

(266) Ishikawa, Y.; Kido, O.; Kimura, Y.; Kurumada, M.; Suzuki, H.; Saito, Y.; Kaito, C. Mechanism of Copper Selenide Growth on Copper-Oxide-Selenium System. *Surf. Sci.* **2004,** *548*, 276-280.

(267) Chen, J. Y.; Wiley, B. J.; Xia, Y. One-Dimensional Nanostructures of Metals: Large-Scale Synthesis and Some Potential Applications. *Langmuir* **2007,** *23*, 4120-4129.

(268) Huang, X. H.; Neretina, S.; El-Sayed, M. A. Gold Nanorods: From Synthesis and Properties to Biological and Biomedical Applications. *Adv. Mater.* **2009,** *21*, 4880-4910.

(269) Biesinger, M. C.; Lau, L. W. M.; Gerson, A. R.; Smart, R. S. C. Resolving Surface Chemical States in Xps Analysis of First Row Transition Metals, Oxides and Hydroxides: Sc, Ti, V, Cu and Zn. *Appl. Surf. Sci.* **2010,** *257*, 887-898.

(270) Bish, D. L.; Howard, S. A. Quantitative Phase-Analysis Using the Rietveld Method. *J. Appl. Crystallogr.* **1988,** *21*, 86-91.

(271) Chen, Y. W.; Li, L.; D'Ulivo, A.; Belzile, N. Extraction and Determination of Elemental Selenium in Sediments - a Comparative Study. *Anal. Chim. Acta* **2006,** *577*, 126-133.

(272) Patterson, A. L. The Scherrer Formula for X-Ray Particle Size Determination. *Phys. Rev.* **1939,** *56*, 978-982.

(273) Omadelung, O.; Schulz, M.; Weiss, H., *Landolt-Borstein - Group Iii Condensed Matter Numerical Data and Functional Relationships in Science and Technology*; Springer-Verlag: Berlin, 1998; Vol. III/17E-17F-41C.

(274) Singh, U. P.; Patra, S. P. Progress in Polycrystalline Thin-Film Cu(in,Ga)Se-2 Solar Cells. *Int. J. Photoenergy* **2010,** *2010*.

(275) Zhai, T. Y.; Fang, X. S.; Liao, M. Y.; Xu, X. J.; Li, L.; Liu, B. D.; Koide, Y.; Ma, Y.; Yao, J. N.; Bando, Y.; Golberg, D. Fabrication of High-Quality In2se3 Nanowire Arrays toward High-Performance Visible-Light Photodetectors. *ACS Nano* **2010,** *4*, 1596-1602.

(276) Peng, H. L.; Meister, S.; Chan, C. K.; Zhang, X. F.; Cui, Y. Morphology Control of Layer-Structured Gallium Selenide Nanowires. *Nano Lett.* **2007,** *7*, 199-203.

(277) Reifsnyder, D. C.; Ye, X. C.; Gordon, T. R.; Song, C. Y.; Murray, C. B. Three-Dimensional Self-Assembly of Chalcopyrite Copper Indium Diselenide Nanocrystals into Oriented Films. *ACS Nano* **2013,** *7*, 4307-4315.

(278) Phan, N. T. S.; Van Der Sluys, M.; Jones, C. W. On the Nature of the Active Species in Palladium Catalyzed Mizoroki-Heck and Suzuki-Miyaura Couplings - Homogeneous or Heterogeneous Catalysis, a Critical Review. *Adv. Synth. Catal.* **2006,** *348*, 609-679.

(279) Niu, D. C.; Wang, X.; Li, Y. S.; Zheng, Y. Y.; Li, F. Q.; Chen, H. R.; Gu, J. L.; Zhao, W. R.; Shi, J. L. Facile Synthesis of Magnetite/Perfluorocarbon Co-Loaded Organic/Inorganic Hybrid Vesicles for Dual-Modality Ultrasound/Magnetic Resonance Imaging and Imaging-Guided High-Intensity Focused Ultrasound Ablation. *Adv. Mater.* **2013,** *25*, 2686-2692.

(280) Wang, X.; Chen, H. R.; Chen, Y.; Ma, M.; Zhang, K.; Li, F. Q.; Zheng, Y. Y.; Zeng, D. P.; Wang, Q.; Shi, J. L. Perfluorohexane-Encapsulated Mesoporous Silica Nanocapsules as Enhancement Agents for Highly Efficient High Intensity Focused Ultrasound (Hifu). *Adv. Mater.* **2012,** *24*, 785-+.

(281) Pyrz, W. D.; Buttrey, D. J. Particle Size Determination Using Tem: A Discussion of Image Acquisition and Analysis for the Novice Microscopist. *Langmuir* **2008,** *24*, 11350-11360.

(282) Friedrich, J. M.; Rivers, M. L.; Perlowitz, M. A.; Meinhart, Z.; Ramirez, V. V. Characterization of Particle Size Standard Nist 1019b with Synchrotron X-Ray Microtomography and Digital Data Extraction. *Part. Part. Syst. Charact.* **2012,** *29*, 35-42.

(283) Boyd, R. D.; Pichaimuthu, S. K.; Cuenat, A. New Approach to Inter-Technique Comparisons for Nanoparticle Size Measurements; Using Atomic Force Microscopy, Nanoparticle Tracking Analysis and Dynamic Light Scattering. *Colloid Surf. A-Physicochem. Eng. Asp.* **2011,** *387*, 35-42.

(284) Beaucage, G.; Kammler, H. K.; Pratsinis, S. E. Particle Size Distributions from Small-Angle Scattering Using Global Scattering Functions. *J. Appl. Crystallogr.* **2004,** *37*, 523-535.

(285) Hostetler, M. J.; Wingate, J. E.; Zhong, C. J.; Harris, J. E.; Vachet, R. W.; Clark, M. R.; Londono, J. D.; Green, S. J.; Stokes, J. J.; Wignall, G. D.; Glish, G. L.; Porter, M. D.; Evans, N. D.; Murray, R. W. Alkanethiolate Gold Cluster Molecules with Core Diameters from 1.5 to 5.2 Nm: Core and Monolayer Properties as a Function of Core Size. *Langmuir* **1998,** *14*, 17-30.

(286) Mie, G. Articles on the Optical Characteristics of Turbid Tubes, Especially Colloidal Metal Solutions. *Annalen Der Physik* **1908,** *25*, 377-445.

(287) Doane, T. L.; Chuang, C. H.; Hill, R. J.; Burda, C. Nanoparticle Zeta-Potentials. *Acc. Chem. Res.* **2012,** *45*, 317-326.

(288) Roberts, G. S.; Kozak, D.; Anderson, W.; Broom, M. F.; Vogel, R.; Trau, M. Tunable Nano/Micropores for Particle Detection and Discrimination: Scanning Ion Occlusion Spectroscopy. *Small* **2010,** *6*, 2653-2658.

(289) Malloy, A.; Carr, B. Nanoparticle Tracking Analysis - the Halo (Tm) System. *Part. Part. Syst. Charact.* **2006,** *23*, 197-204.

(290) Slocik, J. M.; Zabinski, J. S., Jr.; Phillips, D. M.; Naik, R. R. Colorimetric Response of Peptide-Functionalized Gold Nanoparticles to Metal Ions. *Small* **2008,** *4*, 548-551.

(291) Bell, N. C.; Minelli, C.; Tompkins, J.; Stevens, M. M.; Shard, A. G. Emerging Techniques for Submicrometer Particle Sizing Applied to Stober Silica. *Langmuir* **2012,** *28*, 10860-10872.

(292) Holzwarth, U.; Gibson, N. The Scherrer Equation Versus the 'Debye-Scherrer Equation'. *Nat. Nanotech.* **2011,** *6*, 534-534.

(293) Langford, J. I.; Wilson, A. J. C. Scherrer after Sixty Years: A Survey and Some New Results in the Determination of Crystallite Size. *J. Appl. Crystallogr.* **1978,** *11*, 102-113.

Appendices

Appendix A. Electric Field Simulation by COMSOL Finite Element Method

Electric field can be visualized through simulation in COMSOL using finite element method. The finite element method solves a charge conservation equation for the electric potential given the spatial distribution of electric charge in dielectric under static conditions. Both the magnitude and directional components of the electric field are calculated by the finite element method. The flux density (D) and strength of the electric field (E) in a 2D or 3D geometry was determined by solving the following equation,

$$D = \varepsilon_o \varepsilon_r E$$

where ε_o is the electric permittivity of free space (ε_o = 8.85E-12 F/m), and ε_r is the relative permittivity of the isotropic medium. We were able to identify that our nanowires assemble along the direction of the electric field by correlating the experimental data with the simulated electric field. We also verified that the highest concentration of these assembled structures are located in areas of the highest electric field strength in the electrokinetic assembly of selenium and silver nanowires.

Video tutorials on the COMSOL software are posted in the following link, http://www.youtube.com/user/softhummingbird/featured (accessed on September 03, 2013).

For additional information please refer to these books Pryor, Roger W. *Multiphysics modeling using COMSOL: a first principles approach*, Jones and Barlett: Sudbury, Mass. 2011 in the Simon Fraser University Fraser Library (Surrey Campus), and Zimmerman, William B. J. *Multiphysics modelling with finite element methods*, London: New Jersey, 2006 in the Simon Fraser University Bennett Library (Burnaby Campus).

Appendix B. X-Ray Photoelectron Spectroscopy Calibration

Proper calibration of the hemispherical electron spectrometer is essential in obtaining accurate and high quality data with consistency. The instrument's performance is, also, optimized through calibration, making the signal-to-noise ratio higher than an instrument that is un-calibrated. A properly calibrated instrument will allow the users to obtain accurate and high quality data

The X-ray photoelectron spectroscopy (XPS) linear energy scale calibration procedure was performed in accordance to the **ISO 15472** international procedure. For this procedure, all reference standard samples (gold and copper thin films) are etched with Argon ions to remove surface contaminants. The Argon ion etch area is 4 mm x 4 mm. Elemental composition, obtained from a survey scan that spans from 1200 to 0 eV in binding energy, of an Argon sputter cleaned sample should contain less than 1% atomic mass of oxygen and carbon. The elemental composition of Argon sputtered samples were calculated from survey scans of the corresponding reference standards. Survey scans were acquired at 0.5 eV increments, a Pass Engery of 160 eV, with a Mg X-ray source operating at 150 W (10 mA and 15 kV).

Energy scale linearity was calibrated using a dual anode of Al and Mg X-ray sources on Argon sputter cleaned gold and copper substrates. High resolution spectra of Cu $3p_{3/2}$ were obtained with Mg X-rays and the Au $4f_{7/2}$ signal were collected with Al X-rays. Signals were collected at 0.025 eV increments, and the hemispherical spectrometer's electromagnetic lens was set to hybrid mode operating at a Pass Energy of 10 eV. Photoelectrons were collect from a 300 µm x 700 µm area of the sample. The kinetic energy separation between the acquired Cu $3p_{3/2}$ and Au $4f_{7/2}$ peaks should be within $\pm$ 0.025 eV of the theoretical value of 1081.680 eV. Instrument gain is adjusted if the deviation is great than $\pm$ 0.025 eV.

After the linear energy scale calibration was completed, Mg X-ray source was used to acquire a photoemission spectrum of the Au thin film. The signals were collected at 0.025 eV increments, and the hemispherical spectrometer's electromagnetic lens was set to a hybrid mode operating at a Pass Energy of 10 eV. Photoelectrons were collect from a 300 µm x 700 µm area of the sample. Work function of the instrument is then adjusted to position the apex of the Au $4f_{7/2}$ peak at 83.950 $\pm$ 0.025 eV.

Appendix C. Secondary Ion Mass Spectrometry Calibration

Proper calibration of the mass spectrometer is essential in obtaining accurate, consistent and high quality data. The instrument's performance is, also, optimized through calibration, making the signal-to-noise ratio higher than an instrument that is un-calibrated. A properly calibrated instrument will allow the users to obtain accurate and high quality data with great efficiency.

Mass alignment of the Hiden Analytical MAXIM triple filtered quadrupole secondary ion mass spectrometry (SIMS) analyzer was performed with a cesium iodide (CsI) sample drop casted on a ~1 cm^2 piece of polished Si/SiOx wafer. Secondary ions, both positive and negative ions, were created by bombarding the sample with Argon ions at energies of 4.90 kV. Positive and negative ion mass alignments were performed separately using the same CsI sample as the calibration standard. In positive ion mass alignment, atomic masses of 22.99 (Na^+), 132.91 (Cs^+), and 392.71(Cs_2I^+) were selected as the reference masses to calibrate the analyzer linearity and for the negative ion mass alignment, atomic masses of 15.99 (O^-), 126.90 (I^-), and 386.71 (CsI_2^-) were chosen as the reference masses.

NOTE: Please leave this procedure to a properly trained technician. Do not be afraid to request the technician to perform a mass alignment calibration if you think it is out of alignment.

Appendix D. Materials Analysis Using Diffraction by Quantitative Rietveld Refinement

Rietveld quantitative analysis is a method for determining the composition of phase/texture in a sample containing multiple phases or the crystallites have certain preferential orientations. This is an indirect method to determine the phase composition in a multiphase sample, without using internal standards. The method uses the following equation to calculate the ratio of different crystal phases in a sample,

$$Wp = \frac{Sp(ZMV)}{\sum_{i=0}^{n} Si(ZMV)i}$$

where ***W*** is the relative weight fraction of a specific phase ***p*** in a sample that contains ***n*** phases. The equation also takes Rietveld scale factor, ***S***, number of formula units per cell, ***Z***, the mass formula unit, ***M***, and the unit cell volume, ***V***. Each diffraction pattern's intensity and peak width is adjusted so the linear combination of the individual diffraction pattern matches that of the acquired diffraction data. In the synthesis of copper selenide@polystyrene core–shell nanowires from the selenium nanowire template, the diffraction patterns prior to thermal purification consisted of a mixture of trigonal selenium, hexagonal, orthorhombic, and cubic phases of copper selenide. We were able to follow the progress of reaction by XRD and Rietveld quantitative analysis. In addition, we were able to confirm using Rietveld quantitative analysis the successful removal of residual selenium nanowires from the sample by selective thermal evaporation.

Materials Analysis Using Diffraction (MAUD) software was download from http://www.ing.unitn.it/~maud/ (accessed on September 03, 2013).

Video tutorials that demonstrated installation and operation of the MAUD software are posted on Youtube. These tutorial videos can be accessed from this link http://www.youtube.com/user/MaudRietveldProgram (accessed on September 03, 2013).

Reference diffraction pattern data were obtained from Inorganic Crystal Structure Database available to SFU students through the SFU library from the following link http://icsd.fiz-karlsruhe.de.proxy.lib.sfu.ca/icsd/ (accessed on September 03, 2013).

NOTE: Quantitative XRD phase analysis can only be applied to phase quantification only if structures of all phases within the sample are known.

Appendix E. Approximating Size of Crystallites using the Scherrer Equation.

Size of submicron crystallites can be approximated from the corresponding diffraction pattern using the Scherrer equation. This technique works well for samples that are hard to disperse prior to electron microscopy analysis. Also, this method is less time consuming than counting the size of individual particles from electron microscopy images,[281] X-ray microtomography,[282] atomic force microscopy,[283] small angle X-ray scattering,[284-285] dynamic light scattering techniques[286-287], scanning ion occlusion sensing,[288] nanoparticle tracking analysis,[289] differential centrifugal sedimentation,[290] and scanning mobility particle sizing.[291]

Scherrer equation is used for approximating the average size of nanoscale crystallites from the acquired diffraction pattern,

$$\tau = \frac{K \times \lambda}{\beta \cos \theta}$$

where $\boldsymbol{\tau}$ is the approximated crystallite dimension, $\boldsymbol{\lambda}$ is the X-ray wavelength used to obtain the diffraction pattern, $\boldsymbol{\beta}$ is the full width at half maximum (FWHM) of a specific diffraction plane expressed in radians after instrumental peak broadening is removed, $\boldsymbol{\theta}$ is the Bragg angle of the same diffraction plane that defined the FWHM. $\boldsymbol{K}$ is the Scherrer constant, a dimensionless shape factor.[272, 292] For a sample containing crystallites of any shape, a Scherrer constant of 0.9 is sufficient to provide a first approximation.[293] The Scherrer equation gives volume-weighted mean column length. The approximated crystal size of a specific diffraction peak/plane (i.e., (hkl) of Miller index) is average crystallite size perpendicular to the (hkl) plane.

Note: Scherrer equation should only be used to approximate the crystal size of nanoparticles. The equation will not be able to approximate micron sized particles or larger with certainty and precision. Strain induced peak broadening will lead to an underestimation of the nanostructures' size.

Appendix F. Full List of Publications

1. "Tuning Ligand Electronics and Peripheral Substitution on Cobalt Salen Complexes: Structure and Polymerisation Activity," Chiang, L.; Laura, E. N. A.; Alcantara, J.; **Wang, M. C. P.**; Storr, T.; Shaver, M. P. *Dalton Trans.*, **2014**, *ASAP* DOI: 10.1039/C3DT51846A.

2. "Tunable Loading of Single-Stranded DNA on Gold Nanorods through the Displacement of Polyvinylpyrrolidone," Pekcevik, I. C.; Poon, L. C. H.; **Wang, M. C. P.**; Gates, B. D. *Anal. Chem.*, **2013**, *85*, 9960-9967.

3. "Surface-Initiated Atom Transfer Radical Polymerization-Induced Transformation of Selenium Nanowires into Copper Selenide@Polystyrene Core-Shell Nanowires," **Wang, M. C. P.**; Gates, B. D. *ACS Appl. Mater. Interfaces*, **2013**, *5*, 9546-9553.

4. "Comprehensive Structural, Surface-Chemical and Electrochemical Characterization of Nickel-Based Metallic Foams," van Drunen, J.; Kinkead, B.; **Wang, M. C. P.**; Sourty, E.; Gates, B. D.; Jerkiewicz, G. *ACS Appl. Mater. Interfaces*, **2013**, *5*, 6712-6722. (front cover)

5. "Directed Polystyrene/Poly(methyl methacrylate) Phase Separation and Nanoparticle Ordering on Transparent Chemically Patterned Substrates," Saei, S.; **Wang, M. C. P.**; Gates, B. D.; Moffitt, M. *Langmuir*, **2012**, *28*, 10838-10848.

6. "Optimizing the Quality of Monoreactive Perfluoroalkylsilane-Based Self-Assembled Monolayers," Gong, Y.; **Wang, M. C. P.**; Zhang, X.; Ng, H. W.; Gates, B. D. *Langmuir*, **2012**, *28*, 11790-11801.

7. "Synthesis of Selenium Nano-Composite (*t*-Se@PS) by Surface Initiated Atom Transfer Radical Polymerization," **Wang, M. C. P.**; Gates, B. D. *Chem. Commun.*, **2012**, *48*, 8589-8591.

8. "Dual-Function Triazole-Pyridine Derviatives as Inhibitors of Metal-Induced Amyloid-β Aggregation," Jones, M. R.; Servie, E. L.; Thompson, J. R.; **Wang, M. C. P.**; Kimsey, I. J.; DeToma, A. S.; Ramamoorthy, A.; Lim, M. H.; Storr, T. *Metallomics*, **2012**, *4*, 910-920.

9. "Patterning Block Copolymer Aggregates via Langmuir-Blodgett Transfer to Microcontact-Printed Substrates," Saei, S.; **Wang, M. C. P.**; Gates, B. D.; Moffitt, M. *Langmuir*, **2010**, *26*, 5998-6008.

10. "Electrostatic Assembly of Selenium and Silver Nanowires into Macroscopic Fibers," **Wang, M. C. P.**; Majidi, E.; Gates B. D. *ACS Nano,* **2010***, 4,* 2607-2614.

11. "Directed Assembly of Nanowires," **Wang, M. C. P.**; Gates, B. D. *Materials Today*, **2009**, *12*, 34-43.

12. "Stabilizing Dispersions of Large Quantities of Selenium Nanowires," **Wang, M. C. P.**; Gates, B. D. *MRS Symp. Proc.*, **2008**, *1144*, 1144-LL18-25.

13. "Thin-layer Electrochemistry of Ferrocenylbenzene Derivatives: Intramolecular electronic communication," **Wang, M. C. P.**; Li, Y.; Merbouh, N.; Yu, H. Z. *Electrochimica Acta* **2008**, 53, 7720-7725.